Numerical Study on Under-Ventilated Enclosure Fires and Fire Spread on Building Façades

Numerieke studie over ondergeventileerde compartimentsbranden en branduitbreiding op façades van gebouwen

Guoxiang Zhao

Promotoren: prof. dr. ir. B. Merci, dr. T. Beji
Proefschrift ingediend tot het behalen van de graad van
Doctor in de ingenieurswetenschappen: Fire Safety Engineering

UNIVERSITEIT
GENT

Vakgroep Mechanica van Stroming, Warmte en Verbranding
Voorzitter: prof. dr. ir. J. Vierendeels
Faculteit Ingenieurswetenschappen en Architectuur
Academiejaar 2017 - 2018

ISBN 978-94-6355-079-6
NUR 950
Wettelijk depot: D/2017/10.500/114

Promoters:

Prof. dr. ir. Bart Merci, dr. ir. Tarek Beji

Department:

Department of Flow, Heat and Combustion Mechanics (FloHeaCom)
Ghent University
Sint-Pietersnieuwstraat 41
B-9000 Gent, Belgium

Members of the exam committee:

Chairman:	
Prof. dr. ir. Luc Taerwe	Faculty of Engineering and Architecture, UGent
Secretary:	
Prof. dr. ir. Tom De Mulder	Faculty of Engineering and Architecture, UGent
Reading committee:	
Dr. ir. Georgios Maragkos	Faculty of Engineering and Architecture, UGent
Dr. ir. Dionysios I. Kolaitis	National Technical University of Athens, Greece
Prof. Jie Ji	University of Science and Technology of China, China
Dr. ir. Ruben Van Coile	Department of Structural engineering, UGent
Other members:	
Dr. ir. Tarek Beji	Faculty of Engineering and Architecture, UGent
Prof. dr. ir. Bart Merci	Faculty of Engineering and Architecture, UGent

Acknowledgments

First of all, I would like to thank my supervisor, Prof. Bart Merci, for giving me the opportunity to join his research group and work with all these lovely people in the group. Thank you for your support, guidance and trust in me during all these four years time. I feel extremely lucky to have had the opportunity to work with you.

I appreciate Dr.Tarek Beji for his guidance and he is always there willing to help me with my research. His encouragement keeps me going when I was confusing. This accomplishment would not have been possible without him.

I thank all my colleagues and friends for their support during the past four years time. It is hard to acknowledge all of them here. Some of them are Georgios Maragkos, Ivana Stanković, Setareh Ebrahim Zadeh, Davood Zeinali, Longxing Yu, Zihe Gao, Jiayun Sun, José Felipe Pérez Segovia, Alessandro D'Ausilio, Boris Kruljevic, Junyi Li, Elise Meerburg, Lies Decroos, Griet Blondé, Anni Harri, and Yves Maenhout. For these friends I met in Ghent, our friendship is really a gift for me, I will always remember all these precious moment we spend together. Furthermore, I would like to thank all badminton and basketball club partners, and other friends from Belgium.

I want to acknowledge the financial support from China Scholarship Council, and the Special Research Fund (BOF) from Ghent University. This PhD would not have been possible without these sustainable support.

Finally, I would like to heartly thank all my family members for their moral support, unconditional love, and encouragement. They were the source for my motivation, with their care and support, I feel very privileged to be able to fully devote myself to purse this PhD.

Guoxiang Zhao
Ghent, December, 2017

Summary

Fires can pose a big threat to the people inside of a building. In recent years, with the rapid economic development and urbanization, there have been more and more large building fires all around the world. Hence, fire safety of high-rise buildings is an important point of attention, especially in cases where flames ejected from an enclosure and attached to the building façade. The ejected flames can spread along the façade, but can also cause a secondary fire, spreading to adjacent floors. Eventually the fire could fully develop over the whole building and it becomes impossible for the firefighters to extinguish the fire. Therefore, it is necessary to understand the involved physics and try to predict the ejected flame spread on a building façade. One way to investigate this problem is performing numerical simulations, using Computational Fluid Dynamics (CFD) codes.

The overall objective of this PhD thesis is to assess the state-of-the-art in CFD modeling, in particular using the Fire Dynamics Simulator (FDS) code, as a basis for understanding fire spread behavior in the context of building façade fires. A step-wise strategy has been employed in the thesis, consisting of three main parts.

In the first part of the thesis, an investigation has been made of the use of FDS for the modeling of fire and smoke dynamics in the gas phase. Two scenarios have been considered. The first scenario is the buoyant flow in the stairwell, aiming to illustrate the potential of CFD modeling in high-rise buildings with a well-ventilated fire and without flame spread. A detailed study has been conducted, discussing the air flow velocity at the opening in the middle of the stairwell, the temperature rise inside the stairwell, the temperature at the middle opening, the influence of the presence of a staircase on the pressure distribution, and the location of the neutral plane height. Moreover, the influence of the turbulence model on the simulation results is discussed. Overall, the obtained results confirm that reliable insights can be retrieved from CFD simulations regarding the motion of smoke in the high-rise buildings. The second scenario is regarding several under-ventilated fire simulations in an enclosure with flames ejecting from its opening. Four different opening geometries are considered in the simulations: 0.1 m x 0.2 m, 0.2 m

x 0.2 m, 0.2 m x 0.3 m, and 0.3 m x 0.3 m. The accuracy of the obtained results has been discussed and comparison has been made with experimental data, as well as empirical correlations. The required resolution of the computational grid has been discussed by analyzing the mass balance 'error' based on the post-processing of the total mass flow rate into and out of the enclosure. Two length scale ratios have been formulated for assessment of the grid resolution, in addition to the conventional D^* criterion. The first ratio is the ventilation factor to the grid cell size, while the second is the ratio of the hydraulic diameter of the opening to the grid cell size. When these two length scale ratios are larger than 10, the corresponding mass balance 'error' is lower than 4%. The results in terms of velocities through the door opening and the temperatures along the doorway are also grid insensitive in this case. The air inflow rate through the opening is found to correlate linearly to the ventilation factor, in agreement with the literature. Moreover, the heat release rate inside the enclosure shows a linear relationship with the ventilation factor, although the value of the slope is lower than the conventional value in the literature. This has been explained through the lower mass flow rate of incoming air and incomplete consumption of oxygen flowing into the compartment. The temperature predictions show that: (1) the temperature at back and front opposite corners are not identical, but meaningful average temperatures inside the enclosure can be defined, (2)such obtained average gas temperatures inside the enclosure deviate less than 10% from Babrauskas correlation for the different opening geometries. It has been shown that FDS can accurately reproduce the neutral plane height position for the various configurations. The external flame height predictions are sensitive to the criterion to define the flame height, namely the choice of flame tip temperature. Nevertheless, the trends have been captured correctly. The predicted height of the ejecting flames increases with the fire HRR. The power dependence of the flame height on the external heat release rate is equal to $2/3$.

The second part of the thesis has been devoted to the coupling of pyrolysis and CFD modeling. It has been recognized that both material and model properties and the scale of the scenario bear crucial importance. Accordingly, the focus is first on the modelling of pyrolysis and then combustion in small scale. The necessary material and model properties have been determined through a simple trial and error procedure. The conducted grid sensitivity study has shown that the D^* criterion is insufficient for coupled gas-solid phase fire simulations. Subsequently, the intermediate scale Single Burning Item (SBI) corner fire tests has been considered. Correspondingly, several simulations of SBI experiments have been conducted with MDF panels, using material properties determined from the previous part, as well as a calibration test with calcium silicate panels. The significance

of the completeness of the enclosure geometry has been investigated. Both 'complete' and 'simplified' geometry models have been considered to investigate the influence of the geometry on the predictions. Significantly different flow patterns have been observed between the complete and the simplified model cases. In general, the complete model case features higher heat fluxes than the simplified model case. Similar to the heat flux predictions, a higher peak HRR has been obtained in the complete model case. The overall trend has been reasonably captured with the numerical model in both cases.

In the third part of the thesis, the use of the FDS code for the modeling of façade fires has been illustrated through a fictitious scenario, in which both inert and MDF panels have been used as the façade wall material, with an under-ventilated enclosure fire source. First of all, the characteristics of the façade fire have been discussed, in terms of the HRR, heat fluxes on the façade wall, and the propagation of the pyrolysis front on the MDF panel, in the absence of wind. First, results with the inert façade have been discussed. Subsequently, the fire spread in the case with the MDF façade has been explained, through comparison with the inert façade case. Subsequently, the effect of wind on the façade fire spread has been investigated. A simplified wind condition has been considered, with a uniform velocity into the domain. Two directions have been investigated, namely one perpendicular to the façade, and the other parallel to the façade, with various speeds (ranging up to 8 m/s). It has been illustrated that the analysis should be based on the momentum in the flow field. When the wind is perpendicular to the façade, the outflow of unburnt fuel from the compartment is hindered (and, for sufficiently high wind speed, blocked), reducing the height of the ejecting flame. The unburnt fuel is also pushed sideward and downward as it emerges from the opening and may not react (or at least not inside the computational domain). This leads to reduced fire spread. When the wind is parallel to the façade, there is little impact on the mass flow rate, emerging from the enclosure, because the horizontal wind-induced momentum is not in the same direction as the horizontal fire-induced flow momentum. As such, there is no reduced fire spread. For sufficiently low wind momentum, no effect on the shape of the pyrolysis region is observed. For higher momentums, an angle is observed from the vertical direction. This angle increases as the wind speed increases, leading to combined upward and sideward fire spread. All this is an illustration of a proof-of-concept of the potential of using FDS for façade fires, including wind conditions.

Finally, the main conclusions of the thesis work have been summarized. Consequently, recommendations for future work have been made regarding modelling façade fires.

Samenvatting

Brand kan een grote bedreiging zijn voor aanwezigen in een gebouw. In de voorbije jaren, als gevolg van de snelle economische ontwikkeling en verstedelijking, zijn er wereldwijd meer en meer grote branden geweest in gebouwen. Als gevolg hiervan is brandveiligheid van hoge gebouwen een belangrijk aandachtspunt, in het bijzonder in gevallen waar vlammen uitslaan en zich kunnen hechten aan de façade van het gebouw. Deze uitslaande vlammen kunnen uitbreiden over de façade, maar kunnen ook een secundaire brandhaard veroorzaken en aldus uitbreiden naar aangrenzende verdiepingen. Uiteindelijk kan de brand volledig ontwikkelen over het gehele gebouw en wordt het onmogelijk voor de brandweerlui om de brand te doven. Daarom is het noodzakelijk om de onderliggende fysica te doorgronden en om de uitbreiding van de uitslaande vlammen over een façade van een gebouw te proberen voorspellen. Eén manier om dit probleem te onderzoeken is door numerieke simulaties uit te voeren, gebruikmakend van Computational Fluid Dynamics (CFD) codes.

De globale doelstelling van dit doctoraatsproefschrift is om de state-of-the-art van modellering in CFD te beoordelen, meer bepaald bij gebruik van de Fire Dynamics Simulator (FDS) code, als basis om het gedrag van branduitbreiding te begrijpen in de context van façadebranden in gebouwen. Een stapsgewijze strategie is gebruikt in het proefschrift, dat bestaat uit drie onderdelen.

In het eerste deel van het proefschrift is onderzoek uitgevoerd naar het gebruik van FDS voor het modelleren van de dynamica van rook en brand in de gasfase. Twee scenario's zijn beschouwd. Het eerste scenario is de stroming van natuurlijke convectie in een trappenhuis, om het potentieel van CFD-modellering aan te tonen in hoogbouw, voor een goed geventileerde brand en zonder branduitbreiding. Een gedetailleerde studie is uitgevoerd, met bespreking van luchtsnelheden een de opening in het midden van het trappenhuis, van de temperatuurstijging in het trappenhuis, de temperatuur bij de opening in het midden van het trappenhuis, de invloed van de aanwezigheid van de trap op de drukverdeling, en de positie van de hoogte van het neutrale vlak. Bovendien wordt de impact van het turbulentiemodel op de resultaten van de simulaties besproken. Al-

gemeen gesproken bevestigen de verkregen resultaten dat betrouwbare inzichten kunnen worden verworven uit CFD-simulaties, met betrekking tot de beweging van rook in hoge gebouwen. Het tweede scenario betreft verscheidene simulaties van ondergeventileerde branden in een compartiment waarbij vlammen uitslaan uit de opening. Vier verschillende geometrieën van opening zijn beschouwd in de simulaties: 0.1 m x 0.2 m, 0.2 m x 0.2 m, 0.2 m x 0.3 m, and 0.3 m x 0.3 m. De nauwkeurigheid van de verkregen resultaten is besproken en een vergelijking is gemaakt met experimenten en empirische correlaties. De minimaal vereiste resolutie van het rekenrooster is besproken door de 'fout' in de massabalans te analyseren, op basis van post-processing van het totale massadebiet in en uit het compartiment. Twee lengteschaalverhoudingen zijn geformuleerd om de roosterresolutie te beoordelen, bovenop het conventionele D^*-criterium. De eerste verhouding betreft de ventilatiefactor tot de afmeting van de cellen in het rooster, terwijl de tweede de verhouding is van de hydraulische diameter van de opening tot de afmeting van de cellen in het rooster. Wanneer deze twee verhoudingen groter zijn dan 10, wordt de overeenkomstige 'fout' in de massabalans lager dan 4%. De resultaten, in termen van snelheden door de deuropening en temperaturen in de deur, worden dan ook roosterongevoelig in dit geval. Het inlaatdebiet aan lucht doorheen de deuropening neemt lineair toe met de ventilatiefactor, overeenkomstig resultaten uit de literatuur. Bovendien vertoont het warmtevermogen in het compartiment een lineair verband met de ventilatiefactor, weliswaar met een helling die lager is dan wat conventioneel vermeld wordt in de literatuur. Dit werd uitgelegd door het lagere massadebiet instromende lucht en het onvolledige verbruik van de zuurstof die in het compartiment stroomt. De temperatuursvoorspellingen tonen dat: (1) de temperatuur in de tegenoverliggende hoeken achteraan en vooraan zijn niet gelijk, maar het is mogelijk om betekenisvolle gemiddelde temperature te definiëren in het compartiment, (2) de aldus verkregen gemiddelde gastemperaturen in het compartiment wijken minder dan 10% af van de correlatie van Babrauskas voor de verschillende geometrieën van opening. Het is aangetoond dat FDS de locatie van het neutrale vlak nauwkeurig kan weergeven voor de verschillende configuraties. De voorspellingen van de vlamhoogte zijn echter enigszins gevoelig aan het criterium dat wordt gehanteerd om de hoogte te bepalen, met name de keuze van de vlamtemperatuur. Desalniettemin worden de trends correct weergegeven. De voorspelde hoogte van de uitslaande vlammen neemt toe met het warmtevermogen van de brand. De exponent van de macht waarmee de vlamhoogte afhangt van het externe warmtevermogen is $2/3$.

Het tweede deel van het proefschrift is gewijd aan de koppeling van pyrolyse met CFD-modellering. Het is erkend dat zowel materiaaleigenschappen als modeleigenschappen,

alsook de schaal van het scenario, van cruciaal belang zijn. Overeenkomstig hiermee ligt de focus eerst op het modelleren van pyrolyse en vervolgens op verbranding op kleine schaal. De noodzakelijke material en modeleigenschappen zijn bepaald door middle van een eenvoudige 'trial and error'-procedure. De uitgevoerde studie naar de gevoeligheid van de resultaten aan het rekenrooster hebben aangetoond dat het D*-criterium niet volstaat voor simulaties van brand waarbij gasfase en vaste fase gekoppeld worden. Vervolgens werd de intermediaire schaal van de Single Burning Item (SBI) hoekbrandproeven beschouwd. Verschillende simulaties zijn uitgevoerd van SBI-experiments met MDF-panelen, gebruikmakend van materiaaleigenschappen zoals bepaald in het vorige gedeelte, alsook een calibratietest met calciumsilicaatpanelen. Het belang van de volledigheid van de geometrie is onderzocht. Zowel 'volledige' als 'vereenvoudigde' geometriemodellen zijn beschouwd om de invloed van de geometrie op de voorspellingen te onderzoeken. Sterk verschillende stromingspatronen werden waargenomen bij het volledige en vereenvoudigde model. Globaal geeft het volledige model aanleiding tot hogere warmtefluxen dan het vereenvoudigde model. In overeenstemming met de warmtefluxvoorspellingen wordt ook een hoger piekwarmtevermogen verkregen in het volledige model. De algemene trend wordt redelijk goed weergegeven in beide modellen.

In het derde gedeelte van het proefschrift wordt het gebruik van de FDS code gellustreerd voor het modelleren van façadebranden door middel van een fictief scenario, waarbij zowel inerte panelen als MDF-panelen gebruikt zijn als façademateriaal, in combinatie met een ondergeventileerde brandhaard in een compartiment. Eerst en vooral zijn de karakteristieken van de façadebrand besproken, in termen van het warmtevermogen, warmtefluxen op de façadewand en het voortschrijden van het pyrolysefront op het MDF-paneel, in afwezigheid van wind. Eerst zijn resultaten met de inerte façade besproken. Vervolgens is de branduitbreiding in het geval met de MDF-façade uitgelegd, op basis van een vergelijking met het geval met de inerte façade. Vervolgens is het effect van wind op de branduitbreiding op de façade onderzocht. Vereenvoudigde windomstandigheden zijn beschouwd, met een uniforme snelheid in het domein. Twee richtingen zijn onderzocht, namelijk loodrecht op de façade en evenwijdig met de façade, met variabele snelheid (tot 8 m/s). Het is aangetoond dat de analyse moet gebaseerd zijn op impuls in het stromingsveld. Wanneer de wind loodrecht staat op de façade wordt de uitstroom van onverbrande brandstof gehinderd (en, voor voldoende hoge windsnelheid, geblokeerd), hetgeen de hoogte van de uitslaande vlam beperkt. De onverbrande brandstof wordt ook zijwaarts en neerwaarts geduwd terwijl het uit de opening stroomt en reageert daardoor eventueel niet (of tenminste niet in het rekendomein). Dit geeft aanleiding tot verminderde branduitbreiding.

Wanneer de wind evenwijdig met de façade stroomt is er weinig impact op het massadebiet dat uit het compartiment stroomt, omdat de horizontale impuls vanwege de wind niet in dezelfde richting is als de door de brand gecreerde impuls in the uitstroom. Alsdusdanig is er geen verminderde branduitbreiding. Voor voldoende lage impuls van de wind wordt er geen effect waargenomen op de pyrolysezone. Voor hogere impuls wordt een afwijking van de verticale richting vastgesteld. De hoek neemt toe met de windsnelheid, hetgeen aanleiding geeft tot gecombineerde opwaartse en zijwaartse branduitbreiding. Dit alles is een illustratie van een proof-of-concept van het potentieel om FDS te gebruiken voor façadebranden, met ingebrip van de invloed van wind.

Tot slot zijn de voornaamste conclusies van het proefschrift samengevat, gevolgd door aanbevelingen voor toekomstig werk met betrekking tot het modelleren van façadebranden.

Contents

List of Figures

List of Tables

Nomenclature

Acronyms

CFD	Computational Fluid Dynamics
FDS	Fire Dynamics Simulator
LES	Large Eddy Simulation
RANS	Reynolds-Averaged Navier Stokes
SGS	Sub-Grid Scale
TVD	Total Variation Diminishing
MDF	Medium Density Fiberboard
SBI	Single Burner Item test
RTE	Radiative Transfer Equation
FVM	Finite Volume Method
CFL	CourantFriedrichsLewy condition
HRR	Heat Release Rate
TGA	Thermogravimetric Analysis
VDP	Vertical Density Profile
MLR	Mass Loss Rate
MC	Moisture Content
FPA	Fire Propagation Apparatus
MLR	Mass Loss Rate

Roman Symbols

A	Area of the opening (m^2)
c_p	Specific heat (kJ/(kg·K))

D_h	Hydraulic diameter of the opening (m)
g	Gravitational acceleration (m/s^2)
H	Height of the opening (m)
H_N	Height of the neutral plane (m)
h	Heat transfer coefficient (W/(m^2·K))
k	Thermal conductivity (W/(m·K))
$\dot{m}_{in}$	Mass inflow rate through the opening (kg/s)
$\dot{m}_{out}$	Mass outflow rate through the opening (kg/s)
$\dot{m}_{fuel}$	Mass supply rate of the fire source (kg/s)
P	Pressure(Pa)
$\dot{Q}$	Total heat release rate of fire (kW)
$\dot{Q}_{in}$	Heat release rate inside the enclosure (kW)
$\dot{Q}_{ext}$	Heat release rate burning outside the enclosure (kW)
q	Heat flux (kW/m^2)
R	Specific gas constant of air(J/(kg·K))
T	Temperature (K)
T_0	Ambient temperature (K)
T_g	Gas temperature (K)
T_∞	Ambient temperature (K)
t	Time(s)
W	Width of the opening (m)
Z_f	Mean flame height from location of the neutral plane height (m)

Greek Symbols

α	Thermal diffusivity (m^2/s)
ΔH_{air}	Heat of combustion per kg air consumed (kJ/kg)
ℓ_1^*	Length scale ratio based on the opening geometry and the simulation grid size(-)
ℓ_2^*	Length scale ratio based on the hydraulic diameter and the simulation grid size(-)
ρ_∞	Density of gas (kg/m^3)
ϵ	Mass balance error (-)
δ_x	Grid size (m)

Subscripts and Superscripts

atm	Atmosphere
exp	Experiment
sim	Simulation

Chapter 1

Introduction and objectives

1.1 Introduction

Due to the rapid economic development, high-rise buildings are populating more and more the urban landscape. Fire safety of high-rise buildings has attracted extensive attention, especially in cases where flames are ejected from an enclosure and attached on the building façades. Several well-known high-rise fires happened in recent years (Figure 1.1 and Figure 1.2). A non-exhaustive list reads:

- China Central Television office building fire in 2009,
- Shanghai high-rise flats fire in 2010,
- Dubai Torch Tower fires in 2015 and 2017
- London Grenfell Tower fire in 2017.

These fires caused serious numbers of casualties and large economic losses. Understanding and predicting the development of fires in these complex buildings is particularly challenging. The challenges stem from the complexities inherent to enclosure fires (especially in under-ventilated conditions) coupled to the characterization of external flaming and, potentially, subsequent flame spread over façades.

In general, it is a complicated phenomenon with several aspects involved, such as the buoyancy-driven flow, compartment fire, and flame spread on the façade. The fire spread behavior in such a scenario can be divided into four aspects:

- Enclosure fires: under/over-ventilated fires;

- Vertical flame spread on façade;
- Gas phase: turbulent combustion and buoyant flow;
- Solid phase: heat transfer and pyrolysis.

(a) (b)

Figure 1.1: (a) CCTV fire in 2009, (b) Shanghai apartment fire 2010.

1.2 General overall picture: from enclosure fires to external flame spread

In the case of ignition inside the building, the extent of flames when they are first ejected outside depends essentially on the excess fuel that did not burn inside. In many cases, this is due to limited ventilation conditions and/or window breakage.

A key parameter in the estimation of the maximum ventilation flow rate delivered to a naturally-vented enclosure fire (through an open doorway or window) is the ventilation factor expressed as $A\sqrt{H}$ where A and H are respectively the area and height of the opening. The importance of this parameter has first been recognized in the early work of Kawagoe (1958) through small-scale experiments [1]. It has been later derived analytically by applying Bernoulli's principle in conjunction with some simplifying assumptions, e.g., well-mixed conditions within the room. The analytical work, supported by experimental

(a) (b)

Figure 1.2: (a) London Grenfell Tower fire in 2017, (b) Second Torch Tower fire in 2017.

evidence, suggests that the maximum supply of fresh air within the naturally-ventilated enclosure can be estimated to be about $C \cdot A\sqrt{H}$. Different values for C have been reported in the literature (e.g. [2–4]). Thomas and Heselden [3] estimate the value of this constant at 0.5, which is the value most commonly found in the literature. Assuming that the heat of combustion per mass of air for most common fuels is about 3000 kJ/kg, one could estimate the maximum heat release rate (HRR) inside the enclosure to be about $\text{HRR}_{\text{in}} = 1500A\sqrt{H}$. An enclosure fire that generates a HRR that is higher than HRR_{in} is susceptible to yield external flaming with HRR_{ext} = HRR - HRR_{in} as demonstrated in the work of Delichatsios and co-workers [5, 6]. The HRR outside the enclosure (i.e., HRR_{ext}) will then trigger the ignition of the façades if it is made of combustible material. As more and more material burns outside, flames become larger and larger, preheating increasingly extended virgin material-areas under the effect of buoyancy. This mechanism may lead to an accelerating upward fire spread phenomenon from the floor where ignition occurred to higher floors. This fire spread can be affected by environmental conditions such as wind. A lot of efforts have been devoted to study this problem in the fire community, as can be found in several classical text books [7, 8].

Several methods have also been developed, based on experimental data and theoretical analysis, for predicting temperatures in enclosure fires during the fully developed fire stage

[9]. Babrauskas [10, 11] proposed a method based on the energy balance in the enclosure system, which involves terms like heat released per unit time within the enclosure, heat losses through openings by radiation and convection and conduction into the walls, floor and ceiling.

Charge Coupled Device (CCD) cameras are commonly used for recording the external flaming. Using a probabilistic based method to post-process the video footage [12], the flame height value can be determined. This method was employed in previous experimental studies (e.g., [5, 6, 13]). The key parameters in the prediction of the flame shape are the amount of excess heat release rate, the opening geometry, and the atmospheric conditions (e.g., wind). Some theoretical models (e.g., [14–16]) and correlations [5, 6] have been developed, based on experimental data. Only few attempts [17, 18] can be found in the literature to numerically study the height of the flame ejected from the opening of an under-ventilated enclosure fire.

A series of medium-scale and large-scale compartment-facade fire tests were carried out by Asimakopoulou and Kolaitis [19–21]. Several physical parameters affecting the heat exposure of the venting-flame façade system were investigated, including gas and wall surface temperatures, gas velocities through the opening, and heat fluxes on the façade surface. Furthermore, correlations aiming to estimate the geometric characteristics of ejecting flame were evaluated using the results from these medium-scale fire tests [20]. Suzana [22] conducted full scale flashover fires to investigate the likelihood of external fire spread from a burn room window with standard glass, when the external façade is non-combustible. The effects on externally venting flames of internal ventilation conditions, burning rate, burn room size and wind have been studied in detail. Secondary fires and glass breakage have been examined as well.

When the combustible material was ignited by the ejected flame, the fire will spread to the other area of the building along the façade wall. Flame spread behaviors over solid surfaces are the combined results of the heat and mass transfer in solid and gas phases, the pyrolysis in solid phase and the chemical reaction in gas phase. These processes can be affected by many factors, such as the orientation of the burning surface, propagation direction relative to airflow, sample thickness, the material type, ambient wind condition, and so on.

Comparing to downward flame spread, upward flame spread rates (concurrent flow flame spread) are faster and relatively unsteady. Therefore, scenarios involving upward flame spread are of particular interest for the fire community. Quintiere [23] proposed a model to predict the upward flame spread velocity, it can be expressed as: $V = \frac{H_f - H_p}{\tau_{ig}}$,

where τ_{ig} is the characteristic time to ignition, H_f is the flame height, and H_p is the pyrolysis height. The characteristic time to ignition is a function of the forward heating zone heat flux that is assumed to be a constant within the heating zone. Markstein and de Ris [24] examined the upward fire spread rate over textiles. They found an accelerating flame spread rate and characterized it by a power-law relationship between pyrolysis spread rate and pyrolysis height: $V = \beta H_p^n$. From their empirical correlations, it was suggested that spread rate and pyrolysis height increase exponentially with time. Orloff et al. [25] also found flame spread rates accelerate for upward flame spread. However, these models to the prediction of the flame spread are quite restricted by their assumptions.

Some interesting experimental work have also been done recently, Zeinali [26] et al. from Ghent University and Agarwal [27] et al. from FM Global have conducted a multistep study on the pyrolysis and flame spread in a corner configuration in an SBI set-up [28]. Yoshioka conducted a large scale test in 2011, and evaluated the fire properties of non-combustible façade and various types of combustible façade in a scenario where an interior fire has occurred in a compartment and flame is ejected from an opening [29–31].

1.3 The role of Computational Fluid Dynamics (CFD)

The overall picture described above is difficult to address experimentally in all its details (from ignition to external fire spread), given the variety of associated potential fire scenarios. Such variety is induced, for example, by (i) different geometrical configurations and architectural design options for the façade, (ii) potentially different nature of fire loads (inside and outside on the façade) and (iii) the influence environmental conditions such as wind. Comprehensive and well-designed experimental campaigns (as the ones that will be addressed and relied upon in this thesis) do certainly contribute substantially to the understanding of several pieces of the ‘puzzle‘, but might not capture the overall picture of fire dynamics in high-rise buildings as designers, architects and regulating authorities would like to see.

It is in this context that Computational Fluid Dynamics (CFD) is becoming more and more a promising numerical tool to be used as an aid in the design of fire-safe buildings, including high-rise buildings. However, the reliability of CFD must be continuously monitored through well-documented validation studies, before attempting to use the technique as a ‘predictive tool‘ in the design stage of a project where experimental data is typically not available. It is also important to say that advances in CFD create a flexibility in the design that allows to move from ‘prescriptive rules‘ to ‘performance-based‘ criteria, a trend that is more and more promoted worldwide.

However, the complexity of the flame spread problem presents a challenge to fire modellers. In order to achieve reliable predictions for flame spread using CFD, several pyrolysis models have been developed. Arrhenius model [32] was the first model developed to study the decomposition of solid materials, and it is still the most commonly used model. Yan and Holmstedt [33] developed a pyrolysis model having dual mesh, Wasan [34] developed an enthalpy-based pyrolysis model for both charring and non-charring materials in fire, showed good agreement with experiments, and Laughtenburger et al. [35] developed a methodology that generates an optimized set of material properties using a genetic algorithm.

Kwon et al.[36] evaluate the capability of Fire Dynamics Simulator (FDS) (version 4) for predicting upward flame spread, and applied a simplified flame spread model to assess the simulation results. They also presented recommendations for improvements of FDS and practical use of FDS for fire spread. Moreover, numerical methods have also been used to predict the gas temperature. It should be noted that a prerequisite for accurately predicting the gas temperature is accurate modelling of the combustion in under-ventilated fires. This, however, is still a challenge for the fire safety community, although progress is made through several studies dedicated to develop models or theoretical analysis for incomplete combustion and flame extinction (e.g., [13, 37–39].

In the study of Chaos et al.[40,41], the burning behavior of Medium Density Fiberboard (MDF) Panels were simulated with FireFOAM using model-effective material properties. These properties for the pyrolysis have been calculated by optimizing the FireFOAM pyrolysis code to fit the experimental data. Promising results have been obtained in their study. However the capability of current CFD method in predicting the combustible façade fires still need to be further validated and improved.

The fire research community has been making effort to develop a fundamental understanding of fire phenomena and to advance predictive fire modeling. The 'Working Group on Measurement and Computation of Fire Phenomena' (abbreviated as the 'MaCFP Working Group') [42] has been established, aiming to establish a structured effort in the fire research community to make significant and systematic progress in fire modeling, based on a fundamental understanding of fire phenomena. This Ph.D. work is not only a case of practical importance, but can also serve a useful purpose for fire safety science.

1.4 The choice of FDS and modelling approaches

There are several CFD packages that could have been used to undertake this work described herein. The choice of the Fire Dynamics Simulator (FDS) [43–45] has been

motivated by its (1) relatively wide user community that encompasses not only researchers but also architects and regulatory bodies, and (2) the very well documented features and associated verification and validation studies.

FDS is a CFD modeling tool with both the LES and DNS solvers that is under active development the National Institute of Standards and Technology (NIST). It is a full-package fire simulation software where turbulence, combustion, radiation, pyrolysis, and water spray can be modeled. A large variety of fire experiments at different scales, and in all areas of fire development including turbulence, heat transfer, and solid state pyrolysis have been used in the validation of the software. The employed gas phase modelling approaches are presented in this section, including the governing equations, turbulence, combustion and radiation models.

1.4.1 Governing equations

FDS solves the Navier-Stokes equations for the case of low Mach Numbers. This section introduces the basic conservation equations for mass, species, momentum and energy:

• Conservation of mass:

$$\frac{\partial \rho}{\partial t} + \frac{\partial (\rho u_j)}{\partial x_j} = 0 \tag{1.1}$$

where ρ is the density and u_j is the velocity in the j direction.

• Conservation of species:

$$\frac{\partial (\rho Y_k)}{\partial t} + \frac{\partial (\rho u_i Y_k)}{\partial x_j} = \frac{\partial \rho D_k \nabla Y_k}{\partial x_j} + \dot{\omega}_k, \qquad k = 1, ..., N_s - 1 \tag{1.2}$$

where D_k is the species mass diffusion coefficient and $\dot{\omega}_k$ are the molecular diffusive mass flux and reaction source term of species k, respectively.

• Conservation of momentum:

$$\frac{\partial (\rho u_i)}{\partial t} + \frac{\partial (\rho u_i u_j)}{\partial x_j} = -\frac{\partial p}{\partial x_i} - \frac{\partial \tau_{ij}}{\partial x_j} + \rho g_i, \qquad i = 1, 2, 3 \tag{1.3}$$

where p is the pressure, τ_{ij} denotes the viscous stress tensor and g is the gravitational

acceleration. The viscous stress tensor can be expressed by Newton's law as:

$$\tau_{ij} = -\mu\left(\frac{\partial u_i}{\partial x_j} + \frac{\partial u_j}{\partial x_i}\right) + \frac{2}{3}\mu\frac{\partial u_k}{\partial x_k}\delta_{ij} \tag{1.4}$$

where μ is the molecular dynamic viscosity and δ_{ij} is the Kronecker symbol.

• Conservation of energy:

$$\frac{\partial(\rho h_s)}{\partial t} + \nabla\cdot(\rho \boldsymbol{u} h_s) = \frac{Dp}{Dt} + \dot{q}_c''' - \dot{q}_b''' - \nabla\cdot\dot{\boldsymbol{q}}'' \tag{1.5}$$

where h_s is the sensible enthalpy and $\dot{q}_c'''$ is the heat release rate per unit volume from combustion, $\dot{q}_b'''$ is the energy transferred to subgrid-scale droplets and particles, $\dot{\boldsymbol{q}}''$ represents the conductive, diffusive, and radiative heat fluxes:

$$\dot{\boldsymbol{q}}'' = -k\nabla T - \sum_{\alpha} h_{\mathrm{s},\alpha}\,\rho\, D_\alpha \nabla Z_\alpha + \dot{\boldsymbol{q}}_r'' \tag{1.6}$$

where k is the thermal conductivity and D_α is the diffusivity of species α.

Here the gases are considered to behave as ideal gases. In this way, density and temperature are related through the equation of state as:

$$\rho = \frac{p}{RT} \tag{1.7}$$

where $R = R_u/W_k$ is the gas constant, and R_u = 8.314 J/(K.mol) the universal gas constant and W_k is the species molecular weight.

1.4.2 Turbulence model

Three types of turbulence modelling are available: RANS (Reynolds Averaged Navier Stokes), LES (Large Eddy Simulation) and DNS (Direct Numerical Simulation).

In RANS modelling, only the average flow field is calculated, and all turbulent motions are modelled, so that the information on time-dependent behavior of the flow is less reliable.

In LES modelling, the conservation equatios are filtered, and these filtered equations are solved. The large eddies are explicitly solved in a calculation. Small eddies are implicitly accounted for by using subgrid-scale model. This method can provide more reliable results in geometries with strong time-dependent turbulent motions.

In DNS, the grid and time resolution are so fine that the conservation equations can be numerically solved without and turbulence model. However, the computational cost of DNS is very high, even at low Reynolds numbers. For the Reynolds numbers encountered in most industrial applications, the computational resources required by a DNS would exceed the capacity of the most powerful computers currently available.

In the present study where highly transit phenomenon is involved, the LES modelling is employed. The goal of the LES is to evolve the cell mean values of mass, momentum, and energy explicitly, while accounting for the effects that subgrid transport and chemistry have on the mean fields. To this end, we apply the box filter to the DNS equations to obtain the filtered equations. As an example, consider the momentum equation.

The filter width is taken to be the cube root of the cell volume, $\Delta = (\delta x\, \delta y\, \delta z)^{1/3}$, for any continuous field, ϕ, a filtered field is defined as:

$$\overline{\phi}(x,y,z,t) \equiv \frac{1}{V_{\mathrm{c}}} \int_{x-\delta x/2}^{x+\delta x/2} \int_{y-\delta y/2}^{y+\delta y/2} \int_{z-\delta z/2}^{z+\delta z/2} \phi(x',y',z',t)\, \mathrm{d}x'\, \mathrm{d}y'\, \mathrm{d}z' \tag{1.8}$$

It is also conventional to define a mass-weighted or Favre filter such that $\overline{\rho}\,\widetilde{\phi} \equiv \overline{\rho\phi}$. Applying box filter to the momentum equation results in:

$$\frac{\partial \overline{\rho u_i}}{\partial t} + \frac{\partial}{\partial x_j}(\overline{\rho u_i u_j}) = -\frac{\partial \overline{p}}{\partial x_i} - \frac{\partial \overline{\tau}_{ij}}{\partial x_j} + \overline{\rho} g_i \tag{1.9}$$

The cell mean value, $\overline{\rho u_i u_j}$, is not itself a primitive variable in the calculation. it must be decomposed and this leads to closure problems. The next step is to apply the Favre filter:

$$\frac{\partial \overline{\rho}\widetilde{u}_i}{\partial t} + \frac{\partial}{\partial x_j}(\overline{\rho}\widetilde{u_i u_j}) = -\frac{\partial \overline{p}}{\partial x_i} - \frac{\partial \overline{\tau}_{ij}}{\partial x_j} + \overline{\rho} g_i \tag{1.10}$$

where $\sim$ is the Favre filter operator. The first term is now separable, provided we have a solution for $\overline{\rho}$. But still there is no way to compute the correlation $\widetilde{u_i u_j}$ on the grid. One cannot simply use $\widetilde{u}_i\widetilde{u}_j$ as a substitute. Instead, the subgrid-scale (SGS) stress is defined as:

$$\tau_{ij}^{\mathrm{sgs}} \equiv \overline{\rho}(\widetilde{u_i u_j} - \widetilde{u}_i\widetilde{u}_j) \tag{1.11}$$

Substituting Eq. (1.11) into Eq. (1.10) yields

$$\frac{\partial \overline{\rho}\widetilde{u}_i}{\partial t} + \frac{\partial}{\partial x_j}(\overline{\rho}\widetilde{u}_i\widetilde{u}_j) = -\frac{\partial \overline{p}}{\partial x_i} - \frac{\partial \overline{\tau}_{ij}}{\partial x_j} - \frac{\partial \tau_{ij}^{\mathrm{sgs}}}{\partial x_j} + \overline{\rho}g_i \tag{1.12}$$

All variables are primitive or computable once we find a suitable closure for the subgrid scale stress, τ_{ij}^{sgs}. There are a few more modifications we need to make in order to get Eq. (1.12) into shape for FDS. The first is to decompose the SGS stress and apply Newton's law of viscosity as the constitutive relationship for the deviatoric part. The total deviatoric stress is modeled as:

$$\tau_{ij}^{\mathrm{dev}} \equiv \overline{\tau}_{ij} + \tau_{ij}^{\mathrm{sgs}} - \frac{1}{3}\tau_{kk}^{\mathrm{sgs}}\delta_{ij} = -2(\mu + \mu_{\mathrm{t}})\left(\widetilde{S}_{ij} - \frac{1}{3}(\nabla\widetilde{\mathbf{u}})\delta_{ij}\right) \tag{1.13}$$

The turbulent viscosity, μ_t, requires modeling. Define the subgrid kinetic energy as half the trace of the SGS stress,

$$k_{\mathrm{sgs}} \equiv \frac{1}{2}\tau_{kk}^{\mathrm{sgs}} \tag{1.14}$$

and define the modified filtered pressure [47] as

$$\bar{p} \equiv \overline{p} + \frac{2}{3}k_{\mathrm{sgs}} \tag{1.15}$$

Upon substitution of Eqs. (1.13) and (1.15) into Eq. (1.12), we have

$$\frac{\partial \overline{\rho}\widetilde{u}_i}{\partial t} + \frac{\partial}{\partial x_j}(\overline{\rho}\widetilde{u}_i\widetilde{u}_j) = -\frac{\partial \bar{p}}{\partial x_i} - \frac{\partial \tau_{ij}^{\mathrm{dev}}}{\partial x_j} + \overline{\rho}g_i \tag{1.16}$$

Here, in the LES context when we write τ_{ij} we mean precisely τ_{ij}^{dev}, and similarly for pressure in LES p refers to $\bar{p}$.

There are several different options available for the modelling of the turbulent viscosity: Constant coefficient Smagorinsky model, Dynamic Smagorinsky Model, Deardorff's model, and Vreman's model. The default one is the Deardorff model [46]:

$$\mu_{\mathrm{t}} = \rho C_\nu \Delta \sqrt{k_{\mathrm{sgs}}} \quad ; \quad k_{\mathrm{sgs}} = \frac{1}{2}\left((\bar{u}-\hat{\bar{u}})^2 + (\bar{v}-\hat{\bar{v}})^2 + (\bar{w}-\hat{\bar{w}})^2\right) \tag{1.17}$$

where $\bar{u}$ is the average value of u at the grid cell center (representing the LES filtered velocity at length scale $\Delta = (\delta x\,\delta y\,\delta z)^{1/3}$), k_{sgs} is the subgrid kinetic energy, and $\hat{\bar{u}}$ is a weighted average of u over the adjacent cells (representing a test-filtered field at length

scale 2Δ):

$$\bar{u}_{ijk} = \frac{u_{ijk} + u_{i-1,jk}}{2} \quad ; \quad \hat{\bar{u}}_{ijk} = \frac{\bar{u}_{ijk}}{2} + \frac{\bar{u}_{i-1,jk} + \bar{u}_{i+1,jk}}{4} \tag{1.18}$$

The terms $\hat{\bar{v}}$ and $\hat{\bar{w}}$ are defined similarly. The model constant is set to the literature value $C_\nu = 0.1$ [47].

1.4.3 Combustion and radiation models

Combustion and radiation are introduced into the governing equations via the source terms, $\dot{q}_c'''$ and $\dot{q}_r'''$, in the energy transport equation.

FDS uses a combustion model based on the mixing-limited, infinitely fast reaction of lumped species. Lumped species are reacting scalar quantities that represent a mixture of species. For example, air is a lumped species which is a mixture of nitrogen, oxygen, water vapor, and carbon dioxide. The reaction of fuel and oxygen is not necessarily instantaneous and complete, and there are several optional schemes that are designed to predict the extent of combustion in under-ventilated spaces.

For an infinitely-fast reaction, reactant species in a given grid cell are converted to product species at a rate determined by a characteristic mixing time, $\tau_{\rm mix}$. The heat release rate per unit volume, $\dot{q}_c'''$, is defined by summing the lumped species mass production rates times their respective heats of formation

$$\dot{q}_c''' = -\sum_\alpha \dot{m}_\alpha''', \Delta h_{{\rm f},\alpha} \tag{1.19}$$

A simple extinction algorithm based on a critical flame temperature [48] is implemented in FDS.

The net contribution from thermal radiation in the energy equation is defined by:

$$\dot{q}_r''' \equiv -\nabla \cdot \dot{\boldsymbol{q}}_r''(\boldsymbol{x}) = \kappa(\boldsymbol{x}) \left[U(\boldsymbol{x}) - 4\pi I_{\rm b}(\boldsymbol{x}) \right] \quad ; \quad U(\boldsymbol{x}) = \int_{4\pi} I(\boldsymbol{x}, \boldsymbol{s}')\, d\boldsymbol{s}' \tag{1.20}$$

where $\kappa(\boldsymbol{x})$ is the absorption coefficient, $I_b(\boldsymbol{x})$ is the source term, and $I(\boldsymbol{x}, \boldsymbol{s})$ is the solution of the radiation transport equation (RTE), for a non-scattering gray gas it reads:

$$\boldsymbol{s} \cdot \nabla I(\boldsymbol{x}, \boldsymbol{s}) = \kappa(\boldsymbol{x}) \ [I_{\mathrm{b}}(\boldsymbol{x}) - I(\boldsymbol{x}, \boldsymbol{s})] \tag{1.21}$$

The radiation equation is solved using a technique similar to a finite volume method for convective transport, thus the name given to it is the Finite Volume Method (FVM).

For the numerical discretization methods for gas phase, a second-order central difference scheme is used for the diffusion terms, a second-order TVD scheme with Superbee flux limiter is employed for the advection terms, and a fast non-iterative fourier transform algorithm is used to solve the pressure. The reader is referred to [43–45] for more detail.

1.5 Objectives

As implied in the previous section, the work that has been undertaken in this thesis evolves essentially around CFD simulations of several 'elements' of the overall picture of interest here: from enclosure fires to external flame spread.

The overall objective is not to develop novel sub-models for numerical simulations of fire-driven flows. It is rather centered first around a detailed assessment of the accuracy of state-of-the-art CFD, based on available experimental data; and to illustrate the potential of CFD simulations for façade fires, including a preliminary study on the influence of wind. At the same time, I do intend to convey to the reader not only key elements (such as the cell size) to perform 'high quality' simulations, but also 'warnings' about current limitations and challenges (for example in the prediction of flame spread).

1.6 Methodology and thesis structure

The validation studies proposed in this thesis are divided with respect to two aspects: (1) gas phase modelling of enclosure fire and smoke dynamics, and (2) solid thermal degradation and flame spread modelling. For the first aspect (i.e., gas phase) two configurations are examined: the buoyant flow in the stairwell of a high-rise building and ventilation-controlled fires with external flaming (see chapter 2). For the second aspect (i.e., flame spread), the gas phase is coupled to the solid phase in configurations of increasing levels of complexity, i.e., from pyrolysis in an inert atmosphere to flame spread in the Single Burning Item (SBI) test (see chapters 3 and 4).

Finally, in the last chapter before the conclusion (see chapter 5), I intend to illustrate to the reader the potential of CFD simulations in understanding the influence of a practical

element that might be involved in the development of façade fires, namely the wind. This is a practical, yet almost unexplored (or at least scarcely addressed) aspect in the literature. It is indeed quite difficult (and probably very costly) to build, even at a reduced-scale, an experimental rig that allows to study the effect of wind. CFD can provide initial elements of understanding here. As opposed to the other chapters, there is very little experimental data available in the literature. However, the CFD findings are 'backed-up' by a theoretical analysis that gives credibility to the numerical results. The potential of using FDS for façade fires is illustrated by means of a proof-of-concept, including a preliminary study on the influence of wind conditions.

Chapter 2

The use of CFD for fire and smoke dynamics - Gas phase

In this chapter, simulation results are discussed with prescribed fire source, i.e., modeling in the solid phase is avoided. In the step-wise approach, firstly a scenario is discussed that focuses on smoke spread with a fuel-controlled fire (section 2.1). Subsequently, an under-ventilated fire is discussed (section 2.2). Both sections are based on peer-reviewed publications [49–51].

2.1 Buoyant fire-induced smoke movement in a high-rise building stairwell

Fire safety of high-rise buildings has attracted extensive attention in recent years due to the occurrence of many catastrophic fires. Typically, the generated smoke reduces visibility (important for evacuation) and contains toxic gases such as carbon monoxide, the 'chief killer' in fires. The buoyancy can be fire-induced, but can also already be in place prior to the onset of the fire, due to differences in temperature inside and outside the building. Smoke spreading is a serious threat to people's evacuation and rescue activities. A vertical shaft (such as in stairwells and elevators) can serve not only as evacuation passageway, but also as a possible way for smoke and fire to spread in the vertical direction. Therefore, it is of great importance to study smoke movement in the stairwell of high-rise building fires.

Smoke can spread vertically to top floors through the stairwells or elevators. There are many possible driving forces, such as the stack effect (due to differences between the temperature inside and outside the building), fire-induced buoyancy, mechanical ventilation

and wind, driven mainly by fire-induced buoyancy. In the present study, CFD simulations are performed on experiments where the focus was on fire induced buoyancy: model-scale tests were performed inside a lab (no wind, no temperature differences inside and outside the model) and there was no mechanical ventilation.

A large number of studies have been dedicated to study the characteristics of buoyant plume movement in vertical shafts (e.g., [52–54]). However, few studies focused on the cases with a stairwell, as typically encountered in high-rise buildings. Li et al. [55] conducted a set of experiments to study the buoyant smoke movement in a scale model of a 12-storey stairwell. They particularly studied the influence of the fire heat release rate and opening location on the temperature distribution and the location of the neutral plane in the stairwell. Furthermore, they presented a method to predict the location of neutral plane, which shows good agreement with experimental data.

As mentioned, the CFD (Computational Fluid Dynamics) package, namely FDS(version 6.0.1) [43], is used to model the experiments performed in [55]. The primary objective of the present study is to evaluate the agreement of simulations results obtained with FDS 6.0.1, with its default model settings, with experimental data for the case at hand. To that purpose, a detailed study is conducted, discussing the air flow velocity at the opening in the middle of the stairwell, the temperature rise inside the stairwell, the temperature at the middle opening, the influence of the presence of a staircase on the pressure distribution, the location of the neutral plane height. Over-all good agreement is obtained, which is useful information for practitioners (who are likely to use FDS with its default settings). Moreover, given good agreement, insight in the smoke motion can be obtained from the CFD results. At the end of this part, the influence of the turbulence model on the simulation results is discussed.

2.1.1 Experimental and numerical set-up

The experiments were conducted in a reduced-scale (1:3) model of a stairwell with 12 floors. As is shown in Fig. 2.1, this model is 12.2 m high, 2.6 m long and 1.5 m wide. The first floor is 1.2 m high and the other floors are 1.0 m high. The cross-sections of the stairwell and the rooms are respectively 1.5 m x 1.0 m and 0.8 m x 0.8 m.

Each floor has two connected rooms, which are also connected to the outside through a door. These connecting doors have the same dimension, namely 0.6 m high and 0.4 m wide. In the stairwell, there is a 0.7 m x 0.9 m top opening. At the first floor of the building, there is a bottom opening with the same size as the other doors, connecting the room to the stairwell. These doors and the top and bottom openings were always open

in the experiments. Apart from these top and bottom openings in the stairwell, another middle opening was also set in the experiments. At the floor with the middle opening, the stairwell was connected through two rooms to the outside. Varying the location of the middle opening, 11 experiments were conducted.

In this study, the setup used in the modelling (including geometry and material properties) is the same as that in the experiments [55] (see Figs. 2.1). The porous propane burner (0.4 m x 0.4 m) has been set at the center of the first floor to provide a steady heat release rate of 76 kW. As is indicated in 2.2), the burner is directly underneath the staircase on the ground floor. The amount of fuel fed to the burner was monitored using a rotameter. The heat release rate of the fire was determined by multiplying the measured gas flow rate by the heat of combustion, taken equal to 46,350 kJ/kg for propane. The fire size can be scaled up to a real fire of 1.18 MW by means of classical Froude scaling.

The left and front sides of the sidewall were made of 12 mm thick fire-resistant glass for visual observation. The other parts were made of 2 mm thick steel plate. In the calculation, the material properties of the fire resistant glass were taken as follows: the density is 2500 kg/m^3, the thermal conductivity is 1.13 W/(m·K) , the specific heat is 0.84 kJ/(kg·K), and the emissivity is 0.9. The material properties of the steel plate are: the density is 7850 kg/m^3 , the thermal conductivity is 45.8 W/(m·K), the specific heat is 0.46 kJ/(kg·K), and the emissivity is 0.95.

The experiment has been conducted inside a test laboratory, where the ambient temperature was 20$^\circ C$. There was no wind inside the lab and the temperature inside the scale model equaled the temperature in the test lab, so that it can be assumed there was no flow inside the scale model before ignition of the fire (no stack effect and no wind). K-type thermocouples were used for the temperature measurement, which has a resolution of 0.1 $^\circ C$. Velocity probes were arrayed at the openings to measure the flow velocity.

The amount of leakage in the experiments is unknown. In the simulations, there is no leakage. This implies that higher pressures are to be expected in the simulations, as well as a faster rise of the smoke in the stairwell (as no smoke can escape).

2.1.2 Grid resolution

As mentioned in the previous section, FDS (version 6.0.1) [43–45] is employed in this work. As shown in previous studies [56–58], FDS simulation results are sensitive to grid size. Smaller grid cells are generally preferred for more accurate simulations. However, such simulations will also be more expensive in terms of computational cost and storage requirements.

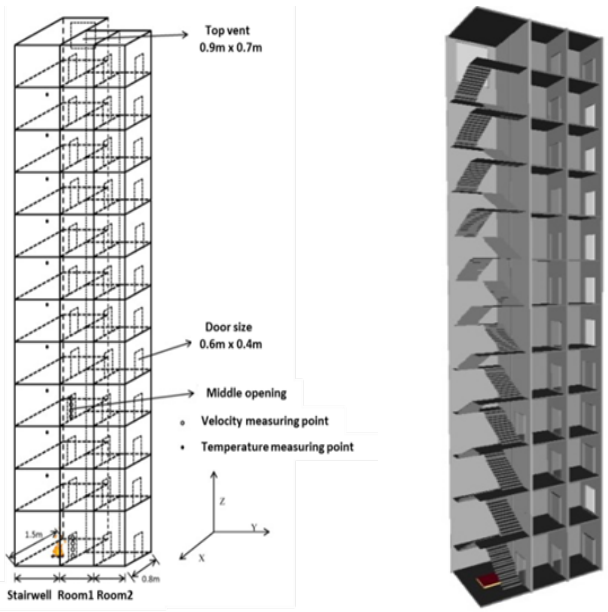

(a) (b)

Figure 2.1: (a)Schematic of the 12-story building [55]. (b)Geometry of the numerical model for case 4.

In the configuration at hand, the grid resolution for both the fire source and openings must be considered. For the fire source, Baum et al. [59] suggested that, in order to correctly capture the impact of burner surface, it is necessary to have 10 x 10 grids over the burner surface. Based on this, for a 0.4 m x 0.4 fire source, a 4 cm cell size is suggested.

For the openings, a length scale ratio ℓ_1^* has been proposed in [49], which concerns both the opening geometry and the grid size. This ratio reads:

$$\ell_1^* = \left(A\sqrt{H}\right)^{\frac{2}{5}} / \delta_x \tag{2.1}$$

In Eq. 2.1, A is the opening area (m^2), H is the opening height (m), δ_x is the grid size. It is suggested in [49] that a length scale ratio larger than 10 is sufficient to ensure the resolution of the vent flow. In this case, with opening sizes of 0.9 m by 0.7 m and 0.4 m by 0.6 m, the corresponding grid size is suggested to be finer than 5.1 cm.

Obviously, the dependence of CFD simulation results on the grid size must be studied. For the case at hand, a grid sensitivity study has been reported in previous work [50], where it was confirmed that a 4 cm cell size or finer is sufficient to ensure the grid insensitivity of the simulation results, focusing on the flow through the bottom opening, as well as the

vertical distribution of temperature in the stairwell. Therefore, in this work the 4 cm grid size has been applied.

2.1.3 Other simulation details

The measurements in the simulations include: (1) the vertical distribution of temperature in the stairwell (obtained with the device 'THERMOCOUPLE'), (2) the vertical pressure distribution inside the stairwell, and (3) the temperature and velocity profiles at the bottom opening.

The temperature distribution in the stairwell has been determined by setting 10 thermocouples at the center of the stairwell for different heights (z = 2, 3, 4, 5, 6, 7, 8, 9, 10, and 11 m)(the axis origin is at the lower left corner). Relative pressure has also been measured at the same locations. In order to obtain more details for the temperature and pressure distribution, slice files have been set up in the planes x = 0.4 m, x = 0.56 m, and y = 0.4 m, y = 0.56 m. For the velocity and temperature at the bottom vent, both gas-phase devices and slice files have been used.

This study comprises 12 cases in total, each corresponding to a certain location of the middle opening (ranging from the 1st to the 11th floor). Table 2.1 shows the list. The column 'Staircase' indicates whether or not a staircase has been included inside the stairwell.

At the level of each floor, one mesh is used for the stairwell and two meshes are used for the two rooms if that floor has the middle opening. In order to better predict the smoke and air flow near the openings, extra meshes were added to extend the computational domain by 0.8 m outside these openings. There are 20 meshes in total, and each one is assigned to one processor.

In case 4, for example, using the 0.04 m x 0.04 m x 0.04 m cell size, the total number of cells is 506, 104. The simulation time is 1200 seconds. The initial time step is 0.00520 s, set automatically during the FDS calculation by dividing the mesh size by the characteristic velocity of the flow. During the calculation, the time step is adjusted such that the CFL (Courant, Friedrichs, Lewy) condition is satisfied. The computing processors are 2.6 GHz CPU with 32 GB RAM. Each computation takes about 280 hours.

Table 2.1: List of simulations.

Case No.	Middle opening position	Staircase
1	-	yes
2	2nd floor	yes
3	3rd floor	yes
4	4th floor	yes
5	5th floor	yes
6	6th floor	yes
7	7th floor	yes
8	8th floor	yes
9	9th floor	yes
10	10th floor	yes
11	11th floor	yes
12	4th floor	no

2.1.4 Results and discussion

2.1.4.1 Velocity at the bottom opening

Figure 2.2 presents comparisons of the air flow velocity at three measuring points at the bottom opening, at z = 0.22 m, 0.38 m, and 0.54 m, respectively. The velocity data have been averaged over the time period from 600 s to 1200 s, which is the same as in the experiment. For measuring points 1 and 2, the average results are under-predicted, with relative differences of 13.32 % and 14.76%, while at measuring point 3, the predicted average velocity is only slightly lower than the experiment (5.37%).

Since the differences of airflow velocity at the three locations are relatively small, one average value of these three values has also been calculated. Figure 2.3 shows the comparison for case 4. A complete comparison of the results for all cases is shown in Table 2.2. ϵ is the relatively difference between the experiment and the simulation. A maximum deviation value of 16.2% is obtained with case 3, where the middle opening is at the third floor. The differences in the calculated errors among the various test cases are noticeable, ranging from -13.3% to 16.2%. This is related to the way how these values are obtained, they are averaged using the velocities at four points along the vertical centerline at the opening. In the experiment, the bottom velocity monotonically increases with the location of the middle opening for lower heights(middle opening below 6th floor), while for higher middle opening the velocity is more or less at the same level. The simulation results are following the same trend except for cases with middle opening at 3rd floor, 5th floor and 8th floor. These floors are corresponding to the cases with larger deviation values

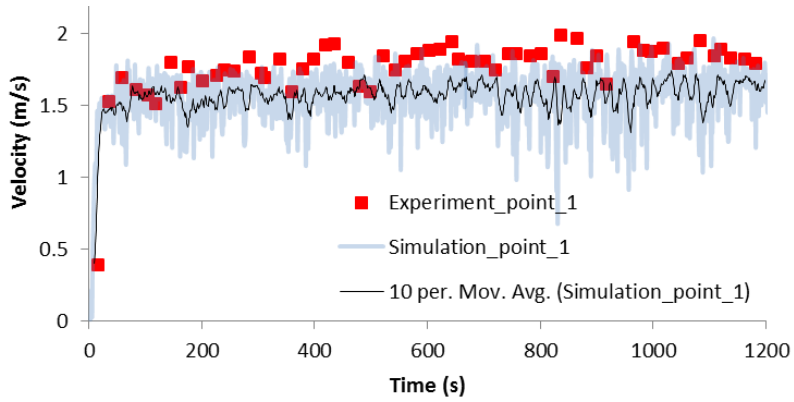

(a)

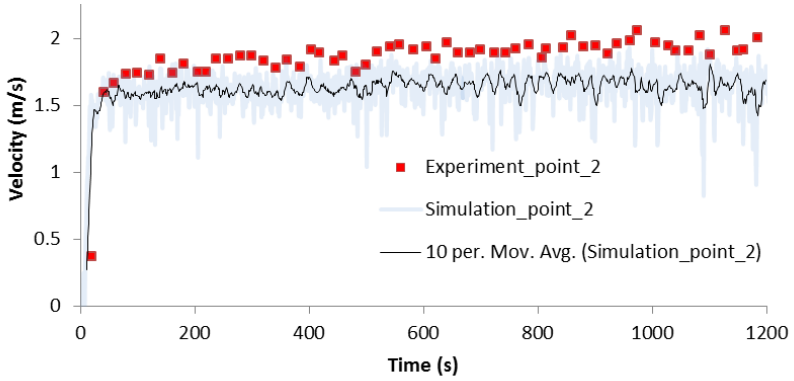

(b)

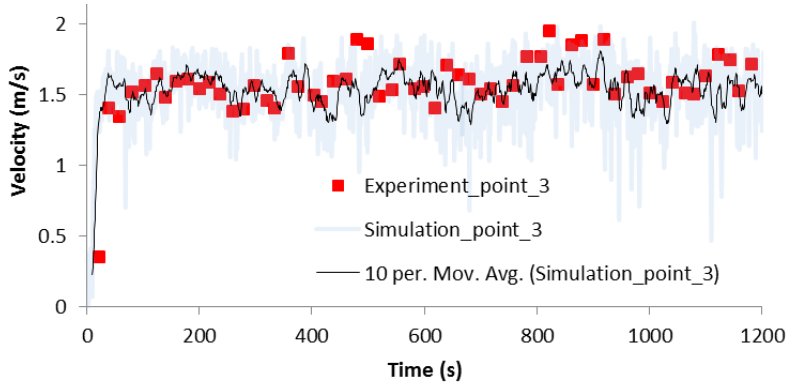

(c)

Figure 2.2: Airflow velocity at bottom opening at height 0.22 m (a), 0.38 m (b), and 0.54 m (c) for case 4 (the black solid line represents the moving average trend line with a period of 10 points).

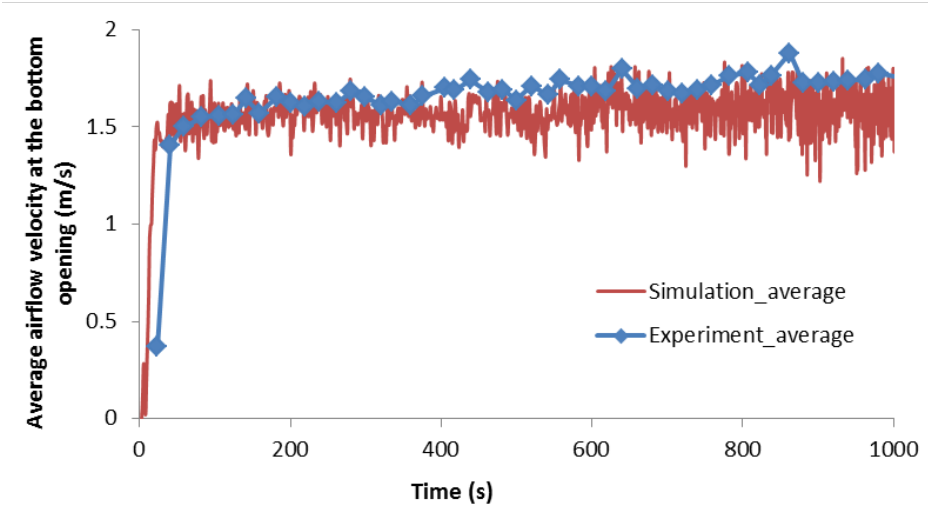

Figure 2.3: Comparison of averaged airflow velocity at bottom opening between experiment and simulation for case 4.

(16.2%, -12.5%, and -13.3%). Actually, a better way should have been employed, which is to output the mass inflow rate and the average density at the opening, then calculate the average velocity at the opening.

Table 2.2: Comparison of the average velocity through the bottom opening between simulations and experimental results or analytical estimations.

Case No.	Middle opening	Exp-Ave-Velocity (m/s)	Sim-Ave-Velocity (m/s)	ϵ (%)
1	-	1.95	1.68	13.8%
2	2nd floor	1.55	1.44	7.0%
3	3rd floor	1.60	1.91	16.2%
4	4th floor	1.71	1.77	3.4%
5	5th floor	1.84	1.57	-12.5%
6	6th floor	1.91	2.03	5.2%
7	7th floor	1.88	2.06	9.6%
8	8th floor	1.95	1.69	-13.3%
9	9th floor	1.91	2.10	5.2%
10	10th floor	1.93	2.1	11.9%
11	11th floor	1.95	2.18	11.8%

2.1.4.2 Temperature rise in the stairwell

The temperature on the vertical centerline of the stairwell is discussed next. Figure 2.4 shows the temporal temperature evolution at height z = 2.04 m in the center of the stairwell for case 4, corresponding to a location where measurements were taken in the experiment. As indicated, the temperature curve reaches a relatively steady period from 800 s

onwards. The results at other heights follow the same trend. Based on this observation, the temperature values are averaged during the time period from 800 s to 1200 s.

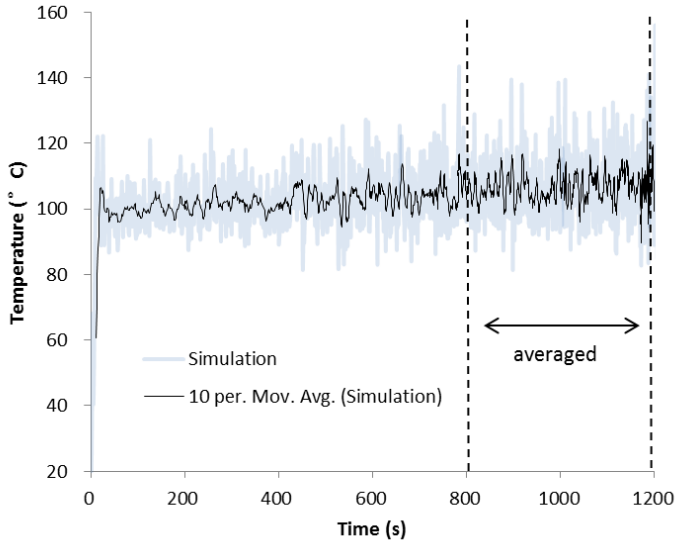

Figure 2.4: Temporal evolution of temperature at height 2.04 m in the stairwell for case 4 (see Table 2.1, the black solid line represents the moving average trend line with a period of 10 points).

Using the time-averaged temperature results, the vertical distribution of temperature on the vertical center line of the stairwell can be analyzed. First, the results for Case 4, with the middle opening at the 4^{th} floor, are compared (Figure 2.5(a)). The temperature decreases with height. The sudden drop at 4 m results from the cooling influence of the inflow of fresh air through the middle opening on the 4^{th} floor (at z = 3.6 m). Very good agreement is achieved for heights above 4 m (maximum relative deviation of 6.6%). As is indicated in Figure 2.5(b), the relative deviation between the experimental data and simulation results remains below 10%. For the two measurement points lower than 4 m, the temperature rise is over-predicted by approximately 8.4% and 12.3%, respectively.

2.1.4.3 Temperature at the middle opening

Figure 2.6 and Figure 2.7 present the temperature results at the middle opening for case 4. Two locations have been considered, namely, 15 cm and 45 cm above the bottom of the middle opening. Both the experimental data and simulation results curves reveal a significant rise during the early stages. This rise indicates the time when the high temperature smoke reaches the middle opening, and thus indicates the speed of the smoke movement.

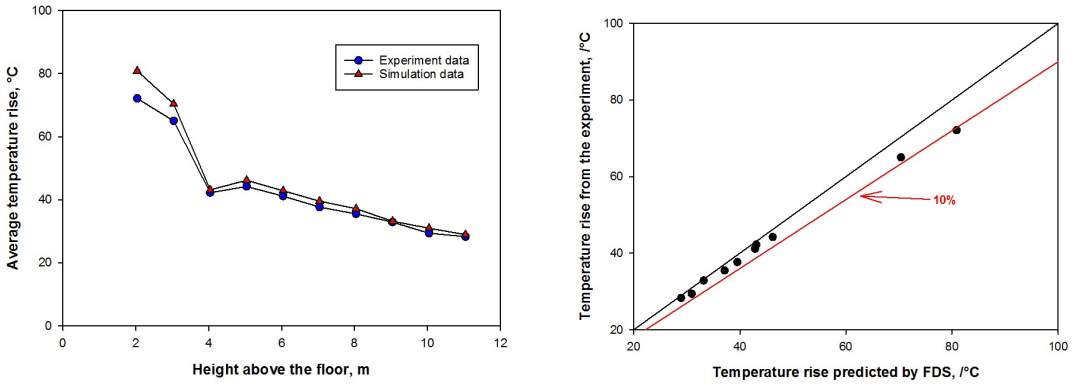

(a) (b)

Figure 2.5: Temperature rise in the stairwell for case 4, averaged between 800 s to 1200 s.

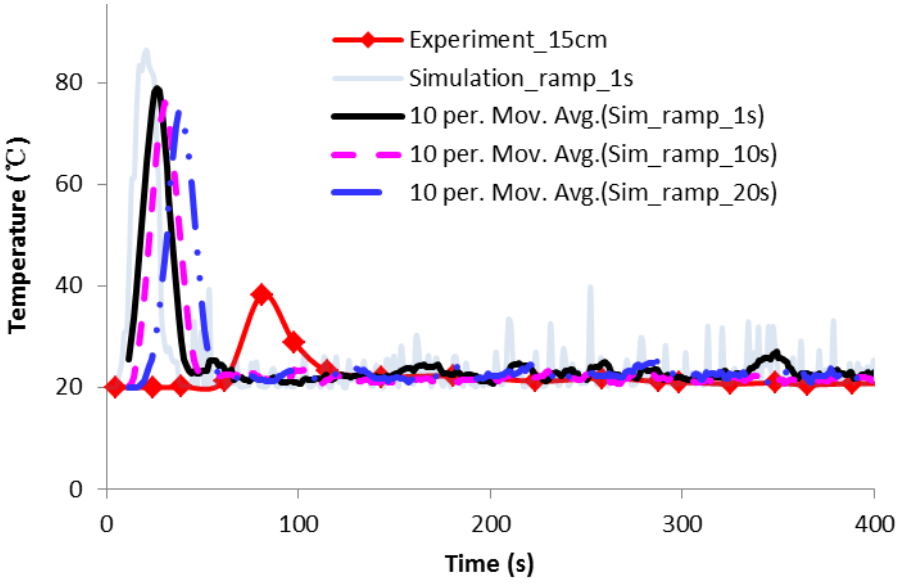

Figure 2.6: Temperature at height 15 cm above the bottom of the middle opening for case 4. The black solid line represents the moving average trend line with a period of 10 points. The lines 'ramp 10 s' and 'ramp 20 s' refer to the start-up ramp of the fire in the simulations (the default value was 1 s).

This rise occurs much faster in the simulations than in the experiments. This indicates that the smoke moves much faster in the simulations than that in the experiment, despite the fact that the flow through the bottom opening was reasonably well predicted (Figure 2.2). There are a few possible explanations. First of all, the faster smoke motion in the simulations is in line with the higher mean temperatures at the lower floors (Figure 2.5), imposing a stronger buoyancy effect. Secondly, there is no leakage in the

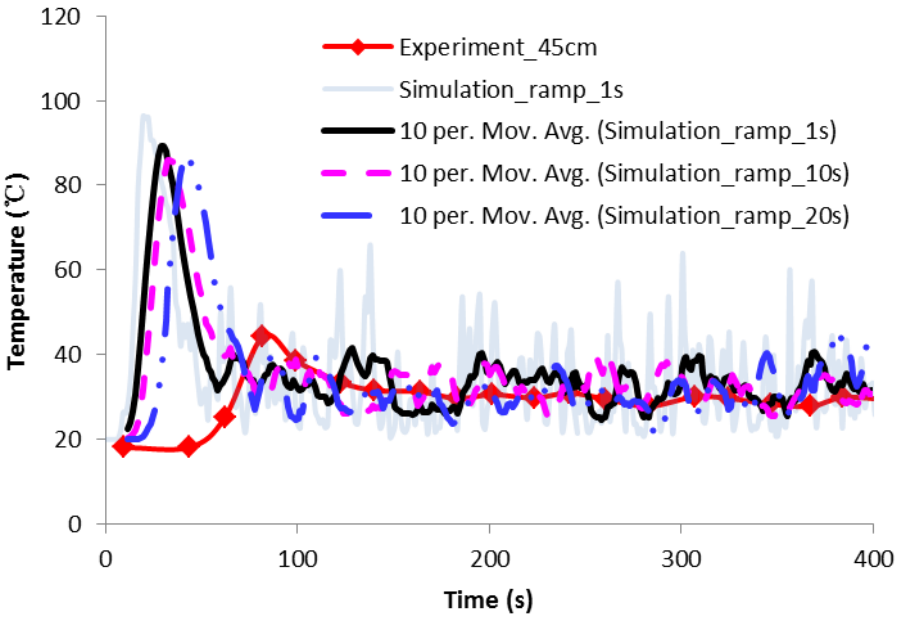

Figure 2.7: Temperature at height 45 cm above the bottom of the middle opening for case 4. The black solid line represents the moving average trend line with a period of 10 points. The lines 'ramp 10 s' and 'ramp 20 s' refer to the start-up ramp of the fire in the simulations (the default value was 1 s).

simulations, so that the smoke is expected to move faster upward (as it cannot leave the configuration). Note that this also implies there is no heat loss through the leakage in the simulations. Another aspect is the uncertainty with respect to the start-up of the burner in the test. In the calculation, it is assumed that the burner reaches its peak value within 1 s. In the test, this ramp time was not recorded, but it is believed to be within 10 s (personal communication with the authors of [55]). In order to numerically investigate the influence of the burner ramp time on the smoke movement in the stairwell, two additional simulations have been conducted, each one with a specific ramp time (namely 10 s and 20 s). As expected, the burner ramp time does have a direct effect on the time for the smoke to reach the middle opening. However, even with a 20 s ramp, the smoke reaches the opening much sooner than observed in the experiments, so that this alone cannot explain the deviations.

Finally, the over-prediction of the smoke movement speed might be due to the impact of the staircase. Further studies are needed to investigate this problem.

Once the transient stage has passed, the temperatures at height 15 cm above the bottom of the middle opening are almost equal to the ambient temperature from 200 s onwards ($23.1°C$ on average). At height 45 cm above the bottom of the middle opening,

the average temperature is 32.9°C. This is due to air inflow into the domain through the bottom part of the opening, while hot smoke flows out through the upper part of the opening. Simulation results are in very good agreement with the experimental data.

2.1.4.4 Pressure distribution in the stairwell

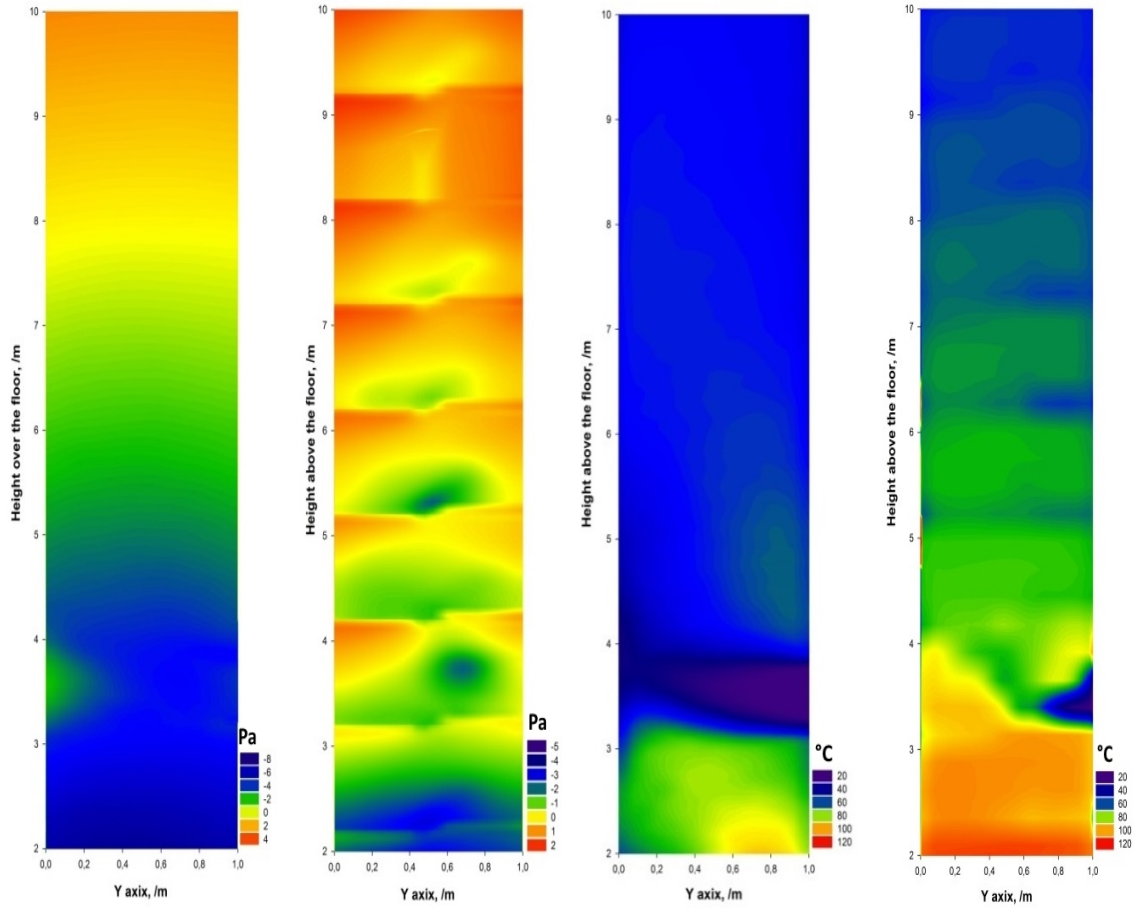

Figure 2.8: Contour plots of relative pressure (a, b) and temperature (c, d) in plane x = 0.4 m in the stairwell from 3rd floor to 10th floor of Case 12(a, c) (i.e., in the absence of staircase, see Table 2.1) and Case 4 (b, d) (i.e., with staircase, see Table 2.2).

The pressure inside the stairwell is an important parameter for the buoyant smoke movement in the stairwell. CFD techniques allow obtaining a detailed distribution of pressure and temperature in the entire stairwell using slice files. With the Fortran program 'fds2ascii.f90', the time averaged data can be obtained from these slice files. Here, the time averaged pressure (in Pa) and temperature distribution at plane x = 0.4 m for case

4 and case 12 are presented in Figure 2.8. The averaging time period is again from 800 s to 1200 s.

In the absence of staircases in the stairwell, the relative pressure, defined as the difference between the pressure inside the stairwell and the pressure outside, is expected to continuously increase along the height of the stairwell. At the bottom, there is a negative relative pressure, whereas at the top there is a positive relative pressure. There is a clear position where the pressure difference between inside and outside is zero, defining the neutral plane position. This is confirmed in Figure 2.8(a).

However, in cases with staircases in the stairwell, the vertical spread of smoke is disturbed by the staircase structure inside the stairwell. As is clearly observed in Figure 2.8(b), the relative pressures do not increase monotonically along the height of the stairwell. Consequently, there is no unique position where the relative pressure is zero. Actually, zero relative pressure positions exist for floors from 3rd to 8th floor, so there is no sharp position of the neutral plane height.

Moreover, the influence of staircase on the temperature distribution in the plane x = 0.4 m in the stairwell is illustrated in Figures 2.8(c) and 2.8(d).

2.1.4.5 Location of neutral plane height in the stairwell

In the experiments [55], the temperature distribution at the middle opening has been analyzed to determine the neutral plane height. Besides that, an analytical expression has also been proposed to predict the neutral plane height in stairwell with multiple openings [55]. This analytical method is based on Bernoulli's equation and the conservation of mass. This method uses a function which is given as follows:

$$f(h) = \frac{gP_{atm}}{RT_0} v_1 \cdot s_1 + \frac{gP_{atm}}{RT_0} v_2^{'} \cdot s_2^{'} + \frac{gP_{atm}}{RT_s(h)} v_2^{''} \cdot s_2^{''} + \frac{gP_{atm}}{RT_s(H)} v_3 \cdot s_3 \tag{2.2}$$

In Eq. 2.2, g is the gravity acceleration, P_{atm} is the atmospheric pressure, R is the specific gas constant for air, T_0 is the temperature of air, $T_s(h)$ is the smoke temperature at height h, $T_s(H)$ is the smoke temperature at the top opening, and v , s are the velocity and flow area at three openings. $v_2^{'}$ and $s_2^{'}$ are the air inflow velocity and the inflow area at the middle opening. $v_2^{''}$ and $s_2^{''}$ are the outflow velocity and the outflow area at the middle opening. The terms on the right hand side are, in order of appearance, the mass flow rate of: inflow air through the bottom opening, incoming air through the middle opening, outflowing smoke through the middle opening, and outflowing smoke through the top opening. If there are h_i and h_j satisfying $h_i < h_j$, $f(h_i) > 0$ and $f(h_j) < 0$, then

there must be a h_m, satisfying $h_i < h_m < h_j$ and $f(h_m) = 0$, which is considered as the neutral plane height.

As demonstrated in the previous section, the pressure differences do not vary monotonically along the height of stairwell. Here the average pressure in the plane x = 0.4 m is calculated for all 12 floors. Figure 2.9 presents the results for Cases 1, 4, 7, and 9. The averaged relative pressure increases with height. The neutral plane height value is determined as the height where the pressure curve crosses the dashed line (see Figure 2.9) for all cases. These simulation results are listed and compared to the experimental and values obtained from the analytical expression in Table 2.3.

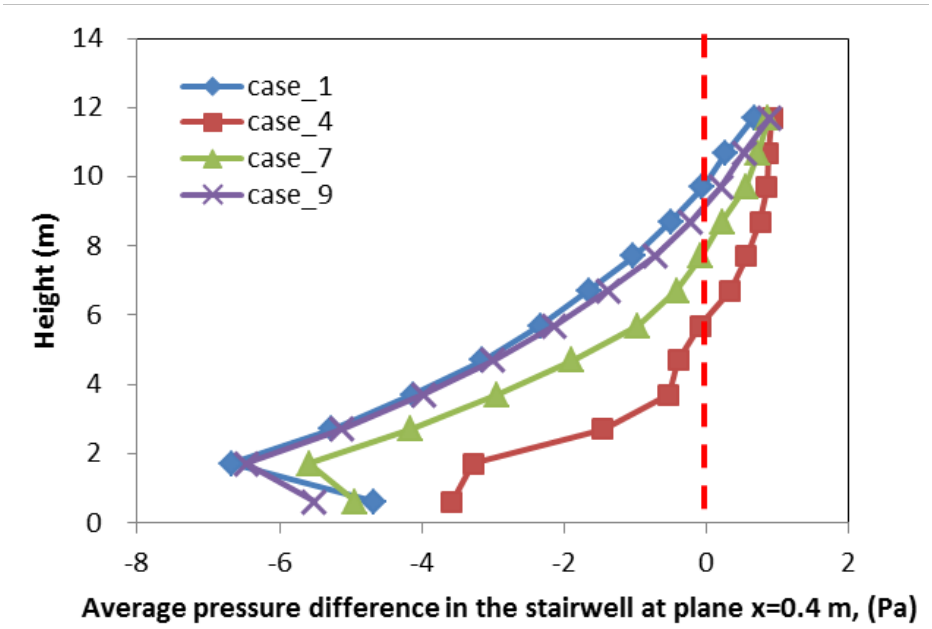

Figure 2.9: Relative pressure distribution in the stairwell for case 1, 4, 7 and 9 (see Table 2.1).

Only the results for Cases 6 through 9 are available from the experimental data. The neutral plane height value for these cases is located at the same floor as the middle opening. The numerical results are in line with the analytical expression in that the neutral plane height position increases for a higher position of the middle opening. However, the numerical results are somewhat higher than the experimental data and the values obtained from the analytical expression. This could be partially attributed to the low instrumentation density that did not allow to have continuous pressure, velocity and temperature profile along the stairwell (as obtained by the numerical simulations) and required an interpolation of the data.

The difference between Cases 4 and 12 is striking, reflecting the influence of the

staircase on the temperature and pressure distribution inside the stairwell.

Table 2.3: Comparison of the neutral plane height between simulations and experimental results or analytical estimations.

Case No.	Middle opening	H_{N-exp}(m)	H_{N-est}(m)	H_{N-sim}(m)
1	-	-	-	9.80
2	2nd floor	-	4.53	4.85
3	3rd floor	-	5.03	5.00
4	4th floor	-	5.50	5.65
5	5th floor	-	6.04	6.15
6	6th floor	5.7(6th floor)	6.68	7.55
7	7th floor	6.7(7th floor)	7.39	8.05
8	8th floor	7.7(8th floor)	8.20	8.20
9	9th floor	8.7(9th floor)	8.70	9.15
10	10th floor	-	9.08	9.85
11	11th floor	-	-	10.2
12	4th floor	-	-	7.60

2.1.4.6 Influence of the turbulence model

As mentioned above, the default turbulence model 'modified Deardorff' has been employed. In order to investigate the influence of the turbulence model, simulations have also been conducted for case 4 using the 'Dynamic Smagorinsky' model (Table 2.4). The results are compared in terms of the temperature rise in the stairwell and the temperature at the middle opening.

Table 2.4: Extra simulations to investigate the influence of turbulence model.

Case No.	Middle opening	Staircase	Turbulence model
4	4th floor	Yes	Deardorff
4_1	4th floor	Yes	Dynamic Smagorinsky

In Figure 2.10, the temporal evolution of temperature at height z = 7.04 m in the stairwell is presented, a location of a measuring point in the experiment. The results are very similar. The average values of the temperature rise in the stairwell for all cases are shown in Figure 2.11. Again, no significant differences are observed.

In Figure 2.12 and Figure 2.13, the temperatures at two locations at the middle opening are compared. The time for the smoke to reach the middle opening, is slightly later using the 'Dynamic Smagorinsky' model, but differences are small. Also the differences in relative pressures as obtained with the different turbulence models are small (Figure 2.14).

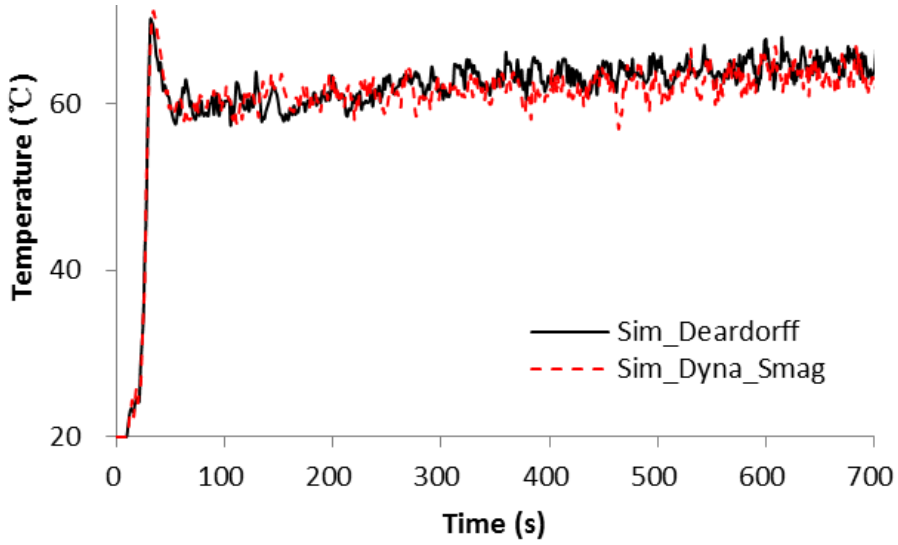

Figure 2.10: Temporal evolution of temperature at height 7.04 m in the stairwell for cases 4 and 4_1 (see Table 2.4).

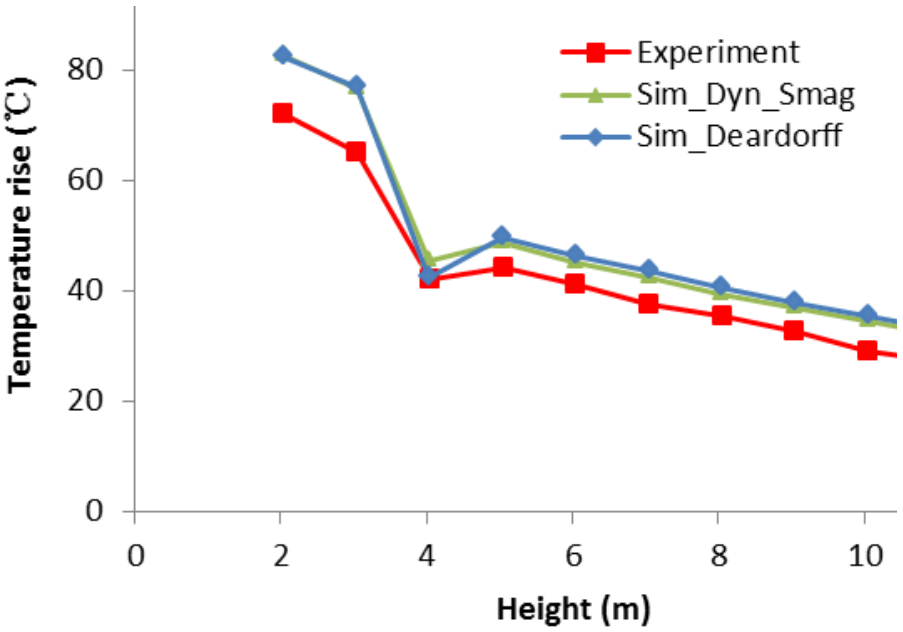

Figure 2.11: Comparison of temperature rise in the stairwell for cases 4 and 4_1 (see Table 2.4) averaged between 800 s to 1200 s.

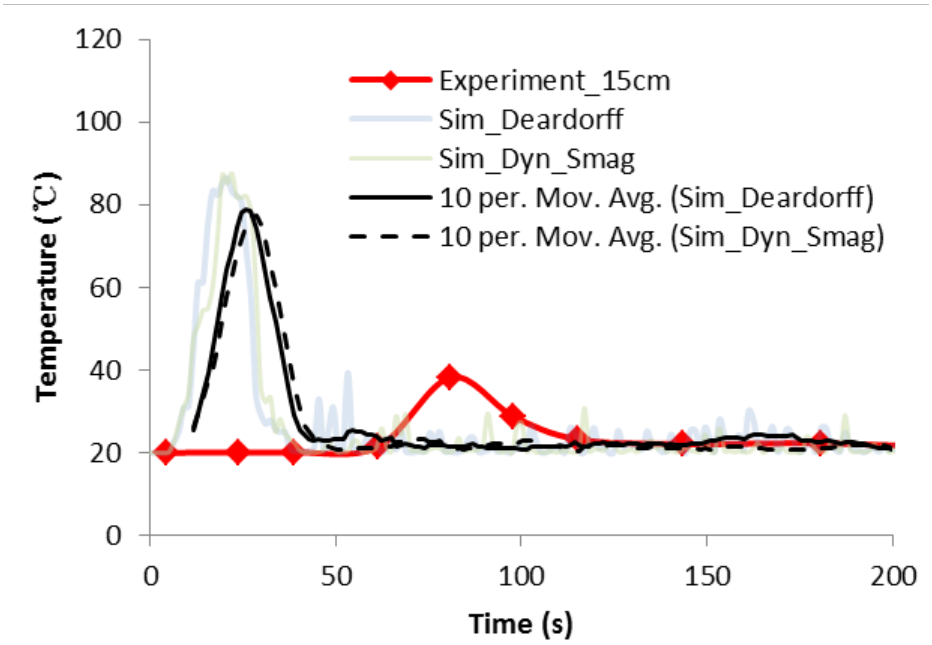

Figure 2.12: Temperature at height 15 cm above the bottom of the middle opening for cases 4 and 4_1 (see Table 2.4).

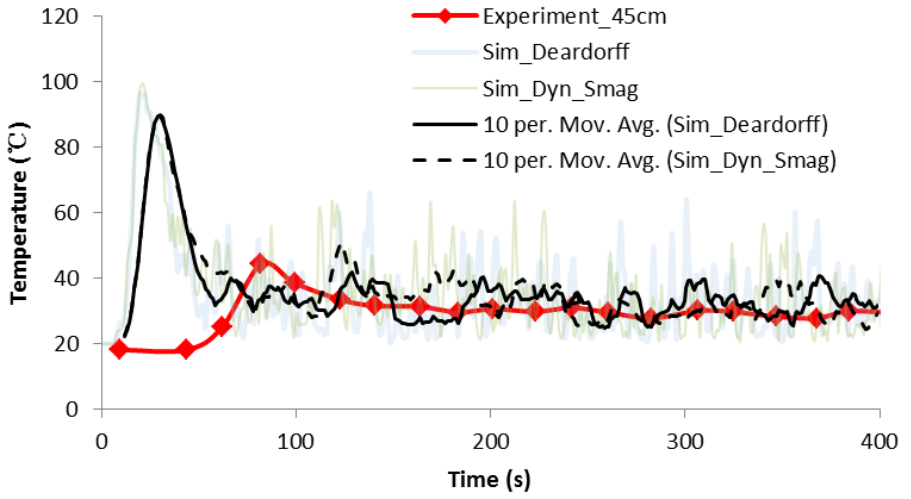

Figure 2.13: Temperature at height 45 cm above the bottom of the middle opening for cases 4 and 4_1 (see Table 2.4).

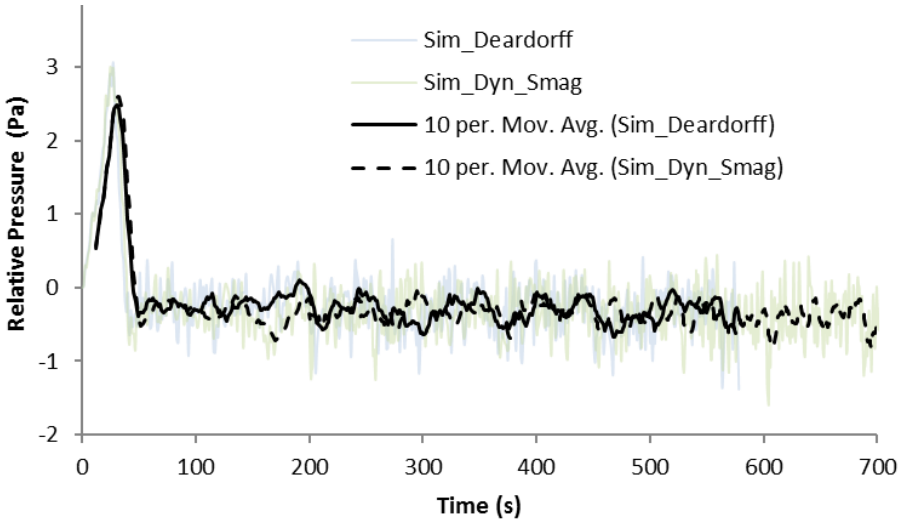

Figure 2.14: Relative pressure at height 7 cm in the stairwell center line for cases 4 and 4_1 (see Table 2.4)

2.1.5 Conclusions

Numerical simulations of fire-induced smoke motion inside the stairwell of a 1:3 scale model of a high-rise building have been discussed. FDS, version 6.0.1, has been employed with default settings. 12 cases have been considered. For the flow through the bottom opening, the overall trend has been well captured. For the average velocity through the bottom opening, a maximum deviation of 16.23% is obtained for case 3 (see Table 2.1).

Good agreement for the temperature inside the stairwell between the experimental and numerical data has been achieved for heights above the middle opening for Case 4 (see Table 2.1 , with a maximum relative deviation of less than 6.6%. For the two measurement points below the middle opening, the temperature rise is over-predicted by respectively 8.4% and 12.3%.

Through the prediction of the temperature at the middle opening, the time for hot smoke to reach the middle opening for case 4 has been obtained. Smoke moves much faster in the simulations than in the experiments. This could be due to the temperature over-prediction at lower floors (inducing too strong buoyancy), due to the absence of leakage in the simulations, due to uncertainty in the start-up of the fire in the experiments and due to the presence of the staircase.

The influence of the presence of a staircase on the pressure distribution has been examined. It was found that the staircase disturbs the flow and as a result the difference between the pressure inside the stairwell and the pressure outside does not increase monotonically with height.

The neutral plane height, obtained by post-processing of the simulation results, is somewhat over-predicted in comparison to experimental and the corresponding analytical expression of [55].

The influence of two turbulence models has been investigated, comparing the default modified 'Deardorff' and 'Dynamic Smagorinsky' model. No significant differences are observed in any of the analysed results.

2.2 Under-ventilated fires with external flaming

2.2.1 Introduction

In cases where flames are ejected from an enclosure and attached to building's façade, the ejected flames can potentially cause secondary fires which might spread from the original floor to upper floors, as well as to adjacent buildings. Therefore, it is necessary to understand the physics involved and provide reliable predictions of the fire dynamics in such scenarios.

This section aims to assess simulation results obtained with FDS (version 6.0.1) for the under-ventilated enclosure fire and external flaming based on a set of experimental data [5, 6]. Various opening geometries and a single inert façade wall are considered. The discussion of simulation results includes the vent flows through the opening, time-averaged gas temperature, HRR inside the enclosure, neutral plane height, and external flame height.

2.2.2 Experimental set-up

The set-up in the modelling corresponds to the experiments reported in [5, 6]. The enclosure dimensions are 0.5 m x 0.5 m x 0.5 m. A fiberboard plate serves as external façade wall, as shown in Figure 2.15. By setting various widths and heights of the opening, under-ventilated conditions has been obtained. A 0.1 m x 0.2 m propane burner provides a fire source with a specific theoretical heat release rate inside the enclosure. The burner is located at the center of the enclosure. All walls, including the façade wall, consist of fiberboard with the following properties: the thickness is 0.025 m, the density is 350 kg/m^3 , the thermal conductivity is 0.3 W/m·K , the emissivity is 0.9, and the heat capacity is 1700 J/kg·K. A more detailed description of this experimental work can be found in [5] and [6].

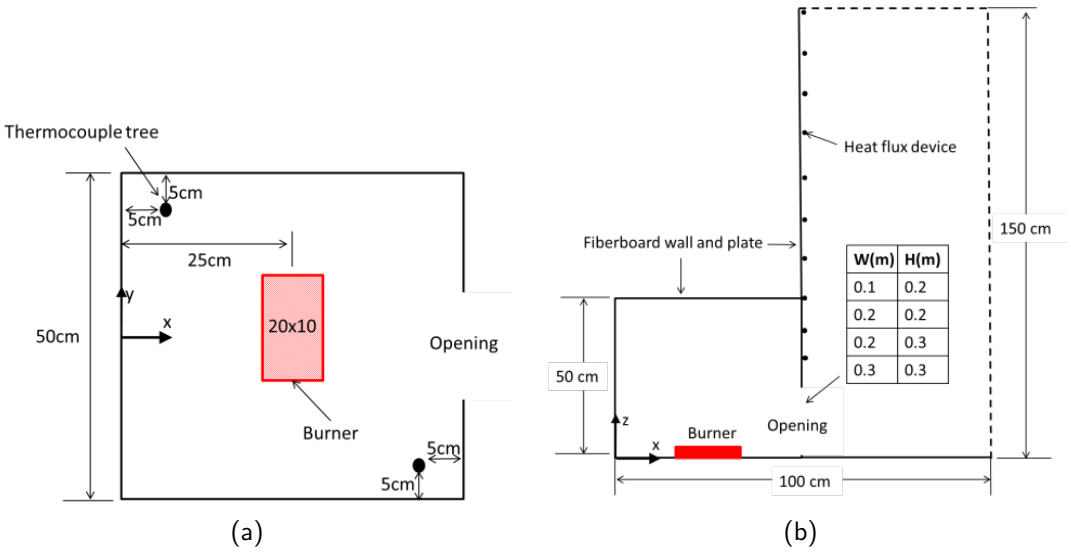

Figure 2.15: Sketch of the experimental set-up. (a)Top view, (b) Side view.

2.2.3 Simulation details

Four different opening geometries are considered: 0.1 m x 0.2 m, 0.2 m x 0.2 m, 0.2 m x 0.3 m, and 0.3 m x 0.3 m. The computational domain has been extended by 50 cm outside the enclosure, as shown in Figure 2.16(a), in order to limit the influence of the 'open' boundary condition on the flow field. As shown in Figure 2.16(b), two meshes are used within the simulation domain. The first mesh contains the entire enclosure and the lower part of the outdoor domain, and the second mesh covers the rest of the domain. The obstructions in the FDS model are made thick (at least one grid cell thick).

First, it is necessary to discuss the required grid resolution for the present study. In case of enclosure fires with external flaming, both the fire source and the vent flow need careful consideration. For the fire source, a characteristic length scale D^* is related to the total heat release rate $\dot{Q}$ by the following relation [60]:

$$D^* = \left[\frac{\dot{Q}}{\rho_\infty C_\infty T_\infty \sqrt{g}}\right]^{5/2} \tag{2.3}$$

In Eq. 2.3, $\dot{Q}$, ρ_∞, C_∞, T_∞, and g are respectively the total heat release rate (kW), the density of air at room temperature (kg/m^3), the specific heat of air (kJ/(kg·K)), the atmosphere temperature (K), and the gravity acceleration (m/s^2). McGrattan et al. [62] suggested a cell size of 10% of the plume characteristic length D^* as adequate resolution, based on careful comparisons with plume correlations. Based on this '10% criterion', the

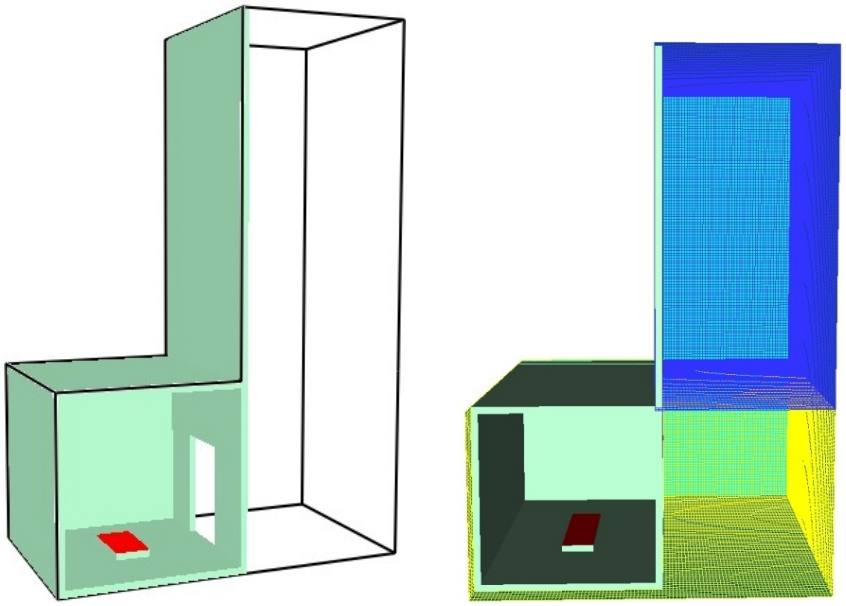

(a) (b)

Figure 2.16: Snapshots of the simulation domain and meshes. (a)Global view of simulation domain (b) Two meshes in the domain.

required cell size for a HRR between 30 kW and 90 kW, is in the range of 2.3 cm to 3.6 cm.

Besides the length scale concerning the fire source, it is also necessary to examine other length scales, concerning the accurate simulation of the flow through the opening. However, this length scale has not been considered systematically in previous numerical studies. The discussion is presented in section 2.2.4.

In this study, cell sizes of 1 cm, 2 cm and 4 cm are used for each opening geometry. In order to get under-ventilated conditions, all the heat release rates of the burner are set to be larger than the value of 1500·A$\sqrt{H}$. Table 2.5 shows a list of all 32 simulations.

In case 27, for example, each cell has dimensions of 0.01 m x 0.01 m x 0.01 m, and the total number of cells in the computational domain is $(102 \times 60 \times 54) + (50 \times 60 \times 100) = 630,000$. The initial time step is 0.00112 s, set automatically during the FDS calculation by dividing the mesh size by the characteristic velocity of the flow. The total simulation duration is set to 20 minutes, as steady state conditions are reached after 8 minutes (see later). For these two meshes of the simulation domain, two computing processors (2.6 GHz CPU with 32 GB RAM) were used. This computation takes about 144 hours. The simulation results discussed in the following sections are mean values, averaged during the period from 500 s to 1200 s.

Table 2.5: List of simulations

Opening geometry		$\dot{Q}_{in}$ (kW)	Fire source HRR $\dot{Q}$ (kW)	Grid size (cm)	Case No.
W(m)	H(m)				
0.1	0.2	13.42	30	4,2,1	1-3
0.1	0.2	13.42	40	4,2,1	4-6
0.2	0.2	26.83	50	4,2,1	7-9
0.2	0.2	26.83	60	4,2,1	10-12
0.2	0.2	26.83	70	4,2,1	13-15
0.2	0.3	49.30	60	4,2,1	16-18
0.2	0.3	49.30	70	4,2,1	19-21
0.2	0.3	49.30	80	4,2,1	22-24
0.3	0.3	73.94	80	4,2,1	25-27
0.3	0.3	73.94	90	4,2,1	28-30
0.2	0.2	26.83	30,40	1	31,32

The mass inflow and out flow rates through the opening have been determined in FDS by setting two measurement devices at the level of the doorway called "Mass Flow +" and "Mass Flow -". The actual heat release rate inside the enclosure has been determined by integrating the Heat Release Rate Per Unit Volume (HRRPUV). Gas temperature inside the enclosure has been determined in two opposite corners (see Figure 2.15) at several heights from floor level (Z=0.04, 0.09, 0.14, 0.19, 0.24, 0.29, 0.34, 0.39, 0.44, and 0.49 m). In this work, a temperature based method has been considered to determine the flame height. The flame tip position is taken as the highest location outside the room volume where the time-averaged mean temperature is $T = 520°C$ (i.e., $\Delta T = 500°C$ compared to ambient) [63]. The reference level for the definition of the flame height is taken as the neutral plane height (see Figure 2.17).

2.2.4 Results and discussion

Since the mass flow rate of air entering the enclosure is not sufficient for complete combustion of the imposed total HRR, the combustible gases leave the compartment. They find fresh air and react outside the enclosure. Figure 2.18 provides a typical snapshot showing external flaming in the simulation.

Figure 2.19 shows the time evolution of mass flow rates through the ventilation opening for case 27. The outflow rate, inflow rate, fuel flow rate, and net flow (the difference between the outflow and inflow), as obtained from post-processing, are approximately constant during most of the time after the ignition, with an average value of 0.0222 kg/s,

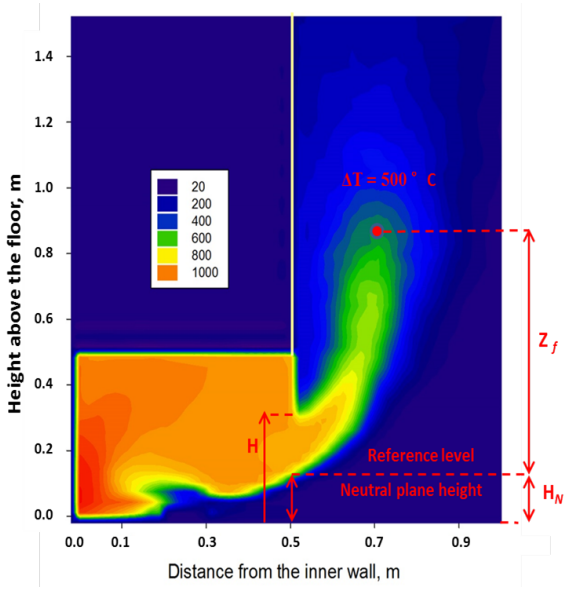

Figure 2.17: Time-averaged temperature contour plot showing the flame tip position and neutral plane height.

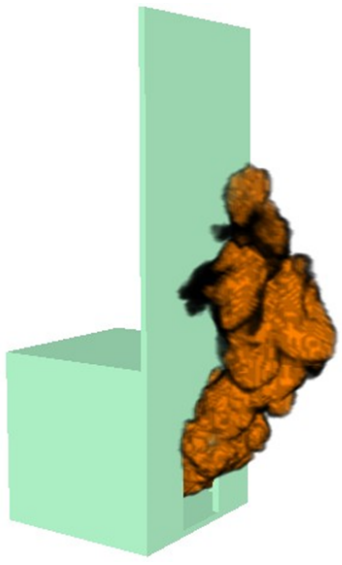

Figure 2.18: Snapshot showing a typical external flaming in the simulation.

0.0201 kg/s, 0.0017 kg/s, and 0.0020 kg/s respectively. The difference between the net mass flow rate and the fuel mass flow rate is discussed in detail in section 2.2.4.

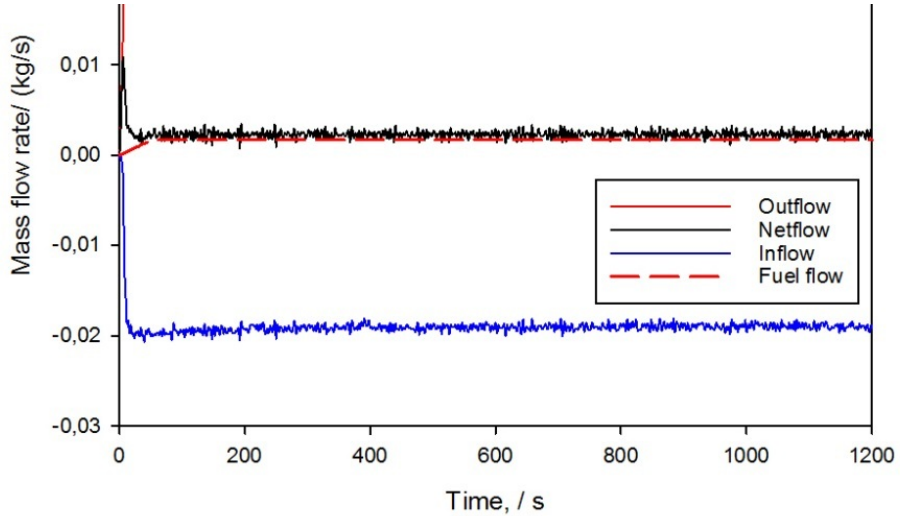

Figure 2.19: Temporal evolution of mass flow rate through the ventilation opening for case 27 (see Table 2.5).

Figure 2.20 shows the temporal evolution of temperatures at several heights for case 27 (see Table 2.5). These temperatures were recorded by the back corner thermocouple tree (see Figure 2.15(a). It is seen that a quasi-steady state condition has been obtained in the simulation roughly from 500 s to 1200 s. The other cases show a similar trend.

The dependence of CFD simulation results on the grid size is studied first, focusing on the flow through the opening. Figures 2.21- 2.24 show, respectively, the steady state horizontal velocity and temperature along the vertical centerline of the opening for cases 22, 23, 24 (cell sizes 4 cm, 2 cm and 1 cm) and cases 25, 26, 27 (cell sizes 4 cm, 2 cm and 1 cm). Similar trends were observed for the other cases. A 2 cm cell size or finer is sufficient to ensure the grid insensitivity of the simulation results.

At a certain height at the opening, the horizontal velocity is zero. This height is called the 'neutral plane height'. The neutral plane height value is determined as the position where the horizontal velocity profile crosses the dashed line (Figure 2.21 and Figure 2.22) for all cases.

2.2.4.1 Flow through the opening

First, the mass inflow rate of air through the opening is discussed. The mass inflow rates for cases with 1 cm grid size for the four different ventilation factors are presented in Figure 2.25 . Not surprisingly, a linear correlation is observed between the mass inflow

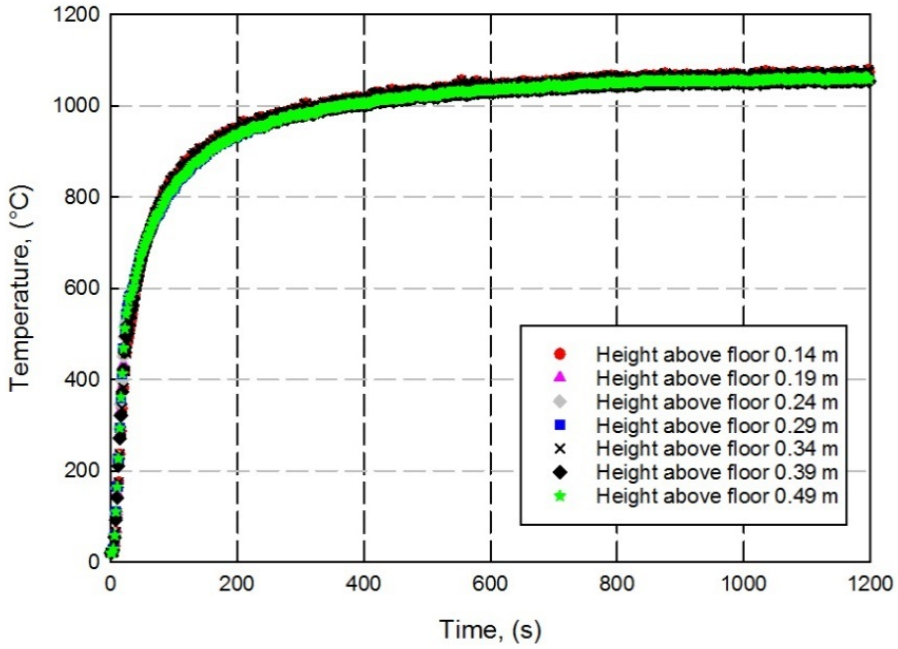

Figure 2.20: Temporal evolution of temperatures at the back corner for case 27 (see Table 2.5).

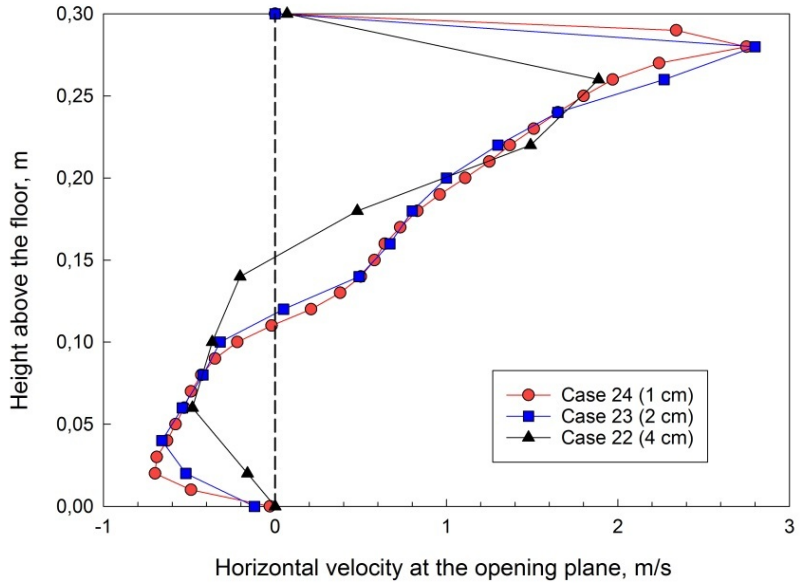

Figure 2.21: Cell size effect on horizontal velocity along the centerline of the opening for cases 22-24 (see Table 2.5).

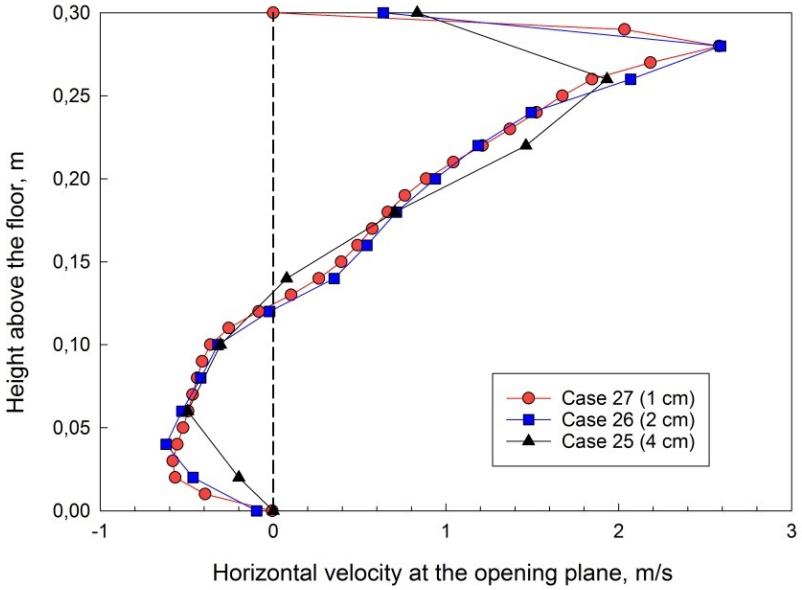

Figure 2.22: Cell size effect on horizontal velocity along the centerline of the opening for cases 25-27 (see Table 2.5).

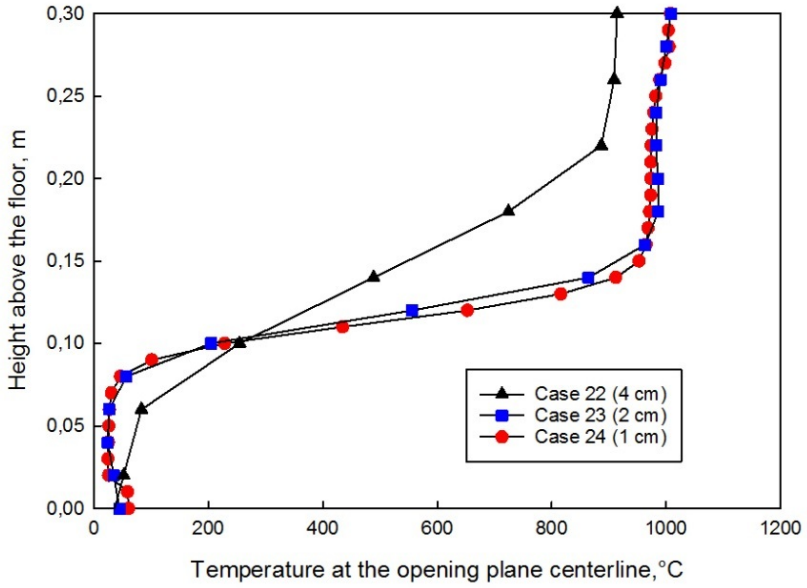

Figure 2.23: Cell size effect on temperature along the centerline of the opening for cases 22-24 (see Table 2.5).

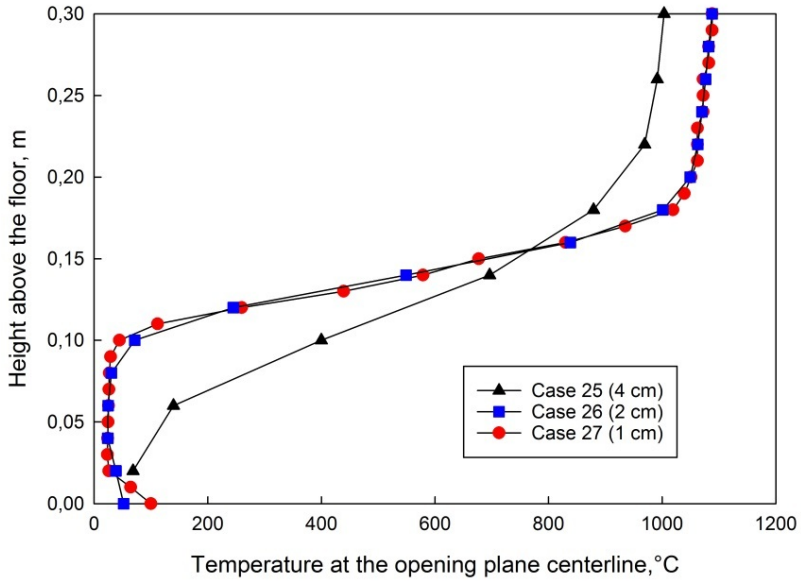

Figure 2.24: Cell size effect on temperature along the centerline of the opening for cases 25-27 (see Table 2.5).

rate and ventilation factor:$\dot{m} = c \cdot A\sqrt{H}$. The constant coefficient c is roughly 0.41. This is at the lower end of the range 0.4-0.61 found in the literature [2].

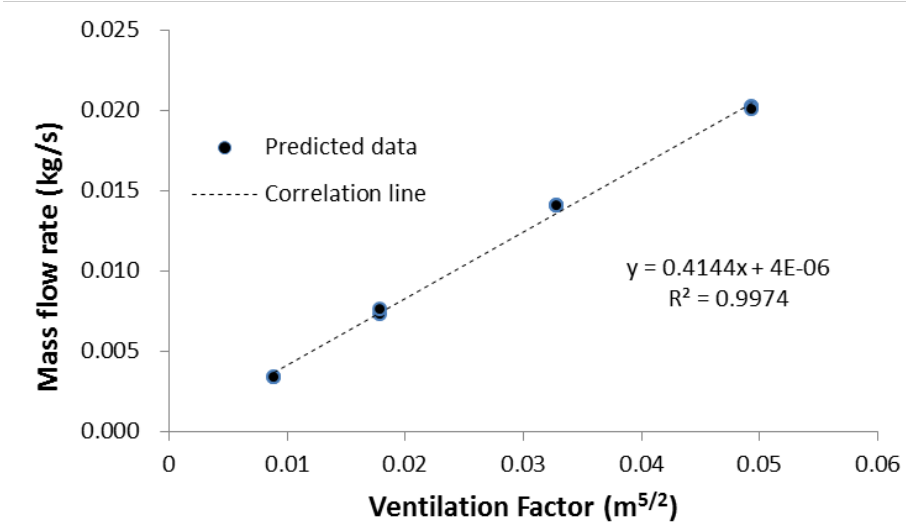

Figure 2.25: The correlation between mass inflow rate and the ventilation factor for 1 cm grid size results.

The prediction of the air mass flow rate through the opening in under-ventilated conditions is of great importance, because it determines the extent of burning inside and outside the enclosure. The required fineness of the grid was already illustrated in Figure 2.21 and

Figure 2.22. In addition hereto, we discuss grid convergence in terms of a mass balance 'error' (Eq. 2.7), based on post-processing of output data, using two length scales ratios. The word 'error' is in between quotes because it is not a true error at the level of implementation (FDS 6 conserves mass). It is merely an apparent error at the level of post-processing.

The first length scale ratio considers the ratio of the ventilation factor to the grid cell size:

$$\ell_1^* = \ell_1/\delta_x = \left(A\sqrt{H}\right)^{2/5}/\delta_x \tag{2.4}$$

This length scale ratio varies from 3.78 to 40 for the cases considered according to the value of the grid size and the opening geometry.

The second length scale ratio considers the ratio of the hydraulic diameter of the opening to the grid cell size:

$$\ell_2^* = D_h/\delta_x = (2W \cdot H/(W+H))/\delta_x \tag{2.5}$$

This length scale ratio varies from 3.33 to 40 for the cases considered according to the value of the grid size and the opening geometry.

At steady-state conditions, the mass balance applied to the enclosure volume reads:

$$\dot{m}_{out} = \dot{m}_{in} + \dot{m}_{fuel} \tag{2.6}$$

where $\dot{m}_{out}$ is the total air mass outflow rate through the opening (kg/s), $\dot{m}_{in}$ is the total air mass inflow rate through the opening (kg/s), $\dot{m}_{fuel}$ is the mass supply rate of the fire source (kg/s). Here a mass balance 'error' is defined as the following:

$$\epsilon = \left|1 - \frac{\dot{m}_{in} + \dot{m}_{fuel}}{\dot{m}_{out}}\right| \times 100\% \tag{2.7}$$

It is stressed again that this is not a real 'error' at the level of implementation. The discussion of Figure 2.26 and Figure 2.27 is based on output values as obtained from post-processing. The implementation in FDS at the level of discretization differs from what is delivered as output. This is discussed in more detail below, but the reader must beware of this issue already now, since true errors in mass balance of more than 1% would already be unacceptable.

Figure 2.26 shows that ϵ varies from 1.4% to 15.0%. It is almost inversely proportional to ℓ_1^*. Like the 10% criterion when choosing cell size for fire plume, a value of 10 is chosen for ℓ_1^*. For $\ell_1^* \geq 10$, ϵ reduces to values below 4%. Such an approach can be used to estimate opening uncertainties associated with the grid size in the prediction of flows through. In the following sections, only the cases with $\ell_1^* \geq 10$ were used for the analyses. The cell sizes used in these cases are smaller than or equal to 2 cm.

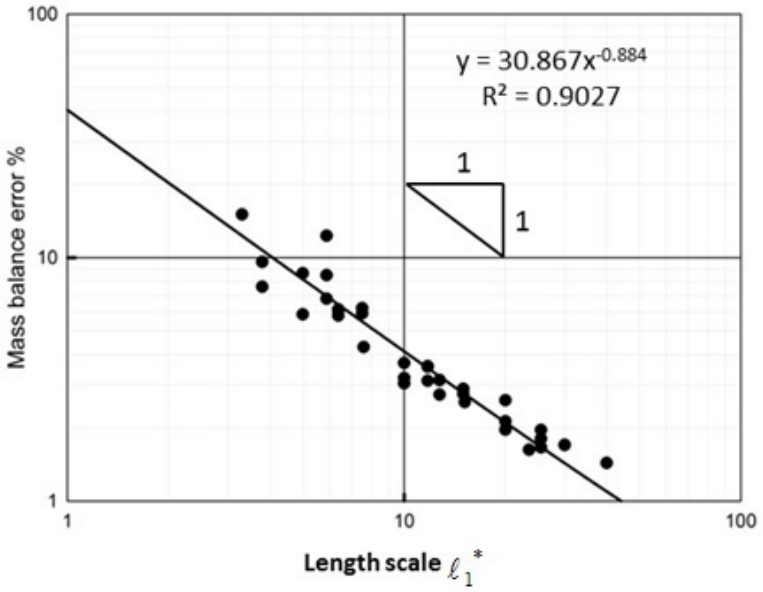

Figure 2.26: Mass balance 'error' ϵ (Eq. 2.7 based on post-processing of output data for all the cases analyzed using length scale ℓ_1^*. The 'error' is not at the level of implementation (FDS 6 conserves mass). It is an apparent error at the level of post-processing.

Figure 2.27 presents ϵ using ℓ_2^*. Similarly as in Figure 2.26, ϵ is almost inversely proportional to ℓ_2^*, and for $\ell_2^* \geq 10$, the mass balance error reduces to values below 4%.

As mentioned, it is stressed that Figure 2.26 and Figure 2.27 refer to post-processing of output data. In the output, FDS uses a simple method to define the mass flux, which differs from what is implemented in the discretization of the mass conservation equation. The output quantities 'MASS FLOW +' and 'MASS FLOW -' are calculated as follows:

$$\dot{m} = \int \rho u \cdot \mathrm{d}A \tag{2.8}$$

The velocity u is the component of velocity in the specified direction. The u-component of the velocity is defined directly in the measurement plane. The density ρ is the average of the densities at each side of the measurement plane. The area A is the sum of the

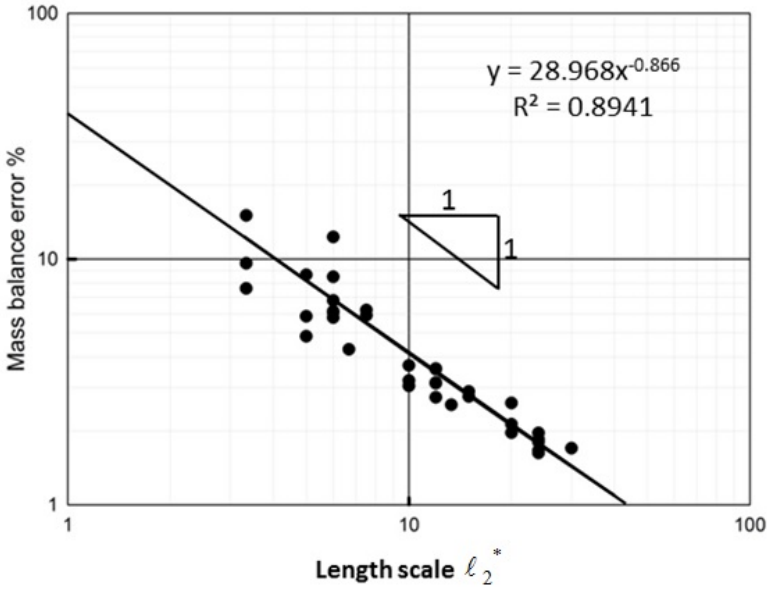

Figure 2.27: Mass balance 'error' ϵ (Eq. 2.7 based on post-processing of output data for all the cases analyzed using length scale ℓ_2^*. The 'error' is not at the level of implementation (FDS 6 conserves mass). It is an apparent error at the level of post-processing.

areas of the cell faces. This form of the mass flow is thus approximate, because the mass transport equation uses a flux limiter to define the mass advection. Thus, the output 'MASS FLOW' is not exact, which is the reason why the non-zero mass balance error is obtained.

However, considering this issue, the method as described is still useful as criterion or indicator to determine the required grid resolution in simulations where flows through opening are crucial. In other words, the ℓ_1^* or ℓ_2^* criterion must be checked in addition to the D^* criterion.

Table 2.6 illustrates once more that ϵ is not a true error in mass balance at the level of implementation (for case 24). Indeed, reducing 'velocity_tolerance' (which refers to possible errors at mesh interfaces) and increasing the maximum number of cells to the pressure solver (max_pressure_iterations) in the FDS input file, does not modify ϵ significantly.

Finally, note that the discussion of the grid convergence based on the mass balance 'error' is more informative than examining inflow or outflow rates directly. Indeed, the absolute values of such quantities depend on, e.g., the heat release rate and opening size (Figure 2.25). Consequently, relative deviations are not directly visible and moreover, in contrast to what has been presented in Figure 2.26 and Figure 2.27, only 3 values for the

Table 2.6: The effect of 'velocity tolerance' and 'max pressure iterations' on the mass balance 'error' for case 24. The 'error' is not at the level of implementation (FDS 6 conserves mass). It is an apparent error at the level of post-processing.

No.	Velocity tolerance (m/s)	Max pressure iterations (-)	$\epsilon(\%)$
1(default)	-	10	2.7308
2	0.001	100	2.7294
3	0.0001	1000	2.7280

length scale ratios can be used per case (since 3 levels of grid refinement have been used for each case).

2.2.4.2 HRR inside the enclosure

The averaged heat release rate inside the enclosure is presented in Figure 2.28. Four groups of data are observed, each of them corresponding to one value of the ventilation factor $A\sqrt{H}$. As indicated in Figure 2.28, the predicted HRR inside the enclosure HRR_{in} shows a linear correlation with the ventilation factor. The linear regression coefficient is 1130.7 kW/m$^{5/2}$.

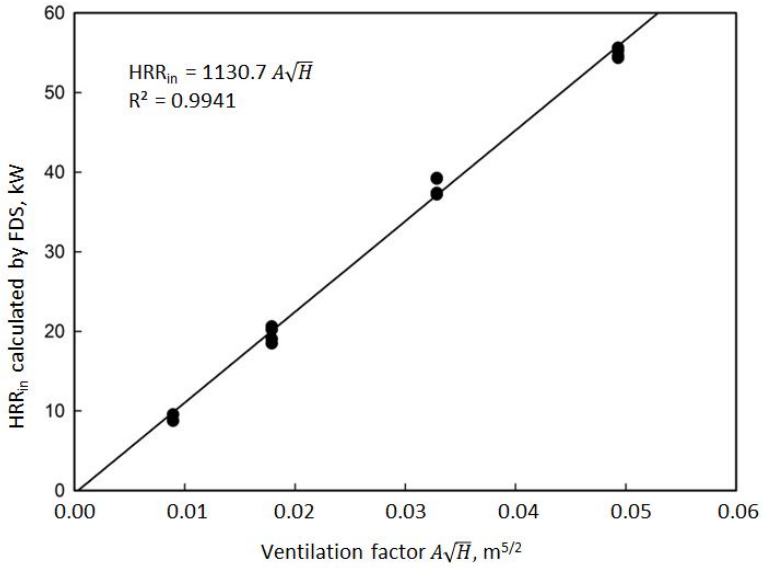

Figure 2.28: Linear correlation between the ventilation factor and predicted HRR inside the enclosure HRR_{in}.

This is approximately 25% below the value 1500 kW/m$^{5/2}$ mentioned above in the empirical correlation. The deviation is mainly related to the air inflow rate and the com-

pleteness of the use of oxygen for combustion inside the enclosure. Note that the constant coefficient C derived from the simulation is 0.41, which is lower than 0.5 (which correspond to 1500 kW/m$^{5/2}$). This should already result in an 18% lower HRR inside. The remainder can be attributed to completeness of combustion.

Indeed, not all oxygen entering the compartment is entirely consumed by the combustion. Some air is immediately entrained into the exiting flow and does not participate in the combustion. In order to illustrate this, the net mass flow rate of oxygen through the opening for case 24 is outputted and shown in Figure 2.29. The average value between 500 s and 1200 s is 0.002528 kg/s. At the same time, the average mass flow rate for air entering the compartment is 0.013910 kg/s. Oxygen mass fraction in ambient air is 0.23. Based on this, the maximum oxygen inflow rate is calculated to be 0.003231 kg/s. This is higher than the actual value 0.002528 kg/s of net oxygen flow rate. This difference implies that there is some oxygen flowing out of the compartment without participating in the combustion inside the enclosure.

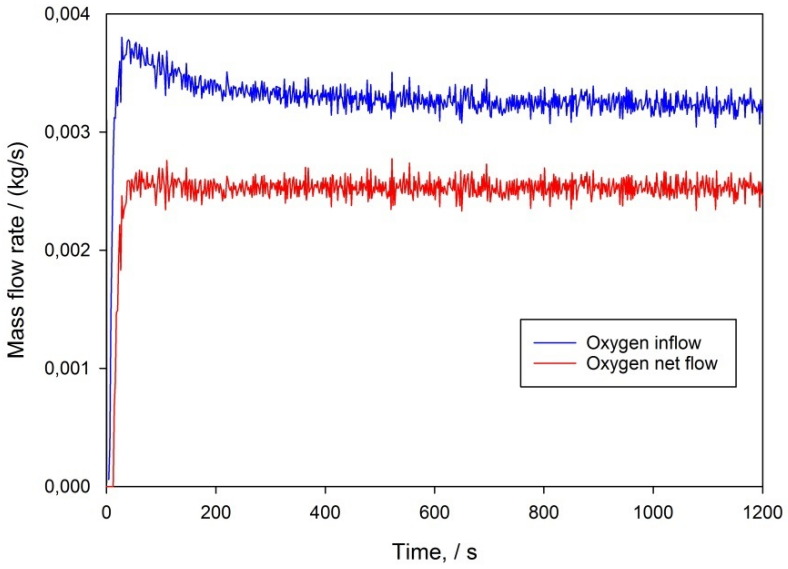

Figure 2.29: Temporal evolution of mass flow rate of oxygen through the opening for case 24 (see Table 2.1).

2.2.4.3 Gas temperature inside the enclosure

In Figure 2.30, the vertical temperature distributions are presented, obtained from two thermocouples trees at two corners of the enclosure for different opening geometries. The temperatures at two opposite corners are similar, but not identical, revealing deviations from the perfectly mixed situation. Similar observation has been made before in [64].

However, deviations are not very large, so that it is meaningful to define an average temperature inside the enclosure.

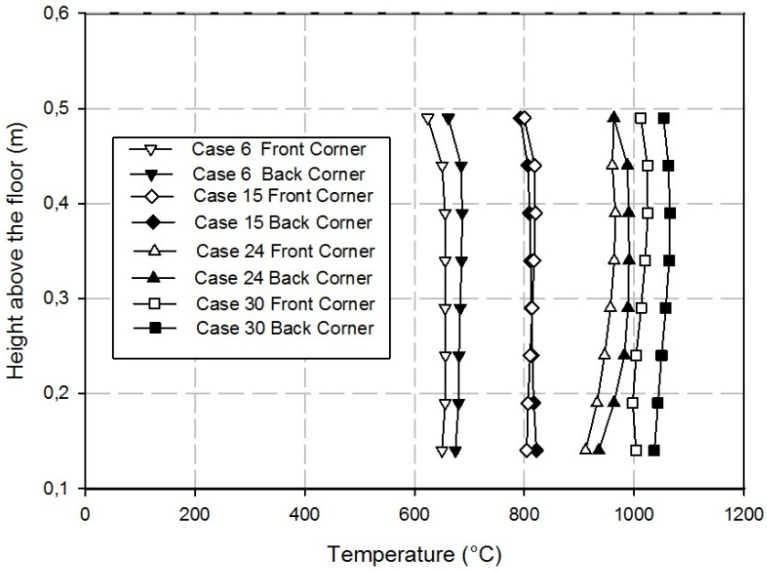

Figure 2.30: Temperature distribution inside the enclosure obtained from front and back corner thermocouple trees for four different opening geometries. Case numbers: see Table 2.5. Closed symbols refer to simulation results in the back corner, while open symbols refer to results obtained in the front corner (see Figure 2.15).

Higher temperatures are observed in Figure 2.30 for higher ventilation factors, as less excess fuel leaves the compartment and HRR_{in} increases (Figure 2.28). Babrauska's correlation [10, 11] can be used to compare with the simulation results of the average temperature inside the enclosure:

$$T_g = T_\infty + (T^* - T_\infty) \cdot \theta_1 \cdot \theta_2 \cdot \theta_3 \cdot \theta_4 \cdot \theta_5 \tag{2.9}$$

In Eq. 2.9, T^* is an empirical constant, set equal to 1725 K, and five factors account for different physical phenomena: the burning rate stoichiometry θ_1, the wall steady-state losses θ_2, the wall transient losses θ_3, the opening height effect θ_4, and the combustion efficiency θ_5.

The five factors in correlation 2.9 can be determined from the material properties and the other parameters used in the simulation. Figure 2.31 shows the comparison between the predicted average temperatures and correlation 2.9. The relative differences are below 10% for all scenarios.

In Table 2.7, the time-averaged gas temperatures at the front corner are compared

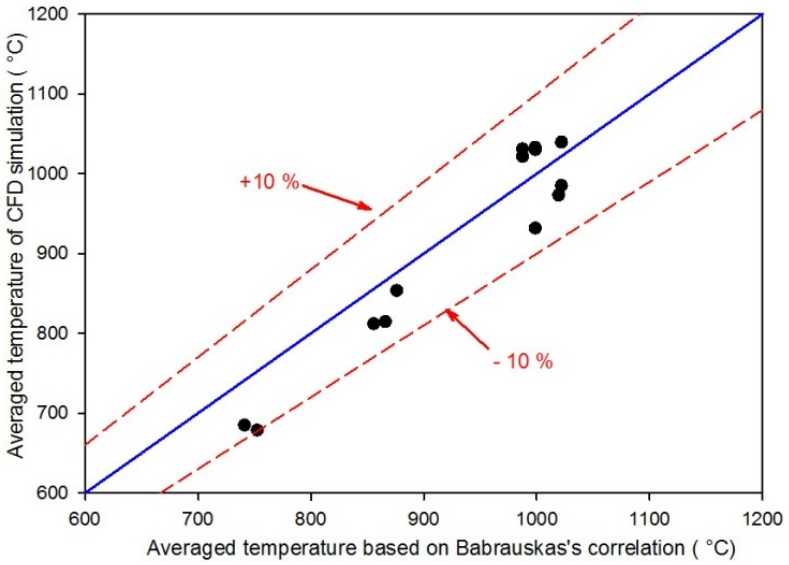

Figure 2.31: Comparison of average temperatures obtained with FDS to correlation 2.9 [10, 11].

with experimental data for cases 8, 11, 31 and 32, which correspond to an opening size of 0.2 m x 0.2 m. As indicated in Figure 2.32, the gas temperatures at heights of 10 cm or more above the floor are approximately uniform. The deviations from the average value are presented in this table as well.

Table 2.7: Comparisons of gas temperatures in simulations and experiments for opening size of 0.2 m x 0.2 m.

Case No.	HRR_{total}(kW)	$T_{exp}(°C)$	$T_{sim}(°C)$	$(T_{exp}\text{-}T_{sim})/T_{exp}(\%)$
11	60	967 $\pm$ 16.4	842.1 $\pm$ 12.6	12.9
8	50	946 $\pm$ 19.0	823.1 $\pm$ 11.6	13.0
31	40	928 $\pm$ 6.6	805.7 $\pm$ 11.7	13.1
32	30	900 $\pm$ 5.9	799.9 $\pm$ 3.4	12.0

In general, the simulation results under-predict temperature, but deviations are less than 13.1%. This is not surprising, taking into account the possible under prediction of heat release rate inside the enclosure as mentioned above. Also this could be related to the fact that no radiation correction has been performed on the experimental data.

2.2.4.4 Flame heights outside the enclosure

In [68], the neutral plane height is estimated to be at a distance $0.4H$ from the bottom of the opening, with H the opening height. Figure 2.33 presents the comparison of the

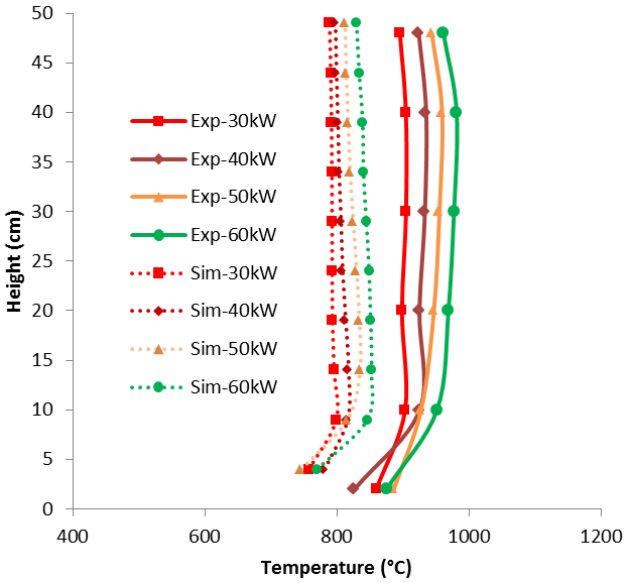

Figure 2.32: Comparison of average temperatures obtained with FDS to experimental data for cases 8, 11, 31, and 32 (see Table 2.5).

neutral plane heights obtained from the simulation to the value from empirical estimations ($0.4H$). Agreement is clearly good (deviations less than 5%).

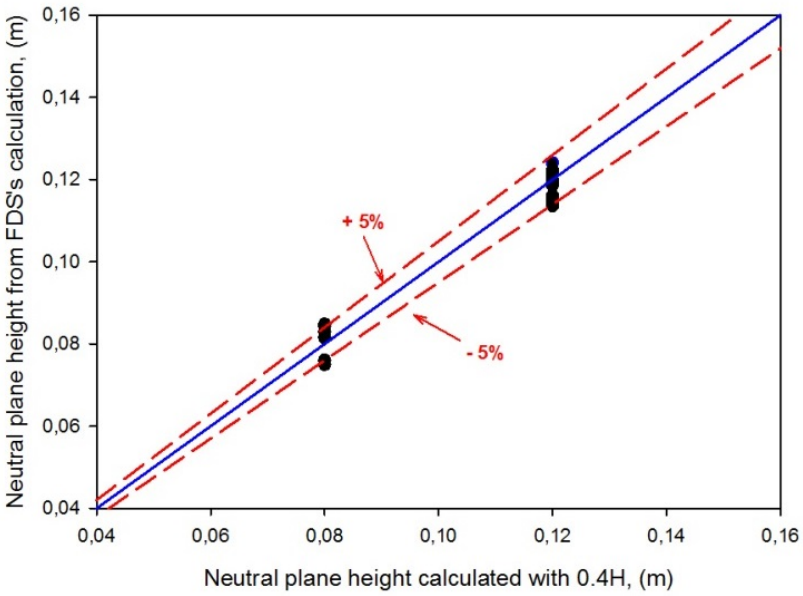

Figure 2.33: Comparison of neutral plane height as obtained from the simulation to the neutral plane height from empirical estimations ($0.4H$) [59]

As mentioned in section 2.2.3, a temperature based method has been used in the post-processing of the simulation results to determine the flame height. Typically temperature

differences ranging between 500 K to 600 K are used in the literature [63]. In order to check the sensitivity of the flame height obtained from the simulation on the chosen value for the reference temperature, three reference temperature values have been considered, namely $T = 520°C$, $T = 570°C$, and $T = 600°C$. Results for cases 8, 11, 31, and 32 are presented in Table 2.8. Note that the flame height is calculated from the neutral plane height.

For the same ventilation factor, the amount of fuel consumed inside the enclosure should remain approximately the same. For a higher total HRR, more excess fuel will burn outside, and a higher flame height value is expected. This is confirmed in the results: regardless of the method used, the flame height value increases with the fire HRR. When using a reference temperature of $T = 520°C$ for the flame tip, FDS over-predicts the external flame height with a maximum relative deviation of about 17.85%.However, the predicted flame height is very sensitive to the choice of the reference temperature for the flame tip. When using a $T = 570°C$ as reference temperature, the predictions for these four cases show good agreement with the experimental results(with a maximum relative deviation 6%). While using a $T = 600°C$ as reference temperature, FDS under-predicts the flame height with a relative deviation up to 42%.

Considering that the height of the flame ejected is mainly determined by two factors, namely the amount of excess fuel and the opening geometry of the enclosure, Lee proposed the following expression for external flame height z_f in [5, 6]:

$$\frac{Z_f}{\left(A\sqrt{H}\right)^{2/5}} = fcn\left[\dot{Q}_{\ell_1}\right] = fcn\left[\frac{\dot{Q}_{ext}}{\rho_\infty C_\infty T_\infty \sqrt{q} A\sqrt{H}}\right] \tag{2.10}$$

where $\dot{Q}_{ext}$ is the external HRR, calculated as $\dot{Q}_{ext} = \dot{Q} - \dot{Q}_{in}$. The external flame height was recorded in [5, 6] by a CCD camera facing the façade. The flame tip was defined as the height where the flame presence probability is 50%. The flame height was measured from the neutral plane level at the opening, which is located at an approximate distance of $0.4H$ from the bottom of the opening [68].

Eq. 2.10 and length scale $\left(A\sqrt{H}\right)^{2/5}$ are used to analyze the flame height values obtained from FDS. In Figure 2.34, the crosses denote the experimental data, while the black dots represent the predicted simulation data. The trend line for all the simulation data, shown as a solid line, has a slope of $2/3$ in this logarithmic scale plot: the power dependence for flame heights on the excess heat release rate is $2/3$, which is similar to

Table 2.8: Comparison of flame height between simulation and experiment for opening size of 0.2 m x 0.2 m.

Case	HRR_{tot} (kW)	Z_{exp} (m)	$Z_{sim-520}$ (m)	$Z_{sim-570}$ (m)	$Z_{sim-600}$ (m)	ϵ_{520} (%)	ϵ_{570} (%)	ϵ_{600} (%)
11	60	0.70	0.81	0.7	0.65	15.71	0.18	40.34
8	50	0.56	0.66	0.59	0.51	17.85	6.13	33.77
31	40	0.40	0.46	0.41	0.37	15.00	2.72	36.20
32	30	0.34	0.37	0.31	0.28	8.82	5.40	42.86

what is observed for wall fires [69,70]. For large flame heights, the predictions show good agreement with the experimental data, while some under-prediction is observed for smaller flame heights.

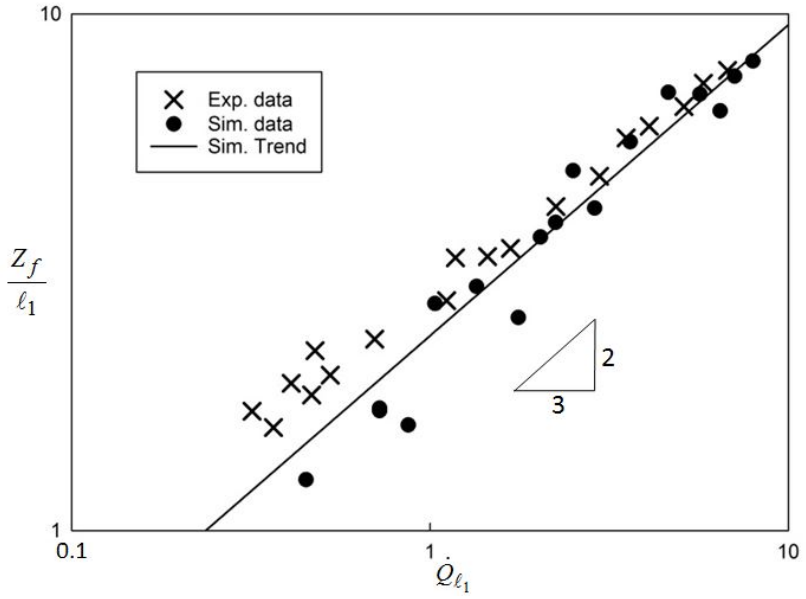

Figure 2.34: Comparion of flame heights obtained with FDS based on the temperature reference ($520°C$) method to experimental data using correlation Eq. 2.10.

2.2.5 Conclusions

Numerical simulations of under-ventilated enclosure fires with external flaming have been discussed. FDS, version 6.0.1, has been applied with the default settings. Four different opening geometries are considered: 0.1 m x 0.2 m, 0.2 m x 0.2 m, 0.2 m x 0.3 m, and 0.3 m x 0.3 m. There are 32 simulations in total. The accuracy of the results obtained has been discussed, comparing to experimental data [5,6] and empirical correlations.

Due to the importance of the flow through the opening, the required fineness of the grid has been discussed by analyzing the mass balance 'error' based on post-processing of the output data. Two length scale ratios have been formulated, in addition to the classical D^* criterion for the fire source. The first ratio is the ventilation factor to the grid cell size $\ell_1^* = \left(A\sqrt{H}\right)^{2/5}/\delta_x$, while the second is the ratio of the hydraulic diameter of the opening to the grid cell size $\ell_2^* = D_h/\delta_x$. When these two length scales are larger than 10, the corresponding mass balance error is lower than 4%. The results in terms of velocities through the door opening and temperature in the door opening are then grid insensitive.

The air inflow rate through the opening is found to correlate linearly to the ventilation factor as $\dot{m} = c \cdot A\sqrt{H}$. The obtained c value is 0.41 which is at the low end of the range 0.4-0.6 found in the literature [2] .The heat release rate inside the enclosure obtained from FDS show a linear relationship with the ventilation factor. The linear regression coefficient is 1130.7 $kW/m^{2.5}$, which is lower than the 'classical' value 1500 $kW/m^{2.5}$. This has been explained through the lower mass flow rate of incoming air and incomplete consumption of oxygen flowing into the compartment. There is also some uncertainty at the level of the experimental data, since the HRR inside the enclosure could not be measured directly.

The temperature predictions show that: (1) the temperature at back and front opposite corners are not identical, but a meaningful average temperature inside the enclosure can be defined, (2) the such obtained average gas temperatures inside the enclosure deviate less than 10% from Babrauska's correlation [10, 11] for the different opening geometries.

FDS has been shown to accurately reproduce the neutral plane height for the various configurations. A temperature based method was employed to define the external flame height. The external flame height is over-predicted when using a reference temperature $T = 520°C$ for the flame tip. The predicted flame height is very sensitive to the choice of the reference temperature for the flame tip. When using a $T = 570°C$ as reference temperature, the predictions for these four cases show good agreement with the experimental results(with a maximum relative deviation 6%). While using a $T = 600°C$ as reference temperature, FDS under-predicts the flame height with a relative deviation up to 42%. The flame height value increases with the fire HRR. The power dependence of the flame height on excess heat release rate is $2/3$.

Chapter 3

Coupling of pyrolysis and combustion – Small-scale Tests

3.1 Introduction

As is mentioned in Chapter 1, a step-wise approach has been employed to study the flame spread. In this chapter, the simulation results of the solid phase and gas phase reactions in small scale are discussed.

In the configuration of flame spread along a vertical combustible wall, thermal radiation of gas-phase combustion products drives the pyrolysis process by heating the unpyrolyzed material surface to pyrolysis temperature. Therefore, a better understanding of the burning behaviour of a material exposed to external radiation is required. A lot of effort has been devoted to study the burning behaviour of both charring and non-charring materials in the literature [27, 40, 71–73]. It has been demonstrated that numerical methods are suitable to predict the mass loss rate and burning rate for non-charring materials. However, the predicted results highly depend on the value of the input parameters, which include the thermal properties of the material and other parameters used in the pyrolysis model (e.g. kinetic parameters).

In this chapter we present numerical simulations of MDF pyrolysis using a one-dimensional heat transfer solver that includes in-depth radiation. A one-step finite rate reaction is assumed; the virgin material is converted to char and the rest is released as pyrolysate. The values of the kinetic parameters and char yield are estimated from Thermogravimetric Analysis (TGA) test results reported in [71]. The thermal properties of virgin MDF and char are taken from the literature. More details on the pyrolysis model are provided in the numerical model section.

The goal of the study in this chapter is to predict the burning behaviour of MDF, with an emphasis on the potential importance of inclusion of the non-uniform mass density profile, and in-depth radiation modeling. The numerical simulation tool used in this study is the Fire Dynamics Simulator (FDS 6.2.0) [74]. The physical processes occurring in the solid phase are solved as a one-dimensional problem with a one-step pyrolysis model. The input parameters include the material properties, kinetic parameters (e.g. pre-exponential factor and activation energy) properties and boundary conditions. A sensitivity analysis is conducted to study the influence of these input parameters on the burning behaviour of MDF. This chapter is based on publication [75].

3.2 Pyrolysis modelling

3.2.1 Pyrolysis test set-up

Small scale tests have been conducted by FM Global in the Fire Propagation Apparatus (FPA) [27]. The MDF sample used in these tests is manufactured by SPANOLUX [76]. Figure 3.1 shows the schematic of this configuration. The back side of the sample is actually insulated with Cotronics ceramic paper, which has a relatively low thermal conductivity (0.028 W/(m·K)). That is why an adiabatic boundary condition is used in the numerical simulations. The dimensions of the sample are 80 mm x 80 mm x 18.4 mm (height).

The tests have been conducted in nitrogen atmosphere in order to eliminate uncertainties related to gas-phase combustion. During these tests, the mass loss rate, surface and back side temperatures have been measured under three constant external heat fluxes, namely 25, 50, and 100 kW/m^2. More details can be found in reference [27].

3.2.2 Numerical models

As mentioned in the introduction, numerical techniques have been employed in this study. In this section, the numerical model and input parameters will be discussed in detail.

3.2.2.1 Pyrolysis model

The pyrolysis process is simplified as a one-step finite rate reaction. Only three species are treated here, namely the virgin solid, char, and pyrolysate. For the solid reaction, the

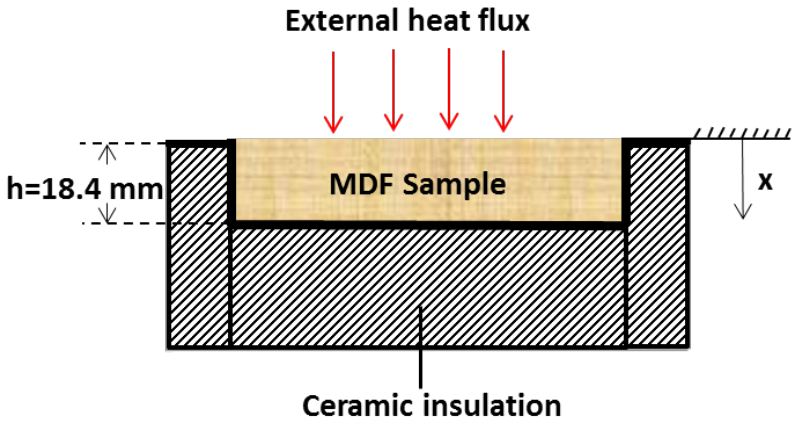

Figure 3.1: Schematic of the MDF sample in FPA test.

virgin is converted to char and releases pyrolysate, as shown in the following reaction.

$$Virgin \rightarrow (1-v_c)Pyrolysate + v_c Char \tag{3.1}$$

where v_c is the yield of char. Since neither shrinkage nor swelling is modelled here (i.e., constant volume), the yield of char can be calculated as $v_c = \rho_c/\rho_v$, where ρ_v and ρ_c are the densities of respectively the virgin and the char.

With this one-step pyrolysis model, the pyrolysis rate of the sample is calculated using a temperature-dependent Arrhenius expression. The mass conservation equations for virgin and char are expressed as follows:

$$\frac{\mathrm{d}Y_v}{\mathrm{d}t} = -AY_v \exp\left(-\frac{E}{RT}\right) \tag{3.2}$$

$$\frac{\mathrm{d}Y_c}{\mathrm{d}t} = -v_c \frac{\mathrm{d}Y_v}{\mathrm{d}t} \tag{3.3}$$

where Y_v and Y_c are the mass fractions of virgin and char respectively. The initial value of the virgin mass fraction $Y_{v,0}$ is equal to 1. T is the temperature (in Kelvin) within the solid. R is the universal gas constant, 8.314 J/(mol·K) . A is the Arrhenius pre-exponential factor, with units of s^{-1}. E is the activation energy, with units of kJ/kmol.

It should be noted that the kinetic parameters are not available for most real materials. In practice, the values of A, E and v_c can be obtained from bench-scale measurements like TGA under an inert atmosphere. These measurements consist of heating the sample at a fixed rate, $\dot{T}$, and measuring the residual mass and the reaction rate (in s^{-1} or min^{-1}) as a function of the temperature (see example in Figure 3.2).

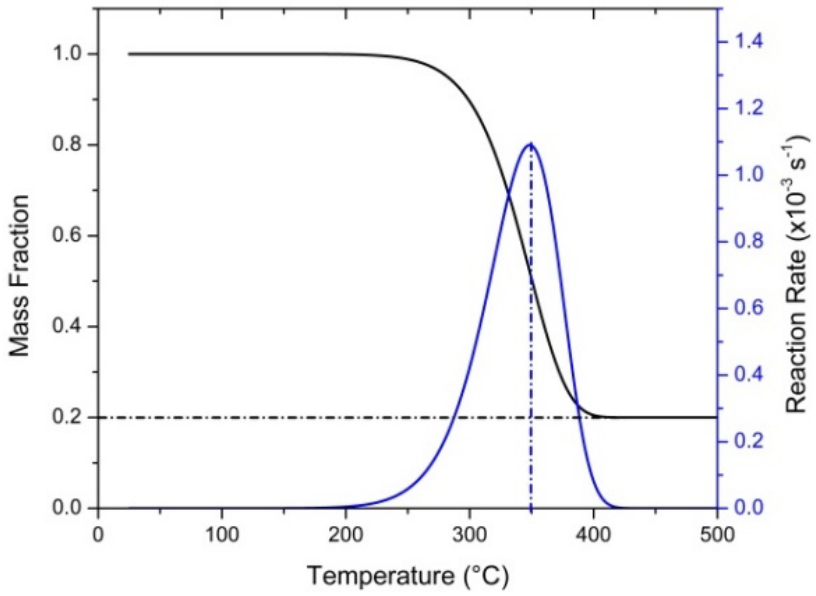

Figure 3.2: Typical TGA results for MDF pyrolysis at a heating rate of $\dot{T} = 5K/min$[71]. (a) black line represents the normalized residual mass (b) blue line represents the reaction rate

The results in Figure 3.2 show a residual mass of 21% at high temperatures. This indicates that we can take $v_c = 0.21$. The peak reaction rate $\gamma_p = 0.0011s^{-1}$ occurs at a temperature T_p=350°C. The blue curve in Figure 3.2 can also be characterised by a pyrolysis range ΔT, which is the approximate width of this curve (in degree Celsius or Kelvin). Assuming a triangular shape for the curve, this width can be estimated as [74]:

$$\Delta T = (1 - v_c) Y_{v,0} \frac{2\dot{T}}{\gamma_p} \tag{3.4}$$

Based on the obtained value of T_p, ΔT and v_c from TGA tests, the kinetics parameters E and A can be estimated as below:

$$E = \frac{2e(1 - v_c) R T_p}{\Delta_T} \tag{3.5}$$

$$A = \frac{e\gamma_p}{Y_{v,0}} \exp\left(\frac{E}{RT_p}\right) \tag{3.6}$$

In this work, the estimated values for A and E are 358000 s^{-1} and 89100 kJ/kmol respectively.

3.2.2.2 Heat transfer

The 1-D heat transfer equation, which accounts for the in-depth radiation absorption with an energy source term, reads:

$$\rho c_p \frac{\partial T}{\partial t} = \frac{\partial}{\partial x}\left(k\frac{\partial T}{\partial x}\right) + \dot{q}'''_{s,c} + \dot{q}'''_{s,r} \tag{3.7}$$

where ρ, c_p and k are respectively the density, specific heat and conductivity of the solid. The variables $\dot{q}'''_{s,c}$ and $\dot{q}'''_{s,r}$ denote respectively a chemical and a radiative source term. Eq. 3.7 is solved using a uniform mesh with a cell size $\Delta x = 0.376mm$. The second order central differences scheme is employed as discretization method for the diffusion terms. The same time step as in the gas phase is employed in the solid phase.

The chemical source term $\dot{q}'''_{s,c}$ is modelled using an Arrhenius expression:

$$\dot{q}'''_{s,c} = -\rho_v A Y_v \exp\left(-\frac{E}{RT}\right) H_p \tag{3.8}$$

where H_p is the heat of reaction in kJ/kg. A positive value of H_p means that the pyrolysis reaction is endothermic, while a negative value of H_p means that the reaction is exothermic.

The radiative absorption term $\dot{q}'''_{s,r}$ is a function of absorption coefficient (κ) and emissivity (ϵ) . For an opaque material, the thermal radiation is absorbed within an infinitely thin layer at the solid surface, and the corresponding absorption coefficient is infinitely large. For some other materials the radiation can penetrate to some finite depth, and the absorption coefficient value is smaller than infinity.

In order to solve the radiative absorption term in the heat conduction equation, a two-flux model is employed in FDS. This model is based on the Schuster-Schwarzschild approximation [77], which assumes that the intensity is constant inside the 'forward' and 'backward' hemispheres. Accordingly, the radiative source term $\dot{q}'''_{s,r}$ is taken as the sum of the 'forward' $\dot{q}^{+}_{r}(x)$ and 'backward' $\dot{q}^{-}_{r}(x)$ flux gradients.

$$\dot{q}'''_{s,r(x)} = \frac{\mathrm{d}\dot{q}^{+}_{r(x)}}{\mathrm{d}x} + \frac{\mathrm{d}\dot{q}^{-}_{r(x)}}{\mathrm{d}x} \tag{3.9}$$

The forward radiative heat flux into the solid is computed as follows:

$$\frac{\mathrm{d}\dot{q}^{+}_{r}(x)}{\mathrm{d}x} = 2\kappa\left(\sigma T^4_{(x)} - \dot{q}^{+}_{r}(x)\right) \tag{3.10}$$

A similar formula can be given for the 'backward' direction. The boundary condition for $\dot{q}_r^+(x)$ at the solid surface is given by:

$$\dot{q}_r^+(0) = \epsilon \dot{q}_e^{''} + (1-\epsilon)\dot{q}_r^-(0) \tag{3.11}$$

The boundary condition at the front surface of the solid reads:

$$-k\frac{\partial T}{\partial x}\Big|_{x=0} = \epsilon \dot{q}_e^{''} - \dot{q}_c^{''} - \epsilon\sigma\left(T_s^4 - T_\infty^4\right) \tag{3.12}$$

On the right hand side, $\dot{q}_e^{''}$ is the incident heat flux, $\dot{q}_c^{''}$ is the convective heat flux. It is calculated with the following expression:

$$\dot{q}_c^{''} = h(T_s - T_\infty) \tag{3.13}$$

where T_s and T_∞ are the surface temperature of the solid and the temperature of the surrounding air; h is the convective heat transfer coefficient, which is calculated based on a combination of natural and forced convection correlations.

3.2.2.3 Boundary condition

The surface opposite the exposed face in the experiment, referred to here as the back side, is simulated as a second layer according to the properties of insulation materials or as different boundary conditions available in FDS, which are discussed later.

For the FPA test, a ceramic blanket was used as insulation material, as is shown in Figure 3.1. The material properity of the used ceramic blanket is listed in Table 3.1. In the numerical model, this was implemented using one extra layer behind the sample layer, using the mentioned properities of the insulation material.

Table 3.1: Material properties of the cotronics ceramic at the back-side in the FPA test.

Property	Value
Density	167.67 kg/m^3
Specific heat	1.05 kJ/(kg·K)
Thermal conductivity	0.054 W/(m·K)(Below 260°C))
	0.086 W/(m·K) (260-537°C)
	0.129 W/(m·K) (537-815°C)
	0.191 W/(m·K) (815-1093°C)

3.2.3 Thermal properties

The properties of MDF and the model parameters will be discussed in this section, including the density, thermal conductivity, specific heat, heat of pyrolysis, emissivity, and the absorption coefficient. In general, determining these parameters is challenging due to their dependency on temperature, test conditions, and uncertainties related to the measurement method.

3.2.3.1 Densities of virgin MDF and char

It has been reported in the literature [27,76,78,79] that the density of the MDF is not uniform along the thickness of the sample (Vertical Density Profile (VDP)), mainly due to the hot-processing operation during its manufacturing. In general, the surface density is considerably higher than the core density. Gupta [80] provided a set of experiment data showing that the vertical density profile of a Newzealand MDF is in a parabolic shape (see Figure 3.3). In this case, the mean density is 632 kg/m^3 which is close to that of the considered MDF (605 kg/m^3). The peak density at the surface is 950 kg/m^3, the lowest density is 516 kg/m^3.

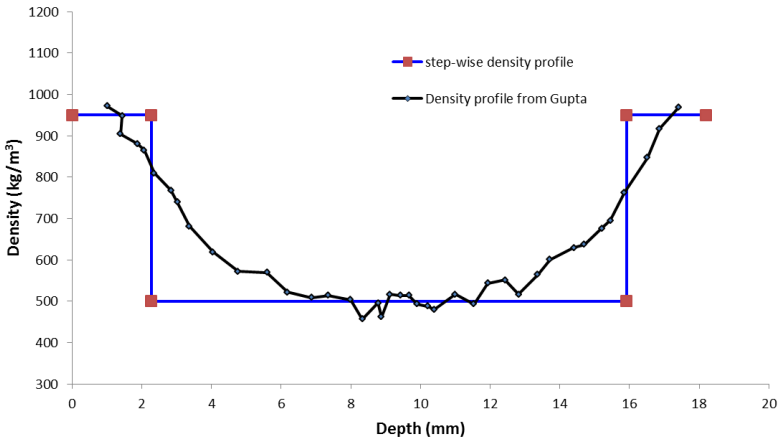

Figure 3.3: Through-thickness density profile of a newzealand MDF by Gupta [80] and the density profile employed in the model.

As shown in the Figure 3.4, there are two denser layers at two surfaces of the sample. The thickness of each layer is measured to be around 2.3 mm.

In the numerical model, a step-wise density profile has been employed to mimic the parabolic density profile. In FDS, the solid can be represented with different layers, and each of the layers having its thermal properties can undergo reactions. For the non-uniform density case, 3 layers have been used to represent the sample (see Figure 3.3 and

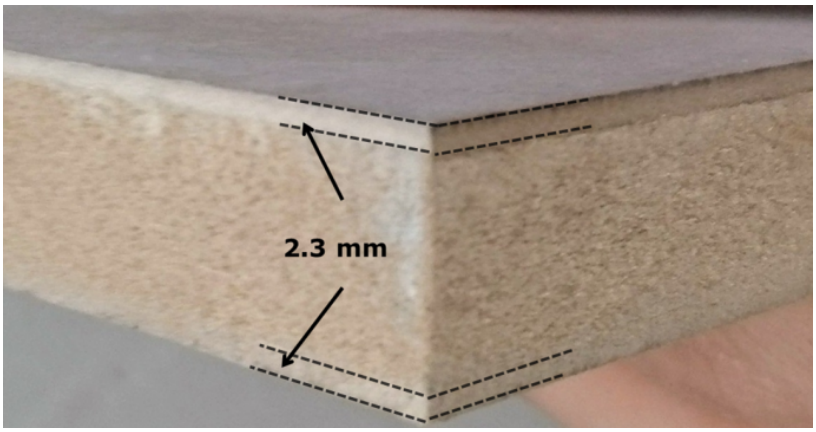

Figure 3.4: Denser layers at the two surfaces of the sample.

Table 3.2). The minimum value is 500 kg/m^3, i.e. at the core of the sample, while the maximum value is 950 kg/m^3, i.e, at the front and back surface. The global mass density is kept the same as the one in the uniform density calculations.

The density of char was calculated based on the assumption that the volume of the solid sample is fixed during the burning process. Considering a value of 0.21 for the char yield [71], a char density of 127 kg/m^3 is approximated.

Table 3.2: Details of the step-wise through-thickness density profile

Parameter	Virgin Density	Char Density	Thickness(mm)	Char Fraction (%)
Layer 1	950	127	2.3	13.4
Layer 2	500	127	13.7	25.4
Layer 3	950	127	2.3	13.4

3.2.3.2 Thermal conductivity

Wood material is an anisotropic material, whose termal conductivity is a function of temperature, density, and moisture [81]. Although the thermal conductivity depends on time-varying temperature and the local density, constant values (effective thermal conductivity) are still widely used in pyrolysis models (for example [82–84]). Here, taking the range of 0.08 to 0.41 W/(m·K) for wood material as reference [85], an effective thermal conductivity of 0.25 W/(m·K) is suggested by [81] for wood at room temperature. The same value is employed for MDF in the basis case. This is an important choice and better choices could be made by conducting a sensitivity analysis study.

The char thermal conductivity of MDF should be similar as that of softwood, since their densities are similar. In [86, 87], the value for wood char is reported within a range

of 0.05 to 0.18 W/(m·K) for temperatures between 300 K and 873 K. Since for the most time during the pyrolysis process, the sample temperatures range from 700 K to 1000 K, a constant value of 0.18 W/(m·K) is considered appropriate.

3.2.3.3 Specific heat capacity

The specific heat capacity of wood based materials depends on the temperature and moisture content of the material, but is independent of density and species [88]. As summarized in the literature [81], one can find that the specific heat capacity of pyrolysing wood is approximately 1.25 kJ/(kg·K) at room temperature, increasing approximately to 1.9 kJ/(kg·K) as the temperature increases to 523 K. Wood converts to char at temperature range 523 K-673 K. The specific heat capacity decreases to 1.5 kJ/(kg·K) by 673 K. As the temperature increases further from 673 K the specific heat capacity increases slightly to 1.75 kJ/(kg·K) at 1083 K.

According to a literature survey by Gronli [85], specific heat capacities used for unreacted wood material in pyrolysis models vary from 1.5 to 2.5 kJ/(kg·K), whereas Gupta et al.[87] report that values from 0.7 to 2.5 kJ/(kg·K) have been used. Karkkainen report that the specific heat capacity for an absolutely dry wood is 1.34 kJ/(kg·K) at temperature range of 273 K - 373 K [89]. In this study, a constant value of 1.34 kJ/(kg·K) is considered for the base case.

The reported values in the literature for specific heat capacity of wood char range from 0.67 to 1.35 kJ/(kg·K) at room temperature [85]. If the temperature increases up to a range of 523 K - 673 K, the specific heat capacity can increase up to 1.9 kJ/(kg·K). Here, the constant value of 1.75 kJ/(kg·K) is used.

3.2.3.4 Heat of pyrolysis

The heat of wood pyrolysis reported in the literature [90] ranges from endothermic (370 kJ/kg) to large exothermic values (-1700 kJ/kg), depending on the experimental conditions. The heat of pyrolysis is not available for MDF used in this study. Here a value of 0 kJ/kg is first considered and other possible values will be discussed in the sensitivity study.

3.2.3.5 In-depth radiation parameters

The values for the emissivity and absorptivity are assumed to be the same in FDS by default. It has been reported in [40] that the effective emissivity of virgin material is a function of temperature. For a temperature range up to 1500 K, the corresponding

emissivity ranges from 0.6 to 0.9. The effective emissivity of char, as reported in [40], is approximately 0.86 and relatively independent of temperature over a wide temperature range (300-3000 K). In the base case, values of 0.86 for both the virgin and char emissivity have been used.

In-depth absorption of radiation has been reported to have a large influence on the burning behaviour of non-charring materials such as PMMA (Polymethylmethacrylate) [91,92]. However, the influence on the burning behaviour of charring materials (e.g.,wood-based products) has not been extensively studied, presumably because opaque conditions are assumed. Nevertheless, in the case of cracks or delamination, in-depth-like radiation absorption may occur.

In this chapter, we are also exploring this idea of using the in-depth radiation in the pyrolysis modelling of MDF.The absorption coefficient of MDF, κ, has been hardly mentioned or discussed in the literature for wood. However, for polymeric materials such as PMMA, it has been investigated in the literature. In [73] a wide range of possible values for κ (from 333 m^{-1} to 2000 m^{-1}), is examined for black PMMA. In our study, first the default FDS value of 50000 m^{-1} is considered for both the virgin material and char, which is deemed suitable for opaque materials. As a consequence, the in-depth radiation is effectively not considered in the equations. Table 3.3 shows the summary of input parameters used in the base case.

Table 3.3: summary of input parameters for base case as well as the 'updated' case.

Parameter	Unit	Base case	'updated' case	Range
Density of virgin MDF	kg/m^3	605	non-uniform	-
Density of char	kg/m^3	127	127	-
Residual fraction	-	0.21	0.21	-
Moisture content	%	0	6	-
Heat capacity of virgin MDF	kJ/(kg·K)	1.34	1.58	[0.67, 2.5]
Heat capacity of char	kJ/(kg·K)	1.75	1.45	[0.67, 1.9]
Conductivity of virgin MDF	W/(m·K)	0.25	0.30	[0.08, 0.41]
Conductivity of char	W/(m·K)	0.18	0.18	[0.05, 0.18]
Emissivity of virgin MDF	–	0.86	0.6	[0.6, 0.9]
Emissivity of char	–	0.86	0.86	-
Heat of pyrolysis	kJ/kg	0	0	[-1700, 370]
Reaction order	–	1	1	-
Pre-exponential factor	s^{-1}	358000	358000	-
Activation Energy	J/mol	89100	89100	-
Absorption coefficient for virgin	m^{-1}	50000	2000	-
Absorption coefficient for char	m^{-1}	50000	50000	-

First, the values for input parameters in Table 3.3 are applied in the simulations, which is the base case simulation. These results of this simulation case, including mass loss rate and front surface temperature, are presented in the following section.

Moreover, a sensitivity study has been conducted for the different model parameters, namely, for the thermal conductivity, specific heat capacity, heat of pyrolysis, emissivity, through-thickness density profile, and absorption coefficient. Consequently, a set of 'updated' parameters have been determined through a simple trial and error procedure, shown in Table 3.3 as the 'updated' parameters.

3.2.4 Base case results

3.2.4.1 Mass loss rate

The mass loss rate results are presented in Figure 3.5(a) - 3.5(c). Three external heat flux values have been considered, namely 100, 50, and 25 kW/m^2.

There are two peaks in the mass loss rate curves for different external heat flux values. The first peak arises due to a high temperature reached at the surface. After the pyrolysis process, a char layer is formed at the surface of the sample. This insulating char layer decreases the gasification rate. As a result, the mass loss rate drops to a lower level. The second peak is mainly due to the heat accumulation at the back side.

The simulated values for the first peak are significantly lower than the measured values with relative deviations of about 21%, 50% and 63% for respective heat flux exposures of 25, 50, and 100 kW/m^2 . Furthermore, the time to reach the first peak is shorter in the predicted profiles by about 34 s, 107 s and 381 s for respective heat flux exposures of 25, 50, and 100 kW/m^2. Deviations are particularly pronounced for the lower external heat flux value (25 kW/m^2). One possible reason could be that the one-step reaction is too strong a simplification for the complex phenomena taking place during the pyrolysis process. The consequence of possible shortcomings in the chemistry is expected to be more pronounced as the pyrolysing zone occupies a larger volume in the material, which is the case for lower heat fluxes. Figure 3.5(d) illustrates this, showing the through-thickness temperature evolution for heat flux values of 100 and 25 kW/m^2 . The thickness in the solid occupied by temperature range [200$^\circ C$-400$^\circ C$], corresponding to the pyrolysing zone (Figure 3.2), is indeed much wider for 25 kW/m^2 than for 100 kW/m^2 (0.0081 m and 0.0022 m respectively).

In order to quantitatively indicate the difference between the experimental data and the predicted results, the time, t_p , to reach the peak, as well as the value of the peak,

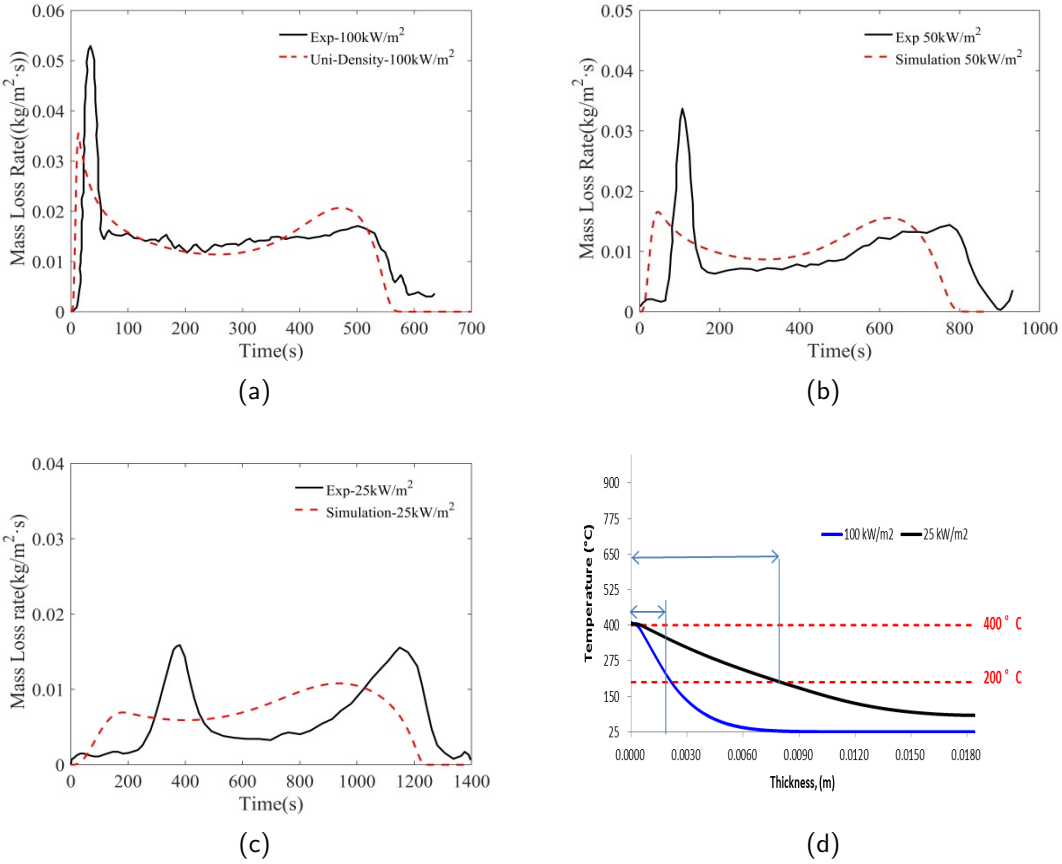

Figure 3.5: Comparisons between experimental data and predicted results for (a) MLR at 100 kW/m^2 , (b) MLR at 50 kW/m^2 (c) MLR at 25 kW/m^2 and (d) through-thickness temperature at exposures of 100 and 25 kW/m^2.

$\dot{m}_p$, are listed in Table 3.4. For the time to reach the peak MLR, the predicted values are much smaller than the experimental results, namely by about 50% to 65%. For the value of the peak, larger deviations are observable for lower heat flux exposures.

3.2.4.2 Front temperature

The experimental and simulated results for the surface temperature are shown in Figure 3.6. The temperatures are overpredicted during the initial heating-up period, roughly in the first 70 s, 130 s, and 400 s at heat flux exposures at 100, 50, and 25 kW/m^2 . This is in accordance with the MLR results displayed in Figure 3.5. After the initial heating-up period, the temperature results for the heat flux exposures at 100 and 50 kW/m^2 cases are well predicted. However, the temperature at the end of the 25 kW/m^2 case is slightly underpredicted.

Table 3.4: Characteristic values of t_p and $\dot{m}''_p$ from the experiments and the predictions with FDS.

Cases	$t_{p-exp}(s)$	$t_{p-sim}(s)$	ϵ_{tp}	$\dot{m}''_{p-exp}(kg/(m^2s))$	$\dot{m}''_{p-exp}(kg/(m^2s))$	ϵ_{mp}
100 kW/m^2	34.3	12.0	-65.0%	0.052	0.041	-21.1%
50 kW/m^2	106.8	40.8	-61.8%	0.034	0.017	-50.0%
25 kW/m^2	380.8	186.0	-51.1%	0.016	0.006	-62.5%

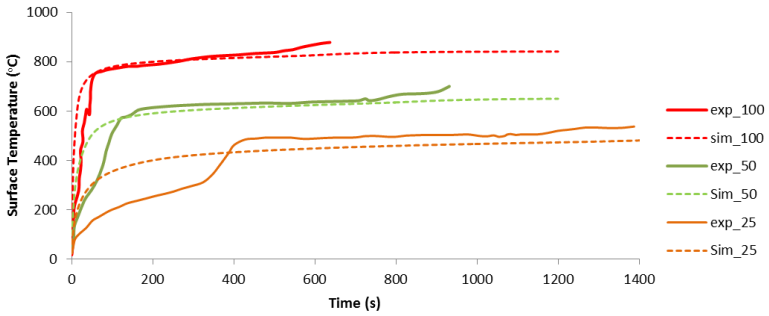

Figure 3.6: Surface temperature comparison between the experiment and simulation for three heat flux exposures.

3.2.5 Influence of input parameters

A sensitivity analysis has been conducted to check the influence of the input parameters on the burning behavior. These parameters include the thermal properties of MDF, namely the conductivity, the specific heat capacity, the heat of reaction, moisture content, emissivity, and the absorption coefficient. The range of these parameters has been determined based on the values reported in the literature, while the applied external heat flux is 50 kW/m^2.

3.2.5.1 Influence of specific heat capacity

A sensitivity analysis has been conducted for evaluating the influence of the specific heat capacity. Three values have been investigated, namely 1, 1.5, and 2 kJ/(kg.K). The results are illustrated in Figure 3.7. With a higher specific heat capacity, more time is required to reach the first peak (e.g., 14% difference between 1.5 and 2 kJ/(kg.K). Furthermore, the peak value is significantly lower (e.g., 28% difference between 1.5 and 2 kJ/(kg.K). Moreover, the front surface temperature for the higher specific heat capacity case is lower than that of the case with lower heat capacity value.

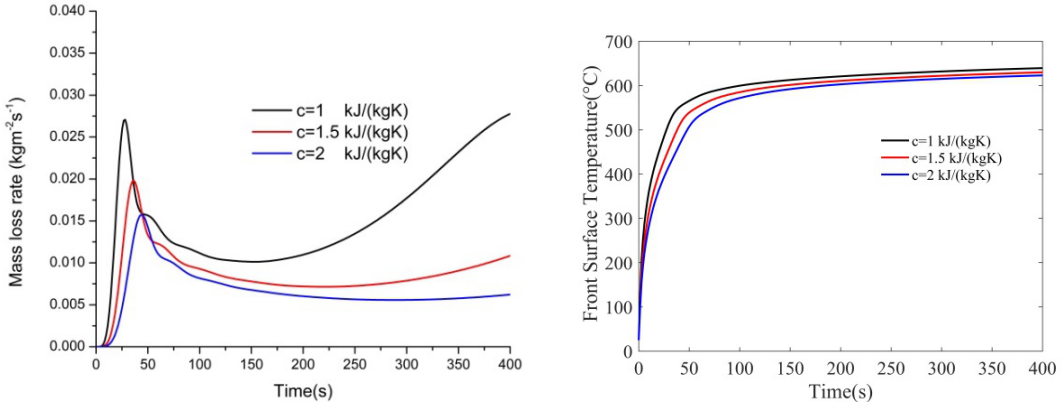

(a) (b)

Figure 3.7: Influence of specific heat on the (a) mass loss rate and (b) surface temperature.

3.2.5.2 Influence of thermal conductivity

A separate sensitivity analysis has been conducted for the thermal conductivity. Three values have been investigated, namely 0.3, 0.2, and 0.1 W/(m·K). The results are demonstrated in Figure 3.8. When increasing the thermal conductivity, the thermal diffusivity $(k/\rho c)$ increases. Thus, heat can penetrate deeper into the material in the same time period, thus the pyrolysis process at the surface is slow down during the initial heating-up period.

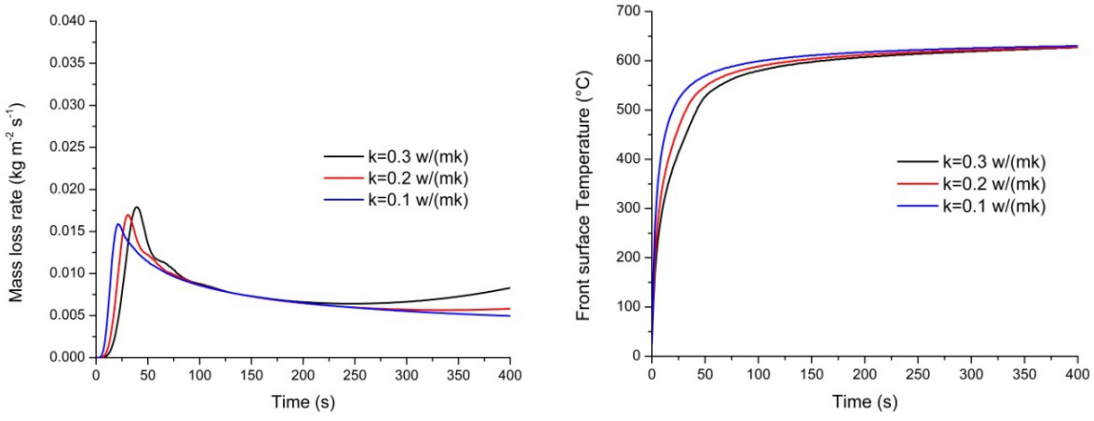

(a) (b)

Figure 3.8: Influence of thermal conductivity on the (a) mass loss rate and (b) surface temperature.

When increasing the thermal conductivity of the virgin material from 0.1 W/(m.K) to 0.3 W/(m.K), the time to reach the peak increases by 31.8% and the value of the

peak increases by 6.4%. Moreover, the surface temperatures take more time to reach the experimental values when the conductivity is higher, as heat is conducted into the material more easily.

3.2.5.3 Influence of the heat of pyrolysis

The heat of pyrolysis does not have a significant influence on the pyrolysis process. Increasing H_p from 0 to 100 kJ/kg results in differences less than 5% in the mass loss rates and the front surface temperatures.

3.2.5.4 Influence of the moisture content

Moisture Content (MC) is a measure of the amount of water within a material. MC is expressed as the percentage of the mass of the material that contributes water content. In this study, the original MC of the sample was approximately 6%.

In order to check the influence of the MC, a second Arrhenius equation for the water evaporation was added. Again Eqs. 3.2, 3.3, and 3.4 were employed to estimate the kinetic parameters A and E. The peak reaction rate $\gamma_p = 0.0016s^{-1}$ occurs at a temperature $T_p = 100°C$. A value of 5 K/s is used for the heating rate. Three MC values have been considered, namely 0%, 5%, and 10%. The comparison of simulation results is displayed in Figure 3.9.

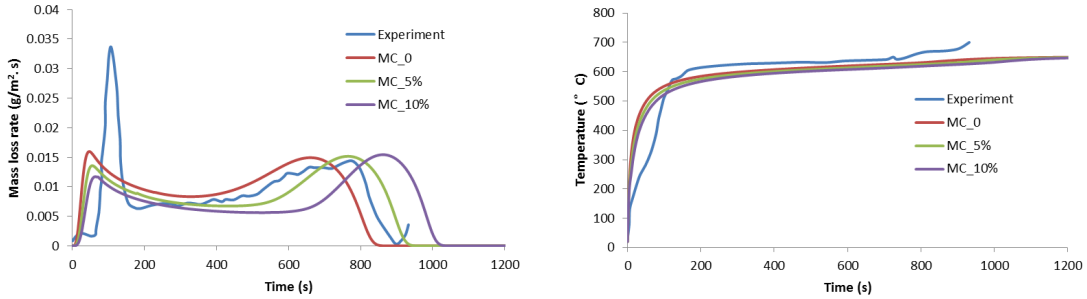

(a) (b)

Figure 3.9: Influence of MC on the simulated (a) mass loss rate and (b) surface temperature.

Increasing the MC from 0 to 5%, the peak value $\dot{m}_p$ decreases by 16.73%, while the time to reach the first peak t_p increases by 17.53%. Moreover, the overall reaction time increases by 20%. This influence can be explained in terms of the amount of energy required for the evaporation process, i.e. more water or moisture content means that the sample needs more energy for water evaporation. Obviously, the MC has a significant influence on the burning behaviour. The 'updated' value of 6% MC will be used hereafter.

Up to this point, the results of the aforementioned sensitivity analysis show that the most significant influence on the peak value for the mass loss rate is caused by the specific heat capacity. Nevertheless, none of these results showed satisfactory results for the time to reach the peak value of the burning rate when compared to experimental data, namely, the predicted time to peak is significantly lower than the measured value.

3.2.5.5 Influence of the emissivity

In light of the above, another sensitivity analysis has been conducted for the effective emissivity of virgin material. The considered range of the emissivity is from 0.5 to 0.8. The comparisons are shown in Figure 3.10. For the boundary condition, we are assuming the absorptivity is equal to the emissivity. When decreasing the emissivity (thus also absorptivity), less energy is received at the sample surface. Therefore, more time is required to reach the first peak in MLR and thus the maximum front surface temperature.

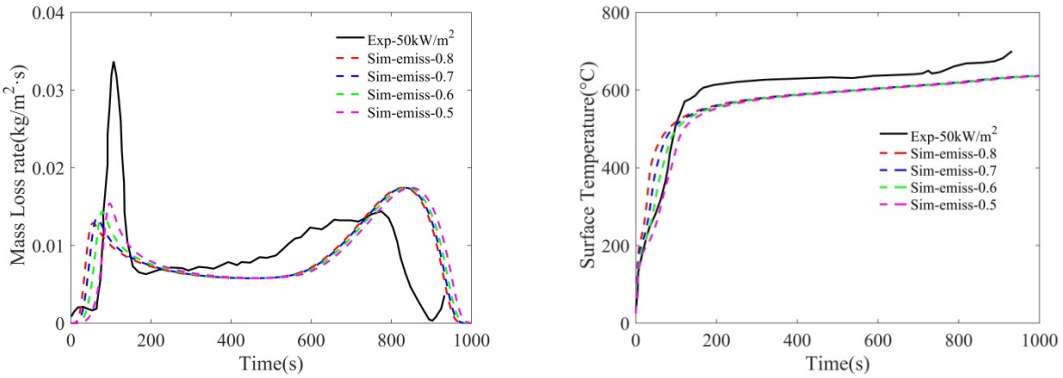

(a) (b)

Figure 3.10: Influence of emissivity on the (a) mass loss rate and (b) surface temperature.

When decreasing the emissivity of virgin material from 0.86 to 0.6, the time to reach the first peak increases by 116%, and the peak value increases by 11.24%. Based on these results, a value of 0.6 for the emissivity of the virgin material is suggested. Consequently, emissivity can be identified as the first parameter that plays a role in the timing of the peak mass loss rate.

3.2.5.6 Influence of the absorption coefficient

Figure 3.11 and Figure 3.12 display the results for the influence of the absorption coefficient on the mass loss rate (a) and front surface temperature (b), fixing the emissivity

of the virgin material at 0.6, and the emissivity of char at 0.86. In general, both the absorption coefficient of virgin and char have significant influence on the mass loss rate curve. In Figure 3.11, when decreasing the values of the absorption coefficient of virgin material from 50,000 m^{-1} to 30 m^{-1} leads to a significant increase in the peak MLR and a delay in the time to reach the peak. Specifically, the values of the absorption coefficient of virgin between 30 m^{-1} and 700 m^{-1} show the most significant influence. The peak value is improved by 48.25%, and the time to reach the first peak is improved by 18.42%.

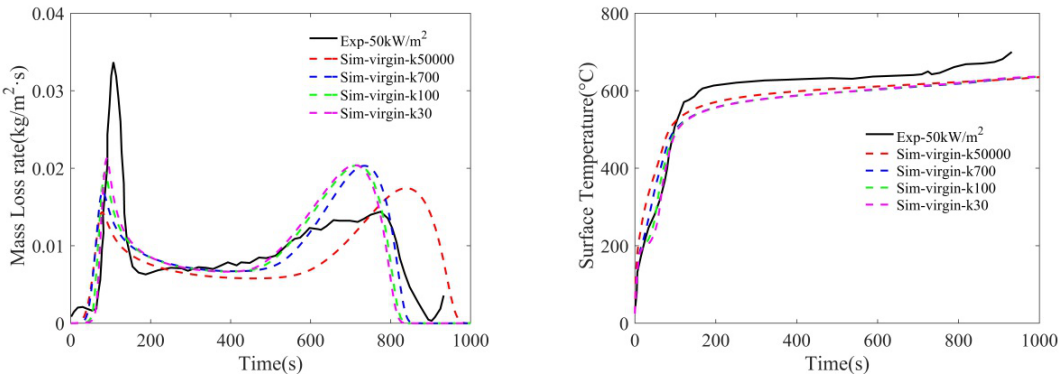

(a) (b)

Figure 3.11: Influence of absorption coefficient of virgin on the (a) mass loss rate and (b) surface temperature.

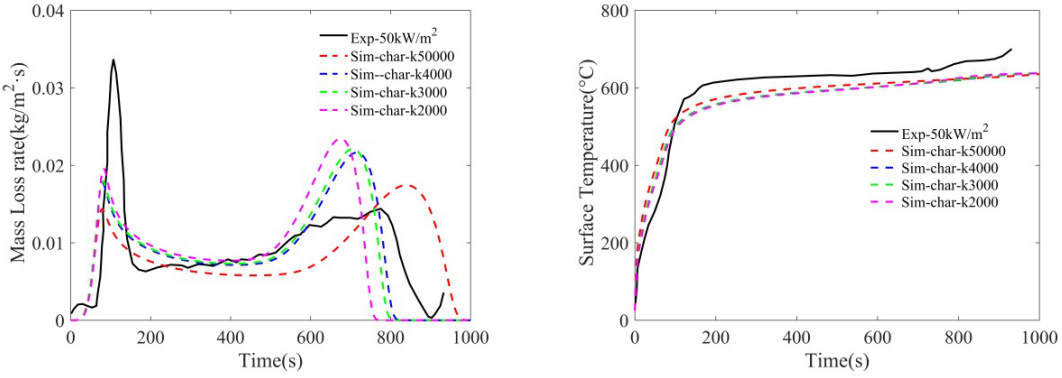

(a) (b)

Figure 3.12: Influence of absorption coefficient of char on the (a) mass loss rate and (b) surface temperature.

As indicated in Figure 3.12(a), the considered range of the absorption coefficient of char between 2000 m^{-1} and 4000 m^{-1} shows significant influence. The peak value is

increased by 39%, while the time to reach the first peak is not improved very noticeably. Furthermore, the absorption coefficient of char has significant influence on the second peak. This could be explained by fact that the top layers of the sample are covered with char. And with the increase of the absorption coefficient of char, the radiation can penetrate deeper into the sample, which accelerates the reaction. Thus the overall reaction time decreases. However, this does not significantly influence the surface temperature, as shown in Figure 3.12(b).

As mentioned in the introduction, the in-depth-like radiation absorption may occur in case of cracks or delamination. Hence, it is reasonable to assume that the material is opaque until it starts charring. Based on this consideration, in order to get better agreement, values of 50000 m^{-1} and 2000 m^{-1} are suggested for the absorption coefficient of virgin and char, respectively.

This finding should be taken into account with caution and must be further investigated. It highlights, nevertheless, the possible importance of in-depth radiation in the pyrolysis modelling of MDF and more generally wood-based materials.

3.2.5.7 Influence of through-thickness density profile

As mentioned in the previous section, both uniform and non-uniform density cases have been considered in this study. The non-uniform through-thickness density profile used here is the one mentioned in previous section, which consists of 3 layers. The results are shown in Figure 3.13. Two heat flux values have been considered here.

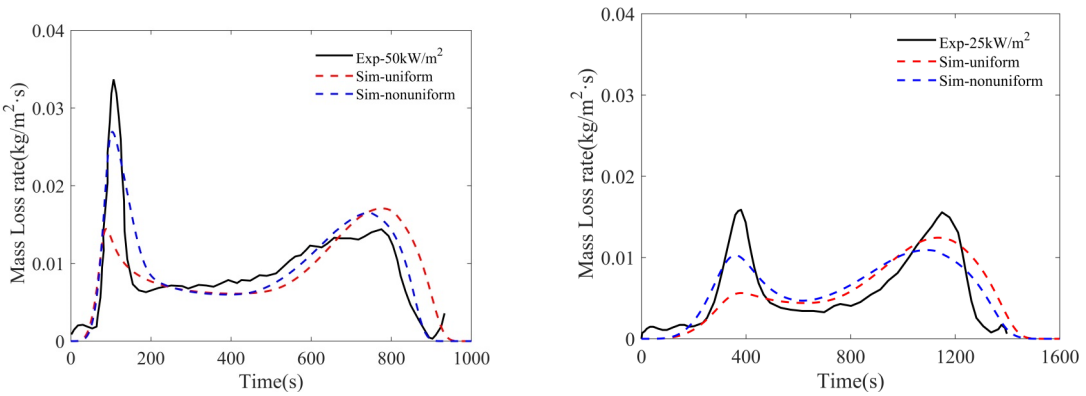

Figure 3.13: Influence of the through -thickness density profile on the mass loss rate for heat flux exposures of (a) 50 kW/m^2 , (b) 25 kW/m^2.

At the heat flux of 50 kW/m^2, the prediction of time to reach the first peak MLR, t_p,

is within 4% of the experimental value in the non-uniform density case, whereas this has been underestimated by 17% in the uniform density case (see Figure 3.13(a)). Similarly, the magnitude of the first peak MLR has been predicted more closely in the non-uniform density case (20% underestimation versus 57% in the uniform density case). Similar trends can be observed for the heat flux exposure of 25 kW/m^2 (see Figure 3.13(b)). Therefore, a non-uniform density profile is suggested for the 'updated' case.

The impact of parameter variations on t_p (time to peak mass loss rate) and $\dot{m}_p$ (peak mass loss rate) is quantitatively shown in Table 3.5 for cases with 50 kW/m^2 heat flux exposure. For the considered range of the parameters, the most significant influence on the time to the first peak comes from the emissivity, followed by the thermal conductivity, specific heat, non-uniform density profile, and moisture content. For the peak mass loss rate, the most significant influence comes from the non-uniform density profile, followed by the absorption coefficient, the moisture content, and finally the specific heat capacity.

Table 3.5: The impact of parameter variations on t_p and $\dot{m}_p$ (50 kW/m^2 heat flux exposure). The percentages show the relative differences between the outcomes of input 1 and input 2.

Parameter	Input 1	Input 2	$dt_p(\%)$	$d\dot{m}''_p(\%)$
Specific Heat capacity of virgin	1.5	2	28	-14
Thermal conductivity of virgin	0.2	0.1	32	6
Absorption coefficient of char	50000	2000	8	39
Heat of pyrolysis	100	50	0	-5
Emissivity	0.86	0.6	116	11
Moisture content	0%	5%	18	17
Density	uniform	non-uniform	16	86

3.2.6 'Updated' model parameters and corresponding results

In order to achieve a better estimation of the burning behavior for MDF material, a simple trial and error optimization procedure has been followed to predict the MLR from the experiment. Consequently, a set of 'updated' parameters has been obtained (see Table 3.3), and these simulation results are demonstrated in this section as well. Figure 3.14 shows the simulation results using these 'updated' values of parameters. These results include the mass loss rate and the front surface temperature for three different external heat flux exposures. In general, as expected a better agreement is achieved when using 'updated' values of model parameters. For the predictions of the mass loss rate, the onset of the pyrolysis was well captured, and significant improvements were also achieved in terms of the value of the first peak in the mass loss rate curve. For the front surface

temperature, the predictions of the initial heating-up period (roughly in the first 70 s, 130 s, and 400 s at the heat flux exposures of 100, 50, and 25 kW/m^2 respectively) were notably improved and fit the experimental data better than those in the preliminary simulations.

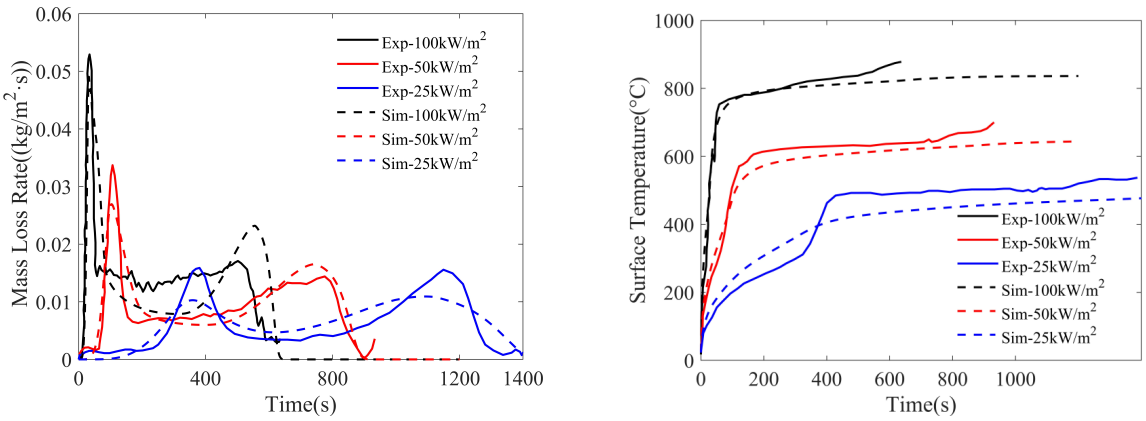

(a) (b)

Figure 3.14: Comparisons between experiment and simulation using 'updated' parameter values (a) mass loss rate, (b) surface temperature.

3.3 Transient external heat flux condition

For cases with combustion in the gas phase, the external heat flux received at the surface of the sample is not constant, it changes over time. Before moving to the next step to model the gas phase combustion, it is necessary to evaluate the predictive capability of this numerical model for scenarios with transient external heat flux. Another FPA test has been conducted for that purpose [**?**].

3.3.1 Case description

The same FPA apparatus was used as described in section 3.2. The heat flux condition applied in this experiment is shown in Figure 3.15. It is a step-wise irradiation condition. For times from the start to 300 s a constant heat flux 50 kW/m^2 was implemented, after which 100 kW/m^2 was applied until the end of the test. The infrared heaters were controlled by a LabVIEW program to achieve the corresponding transient irradiation pattern.

In FDS, a transient external heat flux was implemented using command 'RAMP_EF' in the input FDS file. The employed model properties are the same as the 'updated' case

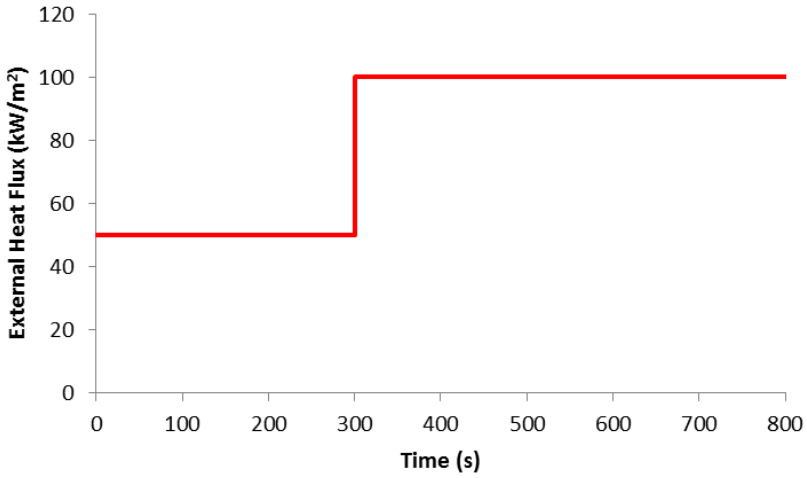

Figure 3.15: The applied transient external heat flux in the test case

as shown in Table 3.3. The back side of the sample was insulated in the same way as in the section 3.2.

3.3.2 Results and discussion

3.3.2.1 Mass loss rate

In Figure 3.16, the prediction of the mass loss rate is presented. The overall trend is generally captured. The first peak of the MLR at around t = 100 s is under-estimated by 34%. The second peak, at around t = 300 s, caused by the jump in the external heat flux, is captured, but under-estimated by 22%. The under-predictions are in line with the above (for constant imposed heat flux). Nevertheless, the results indicate the numerical model captures time-dependent heat fluxes well.

For the predicted MLR curve, there is a clear peak at around 550 s in the simulations, caused by the back effect (insulation of the back boundary). This peak is not observed in the experimental curve, suggesting there is more heat loss through the back side of the sample in the test than in the simulation. In line with this, the predicted reaction process ends sooner than in the experiment (630 s vs. 744 s), with the currently employed model properties.(updated case in Table 3-3)

3.3.2.2 Surface Temperature

Figure 3.17 displays the time evolution of the temperature at the sample surface. In general, the surface temperature is closely predicted with an overall R^2 of 0.98 and an average deviation of 33$^{\circ}C$. At t = 300 s, the temperature jump, caused by the sudden

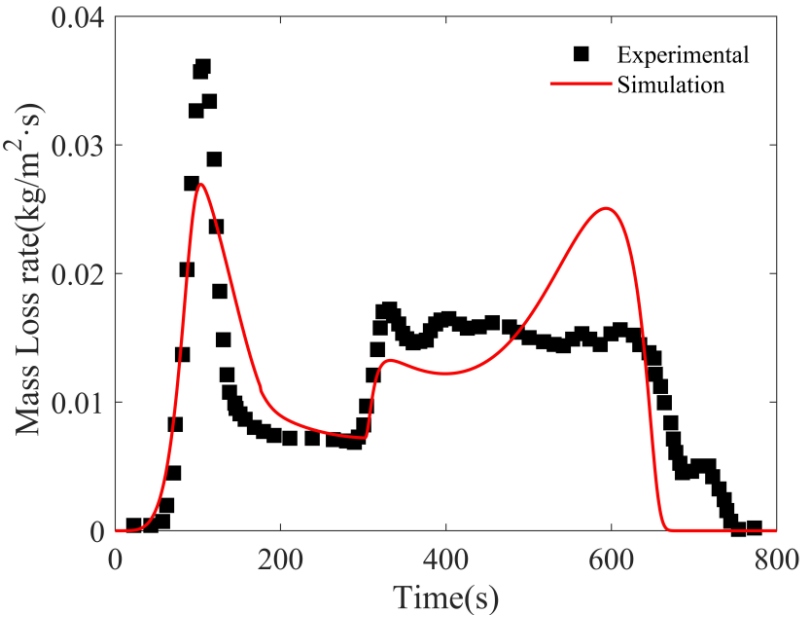

Figure 3.16: Mass loss rate prediction for MDF under transient external heat flux.

change in the external heat flux from 50 kW/m^2 to 100 kW/m^2 , is well captured by the model. This confirms the numerical model responds well to the changing heat flux condition.

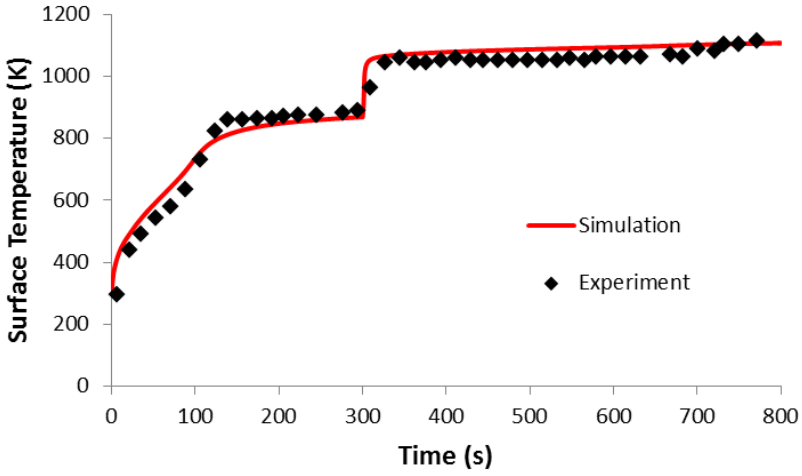

Figure 3.17: Surface temperature of the sample.

3.3.2.3 Back-side Temperature

The evolution of the backside temperature is shown in Figure 3.18. The overall trend is well captured with an overall R^2 of 0.99 and an average deviation of 25 $^{\circ}C$. Both in

the model prediction and the experiment, the time when the heat reaches the back side of the sample is at around 70 s. Once the heat reaches the back surface and until 300 s, the back surface temperatures are under-predicted in the numerical simulations, with an average deviation of 39 $^{\circ}C$. This indicates too low values for thermal diffusivity in the simulations. After that period, the simulation results match the experimental data closely, including the rapid temperature rise at the end of the whole process.

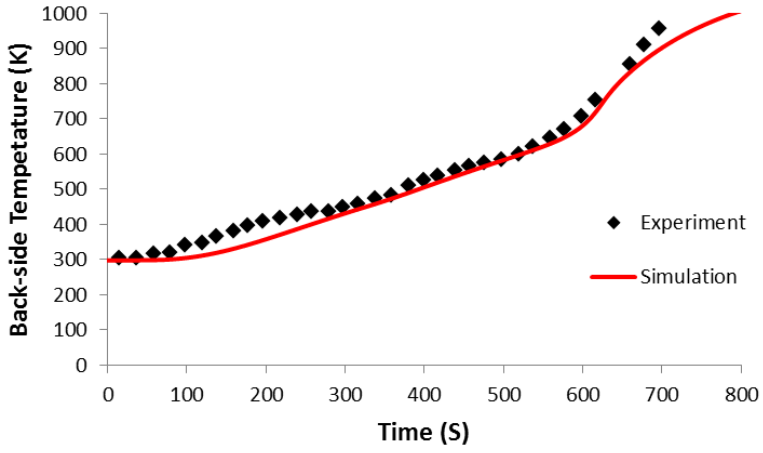

Figure 3.18: Back-side temperature results

Overall, these results demonstrate that the numerical model and these material properties are applicable to cases under transient heat fluxes on the surface of the sample.

3.4 Cone Calorimeter Combustion Test

In the previous section, the pyrolysis of MDF has been studied. The thermophysical properties of the MDF were determined to describe the gasification and the heat transfer process in the solid phase. Based on that, we take one step forward to consider a scenario which includes turbulent combustion in the gas phase. In this study the cone combustion test has been considered, involving processes of both the solid phase and the gas phase. For the solid phase, the process is similar to that happening in pure nitrogen atmosphere. For the gas phase, the released pyrolysate will burn when mixed with high temperature air, and some amount of heat will generate in the meantime. To properly predict these processes, a numerical model taking into account the turbulent combustion and radiation is required. In this section, the details of this numerical study will be presented and discussed.

3.4.1 Experimental set-up

The Cone Calorimeter [93] is the contemporary apparatus widely used in the field of fire safety engineering to study the reaction to fire of small samples. It gathers results regarding the ignition time, mass loss, combustion products, heat release rate and other parameters associated with its burning properties. It allows the sample to be exposed to various heat fluxes over its surface. The principle for the measurement of the heat release rate is based on the Huggett's principle [94] that the gross heat of combustion of any organic material is directly related to the amount of oxygen required for combustion. The experimental set-up is shown in Figure 3.19.

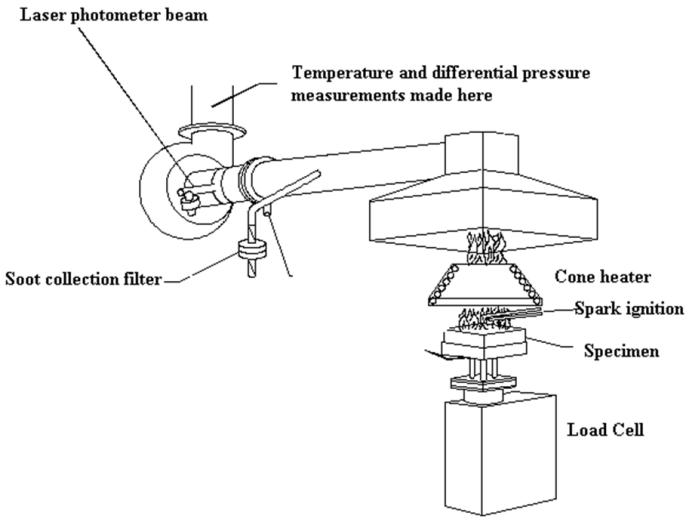

Figure 3.19: Schematic layout of the cone calorimeter apparatus [95].

In this study, the cone calorimeter combustion tests have been conducted by the authors of [96] at Ghent University. The used material is the same MDF material as that in the pyrolysis test. The heat flux from the heating source is fixed at 50 kW/m^2 .

A picture of the MDF sample in the test is demonstrated in Figure 3.20. The dimension of the MDF sample is 0.1 m $\times$ 0.1m $\times$ 0.0184 m. The bulk density is 605 kg/m^3 . As shown in Figure 3.20, the sample is held by an iron frame with all surfaces exposed to the environment.

Three tests have been repeated to check the repeatability and uncertainty. They are named test 1, test 2, and test 3, specifically. For all these three tests, the total heat release rates were recorded. During these tests, the mass of the sample was weighed every 5 seconds. The time evolution of mass for test 1 is shown in Figure 3.21.

With these results, the mass loss rate $\dot{m}_i$ can be calculated using the following five-

Figure 3.20: The MDF sample in the cone calorimeter test.

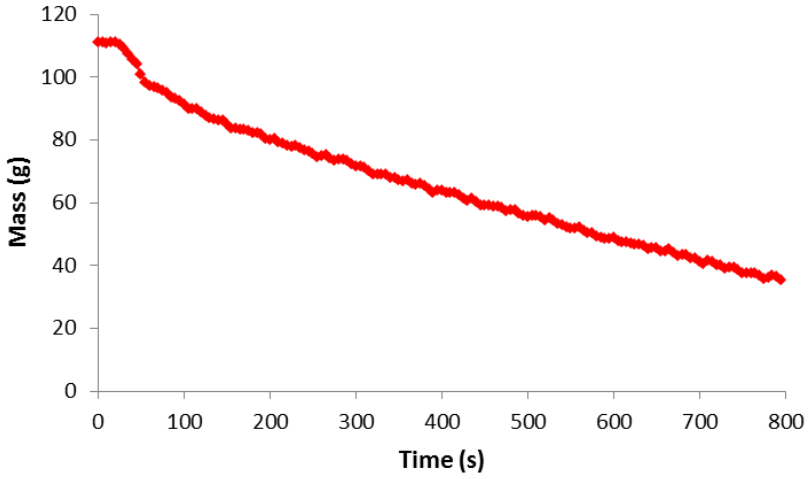

Figure 3.21: Time evolution of mass from the cone calorimeter test.

point numerical differentiation equations [97]:

For the first mass scan $(i = 0)$:

$$[\dot{m}]_{i=0} = \frac{25m_0 - 48m_1 + 36m_2 - 16m_3 + 3m_4}{12\Delta_t} \tag{3.14}$$

For the second mass scan $(i = 1)$:

$$[\dot{m}]_{i=1} = \frac{3m_0 + 10m_1 - 18m_2 + 6m_3 - m_4}{12\Delta_t} \tag{3.15}$$

For any scan for which $1 < i < n-1$ (where n is the total number of scans):

$$[\dot{m}]_i = \frac{-m_{i-2} + 8m_{i-1} - 8m_{i+1} + m_{i+2}}{12\Delta_t} \tag{3.16}$$

For the next to last mass scan ($i = n-1$):

$$[\dot{m}]_{i=n-1} = \frac{-m_n - 10m_{n-1} + 18m_{n-2} - 6m_{n-3} + m_{n-4}}{12\Delta t} \tag{3.17}$$

For the last mass scan ($i = n$):

$$[\dot{m}]_{i=n} = \frac{-25m_n + 48m_{n-1} - 36m_{n-2} + 16m_{n-3} - m_{n-4}}{12\Delta t} \tag{3.18}$$

The raw and smoothed mass loss rate curves obtained from Test 1 are shown in Figure 3.22.

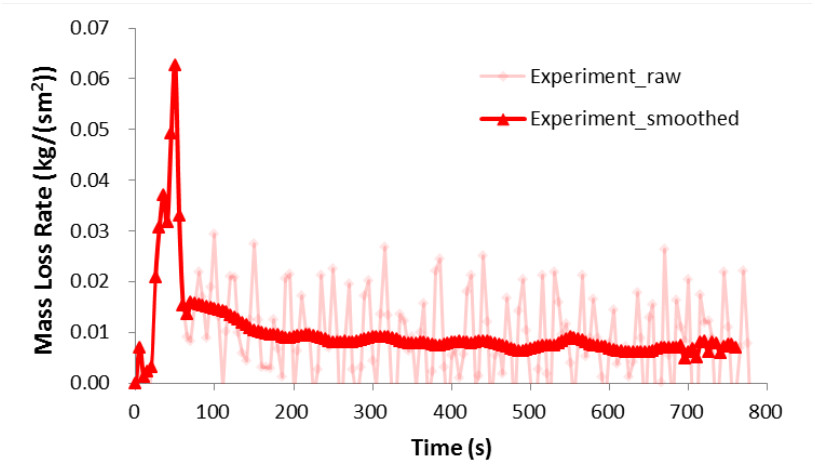

Figure 3.22: Time evolution of mass loss rate from the cone calorimeter test.

The char yield, defined as the ratio of final mass to the initial mass, has been calculated to be 14% from the cone calorimeter test. The value is significantly lower than that of the FPA pyrolysis test in nitrogen. It signifies that the cone calorimeter combustion test yields more char oxidation, which is not included in the model at present.

The heat release rate is determined by measurement of the oxygen consumption derived from the oxygen concentration and the flow rate in the combustion product stream [93]. The results of three cases are shown in Figure 3.23.

The HRR uncertainty of the three experiments can be determined by analyzing their deviation from the average HRR value. The maximum deviation is found to be at the

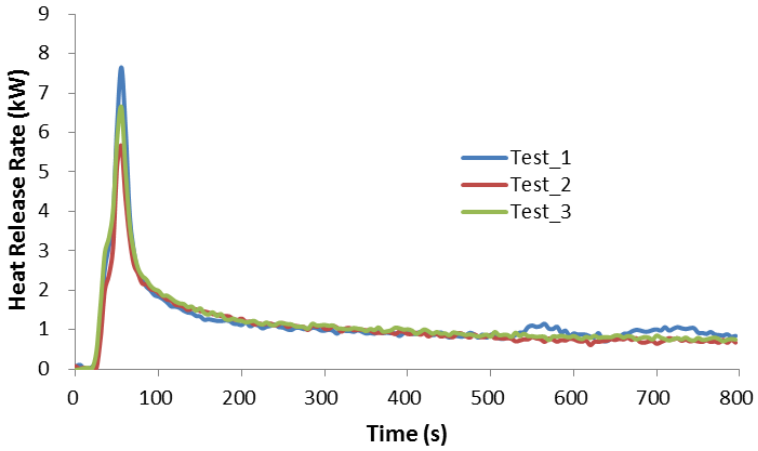

Figure 3.23: Time evolution of heat release rate from the Cone calorimeter tests.

time of the peak. Test 2 has a notably lower HRR peak value, compared to the other 2 tests. This might be due to a higher moisture content at the beginning of the test (but the moisture content has not been measured, unfortunately).

Table 3.6: Comparison of the heat release rate results from experiments.

Case number	t_{peak}(s)	HRR_{peak}(kW)
Test 1	55	7.65
Test 2	55	5.66
Test 3	55	6.64
Average	55	6.65

3.4.2 Numerical setup and simulation details

FDS (version 6.2.0) is employed in this section. In FDS, the heater of a cone calorimeter experiment could be simulated as a complex cone shape with the assignment of temperatures to surfaces so that a corresponding heat flux is directed to the target sample. However, this approach is unnecessarily complex as the selection of the correct temperatures to achieve the desired heat fluxes is crucial in this method [98]. Alternatively, an external heat flux can be directly added to the sample surface boundary condition, representing the cone heater. Matala and Hostikka [99] adopted the 'external heat flux' method to represent the cone heater in their research, and this method is adopted and will be assessed here.

A domain with dimensions of 0.2 m $\times$ 0.2 m $\times$ 0.5 m is used to ensure that the entire

flaming region of the fire plume can be fully captured and the loss of heat to the outside of the domain is minimized. In these simulations, the MDF sample is represented by a surface with properties reported in the previous section. The measurements include the mass loss, and the heat release rate. The ambient temperature was set to be $25^{\circ}C$.

A non-uniform vertical density profile of the MDF has been considered (see Table 3.7). There are 3 layers in total, and each of them has a corresponding char fraction calculated based on the density of the virgin MDF and char.

Assuming a constant sample volume during the burning process, the over-all char density is determined to be 84.7 kg/m^3 based on a 14% char over-all yield value. In the test, the char yield was found to be lower than in the nitrogen atmosphere (21%). The details are shown in Table 3.7. The other values for the material and model parameters are the same as those used in the 'updated' case (see Table 3.3).

Table 3.7: Details of solid layers (step_wise VDP) used in the model

Parameter	Virgin Density	Char Density	Thickness(mm)	Char Fraction (%)
Layer 1	950	84.7	2.3	8.9
Layer 2	500	84.7	13.6	16.9
Layer 3	950	84.7	2.3	8.9

A grid sensitivity analysis is carried out for both the solid phase and the gas phase, in order to determine the appropriate cell size. The numerical model using a 10 mm cell size for the gas phase and 0.34 mm for the solid phase is demonstrated in Figure 3.24.

3.4.2.1 Numerical models

To model this cone calorimeter test, it is necessary to address several processes in the simulation. The first one is the heat transfer. While the heat flux is applied on the surface of the sample, the sample will be heated up on its surface. Following this the heat can be conducted deeper into the sample. Associated with this is the pyrolysis process, which maintains the continuous generation of gases. These processes have been modelled in the nitrogen atmosphere, and they are expected to be similar in the oxygen atmosphere. Linked to that there is a turbulent combustion process in the gas phase, which burns the generated gases and releases an amount of energy. The latter comes in the form of radiation and convection, which transfers part of the heat from the gas phase back to the surface of the sample. For these processes, a turbulent combustion model, a radiation model and a turbulence model are needed.

The combustion model used in this study is a single-step, mixing-controlled combustion

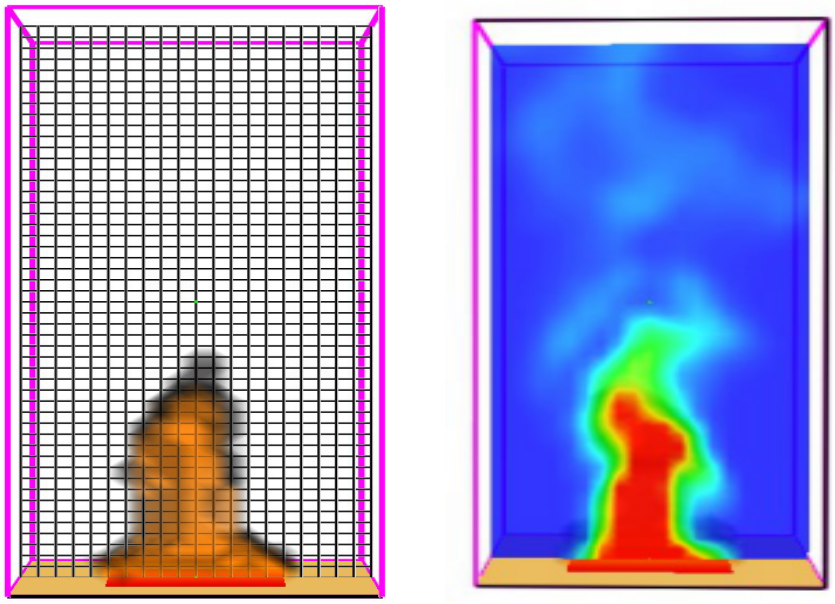

(a) (b)

Figure 3.24: a cone calorimeter simulation in FDS6 for MDF at 50 kW/m^2 at 100 s: (a) Meshing of the simulation domain and (b) Temperature slice at the middle of the computational domain.

model. The HRR per unit area $\dot{q}''$ generated from the burning of the combustible gases can be calculated by multiplying the mass flux with the effective heat of combustion of the material $\Delta H_{c,eff}$:

$$\dot{q}'' = \dot{m}'' \cdot \Delta H_{c,eff} \tag{3.19}$$

According to the ISO 5660 standard [97], a time-varying value of the effective heat of combustion (kJ/kg) can be determined with the following equation:

$$\Delta H_{c,eff} = \frac{\dot{q}_t}{-\dot{m}} \tag{3.20}$$

where $\dot{m}$ is the mass loss rate (kJ/s), $\dot{q}_t$ is the heat release rate (kW).

The experimental results from Test 1 are shown again in Figure 3.25. Note that there is a time delay between these two measurements. Compared to the mass loss rate (MLR), the heat release rate (HRR) is measured with roughly 5 s delay. This is caused by the way they are measured. The heat release rate is obtained by analyzing the oxygen concentration of the smoke entering the hood, while the mass is measured directly on the

load cell. Accordingly, the HRR and MLR results presented here have been synchronized, taking into account the time difference between the original signals.

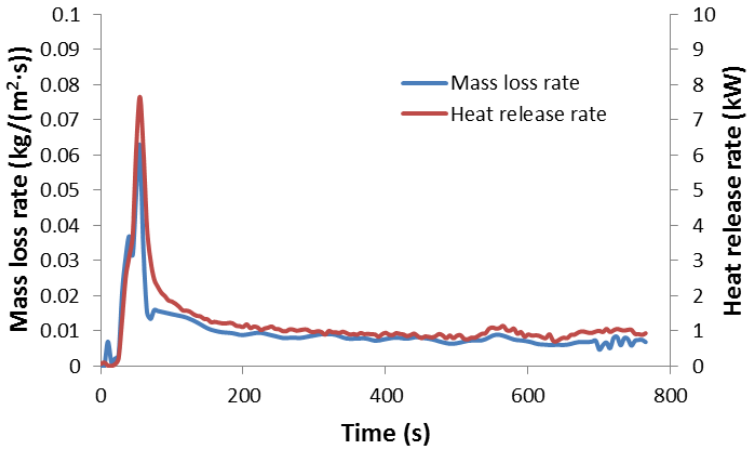

Figure 3.25: Synchronized mass loss rate and heat release rate results from the cone calorimeter test (Test 1).

Based on Eq. 3.20, a time-varying effective heat of combustion is obtained in Figure 3.26. The average time period is from 100 s to 700 s. A value of 11.94 MJ/kg has been determined for this time period. At the time the MLR and HRR curve reach their peak, a similar value (12.22 MJ/kg) can be calculated. Therefore, a value of 12 MJ/kg is applied in this study.

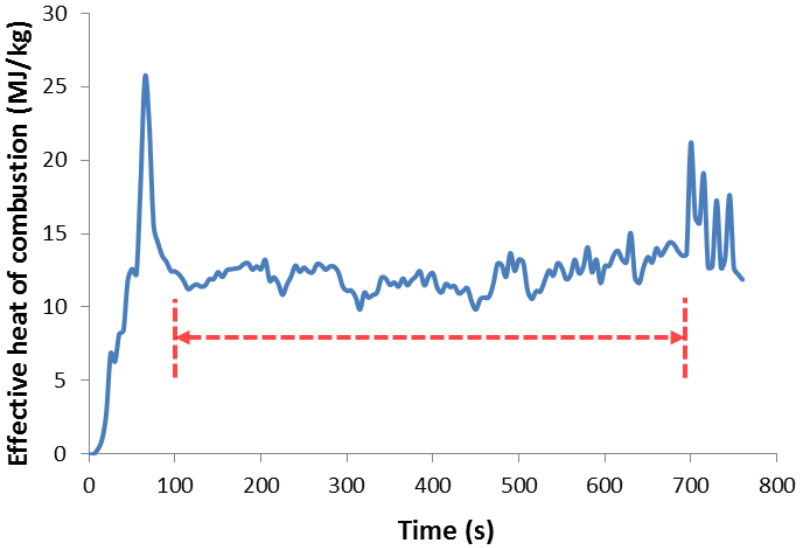

Figure 3.26: Time-varying effective heat of combustion results from the cone calorimeter test.

In this case, both the gas phase and solid phase are involved. In these simulations, all walls are treated as being smooth. A Werner-Wengle [101] wall model has been used for the velocity near walls.

3.4.2.2 Boundary Conditions

The front surface is subjected to a constant external heat flux. In FDS this can be achieved using a command 'EXTERNAL_FLUX=50.0/' in the input file. It should be noted that this does not mean that the heat flux received on the surface of the sample is exactly 50 kW/m^2 during the whole burning process. In fact, a separate radiation part from the flame to the sample surface is taken into account as well. In order to verify this, a preliminary simulation is conducted to check the heat flux received on the surface of the sample. A heat flux device was set at the center of the sample to measure the heat flux. The results are shown in Figure 3.27.

At the beginning and the last stage (roughly after 900 s), the incident heat flux received on the surface is 50 kW/m^2 , which stems from the heater only. For the time between this period, the heat flux is well above 50 kW/m^2 (around 80 kW/m^2), because this includes the radiation and convection heat transfer from the flame.

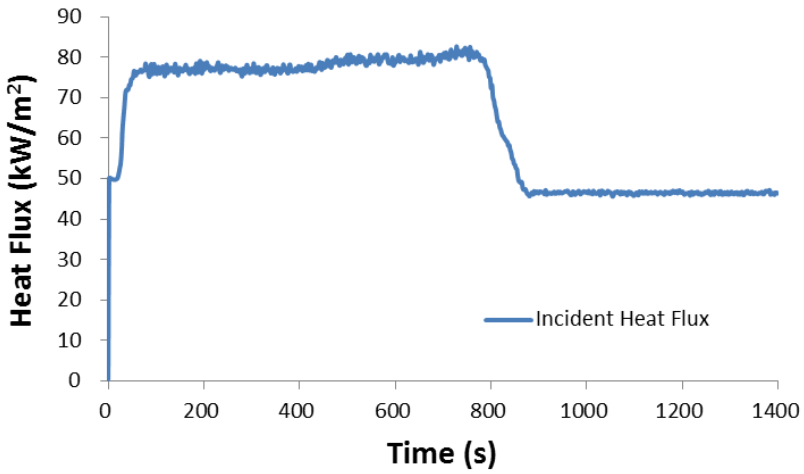

Figure 3.27: Heat flux received on the surface of the sample.

For the back side, the MDF sample is exposed to the environment during the test. This is implemented using the command 'BACKING='VOID" in the input file.

3.4.3 Results and discussion

In this section, the simulation results for the cone calorimeter test are presented and compared with experimental data. First, however, a grid sensitivity analysis is conducted

to determine the appropriate grid resolution.

3.4.3.1 Grid resolution analysis

3.4.3.1.1 Solid phase To compute the temperature and reactions inside the solids, FDS solves the one-dimensional heat transfer equation numerically. The size of the mesh cells on the surface of the solid is automatically chosen using a rule that makes the cell size smaller than the square root of the material diffusivity. By default, the solid mesh cells increase towards the middle of the material layer and are smallest on the layer boundaries.

The default parameters are usually appropriate for simple heat transfer calculations but sometimes the use of pyrolysis reactions makes the temperatures and burning rate fluctuate. Adjustments may also be needed in case of extremely transient heat transfer situations. The numerical accuracy and stability of the solid phase solution may be improved by one of the following methods: the first one is to set the 'STRETCH_FACTOR' equal to 1, which makes the mesh uniform; the second method is to set 'CELL_SIZE_FACTOR' less than 1.0, which makes the mesh size smaller than the default one. For the grid sensitivity study, four cases have been considered, listed in Table 3.8.

Table 3.8: Summary of cases for solid phase grid sensitivity study

Case	Solid cell size (mm)	Computational Time(h)	Cell size factor
S_1	0.34	0.62	1.0
S_2	0.18	0.68	0.5
S_3	0.093	0.75	0.25
S_4	0.047	0.85	0.125

The results are shown in Figure 3.28. The differences are negligible, indicating the prediction is insensitive to the solid phase cell size. Consequently, the gas phase predictions are independent of the cell size in the solid phase. Therefore, a 0.34 mm cell size (the default value) is employed to save computational time.

3.4.3.1.2 Gas phase For the gas phase simulation, a sufficiently fine cell size should be employed to properly capture the details in the gas phase. The required grid resolution has been determined by conducting a gas phase grid sensitivity study.

Baum et al. [62] suggested that, in order to correctly capture the fire and smoke plume, it is necessary to have 10 $\times$ 10 cells across the span of the burner surface. Based on this, a 10 mm cell size is suggested for a 0.1 m $\times$ 0.1 m solid sample. However, in order to capture the mixing and heat transfer close to the surface, it may be important to capture much more detail in the boundary layers close to the surface. To conduct a

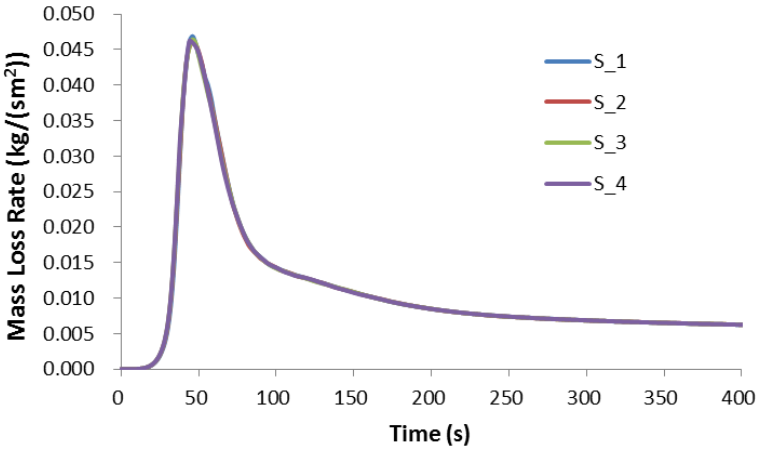

Figure 3.28: Solid phase grid sensitivity of mass loss rate evolution (legend: see Table 3.8).

complete grid sensitivity analysis, the considered gas phase cell sizes are 20 mm, 10 mm, 5 mm, and 4 mm. The details of these cases are listed in Table 3.9.

Taking case G_3, which uses a 5 mm cubic grid as an example, the number of cells for the gas phase domain is 160,000. For a simulation time of 600 seconds, the simulation takes about 87 hours using a computing processor of 2.6 GHz CPU with 32 GB RAM. In this case the initial time step is 0.011 s.

Table 3.9: Summary of cases for gas phase grid sensitivity study.

Case number	Gas phase cell size (mm)	Computational Time (h)
G_1	20	0.3 (800 s simulation time)
G_2	10	6 (800 s simulation time)
G_3	5	87 (600 s simulation time)
G_4	4	210 (600 s simulation time)

As shown in Figure 3.29, the MLR predictions, mainly in terms of the time to reach the peak and the peak value, are sensitive to the gas phase grid size. The ignition time, t_{ig}, is the same for all these cases considered. This is logical: there is no gas phase combustion yet.

The time to reach the peak is denoted as t_{peak}, and the peak MLR as $\dot{m}''_{\text{peak}}$. For cases G_1 and G_2 the t_{peak} are the same, namely 46 s, while slightly shorter values are observed for cases G_3 (42 s) and G_4 (40 s). The peak MLR value, $\dot{m}''_{\text{peak}}$, of cases G_3 (0.049 kg/(m^2·s)) and G_4 (0.050 kg/(m^2·s)) are also higher than the other two cases. The details of the comparison are shown in Table 3.10.

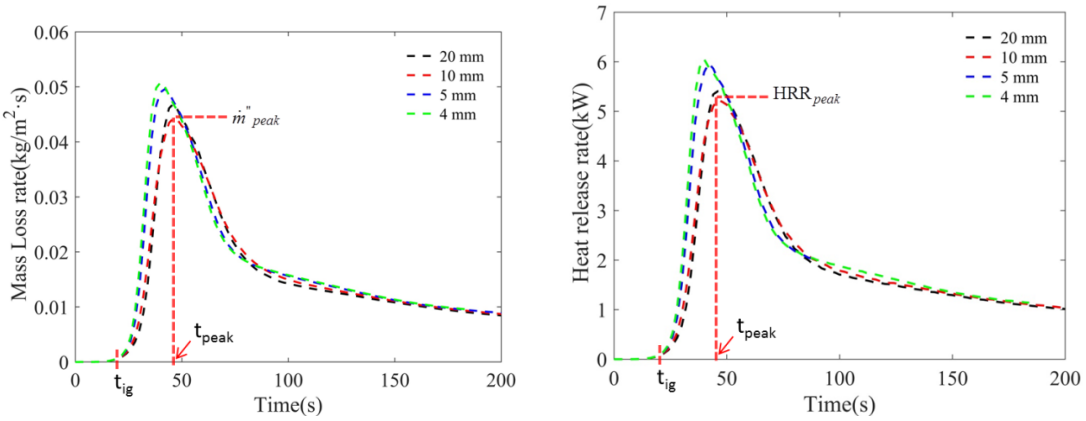

(a) (b)

Figure 3.29: MLR (left) and HRR (right) evolution of simulations using different gas phase cell size.

Table 3.10: Influence of the gas phase cell size on the MLR and HRR results.

Case number	Cell size(mm)	$t_{\text{peak}}(s)$	$\dot{m}''_{\text{peak}}$(kg/(m^2·s)	HRR_{max}(kW)
G_1	20	46	0.046	5.41
G_2	10	46	0.044	5.23
G_3	5	42	0.049	5.97
G_4	4	40	0.050	6.05

The HRR results are, as expected, very similar to the MLR evolutions. As soon as the mesh is fine enough, the finer sizes lead to higher HRR values and the peak is obtained at a sooner time. This is due to a higher incident heat flux onto the surface (see Table 3.11), which is in turn a consequence of the higher flame temperatures and the position of the flame (see Figure 3.30, showing time-averaged temperature contours in the vertical plane through the middle of the sample around t_p; averaging is performed over a period of 6 s). Additionally, as is shown in Table 3.11, the contributions from the convective and radiative heat fluxes in the total incident heat fluxes are presented. Both of the the convective and radiative heat flux are grid sensitive. All in all, these observations confirm that the D^* criterion is insufficient for coupled gas phase-solid phase fire simulations.

As mentioned earlier the Werner-Wengle wall model has been employed, it is important that the first grid point adjacent to the wall has an appropriate $y+$ distance. This value has been checked, as is show in the Figure 3.31. This is the time-averaged $y+$ value of the first grid adjacent to the solid surface(averaging is performed over a period of 20 s from 180 s to 200 s), these values are smaller than 10 at the entire surface.

Table 3.11: Influence of the gas phase cell size on the surface averaged incident heat flux (averaged over time 180 s to 200 s).

Case number	Cell size(mm)	$HF_{inc}(kW/m^2)$	$HF_{conv}(kW/m^2)$	$HF_{rad}(kW/m^2)$
G_1	20	12.79	9.05	3.73
G_2	10	14.81	11.09	3.72
G_3	5	17.21	14.25	2.96
G_4	4	17.96	15.16	2.80

In the following, a 10 mm cell size is applied to the gas phase computation in order to save computational time. Nevertheless, it must be kept in mind that under-predictions of MLR and HRR, and thus flame spread, may result from this choice.

3.4.3.2 Comparison with experimental results

Numerical predictions, obtained with cell sizes of 10 mm (gas phase) and 0.34 mm (solid phase) are compared to experimental data.

The MLR and HRR evolutions are shown in Figure 3.32 and Figure 3.33. In general, the overall trends are well captured by the numerical model. In the test, the ignition time was recorded to be around 20 s after the start of the test with a 0.06 kW HRR. Here the ignition time is determined as the time when a notable and sustainable increase is observed on HRR curve (Figure 3.29). In the simulation, a value of 0.068 kW is obtained at 20 s. Taking this as the predicted ignition time, the numerical model shows good agreement with the experiment.

Both the MLR curve and the HRR curve show a peak after the ignition at around 50 s. For the MLR comparison, the time to reach the peak, t_{peak}, is well captured in the simulation. The peak value is underestimated by 25% (see Table 3.12), as expected. Note, however, that Figure 3.23 showed variations in HRR, so comparable variations may be expected in the MLR. Given that Test 1 corresponds to the highest HRR, it can be expected that also the MLR was the highest, so the under-prediction is most probably less bad than it looks at first sight. For times after 100 s, the simulation results are in good agreement with the filtered experimental data.

In line with the MLR prediction, the HRR curve agrees well with the experimental data (Figure 3.33). The under-prediction of the peak value is as expected. Details of the comparisons are presented in Table 3.12, comparing to the 'average' experimental HRR curve (see Table 3.7 above).

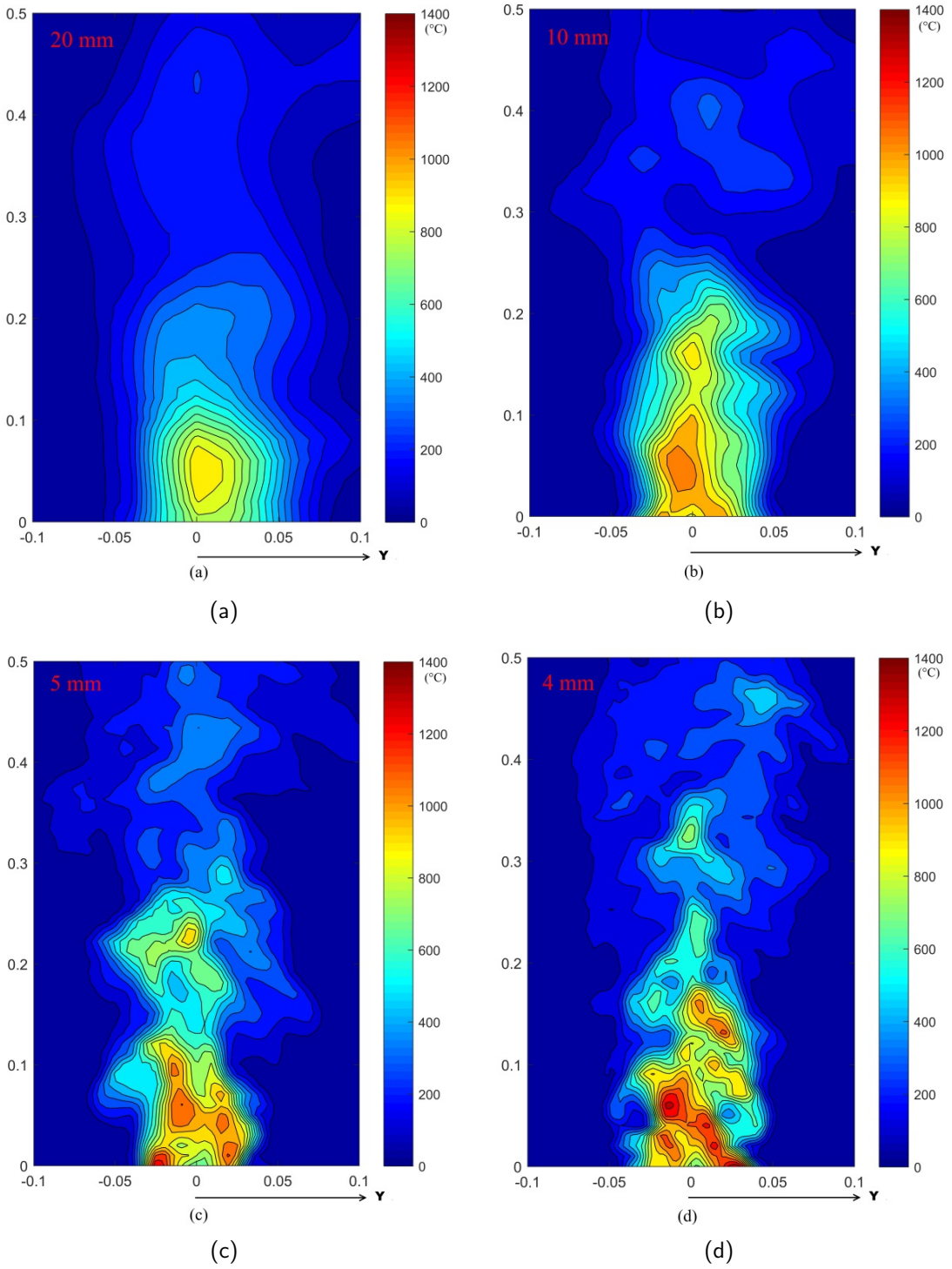

Figure 3.30: Time-averaged temperature contours in the vertical plane through the middle of the sample around t_p (averaging is performed over a period of 6 s) using different gas phase cell size.

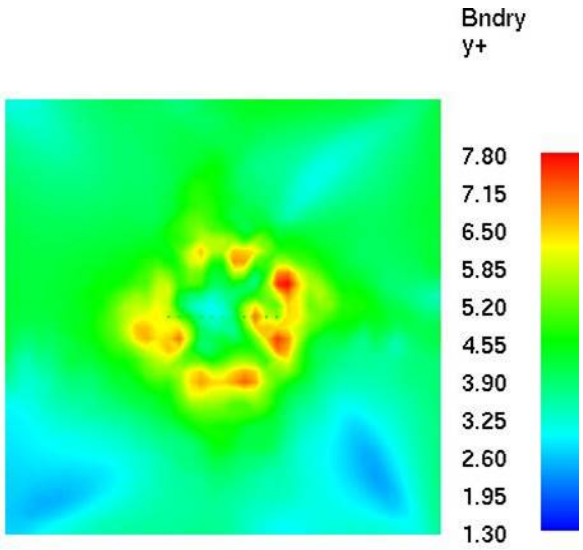

Figure 3.31: Time-averaged $y+$ value at the first grid adjacent to the solid surface

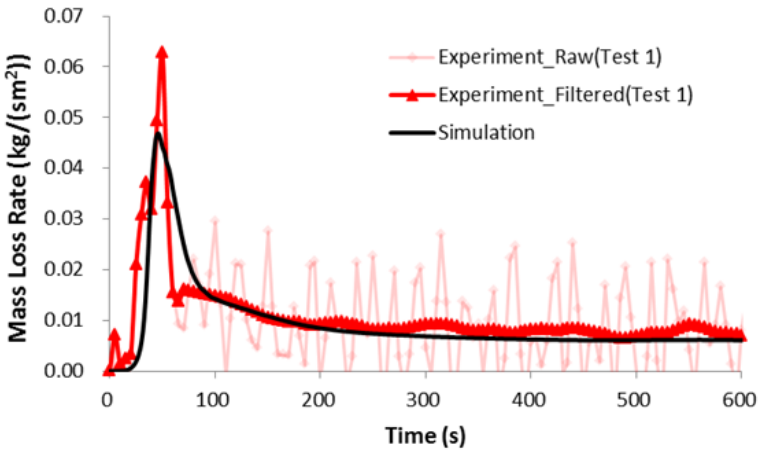

Figure 3.32: Mass loss rate comparison between the simulation and cone combustion test 1.

3.5 Conclusions

In this chapter, pyrolysis behaviour of the MDF material has been studied numerically using a one-dimensional heat transfer solver, and a one-step Arrhenius type pyrolysis model. The numerical simulation tool used in this study is the Fire Dynamics Simulator (FDS 6.2.0). Within this model, the non-uniform density profile and in-depth radiation has been taken into consideration. The values of the kinetic parameters and char yield are estimated from TGA test results reported in [63]. The thermal properties of virgin MDF

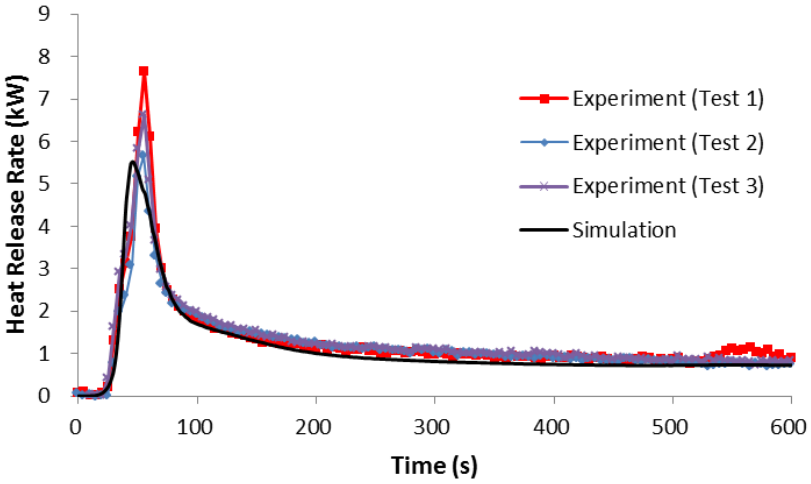

Figure 3.33: Comparison of the heat release rate between experiment and simulation.

Table 3.12: Comparison of the MLR and HRR results between experiment and simulation.

Case	$MLR_{max}(kg/(m^2 \cdot s))$	$HRR_{max}(kW)$
Experiment	0.0625	7.65
Simulation	0.0468	6.08

and char are taken from the literature for the base case. It is assumed that no shrinkage and swelling occur during the whole process.

The base case does not show satisfactory results for the time to reach the first peak and the value of that peak in the mass loss rate curve when compared to experimental data. The predicted time to peak and the value of that peak are significantly lower than the measured value, namely by about 50% to 62%. The influence of the material properties and model parameters on the pyrolysis behaviour of MDF has been investigated in detail through a sensitivity analysis. The parameters include thermal conductivity, specific heat, heat of reaction, the emissivity, absorption coefficient, moisture content, and through-thickness density profile.

Based on the results of the sensitivity analysis study, it can be concluded that, for the considered range of the parameters, the most significant influence on the time to the first peak comes from the emissivity, followed by the thermal conductivity, specific heat, non-uniform density profile, and moisture content. For the peak mass loss rate, the most significant influence comes from the non-uniform density profile, followed by the absorption coefficient, the moisture content, and finally the specific heat capacity.

Through a simple trial and error procedure, a set of 'updated' parameter values has been obtained (see Table 3.3). During this optimization procedure, the parameters showing significant influence have been considered, including the in-depth radiation, which shows better agreement with experimental data.

The rest of the chapter has been devoted to the coupling of pyrolysis and CFD modeling, including both gas phase and solid phase. First, it has been proved that the numerical model and these material properties are applicable to cases under transient heat fluxes condition. Then the cone combustion test has been considered, involving processes of both the solid phase and the gas phase. The conducted grid sensitivity study has shown that the D^* criterion is insufficient for coupled gas-solid phase fire simulations. The other results including MLR and HRR have been shown to be reasonable.

Chapter 4

The use of CFD for flame spread - SBI tests

4.1 Introduction

As mentioned in the introduction, flame spread is a complicated phenomenon involving several processes, such as heat transfer by radiation, convection and conduction, chemical and physical reactions in the solid phase, and turbulent combustion in the gas phase. To reasonably predict flame spread, sub-models are required to represent these phenomena. As mentioned in the previous chapters, a step-wise strategy has been employed to study the flame spread behavior on building's façade. Up to now, we have investigated the buoyant flow, under-ventilated enclosure fire, pyrolysis and combustion of MDF in small-scale. Now we move to the case of intermediate scale, namely the Single Burning Item (SBI) test [28] in a corner configuration.

Zeinali et al. [96] conducted SBI tests with MDF panels placed in a corner configuration, see Figure 4.1. The material is the same MDF as in the small scale tests of section 3.3. The Heat Release Rate, total heat fluxes, and temperatures in the panels at several characteristic points were measured in the test. The experimental setup is shown in Figure 4.2, including an enclosure and a testing trolley. The long panel is 1.5 m high and 1.0 m wide, while the short panel is 1.5 m high and 0.5 m wide. Figure 4.3 indicates the location of the measurement points of the heat fluxes and temperatures.

The triangular propane burner, with sides of length 0.25 m, is located at the corner (with a 0.04 m gap from the panels). It takes 30 s for the burner to reach its peak HRR of 30 kW, after which it is fixed until the end of the test (see Figure 4.4).

Before conducting the MDF panel tests, a calibration test has also been conducted

with inert calcium silicate panels. More details can be found in [96].

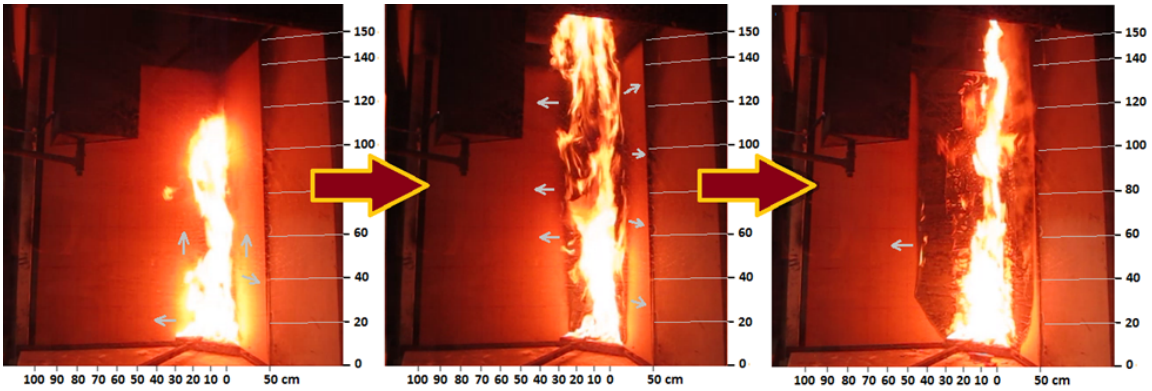

Figure 4.1: Flame spread over MDF panel in a corner configuration of SBI test. [Reproduced with permission from [96].

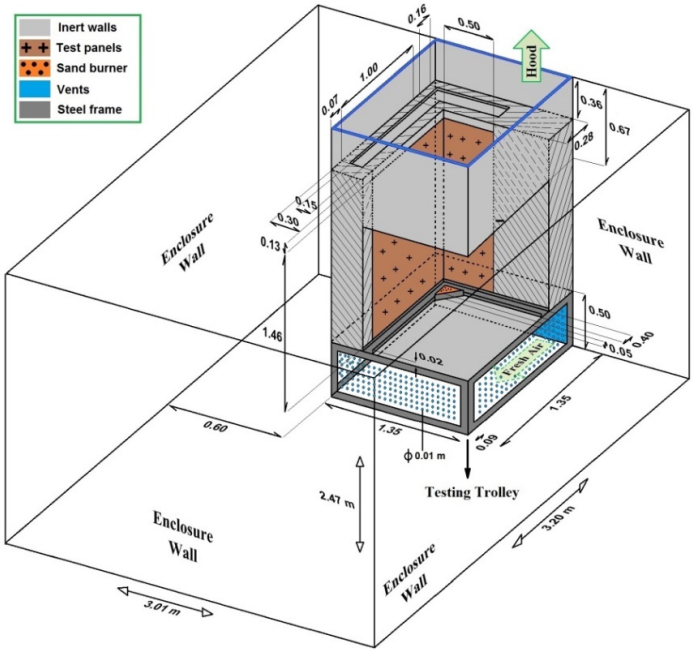

Figure 4.2: Schematic of the SBI test. [Reproduced with permission from [96].

4.2 Numerical setup and simulation details

FDS (version 6.2.0) is employed in this section with default turbulence (modified Deardorff) and combustion models, as well as the default radiation fraction of 0.35 as lower bound to limit the uncertainties in the radiation calculation induced by uncertainties in the temperature field.

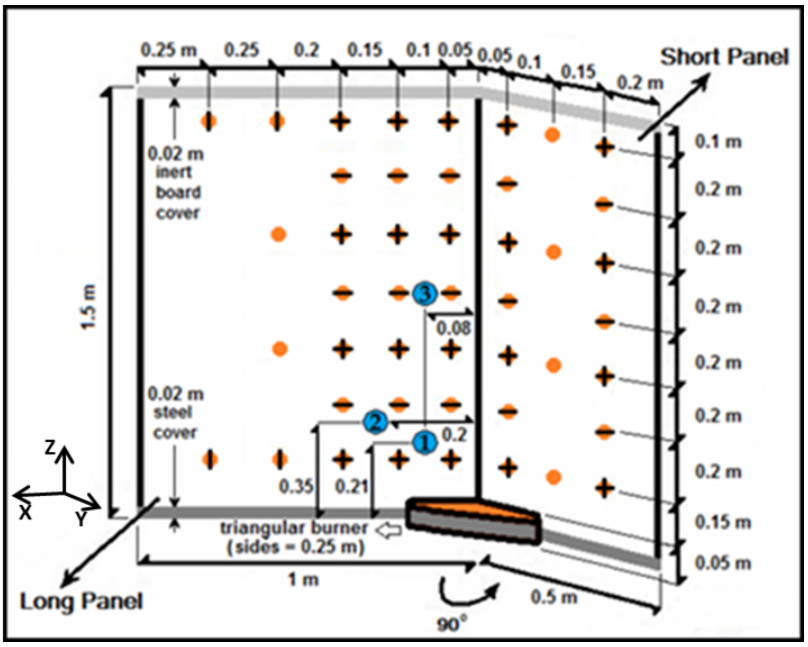

Figure 4.3: The geometry of panels and the measurement points of the temperatures (orange points) and total heat fluxes (blue points). Reproduced with permission from [96].

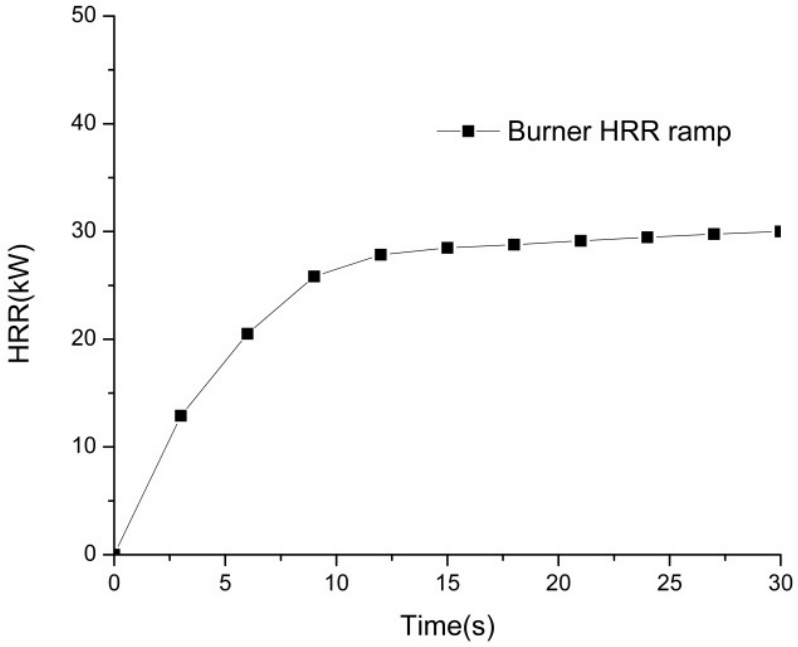

Figure 4.4: The HRR ramp of the burner in the SBI tests.

For the inert wall case, the wall material is calcium silicate board, 12.3 mm thick. The density of the calcium board is 1005 kg/m^3. The thermal conductivity is 0.17 W/(m·K), the specific heat is 920 J/(kg·K). A value of 0.9 is used for both the emissivity and absorptivity. The material properties of the calcium silicate panels are presented in Table 4.1, from the technical specification sheet provided by the supplier.

Table 4.1: Material properties of the calcium silicate panel

Property	Value
Thickness [m]	0.0123±0.001
Density [kg/m^3]	1005±5%
Moisture content [%]	5-10
Thermal conductivity [W/(m·K)]	0.17[a]
Specific heat capacity [J/(kg·K)]	920[b]

[a] The nominal value of thermal conductivity is 0.17, 0.19 and 0.21 W/(m·K) at temperatures of 293, 373 and 473 K.
[b] The nominal value at 673 K.

For the MDF panel case, the same pyrolysis model has been applied as described in section 3.2.2. The value of 12 MJ/kg has been used for the heat of combustion, as obtained from the cone calorimeter test (see section 3.4.2). This value is an effective value, which accounts for the combustion heat of both MDF and char. The dimensions of the MDF panels are the same as the calcium boards (Figure 4.3). The other parameters of the model are the same as in the updated case in Table 3.3.

The simulation domain was first chosen as 1 m x 2 m x 1 m. In order to save computational time, a finer cell size has been used for the area near the burner, and a coarser cell size was applied to the rest of the domain (Table 4.2). The simulation time is 900 s

4.3 Inert wall case

For the modelling of flame spread on any combustible material, the heat flux received on the surface is essential. Hence, the heat flux prediction of the inert wall case is studied first. Additionally, the surface and backside temperatures have been measured during the experiment at different locations. The results are discussed in this section.

The calculation is expensive in terms of the computation time for cases using the complete enclosure geometry, including the exhaust hood, all enclosure walls, the opening on the side wall, and the trolley, etc. Therefore, most of the numerical studies from the

literature are considering simplified enclosure geometry, which exclude the enclosure walls and the side wall opening, presuming this has a negligible influence on the flow field and the flame spread behaviour. However, one can also consider 'complete' enclosure geometry. Figure 4.5 illustrates the computational domain for the 'complete' enclosure geometry and the 'simplified' enclosure geometry. As can be seen in the left figure, the 'compelete' enclosure geometry includes the entire enclosure of the test. There is a bottom opening at the backside of the enclosure, through which fresh air flows into the domain. First of all, a simplified model has been considered.

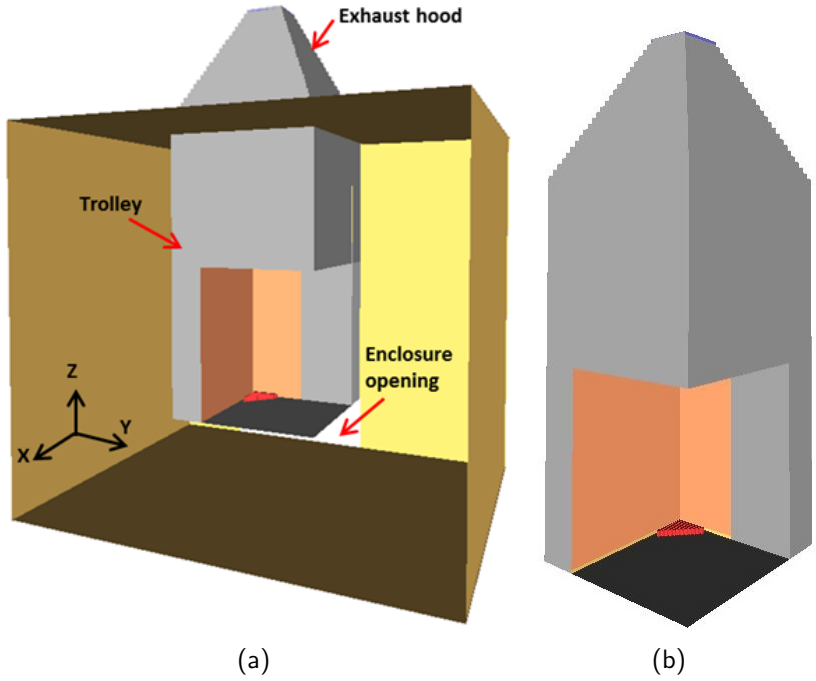

Figure 4.5: The computational domain of the 'complete' model (a) and 'simplified' model (b).

4.3.1 Grid size

A grid sensitivity study has been performed for the heat flux predictions, considering three grid cell sizes: 4 cm, 2 cm, and 1 cm. Three different cell sizes have been applied for each of the inert wall case, namely 1 cm, 2 cm, and 4 cm. Table 4.2 shows a summary of these simulations.

In order to set up an LES model of good quality, a sufficient amount of the Turbulent Kinetic Energy (TKE) should be resolved on the mesh. In the literature, the criterion of Pope [105] stating that at least 80 % of the TKE should be resolved on the mesh, is quiet common. In FDS a Measure of Turbulence Resolution (MTR) is used as an approximation

Table 4.2: Summary of the SBI test simulations.

Case number	Wall material	Geometry	Finest cell size
Case 1			1 cm
Case 2	Calsium silicate	simplified	2 cm
Case 3			4 cm

to the Pope criterion [106]. MTR value near 0.2, means 80 % of the kinetic energy are resolved. As is shown in Figure 4.6, for case with 2 cm cell size, the time-averaged MTR values of the entire plane are lower than 0.2(the averaging time period is from 200 s to 400 s), this meet Pope's criterion.

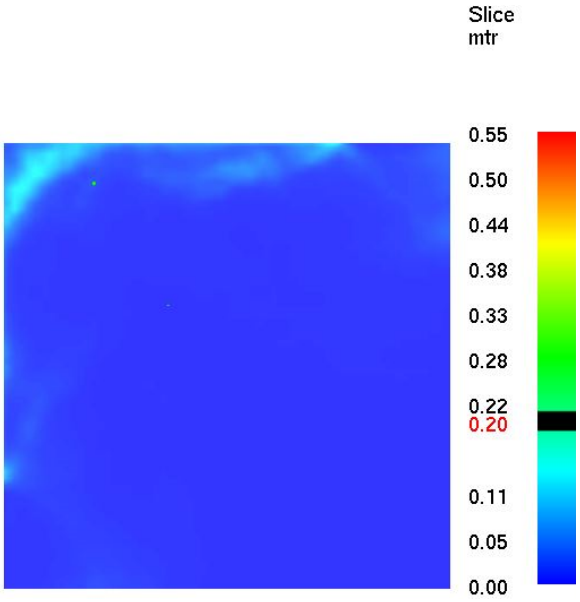

Figure 4.6: Time-averaged Measure of Turbulence Resolution in the inert wall case using a 2 cm cell size

The heat flux predictions on the panel at three characteristic points, namely points 1 (x = 0.08 m, y = 0 m, z = 0.21 m), 2 (x = 0.2 m, y = 0 m, z = 0.35 m) and 3 (x = 0.08 m, y = 0 m, z = 0.8 m), are demonstrated in Figure 4.3. The comparison between the time-averaged prediction and test measurement is presented in Table 4.3, reporting average values for the time period from 100 s to 300 s.

The deviation ϵ_{hf} is defined as follows:

$$\epsilon_{hf} = \left| 1 - \frac{q''_{exp} + q''_{sim}}{q''_{exp}} \right| \times 100\% \tag{4.1}$$

Where q''_{exp} is the heat flux measurement from the test, and q''_{sim} is the model prediction.

Table 4.3: Heat flux on the panel at 3 points (averaged values from 100 s until 300 s).

Scenario	Heat flux 1 (kW/m^2)	Heat flux 2 (kW/m^2)	Heat flux 3 (kW/m^2)	Simulation time (h)
Experiment	48.7	17.5	25.3	-
1 cm cell size	48.7(0.1%)	7.5(57.0%)	20.5(19.1%)	301
2 cm cell size	41.1(15.6%)	6.0(65.7%)	17.4(31.1%)	174
4 cm cell size	27.7(43.0%)	3.6(79.2%)	4.2(82.5%)	7

In general, a finer grid size produces higher heat fluxes, as explained in section 3.4, which are in better agreement with the experimental data.

For points 1 and 3, the predictions on the finest mesh are relatively close to the experimental data, while for point 2 it is strongly under-estimated (by 57% even on the finest mesh). A similar trend has been reported in the numerical study with FDS using the simplified enclosure geometry in [100]. It should be noted that points 1 and 3 (x = 0.08 m) are much closer to the corner than point 2 (x = 0.2 m). As a consequence, points 1 and 3 are continuously within the flame zone, while point 2 is in the intermittent flame zone in the simulations. In other words, the heat flux at point 2 is strongly related to the flame shape, which is in turn driven mainly by the flow field in the domain. The flow pattern might be affected by the use of the simplified geometry, not capturing the effect of the enclosure as in the experiments. This is discussed in the following section.

4.3.2 Results and discussion

In order to investigate the potential influence on the flow field and further influence on the burning of the combustible panels, four scenarios have been conducted as listed in Table 4.4.

The volume flow rate from the exhaust hood on top of the testing trolley is set to be 0.60±0.05 Nm^3/s (normal cubic meter per second at 298 K). A value of 0.6 m^3/s is applied in the numerical model.

4.3.2.1 Flow field

The flow field was first analyzed for cases 1 and 2 with the hood activated and the burner switched off, in order to compare the influence of the geometry model on the flow

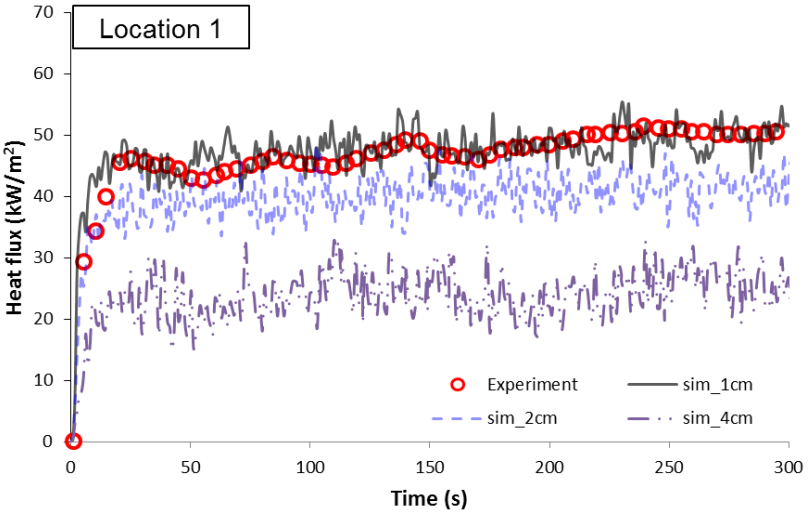

Figure 4.7: Heat flux evolution at Point 1 (x = 0.08 m, y = 0 m, z = 0.21 m) for three grid cell sizes.

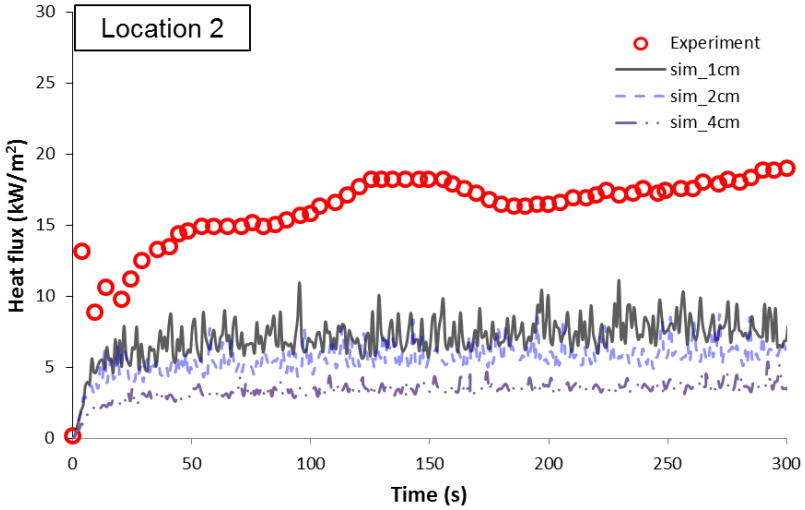

Figure 4.8: Heat flux evolution at Point 2 (x = 0.2 m, y = 0 m, z = 0.35 m) for three grid cell sizes.

Table 4.4: List of scenarios to investigate the influence of the geometry in the SBI test.

Scenario	Enclosure geometry	Burner	Panel	Finest cell size
Case 1	simplified	off	Calsium silicate	2 cm
Case 2	complete			2 cm
Case 3	simplified	on	MDF	2 cm
Case 4	complete			2 cm

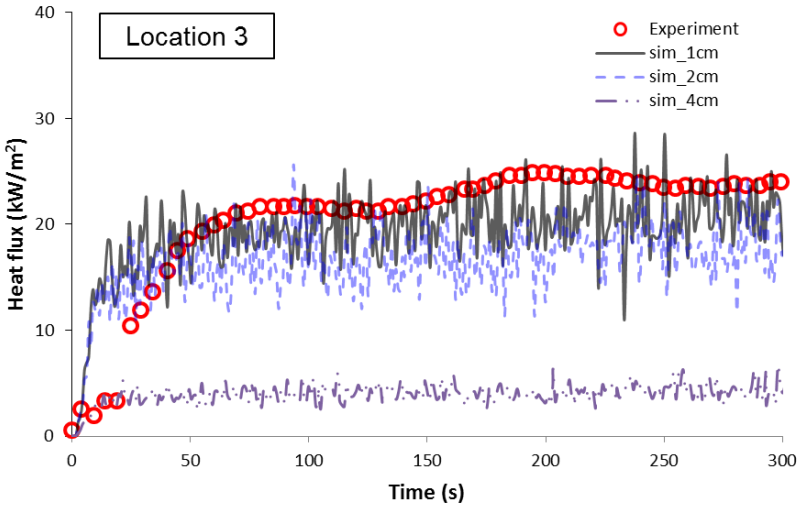

Figure 4.9: Heat flux evolution at Point 3 (x = 0.08 m, y = 0 m, z = 0.8 m) for three grid cell sizes.

field induced by the extraction flow rate. In the figures below, the vector slice files of the velocity at t =100 s at the corner are demonstrated at height 0.8 m above the floor. A clear anticlockwise rotation near the corner is observed in the flow field for case with complete enclosure geometry, while for simplified case there are two separate rotating vortices further away from the corner. To show this in another way, the time-averaged u-velocity and v-velocity of both cases are presented in Figure 4.11 and Figure 4.12 at the plane of height z = 0.8 m. The averaging time period is from 200 s and 700 s. Significantly different flow patterns have been observed between cases with 'complete' model and 'simplified' models, this would definitely influence the heat flux distribution on the panel and the buoyant flow, and then influence flame spread in the combustible wall scenario.

4.3.2.2 Total Heat flux

As presented in Figure 4.13, the time-averaged contour plot of the heat fluxes received on the short and the long panels are compared for the case 3 and case 4 (see Table 4.4). The averaging time period is from 200 s to 700 s. In general, the area of the panel with 20 kW/m^2 or higher heat fluxes of the 'simplified' model case is narrower and higher than in the case with 'complete' enclosure geometry. Point 2, for instance, falls in the intermittent flame zone, which is consistent with the experimental observation. However, the time-averaged heat flux received in the 'complete' model is relatively higher than in the 'simplified' one. Moreover, the heat flux at height z= 1 m for the 'simplified' case is higher.

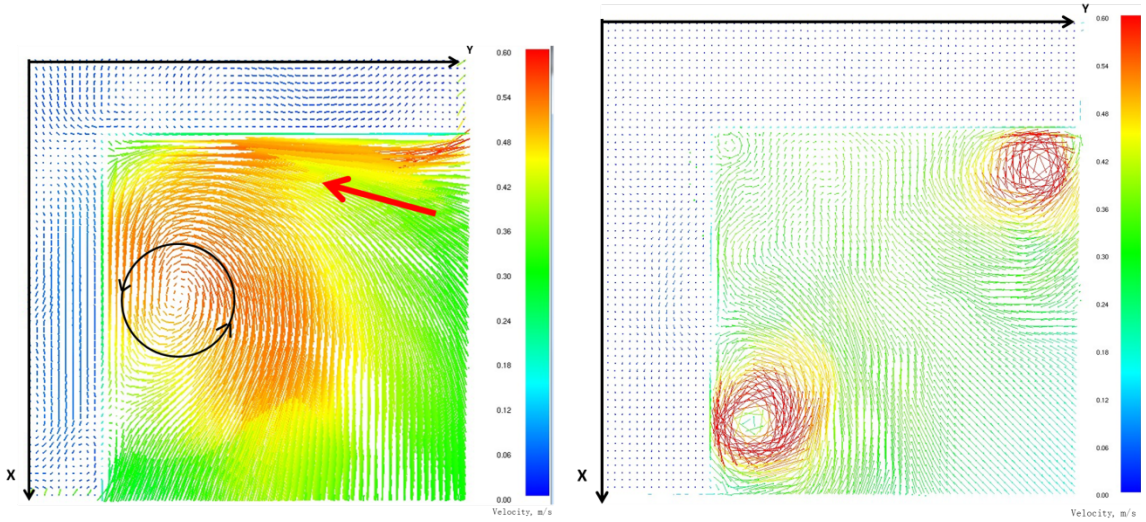

(a) (b)

Figure 4.10: Velocity at plane of height z = 0.8 m at time t = 100 s for cases with 'complete' model (a) and with 'simplified' model (b).

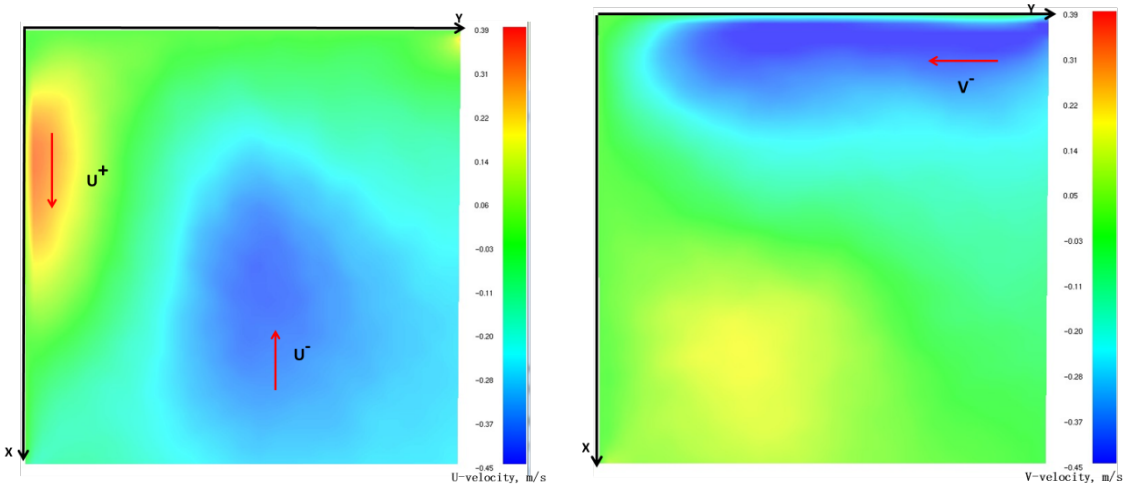

(a) (b)

Figure 4.11: Time-averaged u-velocity (a) and v-velocity (b) at height z =0.8 m in case with 'complete' model.

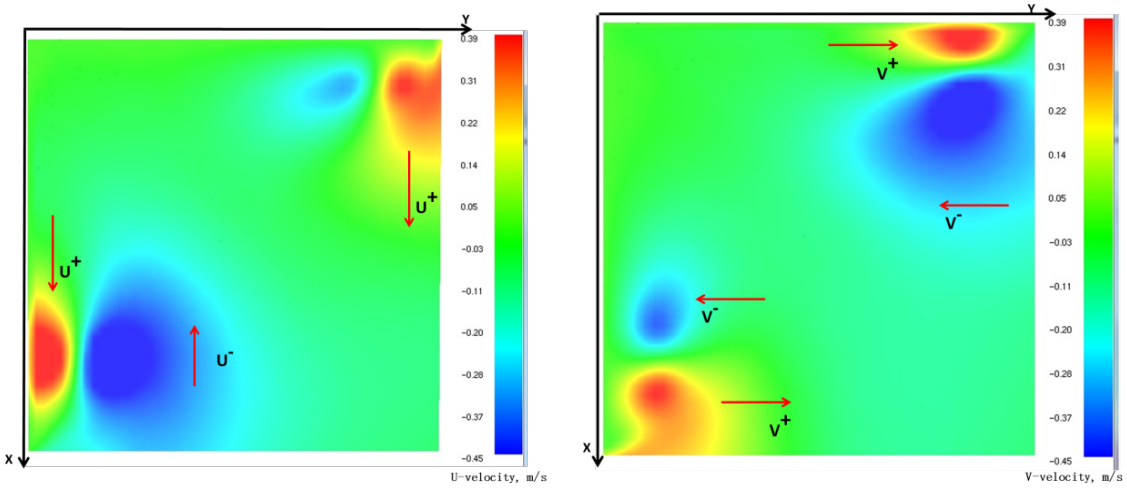

(a) (b)

Figure 4.12: Time-averaged u-velocity (a) and v-velocity (b) at height z =0.8 m in case with 'simplified' model.

A higher heat flux is observed at the area near the core of the contour plot for the 'complete' case, which is the persistent flame zone. Location 1 is close to this zone, which is constantly covered by a strong heat flux in both cases. A quantitative analysis will be presented in the following part.

As shown in Figures 4.14-4.16, comparisons of the heat flux evolution of location 1, 2 and 3 are presented. The time-averaged values have also been determined for these results, the averaging time period is from 100 s to 300 s, during which period a relatively steady state has been reached for these locations.

In general, the heat fluxes are underpredicted for all three locations. Results from cases using 'complete' model are more fluctuating, especially at locations 1 and 2.

For location 1, which is close to the corner (see Figure 4.13), the heat flux predictions from 'complete' model case are in good agreement with the experiment data (with a 2.2 % deviation), while the results from 'simplified' model case are 15.6 % lower than the experiment data (see Table 4.5).

For location 2, which is 0.2 m away from the corner, the heat fluxes are well underestimated in both cases, by 44.5 % in the 'complete' model case and 65.7% in the 'simplified' model case, respectively. The predictions at locations 1 and 2 are clearly improved with 'complete' model. As has been discussed in section 4.3.2.1, this probably relates to the predicted shape of the flame, and the measuring point 2 is out of the intermittent flame zone in the 'simplified' model case (the predicted flame with the 'simplified' model is

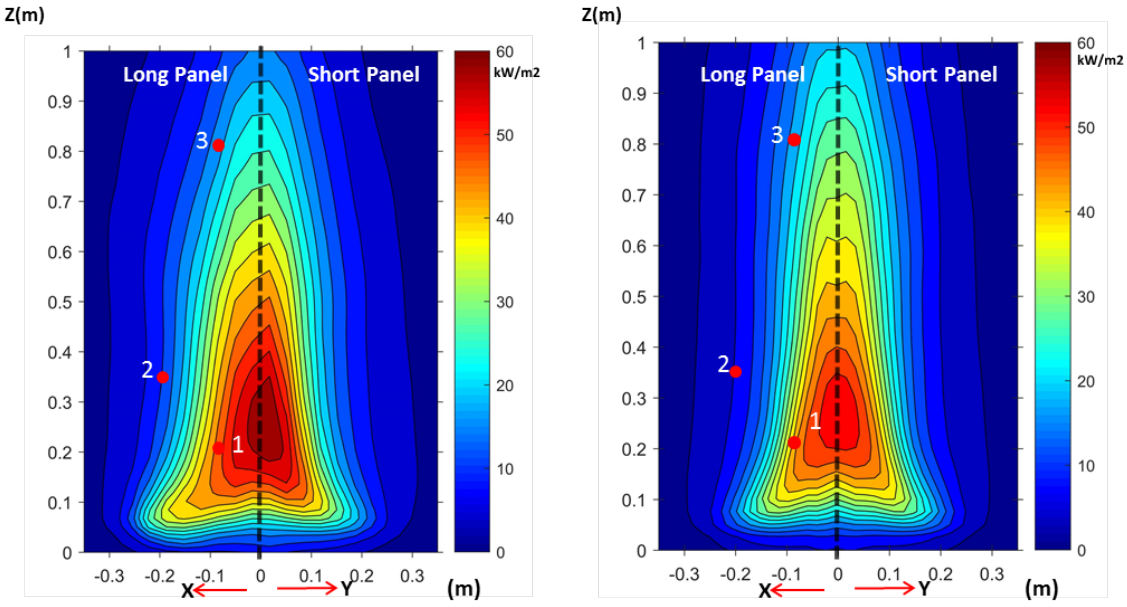

(a) (b)

Figure 4.13: Time-averaged heat flux on the panels for case 3 with (a) 'complete' model, and case 4 (b) 'simplified' model (see Table 4.4).

narrower than with the 'complete' model).

For location 3, although the heat fluxes of both cases are lower than the experimental data, they are quite close to each other, while the results from 'simplified' model are slightly higher (deviation of 35.2 % and 31.3 %, respectively). Together with the time-averaged heat flux contour plots in Figure 4.13, a higher flame is expected in the 'simplified' case.

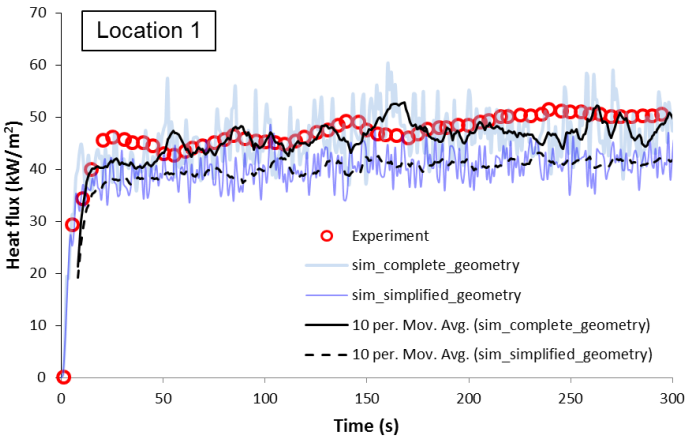

Figure 4.14: Comparison of heat fluxes at location 1 (x=0.08, y=0, z=0.21) between cases with complete enclosure geometry and simplified enclosure geometry in the inert wall case.

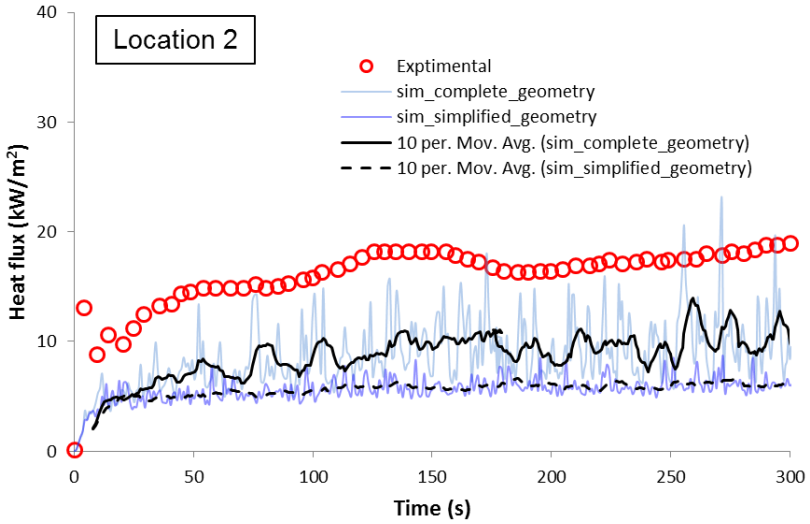

Figure 4.15: Comparison of heat fluxes at location 2 (x=0.2, y=0, z=0.35) between cases with 'complete' enclosure geometry and 'simplified' enclosure geometry in the inert wall case.

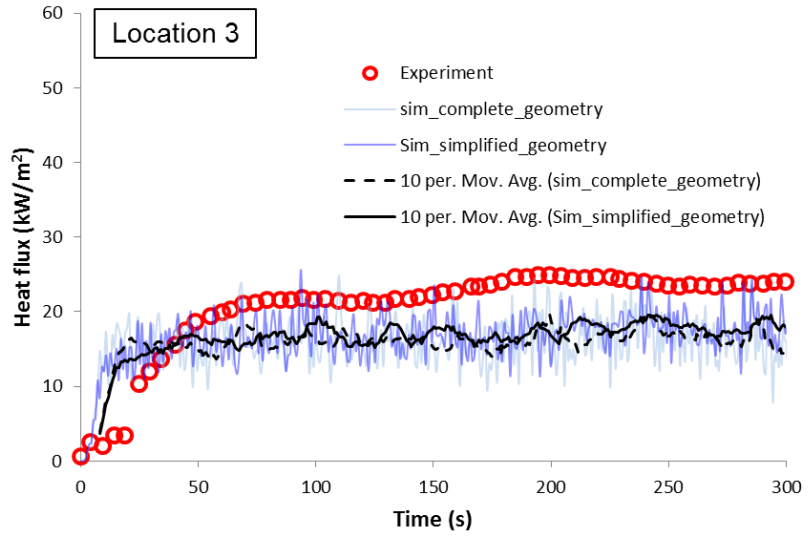

Figure 4.16: Comparison of heat fluxes at location location 3 (x=0.08, y=0, z=0.8) between cases with 'complete' enclosure geometry and 'simplified' enclosure geometry in the inert wall case.

Generally, the choice of the enclosure model has a clear influence on the flow field and heat flux predictions, and a 'complete' model is recommended. However, the computational time using complete enclosure geometry is much longer than the 'simplified' model. The possible effects of the enclosure geometry on the flame spread over the panel need further investigation.

Table 4.5: Heat flux comparison on the panel at 3 points (averaged values from 100 s until 300 s).

Scenario	Heat flux 1 (kW/m^2)	Heat flux 2 (kW/m^2)	Heat flux 3 (kW/m^2)
Experiment	48.69	17.48	25.33
Complete case	47.6 (2.2%)[a]	9.7 (44.5%)	16.4(35.2%)
Simplified case	41.1(15.6%)	6.0(65.7%)	17.4(31.3%)

[a] The percent deviation from experiment data.

4.4 Combustible wall case

Now we focus on the combustible wall case. As already has been discussed in section 4.3.2.1, different flow patterns near the corner and heat flux distribution on the panels have been observed between cases with 'complete' model and 'simplified' model. This would influence the flame spread behavior in scenarios with MDF panels on the wall. Moreover, we have studied the pyrolysis and combustion in small scale test in chapter 3, coupling with that enables us to study the fire behavior in an intermediate scale combustible wall case, namely the SBI test [96]. In this section, the material and model parameters of the MDF panel are the same as the updated case from Table 3.3 in chapter 3.

4.4.1 Heat Release Rate

Figure 4.17 shows the HRR comparison between the experiment and simulations of cases using simplified model and complete model. The experimental curves are averaged from three repeat tests. Although the overall trend of the HRR curve is well captured, both cases upderpredicted the HRR for most of the time. The time to reach the peak of the HRR curve is well predicted by both cases. In the experiment, the HRR reaches a relatively sharp peak of 152 kW at around 156 s, while in the simulations, relatively smooth peaks are obtained with peak values of 135 kW in the complete model case and 127 kW for the simplified model case at the time period around 156 s.

Note that, the predicted HRR from the ‘complete‘ model case is slightly higher than the simplified model case for the time period roughly between 70 s and 300 s. From 320 s until the end of the simulation, both cases are at the same level and in line with eath other. For the time from the start to 500 s, there are slightly more heat released in the complete case.

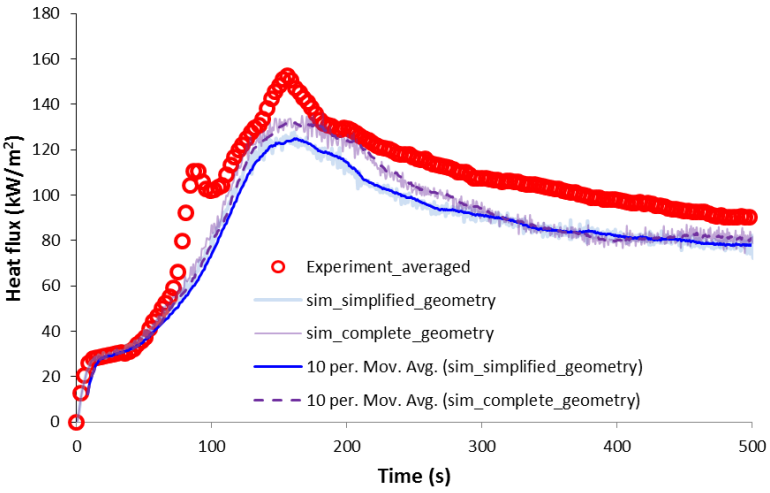

Figure 4.17: Heat Release Rate comparisons between experimental data and simulations using 'complete' model and simplified model.

4.4.2 Total Heat fluxes

Figure 4.18-4.20 display the total gauge heat flux between simulations using 'complete' and 'simplified' model and those recorded in the experiments with MDF panels [96].

As opposed to the inert case, the experimental profiles are more fluctuating and no steady state can be obtained. Much similar to the heat flux profiles of simulation with inert panels, the heat flux profiles in both cases are underpredicted for all three locations. In general, simulation of 'complete' model case features higher heat fluxes than 'simplified' model case for these three locations.

For location 1, which is located nearest to the burner, the prediction can be considered most reasonable (as opposed to the other locations), because heat fluxes at this location are mainly from the burner.

For locations 2 and 3, it is more challenging to provide accurate predictions, since they are further away from the burner, requiring accurate prediction of the flame shape. Consequently, the heat flux is substantially underpredicted. This trend is similar to the inert wall case. Moreover, the predicted heat fluxes at location 2 are quiet close to those in the inert wall case, which failed to capture the overall trend of the experimental profile. Further investigations are needed to better predict the flame shape.

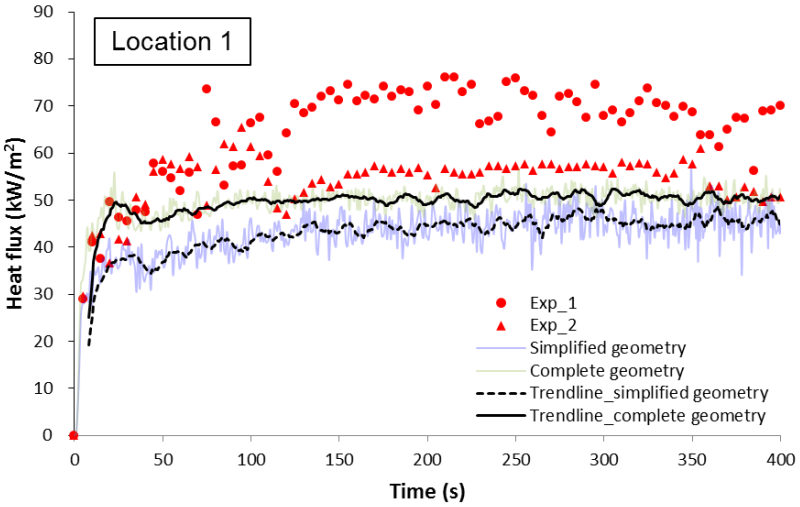

Figure 4.18: Comparison of heat flux at location 1 (x=0.08, y=0, z=0.21) between cases with 'complete' enclosure geometry and 'simplified' enclosure geometry in the MDF panel case.

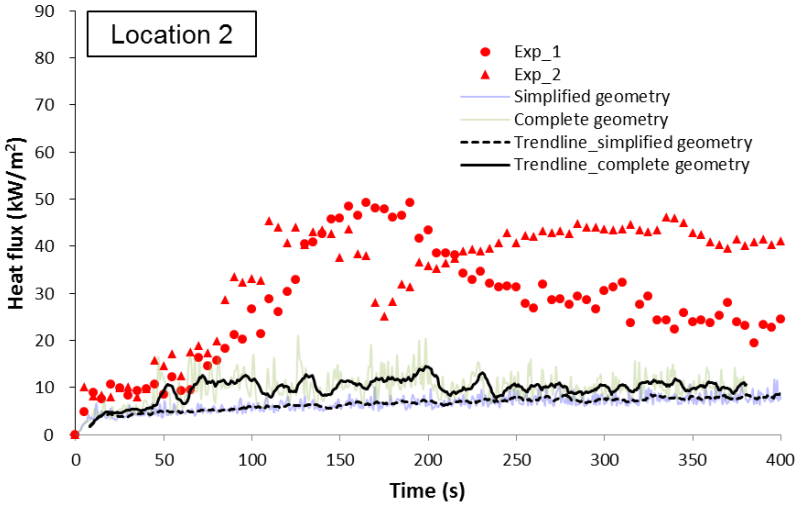

Figure 4.19: Comparison of heat flux at location 2 (x=0.2, y=0, z=0.35) between cases with 'complete' enclosure geometry and 'simplified' enclosure geometry in the MDF panel case.

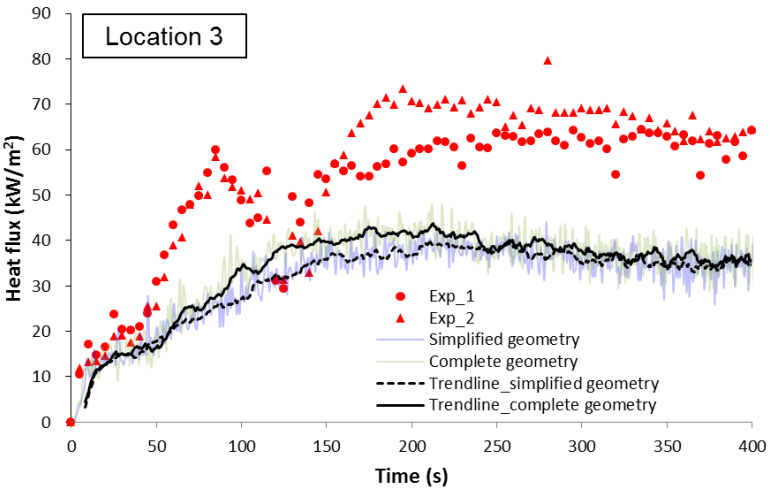

Figure 4.20: Comparison of heat flux at location 3 (x=0.08, y=0, z=0.8) between cases with 'complete' enclosure geometry and 'simplified' enclosure geometry in the MDF panel case.

4.5 Conclusions

In this chapter, the use of CFD for flame spread has been studied in a scenario with intermediate scale, namely the SBI test in a corner configuration. This was done through simulation of several SBI corner fire experiments conducted with MDF panels and a calibration test with calcium silicate panels, using updated material properties determined in chapter 3.

A grid size sensitivity study has been conducted comparing the heat fluxes at three characteristic points for the inert wall case. In general, a finer grid size produces higher heat fluxes, and shows better agreement with the experimental data. Taking into account of the computational time and the accuracy, a 2 cm cell size is deemed suitable.

Both 'complete' and 'simplified'geometry models were considered to investigate the influence of the completeness of the geometry in the model on the predictions. Significantly different flow patterns have been observed between the 'complete' model case and 'simplified' model case.

Further investigations have been made of the total gauge heat fluxes at several characteristic locations on the MDF panels. The total gauge heat flux predictions from both 'complete' model case and 'simplified' model case were reasonably similar to the experimental data in both the inert wall and MDF panel cases. Most differences in the simulations were observable further away from the corner, where an accurate prediction

of the flame shape proved challenging for both cases, resulting in great fluctuations in the heat flux predictions. In general, the simulation of the ‘complete‘ model case features higher heat fluxes than the ‘simplified‘ model case for these three locations. Similar to the heat flux prediction, higher HRR peak has been obtained in the ‘complete‘ model case than ‘simplified‘ model case, and the overall trend has been reasonably captured with the numerical model.

Based on the findings of this study, it is recommended for future computational assessment of SBI-like scenarios to properly account for the completeness of the enclosure geometry. The choice of the enclosure model is expected to influence the flow field, the radiation on the panels and the flame spread on the combustible wall. A ‘complete‘ model is recommended if computational resources allow it.

Chapter 5

Proof of concept of the use of CFD for façade fires

5.1 Problem description

In the previous chapters, the use of CFD has been studied in terms of the coupling of gas phase and solid phase reaction, and the vertical flame spread over combustible wall in SBI test. These studies enable us to assess the potential use of CFD for façade fires. In this chapter, a fictitious numerical test case is designed and studied, in which the MDF panel is used as façade wall material in the under-ventilated enclosure configuration.

In this chapter, characteristics of the flame spread in a façade fire are first studied, including the heat release rate, heat fluxes on the façade wall, burning rate of MDF panel, and pyrolysis height. Besides that, wind obviously plays an important role in the development of the façade fire. When studying the flame spread behavior in façade fires, one cannot ignore the influence of the wind in the environment. It can dramatically change the fire dynamics. Therefore, the wind effect on the flame spread in this scenario is numerically investigated as well.

For simplicity, the wind condition designed in this test case is assumed to be constant. The influences of the wind condition on the flame spread behavior are discussed. These evaluations serve as a proof of concept for the use of CFD for understanding façade fires.

5.2 Numerical set-up and simulation details

5.2.1 Geometry

In this fictitious test case, the same experimental set-up and measurements are employed as that in the under-ventilated enclosure case discussed in section 2.2 (see Figure 2.15 and Figure 2.16). The dimensions of the enclosure, the façade wall and the burner are also the same. Instead of an insulation fiberboard plate, an MDF panel is used as external façade wall material in this study. The material and model properties of the MDF panel are the same as those of the SBI case in chapter 3, which are shown in Table 3.3 (the updated case).

As shown in Figure 5.1(a), the computational domain is based on 2.02 m high in the z-direction, 1.1 m in the x-direction, and 0.8 m in the y-direction. All the boundaries are set to be open, except for the case with external wind.

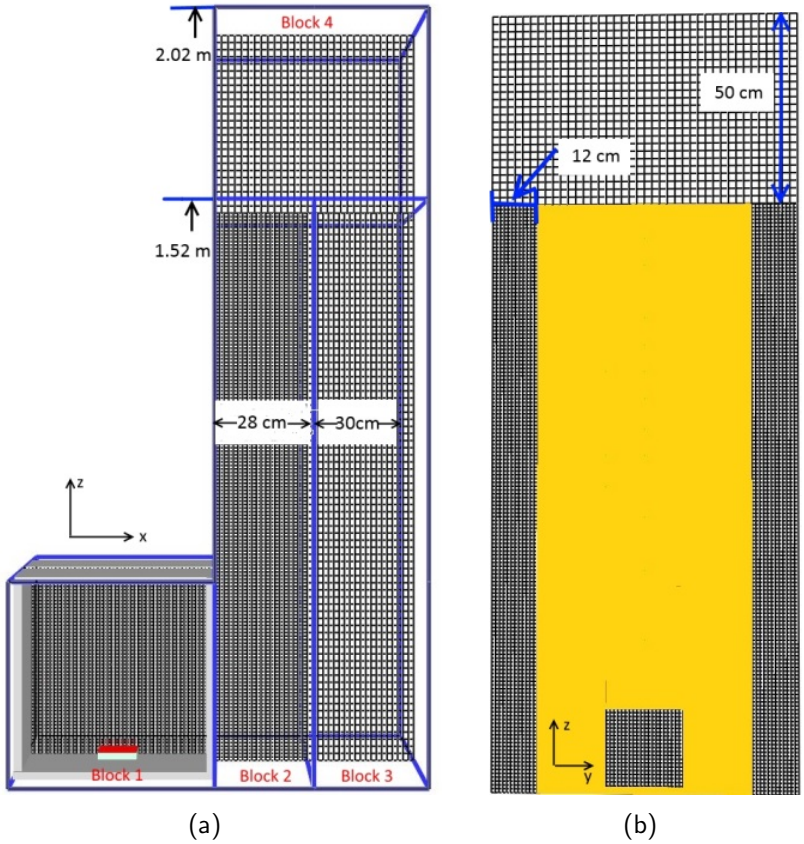

Figure 5.1: Sketch of the computational mesh and domain, (a): Global view showing 4 meshing blocks;(b): side view showing the façade wall.

In order to limit the influence of the 'open' boundary condition on the flow field, the computational domain has been extended by 50 cm at the domain above the façade wall. Besides, the computational domain also extends 12 cm beyond the sides of the façade MDF panel, to allow the flame to extend beyond the façade wall as well. This has been demonstrated in Figure 5.1(b). For the case with wind from the side direction, the domain in y-direction has been extended to 1.2 m

5.2.2 Grid resolution

Grid resolution plays an import role as shown in the previous chapters. In this case, the grid resolution for both the fire source and the openings needs to be considered. As has been illustrated in section 2.2, the required cell size needs to be 2 cm or finer for this consideration. However, as shown in section 2.2, a 1 cm or finer cell size is required for coupled gas phase-solid phase fire simulations.

Subsequently, the grid used for this case features two levels of resolution, namely 1 cm and 2 cm cell size. As shown in Figure 5.1(a), there are four meshing blocks in total within the computational domain. Block 1 is used for the entire enclosure, and block 2 is assigned to the part of the domain where a strong interaction occurs between the gas phase (from the external flame) and the solid phase (i.e., the MDF façade). A finer cell size of 1 cm is used for blocks 1 and 2, while a coarser grid is employed for the other two blocks (2 cm cell size). This grid size results in 554,000 cells in total. Four computing processors (2.6 GHz CPU with 32 GB RAM) were used.

5.2.3 Other settings

A 0.1 m x 0.2 m propane burner provides a fire source with 60 kW theoretical heat release rate. It is very important that all the quantitative results are linked to this (from a conceptual point of view essentially arbitrary) choice of HRR. Qualitatively, the discussion holds for any HRR value, in particular for under-ventilated conditions.

The burner is located at the center inside the enclosure. In order to obtain under-ventilated conditions inside the enclosure, an opening size of 0.2 m x 0.2 m is considered. It is positioned centrally in the façade, bottom side flush with the floor. It is very important that all the quantitative results are linked to this (from a conceptual point of view essentially arbitrary) choice of opening size and position. Qualitatively, the discussion holds for any HRR value, in particular for under-ventilated conditions. With this opening geometry, the maximum value of heat release rate inside the enclosure can be estimated to be 26.8 kW (using $1500A\sqrt{H}$). In other words, under-ventilated conditions prevail for

a HRR of 60 kW. The ambient temperature is set to be $20°C$.

The MDF panel used in this study was 0.018 m thick, 0.56 m wide and 1.52 m high. For the inert wall case, the same fiberboard plate was used as in section 2.2. The backside of the panel is exposed to the surrounding air to allow for the heat loss from the wall.

Several heat flux gauges and thermocouples (TCs) were placed at various heights at the centerline of the façade wall. The mass inflow and outflow rates through the opening have been monitored. The actual heat release rate has been determined by integrating the heat release rate per unit volume 'HRRPUV'.

The wind effect on the flame spread on building façade has also been investigated in this chapter. Several values of the wind speed ranging from 0 - 8 m/s have been considered. Two wind directions have been investigated, namely perpendicular towards the façade wall, and parallel to the façade wall. Table 5.1 shows a list of simulations conducted in this study. The simulation results are discussed in the following sections. wo

5.3 Results and discussion

An extensive study is carried out to investigate the characteristics of flame spread in the façade fire scenario.

5.3.1 Heat Release Rate

First, a brief description of the fire behaviour is presented. As the opening size limits the fire size inside the enclosure, the unburned gases have to find some fresh air outside the enclosure, and continue to burn in the form of ejecting flames. This occurs very fast in the simulation for this set-up, i.e., flames eject at around t = 10 s. As shown in Figure 5.2, both total HRR curves of the MDF panel case and inert wall case have a drop at around t = 10 s, at a value of HRR about 24 kW. After that, the fire size continues to increase in both cases.

In order to explain this drop in the HRR, the 2-D plots of the HRRPUV are presented in Figure 5.3. At the beginning of the simulation, the fuel reacts mainly with the oxygen, initially present inside the enclosure, so the fuel burns mainly inside the enclosure, until it reaches a value of approximately 40 kW. After that, the opening size limits the oxygen supply and the fire experiences under-ventilated conditions inside the enclosure, resulting in a drop in the fire HRR to a value about 24 kW. It is interesting to note that this value is in line with the value estimated from $(1500A\sqrt{H})$. Subsequently, the fuel travels

Table 5.1: List of simulations

Case No.	Wall type	Wind direction	Wind (m/s)
1	MDF	-	0
2	MDF	perpendicular	0.1
3	MDF	perpendicular	0.2
4	MDF	perpendicular	0.4
5	MDF	perpendicular	0.6
6	MDF	perpendicular	0.8
7	MDF	perpendicular	1
8	MDF	perpendicular	1.2
9	MDF	perpendicular	1.4
10	MDF	perpendicular	1.6
11	MDF	perpendicular	1.8
12	MDF	perpendicular	2
13	MDF	perpendicular	4
14	MDF	perpendicular	6
15	MDF	perpendicular	8
16	Inert	perpendicular	0
17	Inert	perpendicular	0.1
18	Inert	perpendicular	0.2
19	Inert	perpendicular	0.4
20	Inert	perpendicular	0.6
21	Inert	perpendicular	0.8
22	Inert	perpendicular	1
23	Inert	perpendicular	1.2
24	Inert	perpendicular	1.4
25	Inert	perpendicular	1.6
26	Inert	perpendicular	1.8
27	Inert	perpendicular	2
28	Inert	perpendicular	4
29	Inert	perpendicular	6
30	Inert	perpendicular	8
31	MDF	parallel	0.2
32	MDF	parallel	0.4
33	MDF	parallel	0.8
34	MDF	parallel	1.2
35	MDF	parallel	2
35_1	MDF	parallel	4
35_2	MDF	parallel	6
35_3	MDF	parallel	8
36	Inert	parallel	0.2
37	Inert	parallel	0.4
38	Inert	parallel	0.8
39	Inert	parallel	1.2
40	Inert	parallel	2
40_1	Inert	parallel	4
40_2	Inert	parallel	6
40_3	Inert	parallel	8

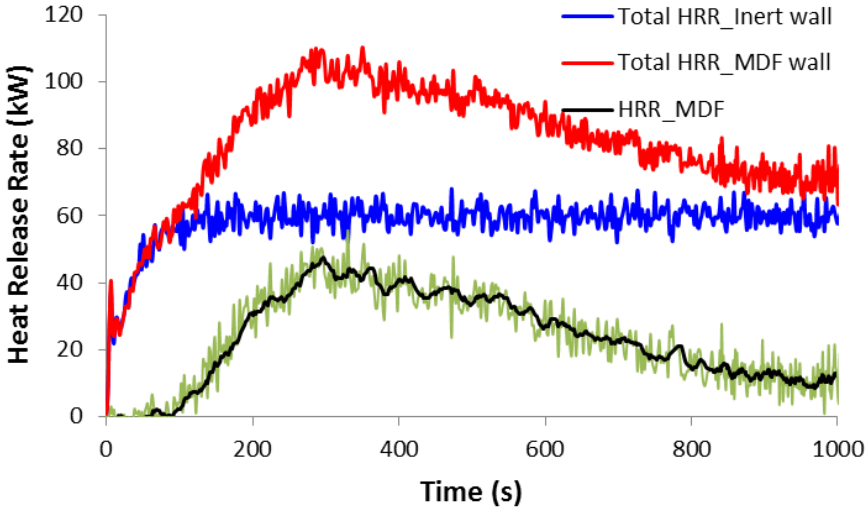

(a)

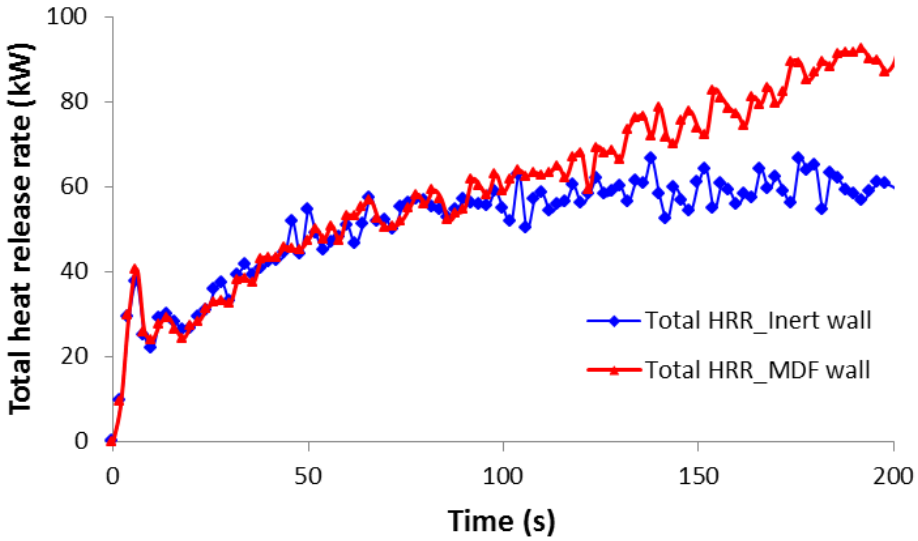

(b)

Figure 5.2: Heat release rate in the MDF panel case (case #1) and in the inert wall case (case #16); (b): zoom of the first 200 s. Note that the total HRR profiles include the HRR from the burner.

towards the opening to find oxygen from outside of the enclosure and the flame ejects and burns outside. A similar phenomenon has already been observed in [102] in a corridor-like scenario.

The ejecting flames serve as an external heat source, pyrolyzing the MDF panel on the façade wall. For the inert wall case, the heat release rate curve reaches a relative steady state at around t = 130 s onward with a value of 60 kW, and maintains this value until the end. This is logical since all the fuel from the burner burns inside the computational domain. The total heat release rate of the MDF panel case exceeds that of the inert wall case at around t = 72 s. This is when the MDF panel starts to burn.

With the spread of flame over the MDF façade, the total HRR increases rapidly. At around t = 260 s, the pyrolysis front reaches the top of the façade wall. The total heat release rate reaches its peak at t = 285 s with a peak value of 109 kW. It was confirmed that all the fuel released in the gaseous phase burns inside the computational domain, by checking the HRRPUV results. Therefore the HRR from the burning of the MDF panel can be calculated by subtracting the HRR from the fire source inside the enclosure. This is demonstrated in Figure 5.2 as well. The maximum heat release rate from the MDF façade is 50 kW.

5.3.2 Heat flux on the Panel

The gauge heat flux at the façade centerline have been monitored at heights z = 0.2 m,0.24 m, 0.3 m, 0.38 m, 0.48 m, 0.63 m, 0.78 m, 0.93 m, 1.01 m, 1.22 m, 1.36, 1.43 m, and 1.5 m for both the MDF case and the inert wall case. Figure 5.4 shows the gauge heat flux evolution for both cases. The profiles in both cases indicate a rapid increase at the first stage for all the heights. After that, for the inert case, the heat fluxes reach a relative steady state from around t = 130 s onward (the lower the height, the faster to reach the steady state). This is also when the heat release rate reaches the peak value, maintaining this value until the end.

The distribution of the time-averaged heat flux on the centerline of the façade is presented in the Figure 5.5 (including the total incident heat flux, and its radiative and convective contribution). Figure 5.6 shows the time-averaged 2-D contour plots of temperature and velocity of the inert wall case. The averaging time period is from 200 s to 600 s. First, the incident heat flux slightly increases from 26.6 kW/m^2 at height of 0.2 m to 29.3 kW/m^2 at height of 0.5 m, and decreases back to around 26 kW/m^2 at height of 0.8 m, then dramatically decreases as the height increases, to 2.4 kW/m^2 at the top of the façade. Moreover, the heat transfer is mainly dominated by radiation. The convective

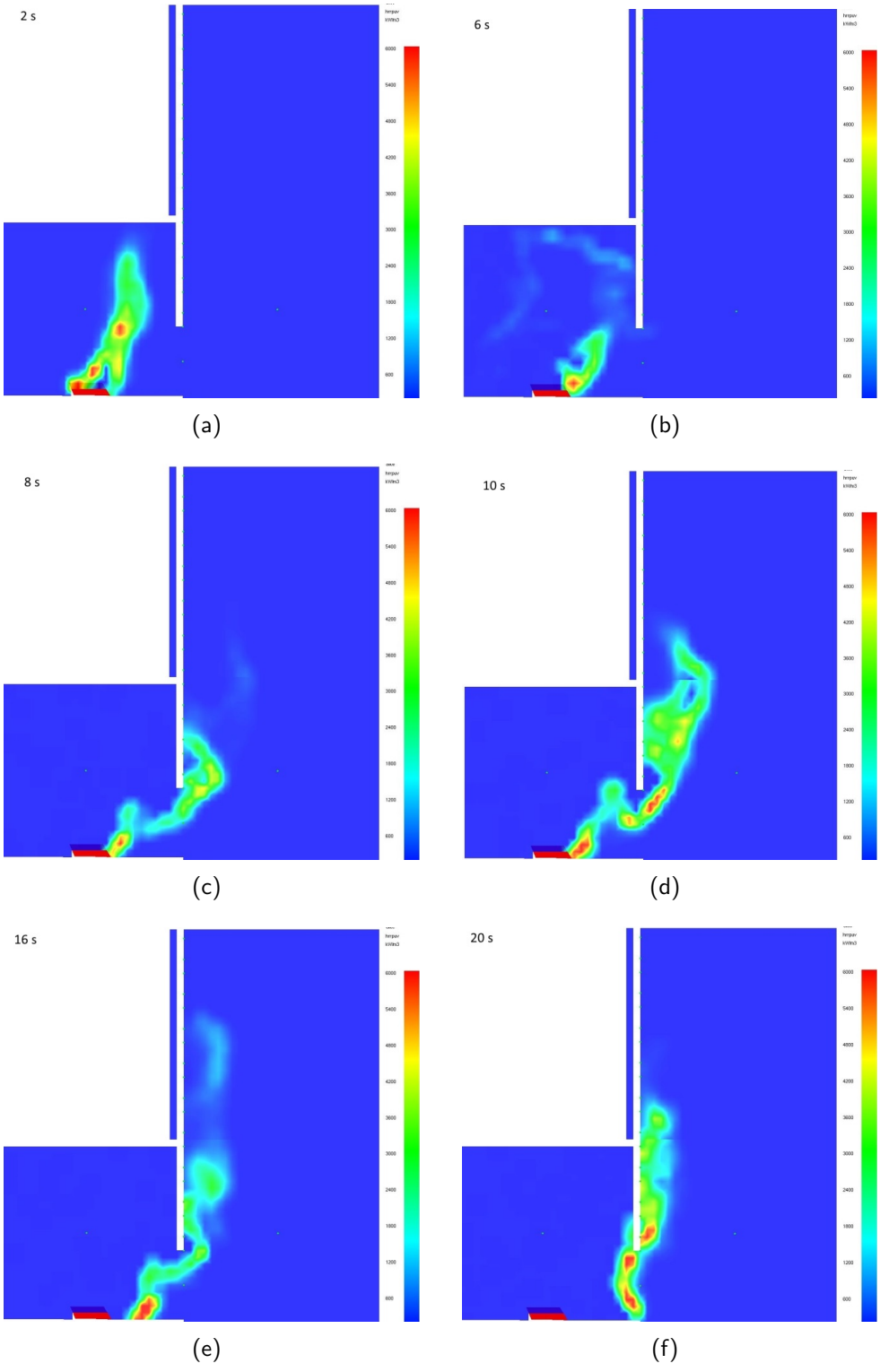

Figure 5.3: 2-D contour plot of the HRRPUV for the first 20 s.

heat fluxes on the centerline of the façade are always higher than 10 kW/m^2.

As shown in Figure 5.4, for the MDF wall case, there are also steady state periods in the heat flux profiles at lower heights (below 0.78 m). For higher locations, a different pattern is observed. There is no steady state period for these curves, i.e., heat fluxes drop after reaching the peak value. However, the differences between heat flux values obtained for the inert case and the MDF case are smaller at lower positions (z $<$ 0.78 m) than at higher positions (z $>$ 0.78 m).

In order to explain this, we compare the temperature contour plots of the inert wall case (averaged between 200 s and 600 s) and the MDF case (averaged between 280 s and 320 s) in Figure 5.7. The latter period has been chosen, because the HRR reaches a maximum value (see Figure 5.2). The distribution of heat fluxes on the façade wall centerline for the MDF case is shown in Figure 5.8. The flame in the MDF case is obviously much higher, due to the additional burning region at the upper part of the panel. However, at low heights (z $<$ 0.78 m), the view factor for radiation from the flames stemming from the additional burning region from the MDF panel is small. Moreover, there is no convective contribution from these flames to the bottom part (z $<$ 0.78 m) because the flow is upward. Thus, the differences in heat flux values between the inert case and MDF case are small in this region. In the upper region (z $>$ 0.78 m) on the other hand, the radiative heat flux from the flame is higher than the inert case, even though the convective part is lower(less than 5 kW/m^2, this is probably due to the blowing effect in the pyrolysis region), the overall heat flux are higher than in the inert case.

As also shown in Figure 5.4, the time for the MDF curve to reach the peak heat flux is later for higher locations, this relates to the vertical flame spread. That will be discussed in the following section.

5.3.3 Pyrolysis height

The pyrolysis heights were determined by considering a critical value for the mass loss rate of the MDF panel. The idea is that a sufficient amount of pyrolysis gases must be generated for a diffusion flame to establish above the surface. This idea was first proposed by Bamford [103]. In the literature, the critical mass flux value is reported to vary between 1 - 3 g/(m^2·s) for wood material [104]. Within the range in the literature, a value of 2 g/(m^2·s) was chosen as a criterion, interestingly, this value also corresponds to the maximum value of the mass flux at the moment when the MDF starts to contribute to the HRR (see Figure 5.2). Based on this criterion, the pyrolysis front of the flame spread over the façade panel was located. The results have been demonstrated in Figure 5.9.

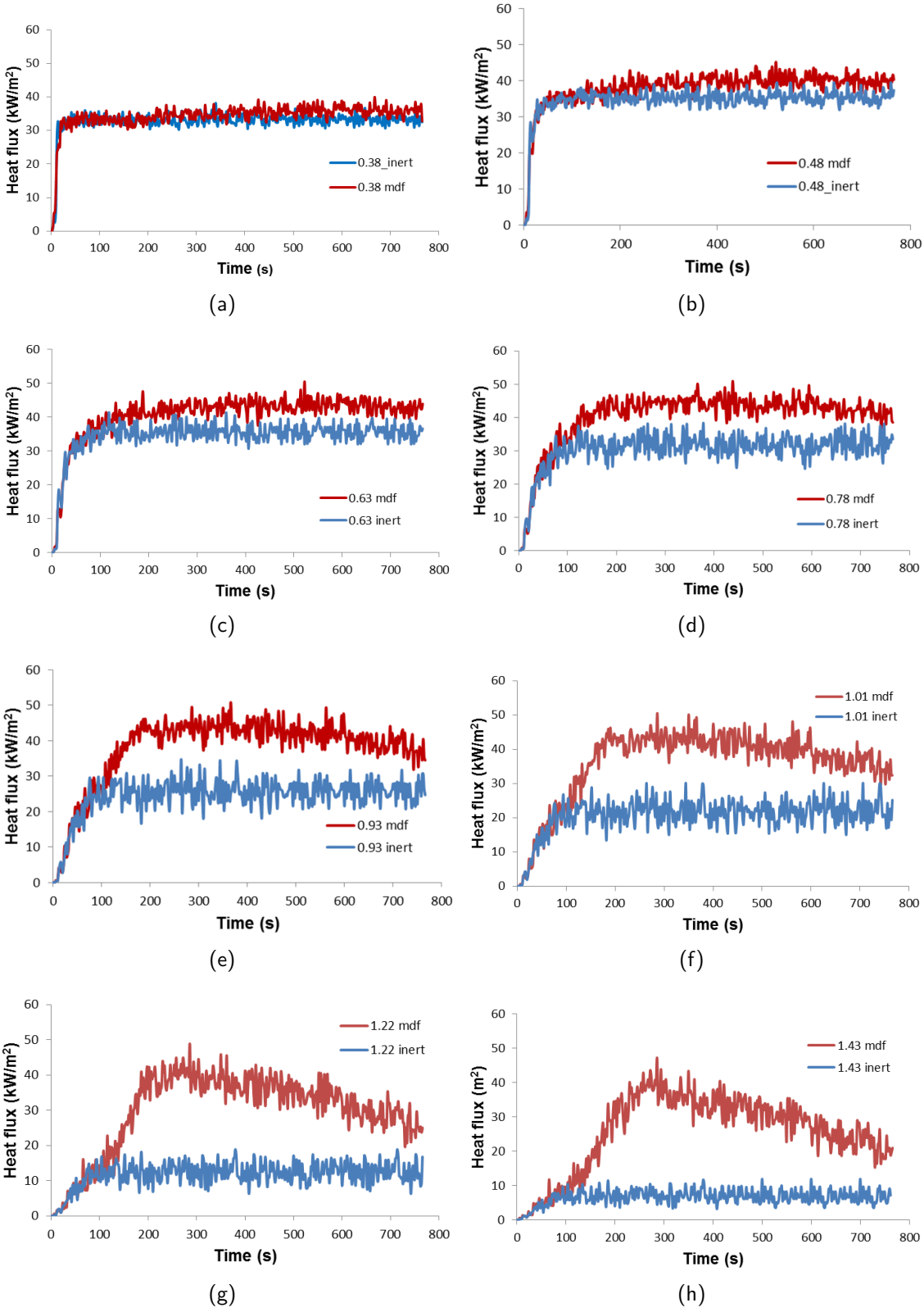

Figure 5.4: Heat flux evolution profiles at heights z = 0.38 m, z = 0.48 m, z=0.63 m z= 0.78 m z= 1.01 m, z= 1.22 m, and 1.43 m for both the MDF case and the inert wall case (case #1 and #16).

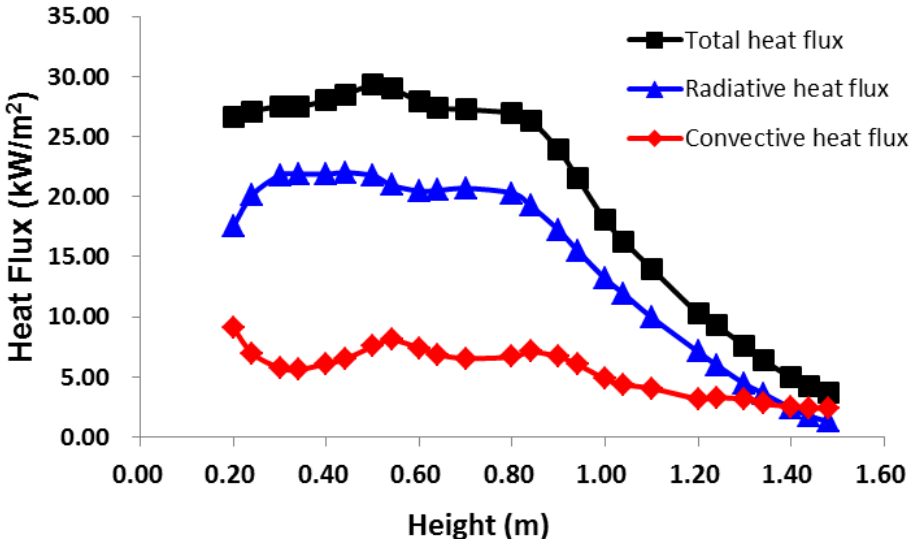

Figure 5.5: Distribution of heat fluxes (the incident heat flux and its radiative and convective contribution) on the façade wall centerline for the inert wall case (the averaging time period is from 200 s to 600 s).

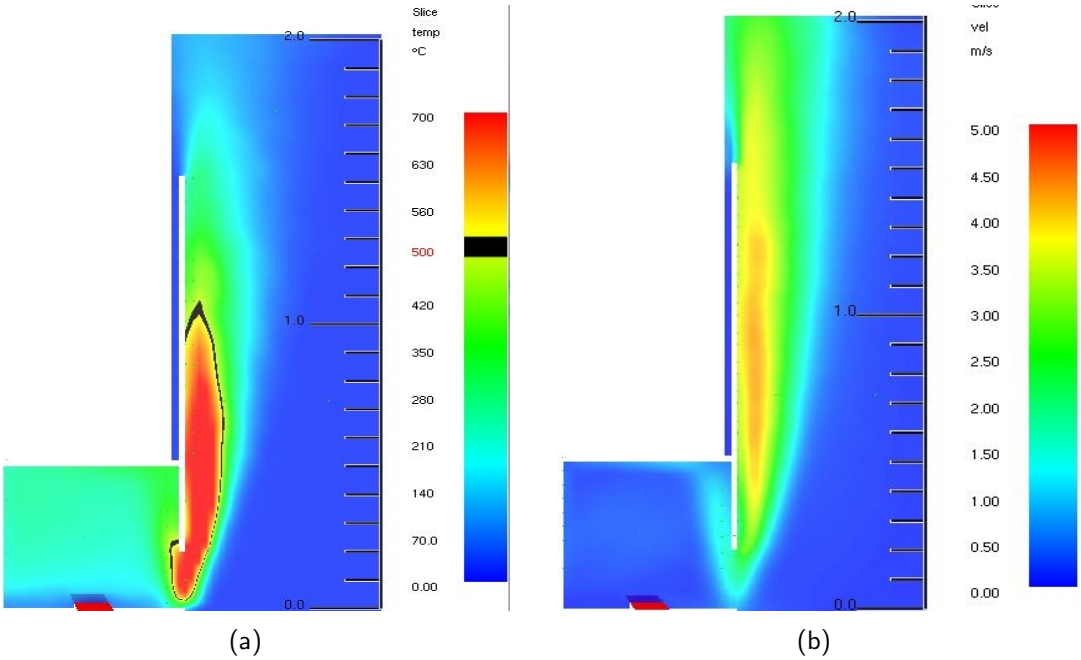

(a) (b)

Figure 5.6: Time-averaged contour plots of temperature (a) and velocity (b) of the inert wall case (the averaging time period is from 200 s to 600 s).

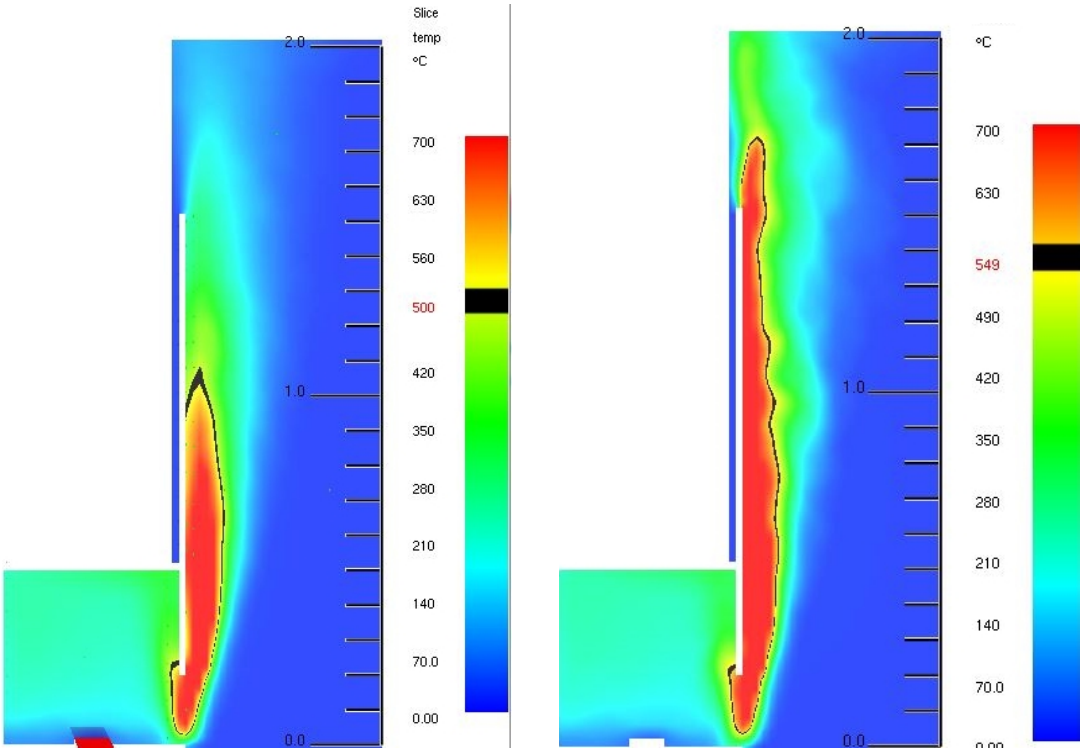

Figure 5.7: Temperature contour plot of the inert wall case (a) (averaged between 200 s and 600 s) and the MDF case (b)(averaged between 280 s and 320 s).

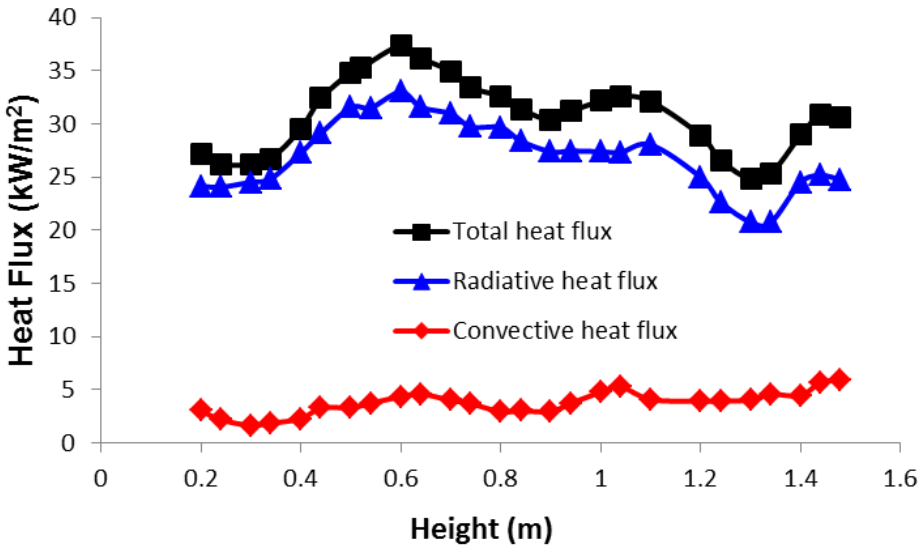

Figure 5.8: Distribution of heat fluxes on the façade wall centerline for the MDF case (the averaging time period is from 280 s to 320 s.).

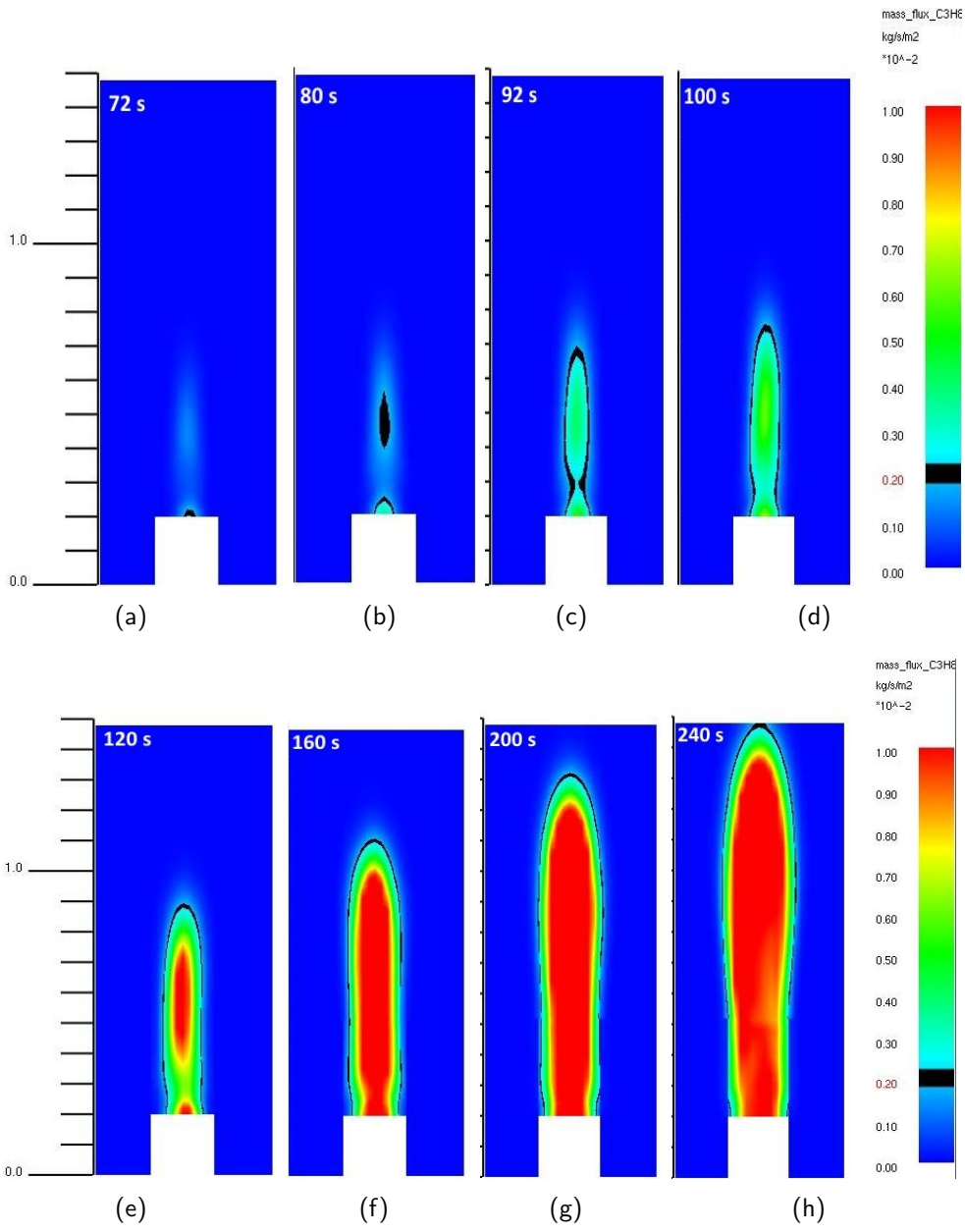

Figure 5.9: Pyrolysis front locations determined using a critical mass flux criterion (2 g/(m^2·s) for the MDF panel case.

As shown in Figure 5.9, the façade panel starts to burn at t = 72 s at the top of the opening. Later, a second burning area appears at heights between 0.4 m and 0.6 m at time t = 80 s. This is in line with the heat flux distribution in the inert case, where a region with lower heat fluxes was illustrated between heights 0.2 m and 0.4 m (see Figure 5.5). At around 92 s, the two areas merge into one and then the burning area expands gradually. At around t = 240 s, the pyrolysis front reaches the top of the MDF panel.

The exact pyrolysis front locations at the centerline of the panel at various times were determined using the mass flux criterion. The mass flux distribution on the MDF panel is plotted in Figure 5.10. For time between t= 80 s and t = 92 s, there are three pyrolysis front locations. Among these three locations, the higher two enclose the upper burning area. After t = 92 s, there is only one pyrolysis front, which is the upper front.

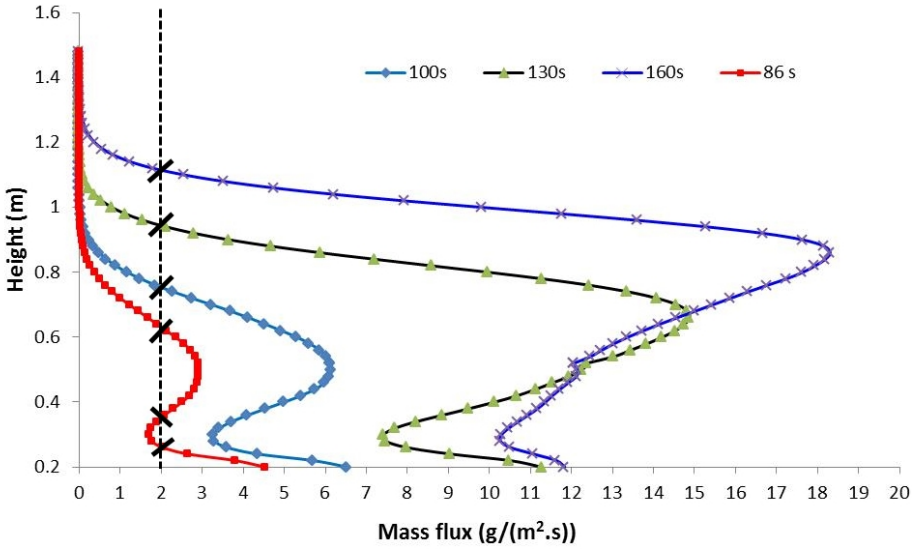

Figure 5.10: Mass flux value along the centerline of the MDF panel at time t = 86 s, t = 100 s, t = 130 s, and t= 160 s.

In order to analyze the spread rate of the pyrolysis height, the pyrolysis height was plotted as a function of time in Figure 5.11. The pyrolysis height jumps to a higher value when the second burning area appears at around 80 s. For the time period from 80 s until 240 s, a linear correlation is observed between the pyrolysis height (H_p) and time after ignition. The dash line in this figure indicates a constant flame spread, with an average velocity of about 0.006 m/s.

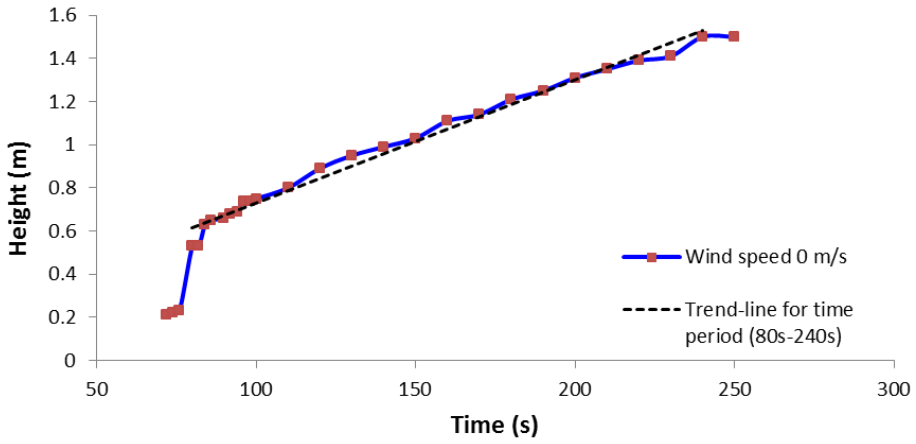

Figure 5.11: Pyrolysis height history in the absence of wind.

5.3.4 Wind effect

As mentioned in the introduction, the wind plays an important role in the development of the façade fire. In this section, the influence from the wind is investigated. The wind velocity was considered to be constant, flowing into the computational domain from the boundary opposite the façade wall and from the side, as shown in Figure 5.12.

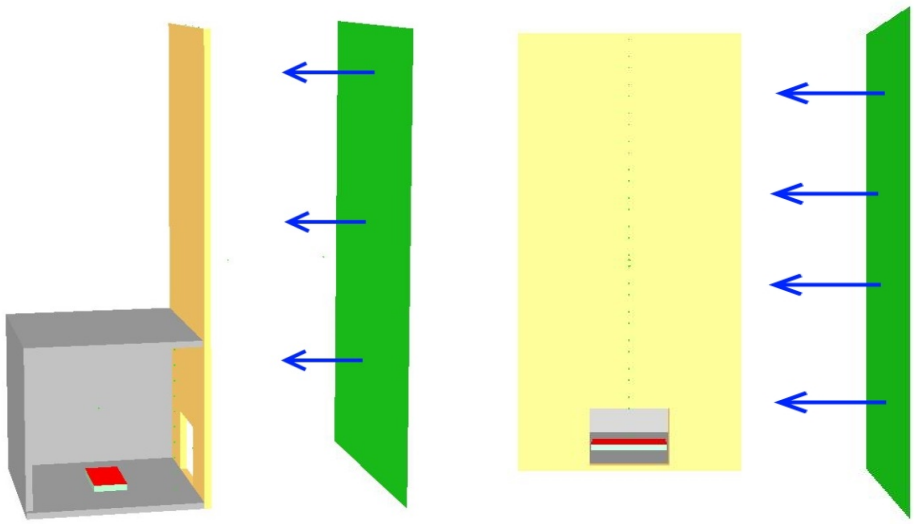

Figure 5.12: Wind condition in the façade wall case. (a): wind perpendicular to the façade, (b): wind parallel to the façade.

A top-hat profile is applied as the boundary condition for the wind velocity. For cases with wind from the opposite boundary, various values of the wind speed ranging from 0 to

8 m/s have been considered, namely 0 m/s, 0.1 m/s, 0.2 m/s, 0.4 m/s, 0.6 m/s, 0.8 m/s, 1 m/s, 1.2 m/s, 1.4 m/s, 1.6 m/s, 1.8 m/s, 2 m/s, 4 m/s, 6 m/s, and 8 m/s for both MDF panel case and inert wall case. For the side wind case, the velocity values of 0.2 m/s, 0.4 m/s, 0.8 m/s, 1.2 m/s, 2 m/s, 4 m/s, 6 m/s, and 8 m/s have been considered for both the inert wall case and MDF case. This wind condition is an idealistic scenario designed mainly to numerically study the influence of different environmental wind conditions, and therefore it is not meant to be an exact reflection of the wind in reality. In the following sections, an extensive study is conducted to discuss the wind effect on the façade fire.

5.3.4.1 Flow rate through the opening

The mass flow rate through the opening plays a significant role in the façade fire scenario, where the amount of supplied fresh air determines the burning condition of the ejecting flame. Changing the wind speed will definitely affect the flow condition through the opening. The wind could also push the ejecting flames closer to the façade.

Figure 5.13 presents the evolution profiles of mass flow rates through the ventilation opening for cases with wind 0 m/s, 4 m/s (wind perpendicular to the facade). Though a higher wind speed tends to induce higher mass flow rate, both the mass outflow and inflow rates are approximately constant during most of the time. For 0 m/s and 4 m/s, the average values of inflow rates are 0.006 kg/s and 0.0217 kg/s, respectively. Similarly, the average values of outflow rates are 0.005 kg/s and 0.0191 kg/s for 0 m/s and 4 m/s, respectively. The averaging period is considered from t= 200 s to 600 s.

The time-averaged mass flow rates for all the wind speed cases have been plotted in Figure 5.14, illustrating the influence of the wind speed on the mass flow rate through the opening. For speeds below 0.8 m/s, both the mass inflow and outflow rates are more or less the same as that of the case with 0 m/s wind speed, namely around 0.006 kg/s outflow rate and 0.005 kg/s inflow rate. For wind speeds between 0.8 m/s and 2 m/s, the mass flow rate slightly drops first for both the inflow and outflow, namely to around 0.005 kg/s and 0.004 kg/s at the wind speed of 1.4 m/s, respectively. Later, the mass flow increases dramatically, up to 0.046 kg/s inflow and 0.039 kg/s outflow at the wind speed of 8 m/s.

Note that as the wind speed increases, the difference between the outflow and inflow rates increases as well. This is due to post-processing in FDS. We have contacted the developers of FDS, it was confirmed: *'This is merely an apparent error at the level of post-processing. In FDS, a simple central difference scheme is used to compute the MASS FLOW for output, which differs from the more complicated flux limiting scheme used at*

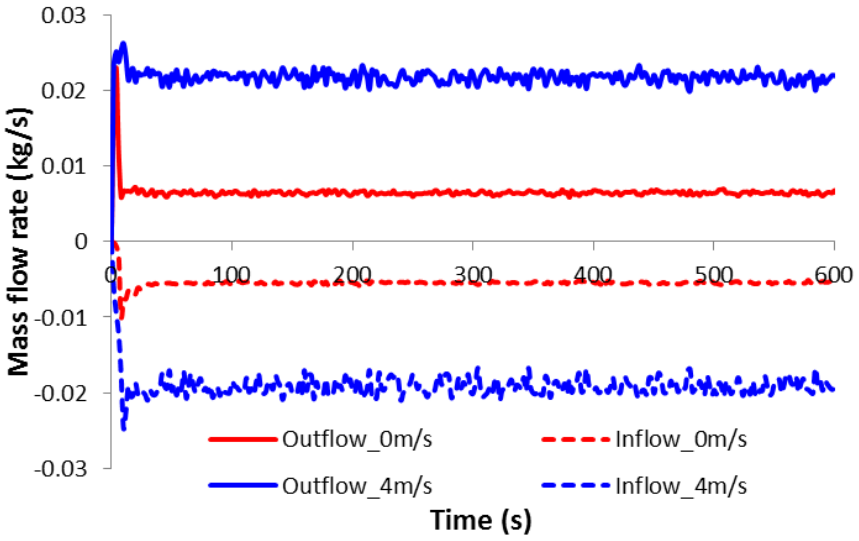

Figure 5.13: Temporal evolution of mass flow rate through the ventilation opening for wind speeds of 0 m/s and 4 m/s.(wind perpendicular to the facade)

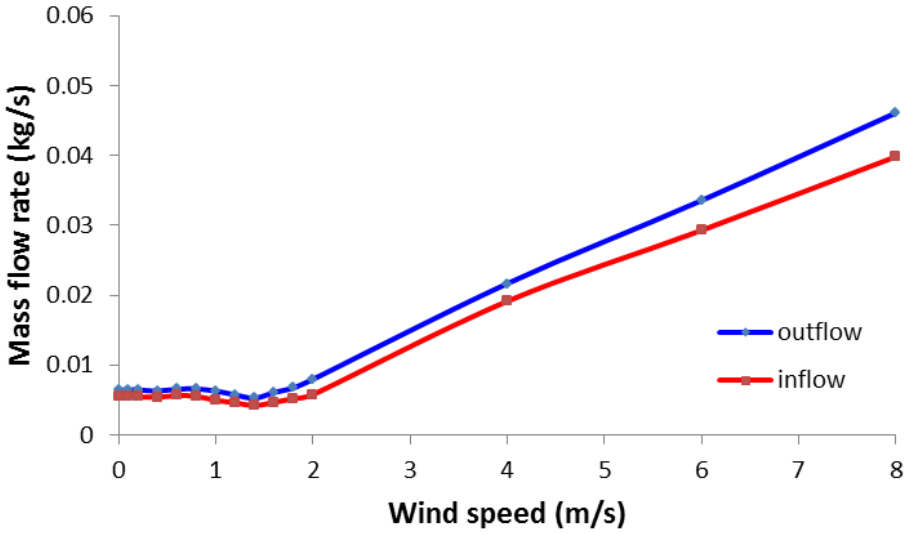

Figure 5.14: Influence of wind speed on the mass flow rate through the opening.

the level of discretization in the actual simulation.' As a result, for higher wind velocity, the output value of the mass flow tends to become unreliable. For the case with wind speed 8 m/s, the mass flow rate out of the compartment is 0.004 kg/s higher than the mass flow rate into the compartment, while the fuel added to the compartment is about 0.0013 kg/s, so this difference is unrealistic. In order to eliminate this post-processing error, one needs to use finer grid size and tighten the pressure tolerance. Unfortunately, that would be extremely expensive in terms of computational time, and we leave this to future work. Nevertheless, the overall trend is meaningful, in that the mass flow rates become much higher for higher wind speeds.

5.3.4.2 Heat release rate

First we focus on the inert wall cases. Figure 5.15 shows the HRR history of inert wall cases with wind speeds of 0 m/s, 2 m/s, 4 m/s, and 8 m/s. It can be seen that the HRR in each case reaches a steady state value, although with different values in each case. The time averaged results are discussed, with an averaging period from t= 200 s to 600 s.

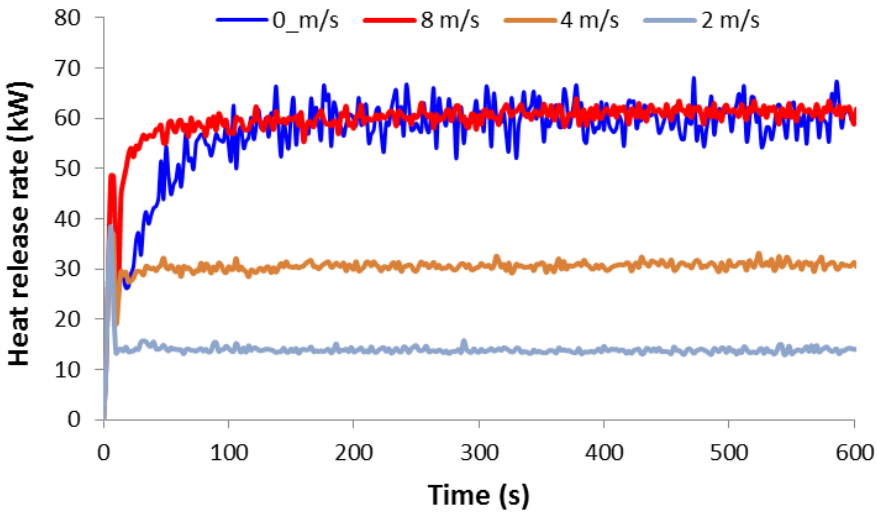

Figure 5.15: Temporal evolution of heat release rate for wind speed 0 m/s and 2 m/s, 4 m/s, and 8 m/s.

Here, the HRR of case with wind speed of 0 m/s is at the same level of that with a high wind speed (8 m/s) for most of the simulation time. However, the flame shape is totally different, as shown in Figure 5.16. In general, the flame without wind is much larger in volume and much higher than in the case with 8 m/s wind speed. The burning area for case with 8 m/s wind speed is limited to a relatively small region near the opening, with a much higher maximum Heat Release Rate Per Unit Volume (HRRPUV) value (27600 kW/m^3

vs. 9600 kW/m^3). The HRR increases more rapidly with 8 m/s wind speed after the drop (see discussion of Figure 5.17), because fresh oxygen is blown into the compartment, so that the fire does not suffer from under-ventilated conditions in the same manner as without wind.

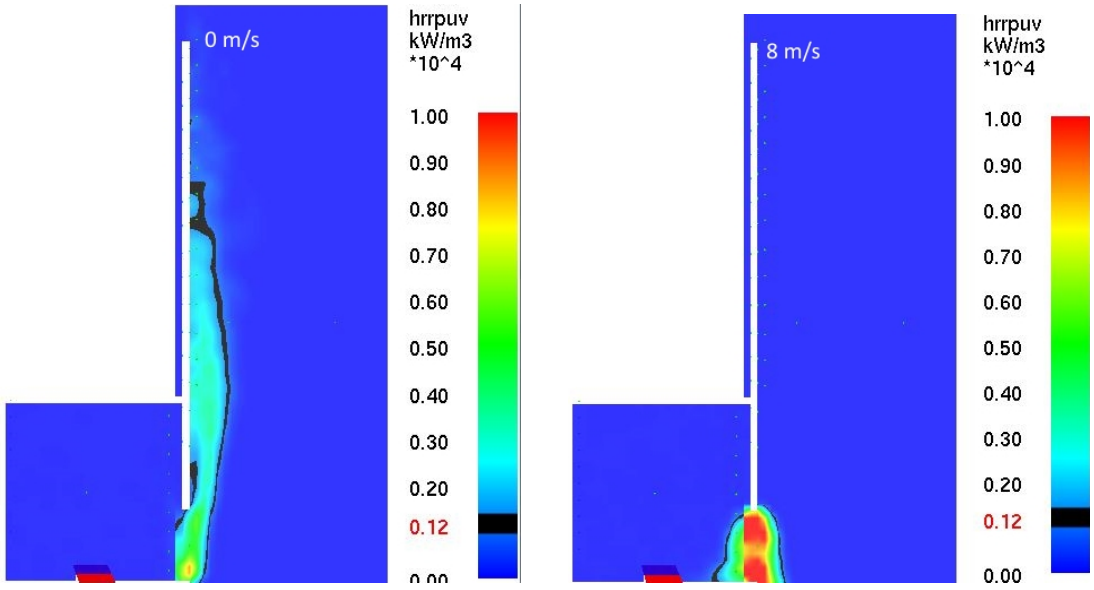

(a) (b)

Figure 5.16: Time-averaged HRRPUV for wind speeds of 0 m/s(left) and 8 m/s (right). (The discontinuity of the flame at near the opening is merely a visualization problem of Smokeview.) (The wind is perpendicular to the façade.)

Figure 5.17 shows the steady-state averaged (between 200 s and 600 s) heat release rate results of all the inert wall cases with wind speeds ranging from 0 to 8 m/s. A similar trend has been obtained as of the mass flow rate results. The steady-state heat release rate is about 60 kW for cases with wind speeds below 0.8 m/s. Increasing the wind speed to higher values, the steady-state HRR value decreases, dropping to a minimum value of 12 kW at the wind speed of 1.6 m/s. Beyond that value, it increases again, up to the maximum value of 60 kW at the wind speed of 8 m/s.

The explanation is based on momentum. In the absence of wind, inflow and outflow through the opening is generated by the fire dynamics from inside the enclosure. Thus, this is one driving force. Outside the enclosure, buoyancy leads to a vertically upward flow of the hot gases and ejecting flames. In case of wind (still perpendicular to the wall for the time being), there is also a momentum force caused by this wind. As a result, there is interaction between the wind-induced and the fire-induced flows near the opening.

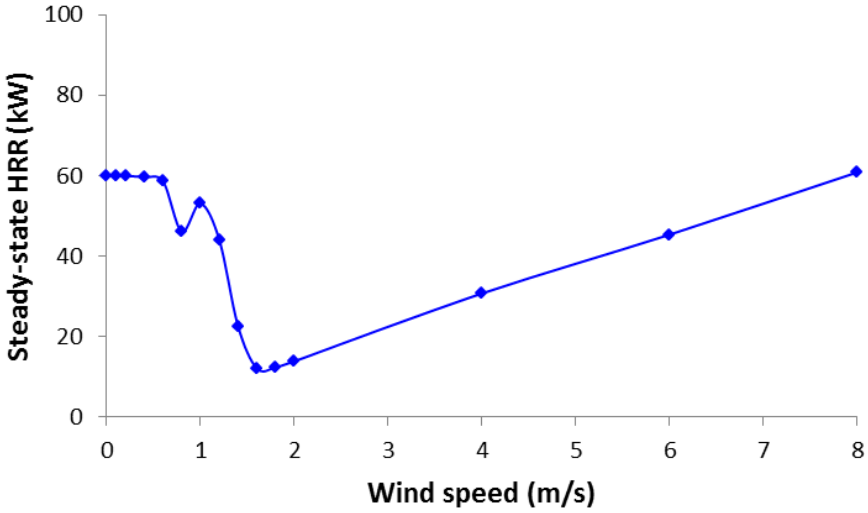

Figure 5.17: Influence of the wind speed on the steady-state HRR (averaged between 200 s and 600 s) for all the inert wall cases. (The wind is perpendicular to the façade.)

Therefore, it is interesting to calculate the momentum of the flow, emerging from the compartment, in the absence of wind. Taking the mass flow rate as 0.006 kg/s, the density of hot gas as 0.35 kg/m^3, and the area of the outflow as (0.2 x 0.2)/2=0.02 m^2, the estimated average velocity is 0.84 m/s. The momentum force is then approximately 0.005 N. This corresponds to a wind speed of 0.45 m/s (with ρ_{amb}= 1.2 kg/m^3). This is the same order of magnitude of the blocking wind speed (0.8 m/s). Note that this estimated wind speed is the value near the opening, and the velocity inlet boundary is 0.58 m away from the opening. As a consequence, for sufficiently high wind speed, some of the unburnt fuel, leaving the compartment, no longer moves upward due to buoyancy, to react in the high-temperature flame region, but also sideward due to the impinging flows (wind-induced versus fire-induced). As a consequence, part of the unburnt fuel can spread out of the computational domain, without reacting. This has been confirmed by checking the mass fraction of fuel across the boundaries. The case with 1.6 m/s wind speed should have the largest amount of the escaped fuel, in line with the lowest HRR value. Further increasing the wind speed results in more fuel blocked within the burning area, rather than first escaping from the compartment and then moving sideward, less fuel now escapes due to the strong momentum of the wind-induced flow. As a result, the amount of escaping unburnt fuel drops and the monitored HRR inside the computation domain increases again. For a wind speed of 8 m/s, all the fuel was blocked within the burning area and completely burnt inside the domain. This is the reason why the HRR of

case with 8 m/s wind speed is 60 kW again.

Figure 5.18 shows the time-averaged temperature contour plots for cases with wind speed of 0 m/s, 0.8 m/s, 1.2 m/s, 1.6 m/s, 4 m/s, and 8 m/s. With the increase of the wind speed, the height of the external flaming tends decrease. For a wind speed higher than 1.6 m/s, there is even no ejecting flame along the façade wall, and the burning is limited to a small area near the opening. Subsequently, the façade wall is exposed to a very limited heat flux, especially at locations further above the opening.

The wind effect on the HRR of the MDF façade case has also been investigated in this study. Based on the method used in section 5.3.1, the heat release rate from the burning of MDF façade is calculated and plotted in Figure 5.19 for cases with wind speed of 0 m/s, 0.8 m/s, 1.2 m/s, 1.6 m/s. Before t = 500 s, the heat release rates are generally higher at lower wind speeds, because a larger area burns for lower wind speed. When the wind speed exceeds to 1.6 m/s, almost no heat is released from the burning of MDF façade (insufficient heat flux from the ejecting flame to ignite the MDF panel). This trend is in line with the previous results. To visualize this, time-averaged temperature contour plots for MDF façade cases with wind speeds of 0 m/s, 0.8 m/s, 1.2 m/s, 1.6 m/s, 4 m/s, and 8 m/s are presented in Figure 5.20.

5.3.4.3 Pyrolysis height

As discussed in the previous sections, the wind has a significant influence on the flow rate through the opening and the burning of the MDF facade. Basically, lower pyrolysis front speeds are expected for higher wind speeds. In fact, at wind speeds higher than 1.6 m/s, no burning occurs on the façade wall at all.

As shown in Figure 5.21, for the case without environmental wind, the pyrolysis front reaches the top of the panel at 240 s. In presence of wind, however, a lower height is observed for the pyrolysis front (namely 0.8 m and 0.5 m at wind speeds of 0.8 m/s and 1.2 m/s, respectively, and no pyrolysis front on the façade at all for cases with wind speeds higher than 1.6 m/s).

The correlations for cases with wind speed of 0.8 m/s and 1.2 m/s are presented in Figure 5.22. Different from the linear correlation obtained in case without wind, both of these trend-lines show a logarithmic correlation between the pyrolysis height and the time, which means the flame spread speed is not constant any more when wind exist.

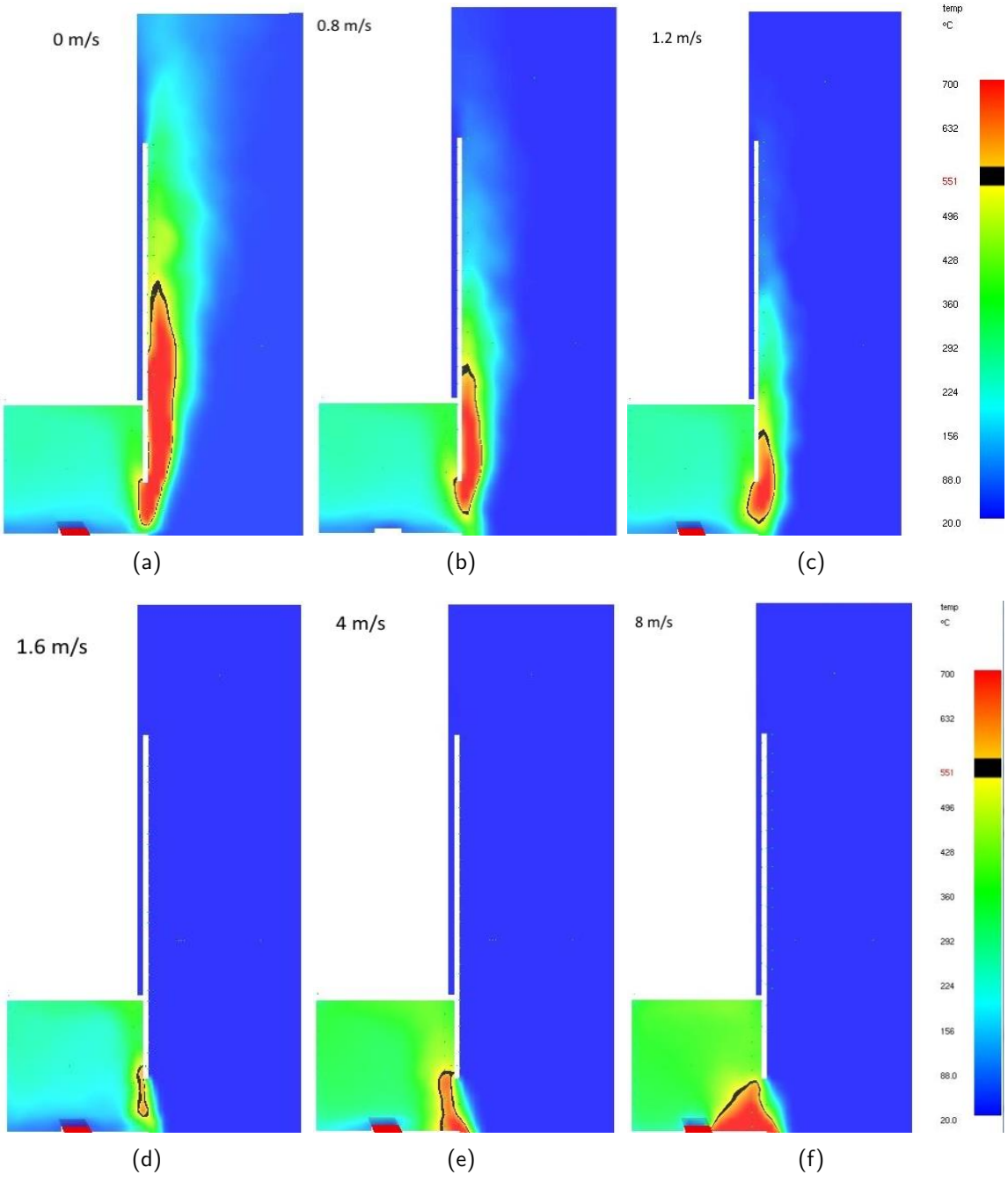

Figure 5.18: Time-averaged temperature contour plots for inert wall cases with wind speeds of 0 m/s, 0.8 m/s, 1.2 m/s, 1.6 m/s, 4 m/s, and 8 m/s (averaged between 200 s to 600 s). (The wind is perpendicular to the façade.)

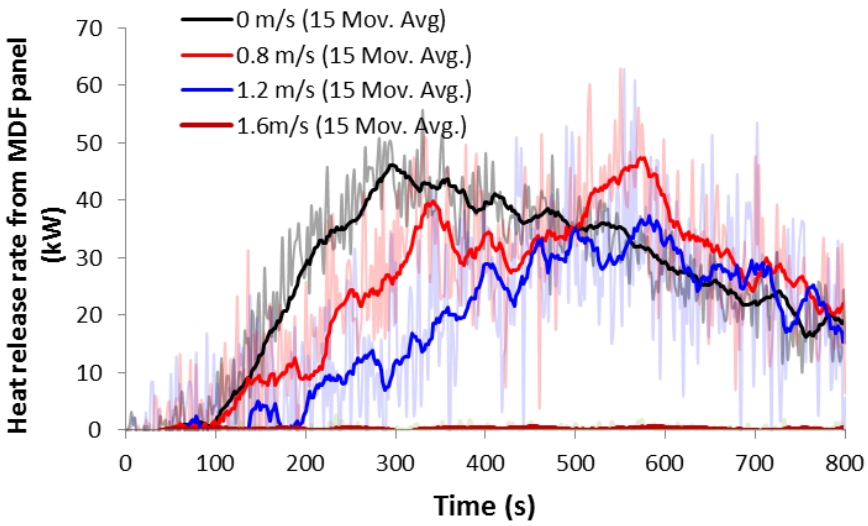

Figure 5.19: Influence of the wind speed on the HRR from the MDF façade for cases with wind speeds of 0 m/s, 0.8 m/s, 1.2 m/s, 1.6 m/s. (The wind is perpendicular to the façade.)

5.3.4.4 Side wind

The influence of the side wind has been studied as well. As illustrated in Figure 5.12, one of the side boundaries is defined as a velocity inlet. In order to capture the flames, the computational domain was extended by 0.32 m at the downstream of the side wind.

In Figure 5.23 and Figure 5.24, the time-averaged temperature contour plots at plane y=0 m and x =0.04 m are presented for cases with wind speeds of 0 m/s, 0.2 m/s, 0.4 m/s, 0.8 m/s, 1.2 m/s, and 2 m/s, 4 m/s, 6 m/s, and 8 m/s. The averageing time period is from 200 s to 600 s. The shape of the flame is significantly affected by the side wind. The flame angle (the angle between the flame and the vertical axis) increases from 0° (no wind) to about 40° (2 m/s wind speed). This can lead to a scenario with combined upward and sideward fire spread.

When the wind is parallel to the façade, there is little impact on the mass flow rate, emerging from the enclosure. This is observed in Figure 5.25, showing the mass flow rates out of the compartment for both wind conditions. This is logical, because now the horizontal momentum of the wind-induced flow does not directly compete with the fire-induced horizontal momentum: in this case they are perpendicular to each other. Moreover, no sharp increase is observed for high wind speed.

The drop in HRR, observed in Figure 5.17, is not present either now (Figure 5.26). The HRR decreases beyond a wind speed of 0.8 m/s, because unburnt fuel is blown sideward

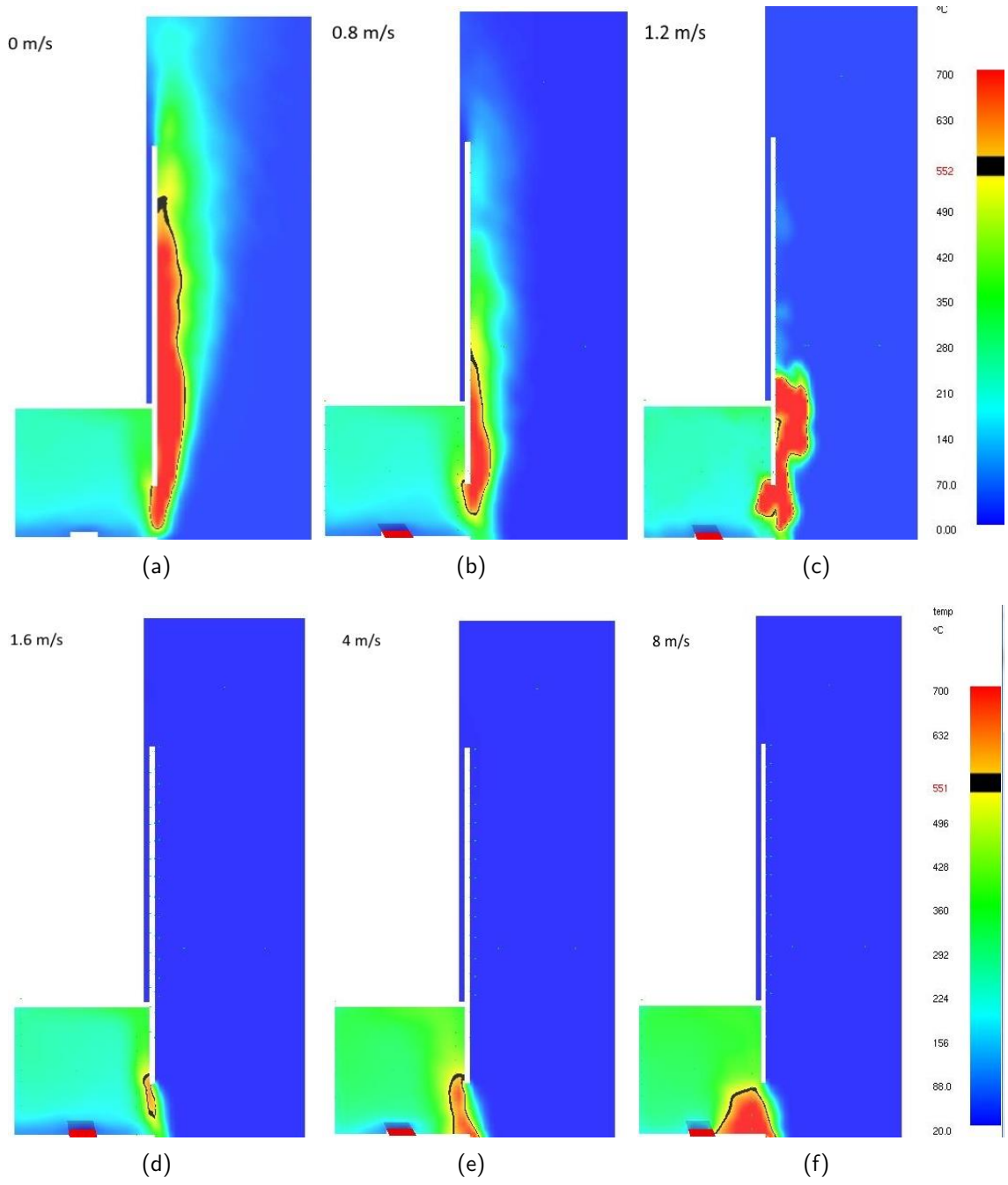

Figure 5.20: Time-averaged temperature contour plots for MDF façade wall cases with wind speeds of 0 m/s, 0.8 m/s, 1.2 m/s, 1.6 m/s, 4 m/s, and 8 m/s (averaged between 140 s to 160 s). (The wind is perpendicular to the façade.)

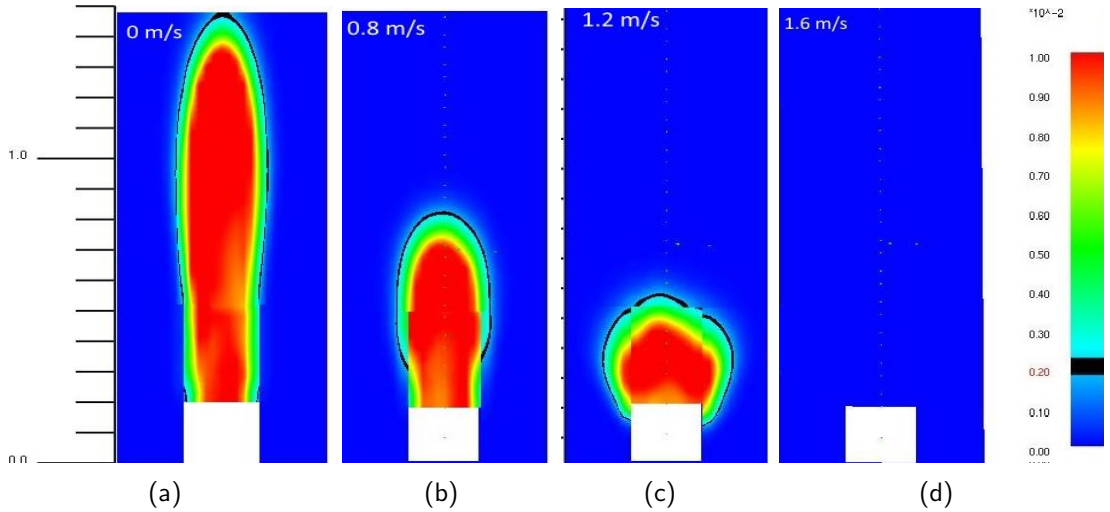

Figure 5.21: Contour plots of the propane mass flux showing the effect of wind on the propagation of the pyrolysis front on the MDF façade (at t = 240s). (The wind is perpendicular to the façade.)

out of the computational domain by the wind-induced sideward momentum. In other words, the explanation is the same as for Figure 5.17, but the interaction of the momenta of the different flows is different, because the wind-induced momentum is not in the same horizontal direction as the fire-induced flow momentum.

The effect of the side wind on the burning behavior of MDF façade case is also presented. Figure 5.27 shows the contour plots of the propane mass flux from cases with wind speeds of 0m/s, 0.2 m/s 0.4 m/s, 0.8 m/s, 1.2 m/s, and 2 m/s at time t = 160 s. The area enclosed by the black line in these figures is the pyrolysis region on the MDF panel. For wind speeds below 0.4 m/s, the influence on the pyrolysis region is small. For wind speeds of 0.8 m/s and higher, the wind-induced momentum creates a clear sideward angle. This is not surprising: from that wind speed onward, the wind-induced momentum becomes comparable to (and higher than) the fire-induced momentum of the flow emerging from the compartment, as discussed above (Figure 5.17).

5.3.4.5 Other wind directions

In this chapter, only two wind directions have been studied, namely horizontal wind perpendicular and parallel to the facade wall, with uniform speed. However, in reality wind conditions are far more complicated. In any case, the impact of wind should be analyzed on the basis of momentum balances. An extensive study of the impact of wind is a PhD by itself and is considered outside the scope of this PhD.

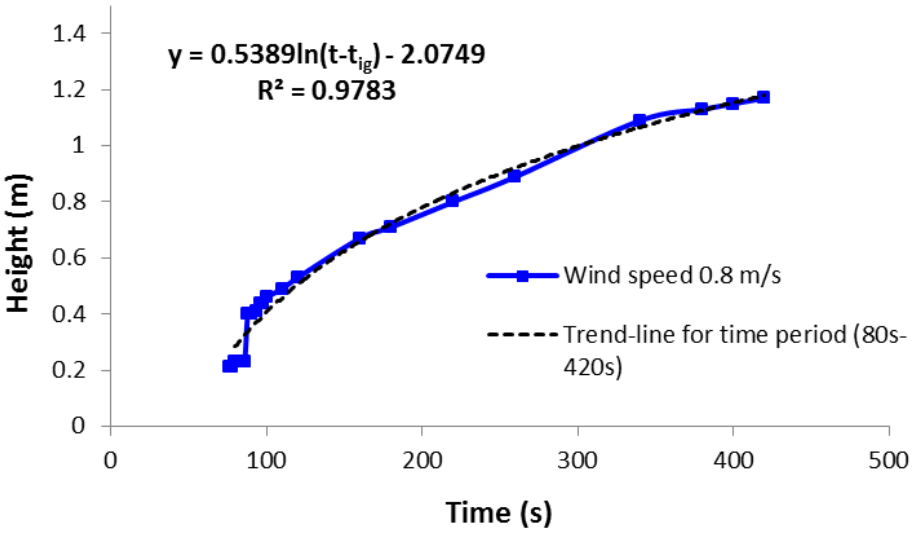

(a)

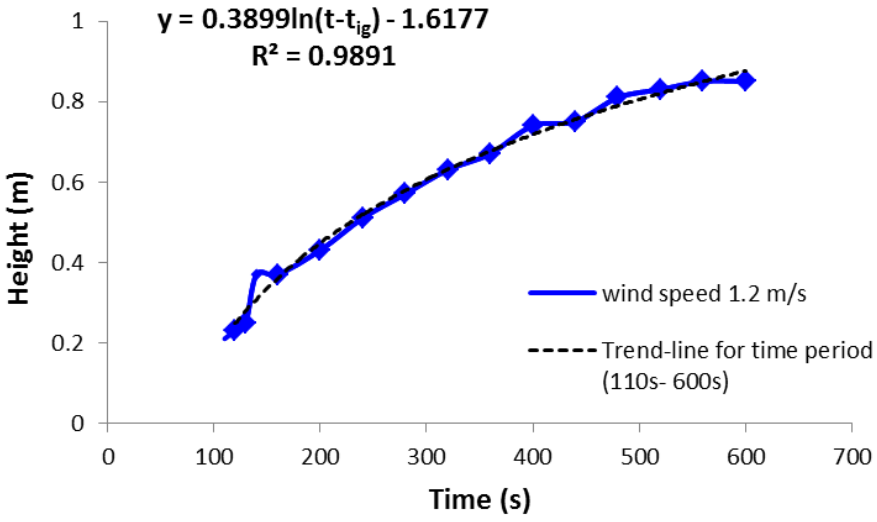

(b)

Figure 5.22: Pyrolysis front propagation over the MDF panel for cases with wind speeds of 0.8 m/s (a) and 1.2 m/s (b).

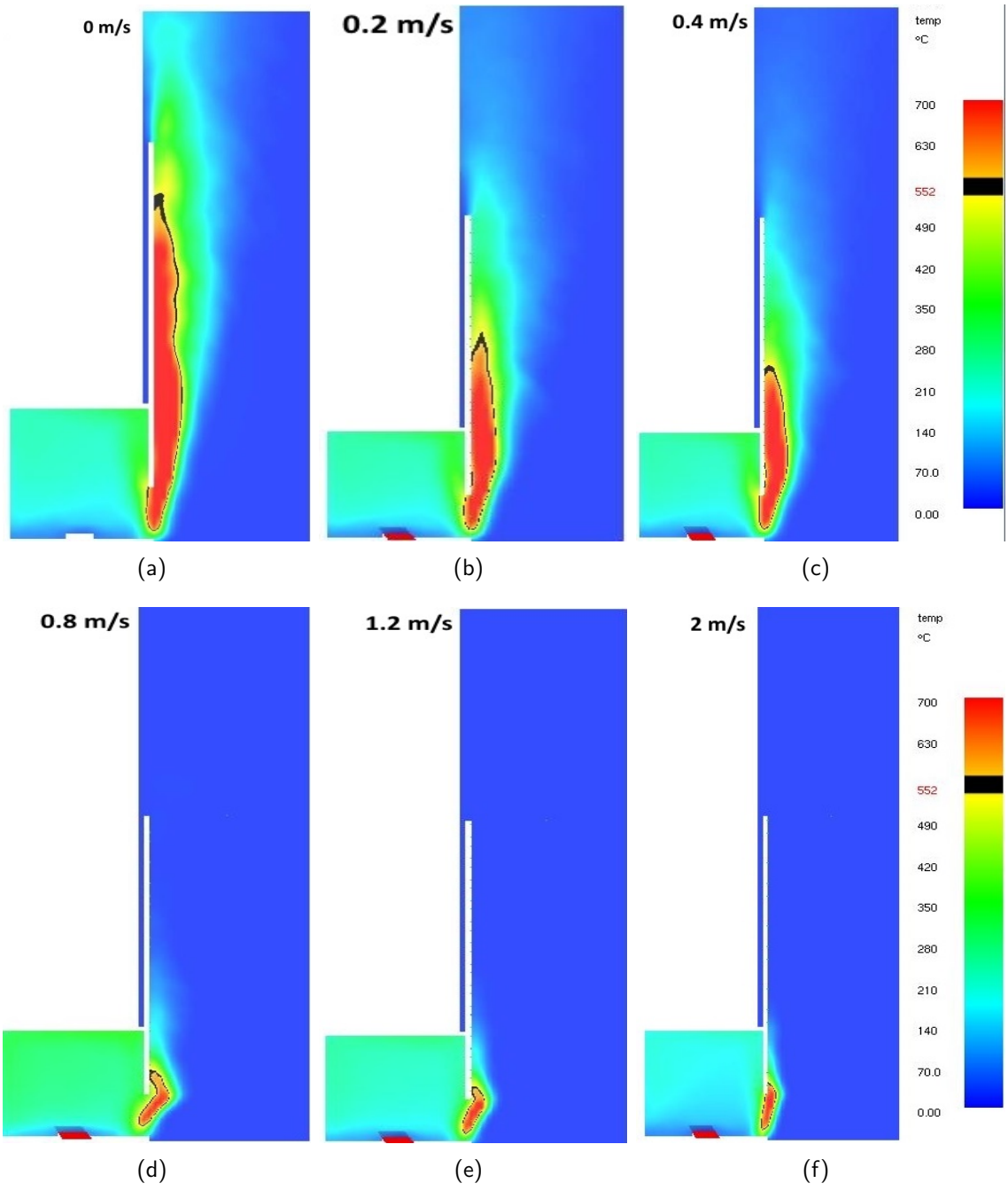

Figure 5.23: Time-averaged temperature contour plots at plane y = 0 m for inert wall cases with wind speeds of 0 m/s, 0.2 m/s, 0.4 m/s, 0.8 m/s, 1.2 m/s, and 2 m/s (averaged between 200 s to 600 s). (The wind is parallel to the façade.)

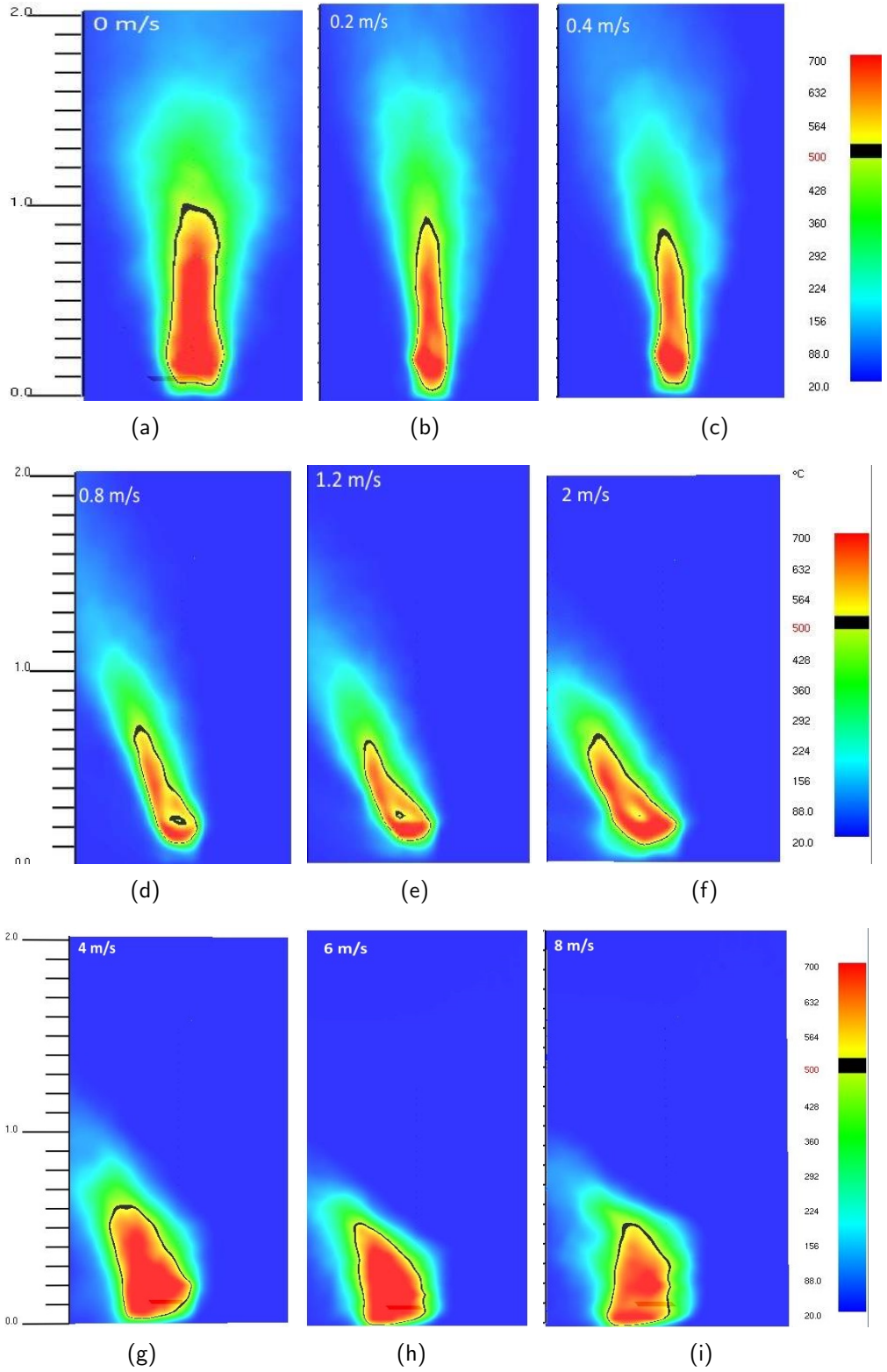

Figure 5.24: Time-averaged temperature contour plots at plane x = 0.04 m for inert wall cases with wind speeds of 0 m/s, 0.2 m/s, 0.4 m/s, 0.8 m/s, 1.2 m/s, 2 m/s, 4 m/s, 6 m/s, and 8 m/s (averaged between 200 s to 600 s). (The wind is parallel to the façade.)

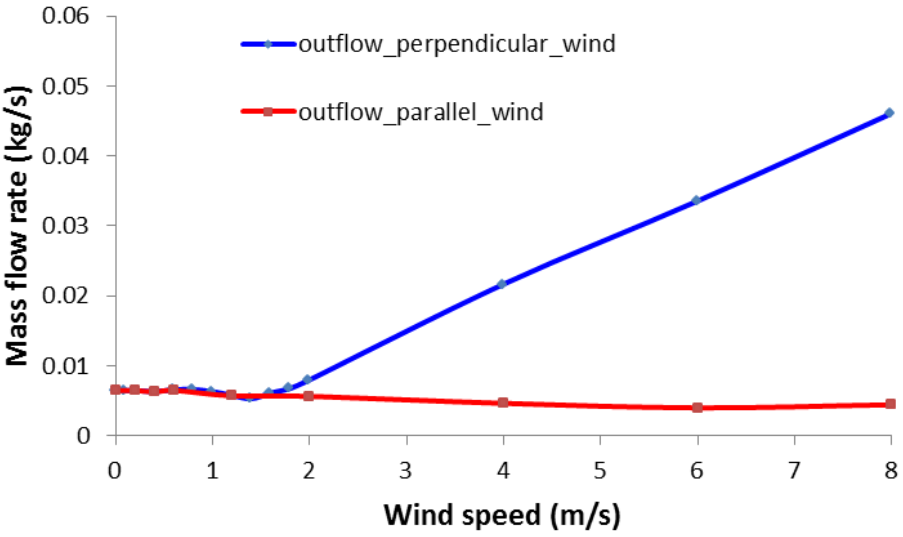

Figure 5.25: Influence of the wind speed on the mass flow rate through the opening. (wind perpendicular and parallel to the façade in the inert wall case.)

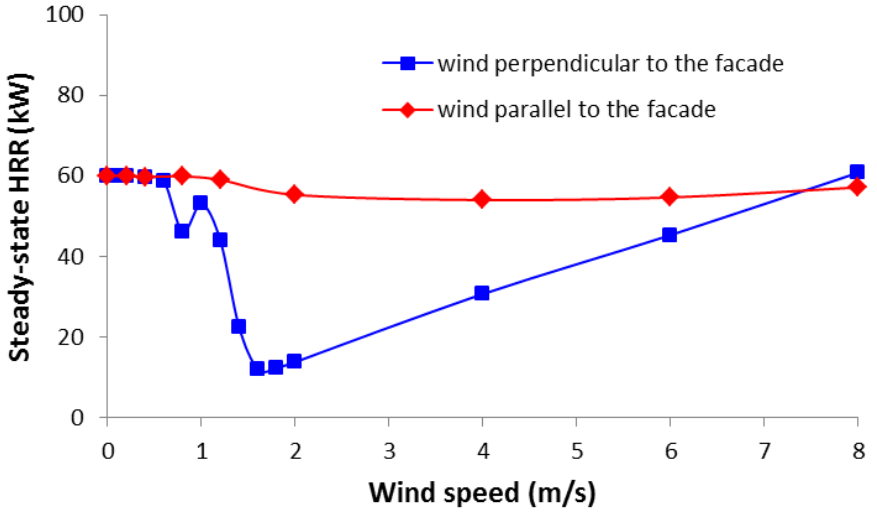

Figure 5.26: Influence of the wind speed on the steady-state HRR for wind perpendicular and parallel to the façade in the inert wall case

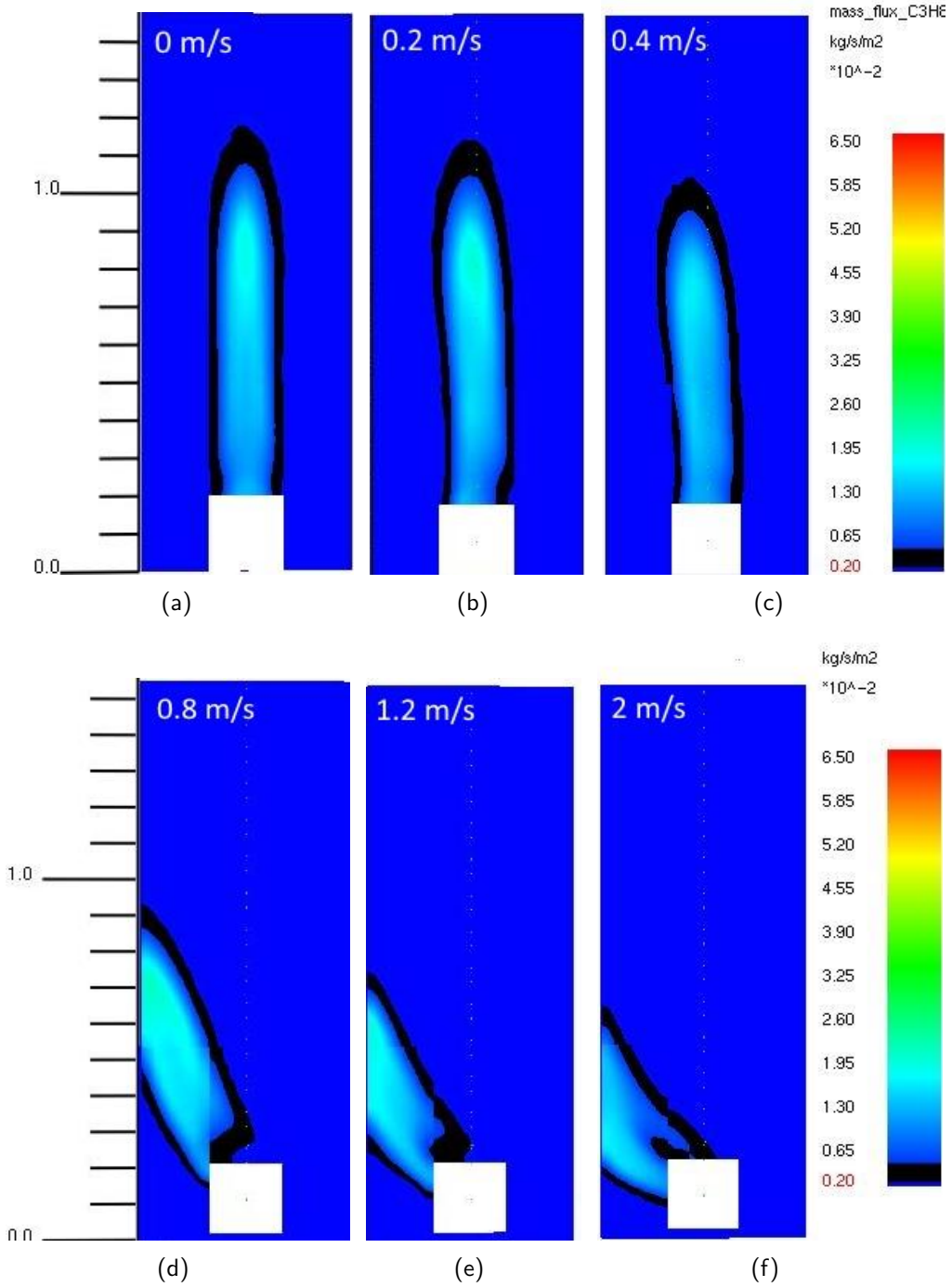

Figure 5.27: Contour plots of the propane mass flux showing the effect of side wind on the propagation of the pyrolysis front on the MDF façade at time 160 s (wind speeds of 0 m/s, 0.2 m/s 0.4 m/s, 0.8 m/s, 1.2 m/s, and 2 m/s). (The wind is parallel to the façade).

5.4 Conclusions

In this chapter, the use of CFD for façade fires has been illustrated by means of a fictitious scenario, in which inert and MDF panels have been used as façade wall material, combined with an under-ventilated enclosure fire. It is stressed that all quantitative information is directly linked to the, from conceptual point of view arbitrary, choices for the enclosure fire HRR (60 kW) and opening size (0.2 m x 0.2 m) and position (central in the façade, bottom side flush with the floor). Qualitatively, though, the discussion holds for any HRR value and opening size and position, in particular for under-ventilated conditions.

First of all, characteristics of the façade fire have been discussed, in terms of the HRR, heat fluxes on the façade wall, and the propagation of the pyrolysis front on the MDF panel, in the absence of wind. Starting from results with inert wall, the fire spread over the MDF panel has been explained, starting from the incident heat flux.

Subsequently, the effect of wind on the fire spread has been investigated. The wind was simplified, injecting a uniform velocity into the domain. Two directions have been investigated, namely perpendicular to the façade and parallel to the façade, with variable speed (ranging up to 8 m/s). It has been illustrated that the analysis should be based on momentum. In case the wind is perpendicular to the façade, the outflow of unburnt fuel from the compartment is hindered (and, for sufficiently high wind speed, blocked), reducing the flame height, ejecting from the opening. Unburnt fuel is also pushed sideward as it emerges from the opening and may not react (or at least not inside the computational domain). This leads to reduced fire spread. When the wind is parallel to the façade, there is little impact on the mass flow rate, emerging from the enclosure, because the horizontal wind-induced momentum is not in the same direction as the horizontal fire-induced flow momentum. For sufficiently low wind momentum, no effect on the shape of the pyrolysis region is observed. For higher momentum, an angle is observed from the vertical direction. The angle increases as the wind speed increases. This leads to combined upward and sideward fire spread.

To summarize, this chapter is an illustration of a proof-of-concept of the potential of using FDS for façade fires, including wind conditions.

Chapter 6

Conclusions and future work

6.1 Overall structure

This Ph.D. thesis described research undertaken into the assessment of the state-of-the-art CFD package (FDS) as a basis for understanding fire spread behavior in the context of building façade fires. Detailed discussions, based on the CFD results, were presented. A step-wise strategy has been employed in this work, consisting of three main parts:

- CFD for fire and smoke dynamics - Gas Phase
  - buoyant flow (high-rise building stairwell)
  - ventilation-controlled fires with ejecting flames (no flame spread)
- CFD for flame spread - Gas and solid phase
  - heat transfer and pyrolysis modeling
  - pyrolysis and combustion (cone calorimeter test)
  - flame spread in SBI test
- Proof of concept of the use of CFD for façade fires
  - ventilation-controlled fire and combustible façade
  - wind effect

The study confirmed, through a proof-of-concept with a fictitious scenario, that state-of-the-art of CFD in general, and FDS in particular, is a very promising tool to investigate façade fires. This overall conclusion is supported by detailed conclusions, as summarized next.

6.2 Detailed conclusions

In Chapter 2, an investigation has been made of the use of FDS for the modeling of fire and smoke dynamics in the gas phase. Two scenarios have been considered. The first scenario is the buoyant flow in the stairwell, aiming to illustrate the potential of CFD modeling in high-rise buildings with a well-ventilated fire and without flame spread. A detailed study has been conducted, discussing the air flow velocity at the opening in the middle of the stairwell, the temperature rise inside the stairwell, the temperature at the middle opening, the influence of the presence of a staircase on the pressure distribution, and the location of the neutral plane height. Moreover, the influence of the turbulence model on the simulation results is discussed. Overall, the obtained results confirm that reliable insights can be retrieved from CFD simulations regarding the motion of smoke in the high-rise buildings.

The second scenario is regarding several under-ventilated fire simulations in an enclosure with flames ejecting from its opening. Four different opening geometries are considered in the simulations: 0.1 m x 0.2 m, 0.2 m x 0.2 m, 0.2 m x 0.3 m, and 0.3 m x 0.3 m. The accuracy of the obtained results has been discussed and comparison has been made with experimental data, as well as empirical correlations. The required resolution of the computational grid has been discussed by analyzing the mass balance 'error' based on the post-processing of the total mass flow rate into and out of the enclosure. Two length scale ratios have been formulated for assessment of the grid resolution, in addition to the conventional D^* criterion. The first ratio is the ventilation factor to the grid cell size, while the second is the ratio of the hydraulic diameter of the opening to the grid cell size. When these two length scale ratios are larger than 10, the corresponding mass balance 'error' is lower than 4%. The results in terms of velocities through the door opening and the temperatures along the doorway are also grid insensitive in this case. The air inflow rate through the opening is found to correlate linearly to the ventilation factor, in agreement with the literature. Moreover, the heat release rate inside the enclosure shows a linear relationship with the ventilation factor, although the value of the slope is lower than the conventional value in the literature. This has been explained through the lower mass flow rate of incoming air and incomplete consumption of oxygen flowing into the compartment. The temperature predictions show that: (1) the temperature at back and front opposite corners are not identical, but meaningful average temperatures inside the enclosure can be defined, (2) such obtained average gas temperatures inside the enclosure deviate less than 10% from Babrauskas correlation for the different opening geometries. It has been shown that FDS can accurately reproduce the neutral plane height position

for the various configurations. The external flame height is sensitive to the criterion to define the flame height, namely the choice of flame temperature. Nevertheless, the trends have been captured correctly. The predicted height of the ejecting flames increases with the fire HRR. The power dependence of the flame height on the external heat release rate is equal to 2/3.

In Chapter 3, pyrolysis behaviour of the MDF material has been studied numerically using a one-dimensional heat transfer solver, and a one-step Arrhenius type pyrolysis model. Within this model, the non-uniform density profile and the in-depth radiation has been taken into consideration. The thermal properties of virgin MDF and char are taken from the literature for the base case. The influence of the material properties and model parameters on the pyrolysis behaviour of MDF has been investigated in detail through a sensitivity analysis. The parameters include thermal conductivity, specific heat, heat of reaction, the emissivity, absorption coefficient, moisture content, and through-thickness density profile. Based on the results of the sensitivity analysis study, it can be concluded that, for the considered range of the parameters, the most significant influence on the time to the first peak comes from the emissivity, followed by the thermal conductivity, specific heat, non-uniform density profile, and moisture content. For the peak mass loss rate, the most significant influence comes from the non-uniform density profile, followed by the absorption coefficient, the moisture content, and finally the specific heat capacity. Hence, only when proper values of the parameters were employed in the simulation, the onset of the pyrolysis process can be reasonably predicted. Through a simple trial and error procedure, a set of 'improved' parameter values has been obtained. The rest of the chapter has been devoted to the coupling of pyrolysis and CFD modeling, including both gas phase and solid phase. The conducted grid sensitivity study has shown that the D^* criterion is insufficient for coupled gas-solid phase fire simulations.

In Chapter 4, the use of CFD for flame spread has been studied in a scenario with intermediate scale, namely the SBI test in a corner configuration. This was done through simulation of several SBI corner fire experiments conducted with MDF panels and a calibration test with calcium silicate panels, using updated material properties determined in chapter 3. A grid size sensitivity study has been conducted comparing the heat fluxes at three characteristic points for the inert wall case. In general, a finer grid size produces higher heat fluxes, and shows better agreement with the experimental data. Taking into account the computational time and the accuracy, a 2 cm cell size has been determined. Both 'complete' and 'simplified' geometry models were considered to investigate the influence of the completeness of the geometry in the model on the predictions. Significantly

different flow patterns have been observed between these two cases. Further investigations have been made of the total gauge heat fluxes predictions at several characteristic locations. The total gauge heat flux predictions from both 'complete' model case and 'simplified' model case were reasonably similar to the experimental data in both the inert wall and MDF panel cases. Most differences in the simulations were observable further away from the corner, where an accurate prediction of the fire edges proved challenging for both cases, resulting in great fluctuations in the heat flux predictions. In general, simulation of 'complete' model case features higher heat fluxes than 'simplified' model case for these three locations. Similar to the heat flux prediction, higher HRR peak has been obtained in the 'complete' model case than 'simplified' model case, and the overall trend has been reasonably captured with the numerical model. Based on the findings of this study, it is recommended for future computational assessment of SBI-like scenarios to properly account for the completeness of the enclosure geometry. The choice of the enclosure model is expected to making influence on the flow field, the radiation on the panels and the flame spread on the combustible wall.

In chapter 5, the use of CFD for façade fires has been illustrated by means of a fictitious scenario, in which inert and MDF panels have been used as façade wall material, combined with an under-ventilated enclosure fire. It is stressed that all quantitative information is directly linked to the, from conceptual point of view arbitrary, choices for the enclosure fire HRR (60 kW) and opening size (0.2 m x 0.2 m) and position (central in the façade, bottom side flush with the floor). Qualitatively, though, the discussion holds for any HRR value and opening size and position, in particular for under-ventilated conditions. First of all, characteristics of the façade fire have been discussed, in terms of the HRR, heat fluxes on the façade wall, and the propagation of the pyrolysis front on the MDF panel, in the absence of wind. Starting from results with inert wall, the fire spread over the MDF panel has been explained, starting from the incident heat flux. Subsequently, the effect of wind on the fire spread has been investigated. The wind was simplified, injecting a uniform velocity into the domain. Two directions have been investigated, namely perpendicular to the façade and parallel to the façade, with variable speed (ranging up to 8 m/s). It has been illustrated that the analysis should be based on momentum. In case the wind is perpendicular to the façade, the outflow of unburnt fuel from the compartment is hindered (and, for sufficiently high wind speed, blocked), reducing the flame height, ejecting from the opening. Unburnt fuel is also pushed sideward as it emerges from the opening and may not react (or at least not inside the computational domain). This leads to reduced fire spread. When the wind is parallel to the façade, there is little impact on the mass flow

rate, emerging from the enclosure, because the horizontal wind-induced momentum is not in the same direction as the horizontal fire-induced flow momentum. As such, there is no reduced fire spread. For sufficiently low wind momentum, no effect on the shape of the pyrolysis region is observed. For higher momentum, an angle is observed from the vertical direction. The angle increases as the wind speed increases. This leads to combined upward and sideward fire spread. To summarize, this chapter is an illustration of a proof-of-concept of the potential of using FDS for façade fires, including wind conditions.

6.3 Suggestions for future work

As shown in chapter 3, the D^* criterion is insufficient for coupled gas-solid phase fire simulations. More elaborate sensitivity studies on the grid size could be useful to define reliable criteria to conduct simulations involving both gas and solid phase processes.

In Chapter 2, it would be interesting to investigate the influence of leakage in the simulation to reproduce the experimental trend (especially for the smoke movement speed).

For future computational assessment of SBI-like scenarios, the choice of the enclosure model is expected to have a significant influence on the flow field and radiation on the panels, as demonstrated in Chapter 4. Therefore, a 'complete' model is recommended. More elaborate studies, including the effect of the extraction flow rate from the hood, are required to quantify this effect. In addition to that, the simulation would be benefit from conducting further investigations on the modelling of turbulence, combustion and radiative and convective heat transfer.

In Chapter 5, the use of the FDS code for the modeling of façade fires has been illustrated through a fictitious scenario, in which both inert and MDF panels have been used as the façade wall material, with an under-ventilated enclosure fire source. The wind effect in such a scenario has been numerically studied as well. However, no experimental work has been done, especially for the wind effect on the fire spread on the façade. It would be of great value to conduct experimental work to study this topic. Moreover, an elaborate CFD study on the wind effect will lead to very useful insights into this topic.

Bibliography

[1] K. Kawagoe. Fire behaviour in rooms, Report No. 27, Building Research institute, Tokyo, 1958.

[2] J.A. Rockett. Fire induced gas flow in an enclosure, Combust. Sci. Technology, 12:165-175,1976.

[3] P.H. Thomas and A.J.M. Heselden. Fully Developed Fires in Single Compartments. Fire Research Note No.923. Fire Research Station, Borehamwood, England, 1972.

[4] T. Tanaka, I. Nakaya, and M. Yoshida. Full scale experiments for determining the burning conditions to be applied to toxicity tests. Proceedings of the first international symposium on fire safety science, 1:129-138, 1986.

[5] Y.P. Lee, M.A. Delichatsios, and G. Silcock. Heat Fluxes and Flame Heights in Facades from Fires in Enclosures of Varying Geometry. Proceedings of the Combustion Institute, 31:2521-2528, 2007.

[6] Y.P. Lee. Heat Fluxes and Flame Heights in External Facade Fires, Ph.D. thesis, University of Ulster, Fire SERT, 2006.

[7] D. Drysdale. An Introduction to Fire Dynamics, third edition, John Wiley and Sons, 2011.

[8] B. Merci and Tarek Beji, Fluid Mechanics Aspects of Fire and Smoke Dynamics in Enclosures, CRC Press, 1st Edition, ISBN-13: 978-1138029606, 2016.

[9] W.D. Walton, P.H. Thomas, and Y. Ohmiya. "Estimating Temperatures in Compartment Fires" in SFPE Handbook of Fire Protection Engineering, New York, NY, USA: Springer, 2016.

[10] V. Babrauskas and R. B. Williamson. Post-flashover compartment fires: basis of a theoretical model, Fire and materials, 2:39-53, 1978.

[11] V. Babrauskas. A closed-form approximation for post-flashover compartment fire temperatures, Fire safety journal, 4:63-73, 1981.

[12] K.B. McGrattan. Improved Radiation and Combustion Routines for a Large Eddy Simulation Fire Model in Fire Safety Science, Proceedings of the Seventh International Symposium, International Association for Fire Safety Science, WPI, MA, USA, pp. 827-838, 2002.

[13] F. Tang and L.H. Hu. Experimental study on flame height and temperature profile of buoyant window spill plume from an under-ventilated compartment fire, International Journal of Heat and Mass Transfer, 55(1-3):93-101, 2012.

[14] M. Law, and T. OBrien. Fire safety of bare external structural steel, The Steel Construction Institute, SCI Publication 009, U.K. ISBN: 0862000262, 1989.

[15] I. Oleszkiewicz. Heat transfer from a window fire plume to a building facade, American Society of Mechanical Engineers, Heat Transfer Division, 123:163170, 1989.

[16] K. Himoto and T. Tsuchihashi, Y. Tanaka, and T. Tanaka. Modeling the trajectory of window flames with regard to flow attachment to the adjacent wall, Fire Safety Journal, 44(2):250-258, 2009.

[17] K. Goble. Height of Flames Projecting from Compartment Openings, Master thesis, University of Canterbury, 2007.

[18] J. Zhang, M. Delichatsios, M. Colobert, and J. Hereid. Experimental and numerical investigations of heat impact and flame heights from fires in SBI tests. Fire Safety Science proceedings of the Ninth International Symposium, pp. 205-216, 2008.

[19] E.K. Asimakopoulou, K. Chotzoglou, D.I. Kolaitis, and M.A. Founti. Characteristics of externally venting flames and their effect on the facade: A detailed experimental study, Fire Technology, 52(6): 2043-2069, 2016.

[20] E.K. Asimakopoulou, D.I. Kolaitis and M.A. Founti. Assessment of fire engineering design correlations used to describe the thermal characteristics of externally venting flames, Fire Technology, 53(2),709-739, 2017.

[21] D.I. Kolaitis, E.K. Asimakopoulou,M. A. Founti. A full-scale fire test to investigate the fire behaviour of the "Ventilated faade" system. Proceedings of the 14th International Conference and Exhibition on Fire Science and Engineering (Interflam 2016), U.K., 1127-1138, 2016.

[22] K. Suzana. Experimental and computational study of flames venting externally during full scale flashover fires. Ph.D. Thesis, Victoria University of Technology, Melbourne, Australia, 1999.

[23] J.G. Quintiere. Surface Flame Spread, Chapter 212, in The SFPE Handbook of Fire Protection Engineering, 3rd Ed., NFPA, Quincy, MA, 2002.

[24] G.H. Markstein and J.N. de Ris. Upward fire spread over textiles, in 14 th symposium(International) on combustion, combustion institute, Pittsburgh,PA,USA, pp.1085-1097, 1972.

[25] L. Orloff, J. de Ris, and G.H. Markstein. Upward turbulent fire spread and burning of fuel surface, in 15 th symposium(International) on combustion, combustion institute, USA, pp. 183-192, 1974.

[26] D. Zeinali, G. Agarwal, A. Gupta, G. Maragkos, T. Beji, M. Chaos, N. Ren, J. Degroote and B. Merci. Computational analysis of pyrolysis and flame spread for MDF panels placed in a corner configuration. 8th ISFEH Proceedings, 2016.

[27] G. Agarwal, M. Chaos, Y. Wang, D. Zeinali, and B. Merci. Pyrolysis Model Properties of Engineered Wood Products and Validation Using Transient Heating Scenarios, Interflam 2016, 14th International Conference and Exhibition on Fire Science and Engineering, Royal Holloway College, UK, 2016.

[28] EN-13823, Reaction to fire tests for building products (2002), Building products excluding floorings exposed to the thermal attack by a single burning item, ed:European standard, 2002.

[29] H. Yoshioka, Y. Ohmiya, M. Noak, and M. Yoshida. Large-scale facade tests conducted based on ISO 13785-2 with non-combustible facade specimens. Fire Science and Technology, 31:1-22, 2012.

[30] H. Yoshioka, Y. Nishio. Facade test on fire propagation along combustible exterior wall systems. Fire science and Technology, 33:1-15, 2014.

[31] H. Yoshioka, H. Yang. Study of Test Method for Evaluation of Fire Propagaion along Faade Wall with Exterior Thermal Insulation. Fire Science and Technology, 30:27-44, 2011.

[32] C.H. Bamford, J. Crank, and D.H. Malan. The combustion of wood. part i. Mathematical Proceedings of the Cambridge Philosophical Society, 42:166182, 1945.

[33] Z. Yan and G. Holmstedt, CFD and Experimental Studies of Room Fire Growth on Wall Lining Materials, Fire Safety Journal, 27:201-238, 1996.

[34] S.R. Wasan, P. Rauwoens, J. Vierendeels, and B. Merci. An enthalpy-based pyrolysis model for charring and non-charring materials in case of fire, Combustion and Flame,157:715-734, 2010.

[35] C. Lautenberger, G. Rein, and C. Fernandez-Pello. The Application of a Generic Algorithm to Estimate Material Properties for Fire Modelling from Bench-scale Fire Test Data, Fire Safety Journal, 41:204-214, 2006.

[36] J. W. Kwon, A. Nicholas. Dembsey, Christopher. W. Lautenberger. Evaluation of FDS V.4: Upward flame spread, Fire Technology, 43:255-284, 2007.

[37] J. Floyd, K. McGrattan. Validation of A CFD Fire Model Using Two Step Combustion Chemistry Using the NIST Reduced-Scale ventilation-Limited Compartment Data, Fire Safety Science proceedings Of The Ninth International Symposium, pp. 117-128, 2008.

[38] Z. Hu, Y. Utiskul, J.G. Quintiere. Towards large eddy simulations of flame extinction and carbon monoxide emission in compartment fires, Proceedings of the combustion institute, 31:2537-2545, 2007.

[39] V. Lecoustre, P. Narayanan, H.R. Baum, and A. Trouve. Local Extinction of Diffusion Flames in Fires. Fire Safety Science, pp: 583-595, 2011.

[40] M. Chaos. Spectral Aspects of Bench-Scale Flammability Testing: Application to Hardwood Pyrolysis. Fire Safety Science, 11: 165-178, 2014.

[41] Y. Wang, M. Chaos, and S. Dorofeev. CFD modeling of flame spread over corrugated cardboard panels, 13th Internal conference and exhibition, San Francisco, USA, 2013.

[42] http://www.iafss.org/macfp/

[43] K. McGrattan, B. Klein, S. Hostikka, and J. Floyd. Fire dynamics simulator (version6), Users Guide, National Institute of Standards and Technology Report NIST special publication, 2012.

[44] K. McGrattan, B. Klein, S. Hostikka, and J. Floyd. Fire dynamics simulator (version6), Technical Reference Guide, National Institute of Standards and Technology Report NIST special publication, 2012.

[45] K. McGrattan, R.J. McDermott, J. Floyd. Computational fluid dynamics modelling of fire. International journal of computational fluid dynamics, 26(6-8):349-361, 2012.

[46] J.W. Deardorff. Numerical investigation of neutral and unstable planetary boundary layers. Journal of atmospheric sciences, 29:91-115, 1972.

[47] Stephen B.Pope. Turbulent Flows. Cambridge University Press, 2000.

[48] C. Beyler. SFPE Handbook of fire protection engineering, chapter flammability limits of premised and diffusion flames. National fire protection association, Quincy, Massachusetts,4th edition, 2008.44

[49] G. Zhao, T. Beji, and B. Merci. Application of FDS to under-ventilated enclosure fires with external flaming. Fire Technology. 52(6):2117-2142, 2015 doi: 10.1007/s10694-015-0552-4.

[50] G. Zhao, T. Beji, and B. Merci. Numerical study on characteristics of buoyant fire-induced smoke movement in a high-rise building stairwell using FDS. Proceedings of the Eighth International Seminar on Fire and Explosion Hazards (ISFEH8), Hefei, China. 2016.

[51] G. Zhao, T. Beji, and B. Merci. Study of FDS simulations of buoyant fire-induced smoke movement in a high-rise building stairwell, Fire Safety Journal, 91:276-283, 2017.

[52] N. R. Marshall. Air entrainment into smoke and hot gases in open shafts. Fire Saf. J., 10(1):37-46,1986, http://dx.doi.org/10.1016/0379-7112(86)90030-5.

[53] W. Z. Black. Smoke movement in elevator shafts during a high-rise structural fire. Fire Saf. J., 44(2):168-182, 2009. http://dx.doi.org/10.1016/j.firesaf.2008.05.004.

[54] D. Qi and L. Wang. An analytical model of heat and mass transfer through non-adiabatic high-rise shafts during fires, Int. J. of Heat and Mass Transfer, 72:585-594, 2014. http://dx.doi.org/10.1016/j.ijheatmasstransfer.2014.01.042.

[55] L Li, C.Fan, J.Sun, X. Yuan, and W. Shi. Experimental investigation on the characteristics of buoyant plume movement in a stairwell with multiple openings, Energy and Buildings, 68(A):108-120, 2014. http://dx.doi.org/10.1016/j.enbuild.2013.09.028.

[56] T. Ma, and J.G. Quintiere. Numerical Simulation of axi-symmetric Fire Plumes: Accuracy and Limitations. Fire Saf. J., 38(5):467-492, 2003. http://dx.doi.org/10.1016/S0379-7112(02)00082-6.

[57] P. Friday and F.W. Mowrer. Comparison of FDS Model Predictions with FM/SNL Fire Test Data. NIST GCR 01-810, National Institute of Standards and Technology, Gaithersburg, MD, USA, 2001.

[58] K.B. McGrattan. Improved Radiation and Combustion Routines for a Large Eddy Simulation Fire Model. Fire Safety Science, Proceedings of the Seventh International Symposium, International Association for Fire Safety Science, pp 827-838, 2003. doi:10.3801/IAFSS.FSS.7-827

[59] H.R. Bram, K.B. McGrattan, and R.G. Rehm. Three dimensional simulations of fire plume dynamics. Fire Safety Science, Proceedings of the Fifth International Symposium, pp 511-522, 1997. doi:10.3801/IAFSS.FSS.5-511.

[60] T. Ma, and J.G. Quintiere. Numerical Simulation of Axi-symmetric Fire Plumes: Accuracy and Limitations, MS Thesis, University of Maryland, 2001.

[61] W. Grosshandle. Report of the Technical Investigation of the Station Night Club Fire, NIST NCSTAR 2: Vol. 1, National Institute Standards and Technology, Gaithersburg, MD, USA, 2005.

[62] K.B. McGrattan, H.R. Baum, and R.G. Rehm. Large Eddy Simulations of Smoke Movement, Fire Safety Journal, 30(2):161-178, 1998.

[63] G. Heskestad. Flame Heights of Fuel Arrays with Combustion in Depth, Fire Safety Science Proceeding of the Fifth International Symposium, pp. 427-438, 1999.

[64] A. Lock and M. Bundy. Experimental Study of the Effects of Fuel Type, Fuel Distribution, and Vent Size on Full-Scale Under-ventilated Compartment Fires in an ISO 9705 Room. NIST Technical Note 1603, pp. 53-54, 2008.

[65] M.A. Delichatsios, W.H. Silcock, X. Liu, M.M. Delichatsios, and Y.P. Lee. Mass Pyrolysis rates and Excess Pyrolysate in Fully Developed Enclosure, Fire Safety Journal, 39:1-21, 2004.

[66] G. Cox. Basic considerations in combustion fundamentals of fire (ed. G. Cox), pp 1-30. Academic Press, London, 1995.

[67] L. Orloff, and de Ris, J.N. Froude modelling of pool fires, 19th Symposium (international) on combustion, The Combustion Institute, Pittsburgh, pp 885-895, 1982.

[68] M.A. Delichatsios, W.H. Silcock, X. Liu, NM. Delichatsios, and YP. Lee. Mass pyrolysis rates and excess pyrolysate in fully developed enclosure. Fire Saf J, 39:121, 2004.

[69] Y. Hasemi. Experimental wall flame heat transfer correlations for the analysis of upward wall flame spread. Fire Sci Technol, 4:7590, 1984.

[70] J. Quintiere, M. Harkleroad, and Y. Hasemi. Wall flames and implications for upward flame spread. Combust Sci Technol, 48(34):191222, 1986.

[71] K. Li and X. Huang. Pyrolysis of Medium Density Fiberboard: Optimized Search for Kinetics Scheme and Parameters via a Genetic Algorithm Driven by Kissingers Method. Energy and Fuels. Combustion, 28:6130-6139, 2014.

[72] F. Kemple, B. Schartel, and G.T. Linteris, A. Hofmann-Bllinghaus. Prediction of the mass loss rate of polymer materials: Impact of residue formation. Combustion and Flame, 159(9):2974-2984, 2012.

[73] N. Bala and G. Rein. On the effect of inverse modelling and compresation effects in computational pyrolysis for fire scenarios. Fire safety journal, 72: 68-76, 2015.

[74] K. McGrattan and R. McDermott. Fire dynamics simulator user's guide, National Institute of Standards and Technology Report NIST special publication, 1019, 2016.

[75] G. Zhao, T. Beji, D. Zeinali and B. Merci. Numerical study on the influence of in-depth radiation in the pyrolysis of medium density fibreboard. Proceedings of the Fire and Materials Conference. pp.863-877, 2017.

[76] MDF material manufacturer : http://www.spanolux.com/en.

[77] R. Siegel and J.R. Howell. Thermal Radiation Heat Transfer. Taylor and Francis, New York, 4th edition, 56-68, 2002.

[78] X. Wang , Mohammad, M., Hu, L.J., and Salenikovich, A., Evaluation of density distribution in wood-based panels using X-ray scanning, Proceedings of the 14th International Symposium on Nondestructive Testing of Wood, University of Applied Sciences Eberswalde, Germany, 2005.

[79] K. Li. Determining thermal physical properties of pyrolyzing new Zealand medium density fibreboard. Chemical engineering science, 95:211-220, 2013.

[80] A. Gupta. Modelling and Optimisation of MDF Hot Pressing. PhD Dissertation, University of Canterbury, Christchurch, New Zealand, 2007.

[81] V. Hankalin. On thermal properties of a pyrolysising wood particle. Finnish-Swedish Flame Days, Naantali, Finland, 2009.

[82] X. Wang, S.R.A. Kersten, and W.P.m Prins. Biomass pyrolysis in a fluidized bed reactor. Part 2: Experimental validation of model results. Industrial &Engineering Chemistry Research, 44:8786-8795,2005.

[83] R. Younsi, D. Kocaefe, Poncsak, and Y. Kocaefe. Thermal modelling of the high temperature treatment of wood based on Luikovs approach. International Journal of Energy Research, Franks, C., Fire and Materials , Interscience Communications Ltd, London, UK, 30: 699-711, 2006.

[84] J. Saastamoinen. Simplified model for calculation of devolatilization in fluidized beds. Fuel,85:2388-2395, 2006.

[85] M.G. Gronli. Theoretical and experimental study of the thermal degradation of biomass. Doctoral dissertation. Trondheim. Norwegian University on Science and Technology, Faculty of Mechanical Engineering, Dept. of Thermal Energy and Hydropower. Norway, 1996.

[86] L. E. Brown. An experimental and analytical study of wood pyrolysis. Doctoral dissertation. The University of Oklahoma, 1972.

[87] M. Gupta, J. Yang, and C. Roy. Specific heat and thermal conductivity of softwood bark and softwood char particles. Fuel,82:919-927, 2003.

[88] W. Simpon and A. TenWolde. Physical properties and moisture relations of wood. In Forest products laboratory. Wood handbook.-Wood as an engineering material, 1999.

[89] V. Hankalin. On thermal properties of a pyrolysising wood particle. FinnishSwedish Flame Days, Naantali, Finland, 2009.

[90] A.F. Roberts. The heat of reaction during the pyrolysis of wood. Combustion and Flame. 17(1):79-86. 1971.

[91] F. Jiang, J.L. de Ris, and M.M. Khan. Absorption of thermal energy in PMMA by in-depth radiation. Fire Safety Journal 44:106-112, 2009.

[92] L. Gregory. Absorption and reflection of infrared radiation by polymers in fire-like environments. Fire and Materials,36(7):537553, 2012.

[93] https://en.wikipedia.org/wiki/Cone_calorimeter.

[94] H. Clayton. Estimation of rate of heat release by means of oxygen consumption measurements. Fire and Materials. 4(2): 61-65, 1980. doi:10.1002/fam.810040202.

[95] R.W. Shivanand. Development of a pyrolysis model for numerical simulations of flame spread over surfaces. Ph.D thesis. University of Ghent, 2010.

[96] D. Zeinali, T. Beji, G. Maragkos, J. Degroote, and B. Merci. Experimental study of upward and lateral flame spread on MDF boards in corner configurations. 2nd European Symposium of Fire Safety Science, Cyprus. 35-40, 2015. ISBN: 978-9963-2177-0-0.

[97] ISO 5660-1:2002(E): Reaction-to-fire tests - Heat release, smoke production and mass loss rate –Part 1: Heat release rate (cone calorimeter method), 2002.

[98] X. Wang, M. F. Charles, and M. J. Spearpoint. Parameterising study of tunnel experiment materials for application to the Fire Dynamics Simulator pyrolysis model. Journal of Fire Sciences, 19-24, 2016. DOI: 10.1177/0734904116667738.

[99] A. Matala and S. Hostikka. Pyrolysis modelling of PVC cable materials. In: Proceedings of the 10th international association for fire safety science (IAFSS), College Park, MD, 10: 917-930, 2011.

[100] M. Hjohlman and P. Andersson. Flame spread modelling of textile materials, SP Technical Research Institute of Sweden, SP Report, 2008. ISBN: 978-91-85829-51-4.

[101] H. Werner and H. Wengle. Large-eddy simulation of turbulent flow over and around a cube in a plate channel. In 8th Symposium on Turbulent Shear Flows, pages 155168, Munich, Germany, 1991.

[102] T. Beji. Theoretical and Experimental investigation on soot and radiation in fires. Ph.D thesis, University of Ulster, 2009.

[103] C.H. Bamford, J.Crank, and D.H. Malan. On the combustion of wood. Part I, Proceedings of the Cambridge Phil., 42:166-182, 1946.

[104] S. McAllister. Critical mass flux for flaming ignition of wet wood. Fire safety Journal, 61:200-206, 2013. https://doi.org/10.1016/j.firesaf.2013.09.002.

[105] S.B. Pope. Ten questions concerning the large-eddy simulation of turbulent flow. New Journal of Physics, 6:35,2004.

[106] R. McDermott. Fire Dynamics Simulator 6: Complex Geometry, Embedded Meshes, and Quality Assessment. In J.C.F. Pereira and A. Sequeira, editors, V European Conference on Computational Fluid Dynamics, Lisbon, Portugal, 2010.